Type-II GaAs/GaSb Quantum-Ring Light Emitting Diodes for Telecom-Band Emission

Gizem Acar Tekin

Department of Physics

Lancaster University

December 2025

This work is supported by European Union's Horizon 2020 research and innovation programme under the Marie Skłodowska-Curie grant agreement n° 956548, project Quantimony.

This thesis is submitted in partial fulfilment of the requirements for the degree of *Doctor of Philosophy* at Lancaster University.

Lancaster University

Declaration

I hereby declare that, except where specific reference is made to the work of others, the content of this thesis is my own work and has not been submitted in substantially the same form for the award of higher degree elsewhere.

Gizem Acar Tekin, December 2025

Abstract

This thesis presents the design, fabrication and experimental characterisation of type-II GaSb/GaAs quantum-ring (QR) light-emitting diode (LED) architectures aimed at enabling future electrically driven single-photon operation at telecommunication wavelengths. Generating high-purity quantum light in the telecom O-band (1260-1360 nm) remains a major challenge for practical quantum communication technologies, and type-II GaSb/GaAs heterostructures offer a promising route due to their reduced strain, strong hole confinement and naturally long-wavelength emission.

A series of GaSb/GaAs QR-LEDs were grown by molecular beam epitaxy (MBE), fabricated in multiple geometries, and characterised electrically and optically. Electroluminescence measurements revealed broadband type-II emission between 1.18 and 1.28 μm, current-induced blue-shifts, temperature-induced red-shifts and activation energies of 110-125 meV, consistent with expectations for strongly confined type-II heterostructures.

To address the intrinsic extraction bottleneck of semiconductor LEDs, a distributed Bragg transmitter (DBT) was designed by transfer-matrix modelling, grown monolithically as a seven-period GaAs/AlGaAs multilayer, and verified structurally by transmission electron microscopy and ellipsometry. DBT-integrated QR-LEDs exhibited a characteristic spectral modulation consistent with measured and simulated DBT transmission, together with enhanced collected electroluminescence. The strongest relative improvement occurred at low injection, where DBT devices showed up to an order-of-magnitude increase in collected output compared with reference devices, although device-to-device variation prevents this from being interpreted as a definitive absolute extraction-efficiency gain.

A cavity-integrated QR-SPLED architecture incorporating a GaAs quantum-dot electron-filter layer and a DBR-defined optical cavity was then realised. Across the full mesa series, these devices exhibited a single cavity-selected O-band line centred near 1.24-1.25 μm, with linewidths remaining stable in the ~10-12 nm range. Under fixed-current operation, the cavity mode remained spectrally robust from 20 °C to 80 °C, while the off-resonant background was systematically suppressed, yielding improved spectral cleanliness at low-to-moderate drive and particularly favourable operation in the 40-80 °C range. Although single-photon statistics were beyond the scope of this thesis, the demonstrated long-wavelength electrical injection, enhanced collected output, cavity-selected emission and thermal stability establish a wafer-scalable platform and define a practical operating window for future telecom-band SPLED implementation.

Overall, this work establishes a wafer-scalable platform for long-wavelength, electrically injected quantum-ring emitters and provides the methodology and experimental foundations required for future demonstration of single-photon performance. The insights obtained extend more broadly to type-II semiconductor optoelectronics and cavity-engineered light-emitting devices.

Acknowledgment

The completion of this thesis has been made possible by the support, guidance, and generosity of many people, to whom I would like to express my sincere gratitude. I would like to express my deepest gratitude to my supervisor, Prof. Manus Hayne, for his guidance, encouragement, and support throughout my PhD. His insight, patience, and continued belief in my work have been invaluable throughout this journey. I am also especially grateful for his generous support and encouragement beyond academia, particularly in opening the door for me to pursue my entrepreneurial path. I would also like to sincerely thank my deputy supervisor, Prof. Robert Young, and my independent advisor, Dr Julie Wardlow, for their support and guidance during my PhD. My special thanks go to Dr Peter Hodgson for carrying out the MBE growths and for the guidance he provided throughout my PhD. I am truly grateful for his support and willingness to share his knowledge.

I would like to thank Prof. Richard Beanland and Dr Francisco Alvarado Cesar at the University of Warwick for the TEM measurements and their valuable contribution to this work. I am also sincerely grateful to Dr Stefan Birner for his hospitality and support during my secondment at nextnano in Germany. My sincere thanks go to Dr Benito Alén, Giulio Barbieri, and Cecilia Cotero at CSIC-IMN Madrid for their help with the PL, TRPL, and ellipsometry measurements, and for their kindness and hospitality during my time in Spain. I would also like to sincerely thank Dr Andrei Schliwa and Dr Lucie Leguay from Technische Universität Berlin (TU Berlin) for their valuable collaboration on the simulation aspects of this work and for the conference paper we co-authored together. I am grateful to all my colleagues in the Manus Hayne group for creating a supportive and stimulating research environment, and for all the discussions, help, and shared experiences along the way. I would also like to acknowledge the Quantimony project and the Marie Skłodowska-Curie Actions programme for providing me with the opportunity to be part of such an inspiring research network. I am thankful to everyone involved in Quantimony for making it such a valuable and enriching experience.

My sincere thanks also go to Prof. Ali Koşar for his support and mentorship both before and throughout my PhD. I would like to express my heartfelt gratitude to Elizabeth Mullis and Jeremy Gidlow for believing in me and supporting me during the journey of building Photarix, and for making me feel that I was not alone on that path.

To my dear friends, Sema Yıldırım, Bahar Aksu, Eda Mert Gökduman, Mustafa Mert Gökduman, and Can Çalışkan, thank you for always being there for me, for your friendship, encouragement, and support through all the highs and lows of this journey.

Finally, I would like to express my endless gratitude to my family; my mother, father, and brother; for their unconditional love, patience, and support. I would not have come this far without them.

And to my beloved husband, Serdar Tekin; thank you for standing beside me through every high and low, and for being my constant through every experiment of life. Without your love, patience and belief in me, this journey would not have held the same meaning.

Publications and Presentations

Publications

Towards GaSb/GaAs Quantum-Ring Single-Photon LEDs: Recent Progress and Prospects *SPIE Photonics West, Conference Proceedings*, Gizem Acar, Lucie Leguay, Samuel Jones, Peter Hodgson, Andrei Schliwa, and Manus Hayne (2024). Proc. SPIE **12906**, Light-Emitting Devices, Materials, and Applications XXVIII, 1290609.

Conference Presentations and Posters

GaSb Quantum Rings for Telecom-Wavelength Secure Photonics, Quantum and Optical Research Initiative (QuORI) Symposium, *Belfast, UK,* Oral Presentation (2025) (Invited)

Enhancing Quantum Photonics: Novel Single Photon LEDs Utilizing GaSb Quantum Rings at Telecoms Wavelength, Iqarus - International Workshop on Quantum Antimonides Research & Upscaling*, San Sebastian, Spain,* Oral Presentation (2024).

Advanced GaSb Quantum Ring LEDs with Distributed Bragg Transmitter for Telecom Wavelength Applications, Iqarus - International Workshop on Quantum Antimonides Research & Upscaling*, San Sebastian, Spain,* Poster (2024).

Telecoms Wavelength Single-Photon LEDs utilising GaSb Quantum Rings, UK Semiconductors Conference, *Sheffield, UK,* Oral Presentation (2024).

Advances in Room-Temperature Single-Photon LEDs Using GaSb/GaAs Quantum Rings, The Annual 37th Semiconductor Integrated OptoElectronics Conference (SIOE), *Cardiff, UK,* Oral Presentation (2024).

Novel GaSb Quantum Ring Light Emitting Diodes (QR-LED) with Distributed Bragg Transmitter (DBT) Operating at Telecommunication Wavelengths, The Annual 37th Semiconductor Integrated OptoElectronics Conference (SIOE), *Cardiff, UK,* Oral Presentation (2024).

Type-II GaSb Quantum Rings for Telecom-Wavelength LEDs, The 12th International Conference on Quantum Dots, *Munich, Germany,* Poster (2024).

Towards GaSb/GaAs Quantum-Ring Single-Photon LEDs: Recent Progress and Prospects, SPIE Photonics West, *San Francisco, USA,* Oral Presentation (2024).

Cavity-Enhanced Emission using GaSb Quantum Rings at Telecom Wavelengths, iNOW 2023-The International Nano-Optoelectronics Workshop, *Wurzburg, Germany,* Poster (2023).

Exploring Cavity-Enhanced Emission from Type-II GaSb Quantum Ring Devices at Telecommunication Wavelengths, UK Semiconductor Conference, *Sheffield, UK,* Oral Presentation (2023)

Enhancing the Efficiency of Type-II GaSb Quantum Ring Devices at Telecommunication Wavelengths Using Cavity Effects, WOCSDICE EXMATEC, *Palermo, Sicily,* Oral Presentation (2023).

Cavity Effects in Type-II GaSb Quantum Ring Devices at Telecommunication Wavelengths, The Annual 36th Semiconductor Integrated OptoElectronics Conference (SIOE), *Cardiff, UK,* Oral Presentation (2023).

Telecoms-wavelength GaSb quantum ring LEDs with a distributed Bragg transmitter (DBT) for enhanced emission, UK Semiconductors Conference, *Sheffield, UK,* Oral Presentation (2022).

Telecoms-wavelength LEDs: Combining GaSb Quantum Rings and Bragg (anti)reflectors For Enhanced Emission, The Annual 35th Semiconductor Integrated OptoElectronics Conference (SIOE), *Cardiff, UK,* Oral Presentation (2022).

Contents

List of Figures

List of Tables

Chapter 1 Introduction

1. 1 Motivation

The generation and control of quantum light, particularly single photons, has become a cornerstone of modern quantum technologies, underpinning quantum key distribution (QKD), photonic quantum computing and secure quantum communication networks. As global quantum infrastructure transitions toward practical deployment, there is an urgent need for room-temperature, electrically driven single-photon light-emitting devices (SPLEDs) operating within the low-loss telecommunications window (1260-1675 nm). Achieving the combination of high efficiency, spectral purity, electrical injection, wafer-scale integration, and cost-effective fabrication remains a formidable challenge. These spectral regions, covering the O-, E-, S-, C- and L-bands, correspond to the minimal-attenuation windows of standard silica optical fibres and therefore define the most favourable operating wavelengths for long-distance quantum communication. Figure 1.1. illustrates their position within the broader electromagnetic spectrum and highlights that telecom-band operation is essential for compatibility with existing fibre networks.

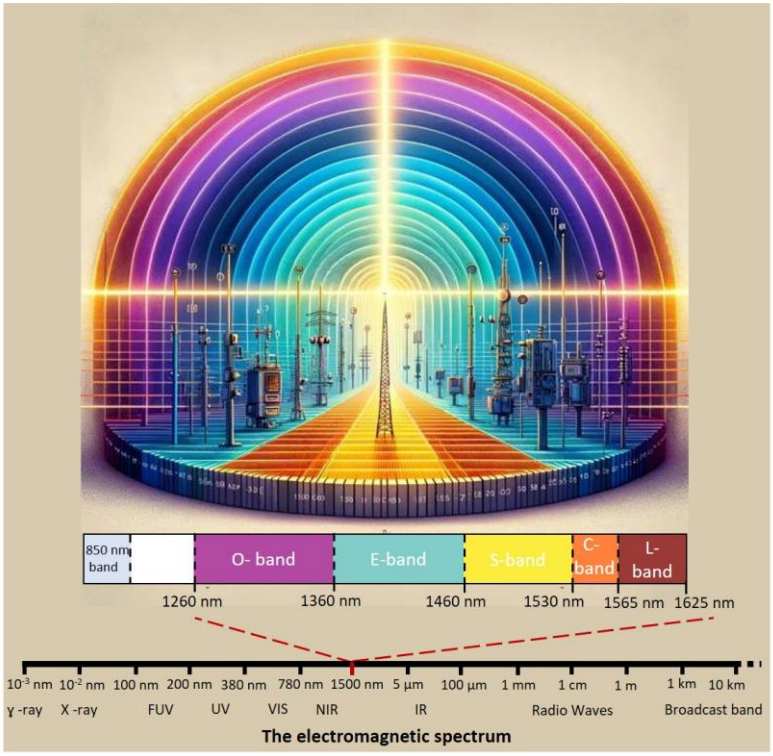

Fig. 1.1: Illustration of the electromagnetic spectrum showing the low-loss telecommunications windows (O-, E-, S-, C-, L-bands). These wavelength regions correspond to the minimal-attenuation windows of standard silica fibres and therefore define the optimal operating range for quantum light sources used in long-distance quantum communication.

Semiconductor quantum nanostructures, especially quantum dots (QDs) and quantum rings (QRs), offer a compelling pathway due to their compatibility with mature optoelectronic fabrication platforms and potential for large-scale integration. Yet many existing implementations are limited by sub-telecom emission, cryogenic operating temperatures or

reliance on complex post-fabrication spectral filtering. As a result, a persistent gap remains: no integrated, electrically injected, wafer-scale single-photon source has demonstrated simultaneous achievement of (i) near-room-temperature operation, (ii) telecom-band emission, (iii) fibre-compatible integration, (iv) practical efficiency.

This thesis addresses this gap by advancing a type-II GaSb/GaAs quantum-ring platform in which the spatial separation of electrons and holes across the heterojunction produces emission naturally aligned with the O-band and lower C-band. Type-II GaSb/GaAs nanostructures benefit from reduced strain, low defect densities and deep hole confinement, enabling efficient operation at accessible temperatures. By integrating quantum-ring emitters with engineered photonic environments, including distributed Bragg transmitters (DBTs) for enhanced out-coupling and distributed Bragg reflectors (DBRs) for cavity-enhanced spectral selection, this work builds a practical architecture for high-performance single-photon sources at telecom wavelengths.

1. 2 Scope and Objectives

The overarching goal of this thesis is to design, fabricate, and experimentally characterize GaSb/GaAs quantum-ring light-emitting diodes (QR-LEDs) and single-photon light-emitting diodes (QR-SPLEDs) optimized for telecommunications applications. Specifically, the work aims to:

• Establish the physical and material foundations underlying type-II heterostructure optoelectronics, including band structure, carrier transport, recombination mechanisms and optical coupling;

• Synthesise the current state of the art in single-photon sources and situate type-II GaSb/GaAs QRs within the broader quantum-light landscape;

• Design, fabricate and characterise GaSb/GaAs QR-LEDs, examining the influence of device geometry and lateral dimensions on current distribution, thermal management and spectral behaviour;

• Enhance extraction efficiency by integrating a novel DBT structure and experimentally validate improvements in photon escape probability;

• Demonstrate an integrated SPLED architecture combining type-II QRs, a GaAs QD single-electron filter and a DBR-defined optical cavity, achieving controlled, thermally stable emission across the 20-80 °C operating range.

In addition to these objectives, the thesis makes the following original contributions: (i) establishing and experimentally validating a telecom-aligned type-II GaSb/GaAs quantum-ring LED platform under electrical injection;

(ii) a systematic study of device geometry and lateral scaling linking current spreading, thermal behaviour and spectral signatures;

(iii) introducing and demonstrating a distributed Bragg transmitter (DBT) concept tailored for telecom wavelengths, supported by transfer-matrix modelling and experimental validation;

(iv) realising a cavity-integrated QR-LED architecture incorporating a single-electron filtering stage, enabling cavity-selected emission with thermal robustness across 20-80 °C and establishing a pathway towards electrically driven single-photon operation.

1. 3 Thesis Structure

Chapter 2 (Background Theory) establishes the essential physics framework. Beginning with the electronic structure of semiconductors, energy bands and carrier statistics, it develops the theory of carrier transport under equilibrium and bias, recombination mechanisms and optical processes central to light-emitting diodes. Special attention is given to III-V compound semiconductors and type-II heterostructures relevant to telecom-wavelength emitters, with all derivations kept to essentials and assumptions clearly stated.

Chapter 3 (Literature Review) presents a comprehensive synthesis of single-photon source (SPS) technologies operating in the low-loss telecom bands. It surveys semiconductor quantum structures, solid-state defect-based emitters, and photon-pair sources, compares their performance metrics and integration challenges and positions type-II GaSb/GaAs quantum-ring emitters within this landscape. The chapter highlights how QR-based devices could address persistent challenges, particularly room-temperature operation and wafer-scale scalability, while acknowledging inherent trade-offs such as slower radiative recombination. It concludes by distilling evaluation criteria that guide the subsequent experimental work.

Chapter 4 (Experimental Methods) outlines the techniques used throughout the thesis: molecular beam epitaxy (MBE) for wafer growth, photolithography and reactive-ion etching for device fabrication, electrical characterization (current-voltage curves), optical characterization (electroluminescence spectroscopy), and structural imaging (transmission electron microscopy). These methods form the backbone of device realization and validation.

Chapter 5 (GaSb Quantum-Ring LEDs) presents the first experimental demonstration of GaSb/GaAs QR-LEDs fabricated from a single MBE-grown wafer. The chapter compares two device geometries, finger-shaped and ring-shaped contacts, across three lateral dimensions (1 mm, 0.5 mm and ≤200 μm), assessing their influence on current-density uniformity, thermal management and spectral stability. Electroluminescence measurements reveal the canonical signatures of type-II emission: broadband spectra in the 1.18-1.28 μm range, current-induced blue-shift driven by field screening and temperature-induced red-shift due to band-gap narrowing. Activation energies around 110-125 meV confirm strong carrier confinement and effective suppression of non-radiative recombination in well-passivated geometries.

Chapter 6 (GaSb Quantum-Ring LEDs with Distributed Bragg Transmitters) addresses a fundamental efficiency bottleneck in semiconductor LEDs: photon escape. By integrating a novel distributed Bragg transmitter, specifically engineered to minimize surface reflection at the target telecom wavelength while maintaining full lattice compatibility, this chapter demonstrates

significant improvements in light extraction efficiency. Transfer-matrix simulations optimize alternating GaAs/ $Al_xGa_{(1-x)}As$ layers for near-zero reflectivity and experimental validation via electroluminescence measurements and transmission electron microscopy confirms the predicted gains in photon transmission from the active region into free space.

Chapter 7 (GaSb/GaAs Quantum-Ring SPLEDs) presents the culmination of the work: an integrated single-photon LED architecture combining type-II GaSb/GaAs quantum rings, a GaAs quantum-dot single-electron filter for resonant carrier injection and a DBR-defined optical cavity for spectral selection. The vertical stack is detailed, from growth sequence through micro-fabrication and experimental characterization demonstrates strong, stable cavity-enhanced emission with diode-like current-voltage behaviour and suppression of off-resonant background as temperature is raised across the practical 20-80 °C range.

Chapter 8 (Conclusion and Future Work) synthesizes the key findings, contextualizes their significance within the broader quantum-photonics landscape, and outlines concrete directions for future development, including scalability, integration platforms and emerging applications in quantum networks.

1. 4 Significance and Impact

This thesis contributes to the development of practical quantum communication technologies by examining the optoelectronic behaviour of type-II GaSb/GaAs quantum rings integrated with engineered optical stacks and single-electron filtering structures. The results provide insight into how these architectures behave under electrical injection at telecom wavelengths and near-room-temperature conditions, and they establish a device platform that may be further refined toward single-photon operation in future work.

By integrating materials engineering, device physics and experimental nanophotonics, this thesis advances the scientific understanding and technological maturity of type-II GaSb/GaAs quantum-ring emitters, offering methodologies and design strategies relevant to a broader class of semiconductor quantum-optical devices.

This work has been disseminated through one peer-reviewed SPIE conference proceeding and multiple conference presentations and posters. Building on the results reported in this thesis, journal publications are planned, focusing on: (i) DBT-enabled extraction enhancement supported by modelling and experimental validation; and (ii) the cavity-integrated architecture incorporating single-electron filtering as a route towards telecom-wavelength single-photon emitters.

Beyond its scientific contributions, this research has also led to the formation of Photarix Ltd, a Lancaster University spin-out company founded to commercialise GaSb/GaAs quantum-ring single-photon sources for quantum-secure communication. The device concepts, design methodologies and experimental results developed in this thesis form a core part of Photarix's underlying technology, illustrating a direct pathway from fundamental research to emerging quantum-technology application.

Chapter 2 Background Theory

Semiconductor devices are governed by the physics of the materials from which they are built. This chapter establishes the physical framework needed to analyse the devices studied in this thesis. We begin with the electronic structure of semiconductors, energy bands, effective masses and carrier statistics, then develop carrier transport under equilibrium and bias, including drift-diffusion, recombination-generation pathways and quasi-Fermi levels. Building on this, we treat optical processes central to light-emitting diodes: radiative efficiency, non-radiative loss channels and the coupling of active regions to optical modes. Where helpful for later chapters, attention is given to III-V compounds and type-II heterostructures relevant to telecom-wavelength emitters. Derivations are kept to essentials; results are stated with assumptions and limits of validity to support practical device modelling.

2.1. Fundamentals of III-V Semiconductor Physics for Optoelectronics

The development of optoelectronic devices such as light emitting diodes (LEDs), lasers, detectors and single-photon emitters critically depends on a thorough understanding of semiconductor physics. In particular, III-V compound semiconductors are formed by combining elements from groups III (e.g., Ga, In) and V (e.g., As, Sb). III-V semiconductors play a central role in modern optoelectronics owing to their direct bandgap properties, high carrier mobility and tuneable electronic structures [13], [14]. These materials underpin devices such as LEDs, laser diodes (LDs), photodetectors operating beyond the silicon band edge and high-efficiency multijunction solar cells, all of which rely on controlled light emission and absorption [14], [15], [16],[17].

Two key aspects fundamentally govern the performance of III-V optoelectronic devices:

1) Electronic band structure and carrier dynamics dictate transport properties and optical interactions [18].

2) Carrier recombination mechanisms determine efficiency by balancing radiative and non-radiative processes [18].

This section explores these aspects in detail, beginning with the fundamental physics of III-V semiconductors and followed by carrier recombination mechanisms. The discussion then turns to GaSb-based type-II heterostructures, a specific material platform that offers advantages for mid-infrared (MIR) applications by reducing Auger recombination and enabling long-wavelength emission[19].

2.1.1. Electronic Band Structure of III-V Semiconductors

The remarkable electrical and optical characteristics of III-V compound semiconductors make them highly important for optoelectronic applications. Their ability to support direct interband transitions makes them highly efficient for photon emission, making them the material of choice for light-emitting diodes (LEDs), lasers and single-photon light-emitting diodes (SPLEDs). The electronic band structure of a semiconductor determines its photon

emission efficiency, absorption properties and carrier dynamics. III-V semiconductors, such as GaAs, InAs and GaSb, exhibit a zinc-blende crystal structure, where the periodic potential of the lattice defines the allowed energy bands for charge carriers [20].

The band structure of a semiconductor describes the allowed energy states for electrons and holes within the material. In III–V semiconductors, the periodic crystal potential gives rise to electronic bands, including a conduction band (CB) and a valence band (VB). Electrons occupy states in the CB, while holes correspond to unoccupied states near the top of the VB and can move through the lattice as effective positive charge carriers. [21]. The energy difference between the conduction and valence bands determines the bandgap energy (E_g), which determines the photon energy and thus the emission wavelength, when electrons and holes recombine radiatively [21].

A key distinction among semiconductors is whether they exhibit a direct or indirect bandgap. In direct bandgap materials, such as GaAs and InAs, the conduction band minimum and valence band maximum occur at the same momentum (k) value. This alignment enables effective radiative recombination, where an electron can transition from the conduction band to the valence band, generating a photon in the process. This characteristic makes direct bandgap semiconductors ideal for optoelectronic applications [22]. GaSb is also typically classified as a direct bandgap material at room temperature [23]. In contrast, indirect bandgap semiconductors, such as silicon and germanium, rely on phonon interactions to conserve momentum during recombination, making photon emission inefficient. This requirement significantly reduces the probability of photon emission, making these materials less suitable for optoelectronic applications [24], [25]. The difference between direct and indirect bandgaps and their impact on absorption and emission processes, is illustrated in Fig. 2.1.

The photon wavelength (λ) of emitted light corresponds to the semiconductor bandgap energy given by

$$Eg = \frac{hc}{\lambda}, \tag{2.1}$$

where h is Planck's constant and c is the speed of light. For example, GaSb has a bandgap of approximately 0.726 eV at room temperature, corresponding to an emission wavelength of around 1710 nm. However, through heterostructure design and quantum confinement, the effective transition energy can be tuned to reach telecom-relevant wavelengths of 1310 nm and 1550 nm, making GaSb-based nanostructures appealing candidates for optical communication applications.

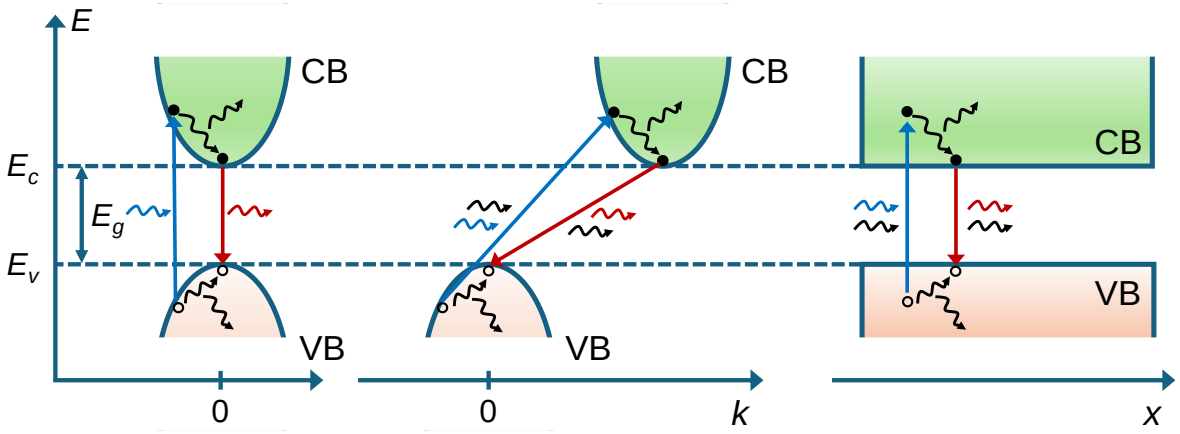

Fig. 2.1: Schematic illustration of simplified semiconductor band structures: (a) direct and (b) indirect band gaps in momentum k space, showing parabolic conduction (CB) and valence (VB) bands and (c) a real-space band diagram with only the band edges indicated. In each case, absorption of a high-energy photon (blue) generates an electron-hole pair, which then loses excess energy through phonon emission (black). Radiative recombination follows, releasing a photon with band-gap energy (red). In indirect transitions, phonon involvement is required, as shown by the black arrows. The vertical axis represents energy in all diagrams [1], [2].

2.1.2. Fermi Level and Carrier Density in III-V Semiconductors with a GaSb/GaAs QR-LED Case Framework

This subsection reviews general equilibrium semiconductor physics (Fermi level, effective density of states, non-degenerate limits) applicable to III-V compounds. Where a concrete example is helpful, we reference a GaSb/GaAs type-II quantum-ring LED as a running case study. Equations are given for bulk, unstrained materials unless stated otherwise.

The Fermi level (E_F) is a fundamental term in semiconductor physics that defines the energy level where the probability of electron occupancy is 50% at thermal equilibrium. In thermal equilibrium, the Fermi-Dirac distribution determines carrier distributions over the conduction and valence bands. For intrinsic semiconductors, E_F is around halfway between the conduction band minimum (E_c) and valence band maximum (E_v). However, with III-V semiconductors such as GaSb (a direct bandgap material), the precise location of E_F is critical due to its direct influence on radiative transitions. Carrier densities are derived from the following expressions [26], [27]

$$n = N_C \exp\left(-\frac{E_C - E_F}{kT}\right), \qquad p = N_v \exp\left(-\frac{E_F - E_v}{kT}\right), \tag{2.2}$$

where N_C and N_v denote the effective density of states in the conduction and valence bands, respectively.

$$N_C = 2\left(\frac{2\pi m_e^* kT}{h^2}\right)^{3/2} \tag{2.3}$$

is the effective density of states in the conduction band and

$$N_v = 2\left(\frac{2\pi m_h^* kT}{h^2}\right)^{3/2} \tag{2.4}$$

is that of the valence band, where m_e^* and m_h^* are the effective masses of electrons and holes, respectively.

The effective masses, m_e^* and m_h^*, come from the curvature of the conduction and valence bands in $E(k)$ space, given by

$$\frac{1}{m^*} = \frac{1}{\hbar^2}\frac{d^2E}{dk^2}. \tag{2.5}$$

A larger band curvature (greater second derivative) corresponds to a lighter effective mass, while a flatter band corresponds to a heavier effective mass.

In III-V semiconductors, these parameters are highly material-dependent at 300 K as summarised as experimental and simulation results in the table 2.1.

Table 2.1. Properties of GaAs and GaSb at 300 K [9],[10], [11], [12].

Material	**Bandgap (Eg)**	m_e^*/m_0	m_h^*/m_0	N_C **(cm⁻³)**	N_v **(cm⁻³)**
GaAs	1.42 eV	0.063	~0.5	~4.7×10^{17}	~9.0×10^{18}
GaSb	0.73 eV	0.041	~0.35	~1.0×10^{17}	~4.0×10^{18}

GaSb has a narrower bandgap and lower effective masses than GaAs, making carrier concentration considerably more sensitive to changes in E_F. A modest upward shift in E_F causes an exponential increase in n, which is advantageous for radiative recombination in light-emitting devices [26], [28].

These bulk material parameters provide the starting point for understanding the GaSb/GaAs quantum-ring LED platform examined in this thesis. When GaSb is combined with GaAs to form a heterostructure, the relative positions of the band edges become as important as the individual bulk bandgaps. In the GaSb/GaAs system, the bands align in a type-II configuration, so electrons and holes preferentially localise in different parts of the structure.

In type-II GaSb/GaAs nanostructures, the spatially indirect transition reduces electron-hole wave-function overlap, leading to longer radiative lifetimes and typically lower spontaneous emission rates than comparable type-I III-V nanostructures. Consequently, device-level efficiency hinges on injection balance and optical extraction rather than intrinsically high radiative strength. In such intrinsic or nearly intrinsic materials, carrier densities are

determined not by impurity ionisation, but by carrier injection from nearby doped areas under forward bias [29], [30].

Because of its intrinsic characteristics, the Fermi level E_F in undoped GaSb is around mid-gap at thermal equilibrium. However, with carrier injection, the system deviates from equilibrium, making the idea of quasi-Fermi levels critical. The chemical potentials of the carrier distributions are represented by the electron and hole quasi-Fermi levels, E_{Fn} and E_{Fp}, whose separation, E_{Fn} - E_{Fp}, controls the rate of radiative recombination [31], [32]

$$R \propto np = N_C N_v \exp\left(-\frac{E_g-(E_{Fn}-E_{Fp})}{kT}\right) \quad (2.6).$$

In equilibrium, the term band gap of GaSb refers to the unstrained bulk value (about 0.73 eV at 300 K; about 0.81 eV at 0 K) [33]. Quantum confinement does not change the band gap; it adds electron and hole quantisation energies, thereby shifting the transition energy observed in nanostructures [34]. In type-II GaSb/GaAs heterostructures, the radiative transition is spatially indirect (electrons in the GaAs side, holes in the GaSb side), so the emitted photon energy is set by band offsets, strain-induced shifts and quantisation, not by the GaSb bulk gap alone [35], [36]. Because the electron-hole wave-function overlap is reduced in type-II systems, radiative lifetimes are typically longer (i.e., intrinsic radiative rates are lower) than in comparable type-I III-V nanostructures [37]. Under injection, the electron and hole electrochemical potentials (often termed quasi-Fermi levels) separate; this splitting controls the nonequilibrium carrier populations and thus the recombination rate, but it does not negate the overlap limitation inherent to type-II alignment [38], [39], [11].

2. 1.2.1. Effect of Doping on Carrier Concentration in GaAs-Based Devices

This subsection treats general doping-carrier statistics with a GaAs/ $Al_xGa_{(1-x)}As$ /GaSb QR-LED as a running framework. Doping is the primary method for tuning the electrical conductivity, Fermi level position and carrier injection efficiency in semiconductor devices. In GaAs-based heterostructures, such as GaAs/ $Al_xGa_{(1-x)}As$ /GaSb quantum ring LEDs, doping is carefully engineered in the GaAs and $Al_xGa_{(1-x)}As$ layers to optimise carrier delivery to the active region, confine injected carriers and minimize non-radiative losses [31], [32].

Doping introduces fixed space charge from ionised dopants and creates mobile carriers. For n-type material, donors ionise as $D^0 \rightarrow D^+ + e^-$, introducing levels near the conduction-band edge (E_C); this raises the equilibrium Fermi level (E_F) and increases the electron concentration (n). For p-type material, acceptors ionise as $A^0 \rightarrow A^- + h^+$, adding levels near the valence-band edge (E_V); this shifts E_F downward toward E_V and increases the hole concentration (p).

In the non-degenerate, fully ionised and weakly compensated limit (e.g. shallow donors/acceptors in GaAs near room temperature), the majority-carrier density follows the

dopant density to first order: $n_e \approx N_D$ (for n-type) and $p \approx N_A$ (for p-type), where N_D and N_A are donor and acceptor concentrations and are assumed to be fully ionised.

More generally, with compensation one has $n_e \approx N_D^+ - N_A^-$ (n-type) and $p \approx N_A^- - N_D^+$ (p-type), while at lower temperatures or with deeper levels incomplete ionisation must be considered.

The n-type GaAs substrates are typically doped with silicon (Si) or tellurium (Te) to provide a reservoir of electrons. For shallow donors that are (near) fully ionised at 300K, $n_e \approx N_D$. $N_D = 10^{17}$ cm^{-3} one finds $E_C - E_F \approx kTln(N_c/n_e) \approx 40$ meV(non-degenerate), while for $N_D = 10^{18}$ cm^{-3} E_F lies about 20meV above E_C (mildly degenerate) [26], [11], [12], [31]. This layer establishes the electrostatic boundary condition for energy band simulations and plays a key role in carrier injection.

The n-type GaAs layer above the substrate provides the lateral electron transport channel and the supply of mobile electrons. The adjacent AlGaAs layer has a larger band gap and a higher conduction-band edge than GaAs, so it acts as a vertical confinement (cladding) layer rather than a source of injection [40]. Under forward bias, electrons travel laterally within n-GaAs and are captured at the GaAs/GaSb interface (type-II alignment), while the AlGaAs barrier suppresses leakage toward the surface and unintended layers by forming a GaAs quantum well relative to AlGaAs ($\Delta E_C > 0$) [40], [41]. In short, the barrier does not push electrons into GaSb; it funnels and retains them on the GaAs side near the active interface, improving carrier availability for recombination [32],[42].

In this work the active GaSb layer is intentionally undoped (i) and sandwiched between an n-type GaAs transport layer (Si/Te-doped) and a p-type $Al_xGa_{1-x}As$/GaAs cladding + cap (Be/C/Zn-doped). This n-i-p arrangement is what we refer to as an asymmetric doping profile: majority electrons are sourced on one side (n-GaAs) and majority holes on the other (p-AlGaAs/GaAs), while the active region remains intrinsic.

The doping concentrations govern the spatial distribution of:

- Built-in electric fields, which arise from charge imbalances across the junction and are described quantitatively by Poisson's equation;
- Band bending, particularly at the AlGaAs/GaAs interfaces, where discontinuities in band edge energies can lead to the formation of potential barriers or wells;
- The carrier diffusion lengths and lifetimes, which are dependent on doping concentration through increased impurity scattering and trap-assisted recombination.

Optimising the doping concentrations across the structure accomplishes several objectives that include:

- Ensure the effective injection of electrons and holes into the undoped GaSb quantum rings;
- Suppressing carrier leakage and decreasing surface/interface recombination, particularly in etched nanostructures;
- Establishing a favourable band alignment at the AlGaAs/GaSb interface to encourage radiative recombination in the GaSb region [43], [44].

2.2. Heterojunctions and Carrier Confinement in LED Structures

The heterostructure concept has been essential to current optoelectronics, allowing for energy band tailoring, selective carrier confinement and efficient photon emission. Heterojunctions produce contacts between different semiconductors, introducing band offsets that may be tailored to regulate carrier dynamics and optical characteristics. This structural flexibility is especially effective in III-V systems, where a diverse variety of binary, ternary and quaternary alloys with lattice-matched combinations are attainable.
In this section, the three main types of band alignments will be evaluated, exploring their influence on carrier recombination and why GaSb-based Type-II heterostructures are highly suited for telecom-wavelength and single-photon light-emitting devices.

2. 2.1. Band Alignments: Type-I, Type-II and Type-III

Heterojunctions are characterised according to the relative locations of the conduction band minima (CBM) and valence band maxima (VBM) of adjacent semiconductors. This alignment determines the spatial spacing of carriers, radiative recombination dynamics and, ultimately, the device's emission wavelength. Figure 2.2 shows the three alignment types.

In practice, the relative band-edge positions can be estimated using the electron affinity rule [31], [45] as a first approximation. If the electron affinities (χ) and bandgaps (E_g) of two semiconductors are known, the conduction-band offset can be approximated as $\Delta EC \approx \chi_2 - \chi_1$, and the valence-band offset follows from $\Delta E_V \approx (E_{g2} - E_{g1}) - \Delta E_C$ (sign conventions depend on the chosen reference). These estimates provide a useful “cartoon” band diagram and allow prediction of type-I/II/III alignment. However, real heterointerfaces can deviate due to interface dipoles, bonding, defects and strain-induced band shifts; therefore, experimentally reported offsets are typically used when quantitative accuracy is required. Complementary evidence for carrier localisation and spatial separation can also be obtained from optical spectroscopy (e.g., temperature-dependent PL/EL) and, where available, magneto-optical measurements (magneto-PL), which probe excitonic confinement via field-dependent energy shifts.

- **Type-I (Straddling Gap)**: Both the CBM and VBM of the narrower bandgap material lie within the bandgap of the wider-gap material. This causes electrons and holes to co-localise, resulting in a significant spatial overlap of their wavefunctions. As a result, radiative recombination is efficient and produces large rates of spontaneous emission. This configuration is common in systems like GaAs/AlGaAs and is typically used in conventional LEDs, lasers and quantum wells [32].
- **Type-II (Staggered Gap):** The CBM and VBM reside in different materials, resulting in spatial separation of electrons and holes across the interface. For instance, in GaSb/GaAs heterostructures, electrons are typically in the GaAs layer, while holes reside in GaSb. This spatial displacement reduces wavefunction overlap, leading to weakened direct recombination rates and significantly extended carrier

lifetimes. The resulting optical transitions occur across the bandgap formed between the two materials, allowing emission at longer wavelengths than either bandgap alone would permit. Type-II heterojunctions are of particular interest in telecom-wavelength emitters and single-photon sources, where both spectral tuning and temporal control over recombination are critical. In systems like GaSb/GaAs, holes are typically localised in GaSb, while electrons are quasi-bound in the neighbouring GaAs layer. The resulting spatially indirect excitons experience reduced overlap but enhanced lifetime and stability, making them attractive for infrared applications. The band alignment features opposing offsets in the conduction and valence bands (ΔE_C , ΔE_V), which set the electron and hole confinement barriers. Because spatial separation reduces wave-function overlap, radiative rates are lower than in type-I structures. The temperature dependence of the emission is then dominated by activation of non-radiative channels (e.g., traps) and thermal escape over the offsets; with high-quality interfaces and sufficiently large ΔE_C, ΔE_V , thermal quenching can be mitigated, but it is not guaranteed [16], [46], [47], [48], [49].

- **Type-III (Broken Gap):** In Type-III alignment, the CBM of one semiconductor lies below the VBM of the adjacent material, leading to a band overlap. This "broken-gap" condition enables interband tunnelling, making such systems attractive for tunnelling field-effect transistors (TFETs) and infrared detectors. For example, InAs/GaSb superlattices, which are foundational in interband cascade lasers and resonant tunnelling devices [50], [51], [52].

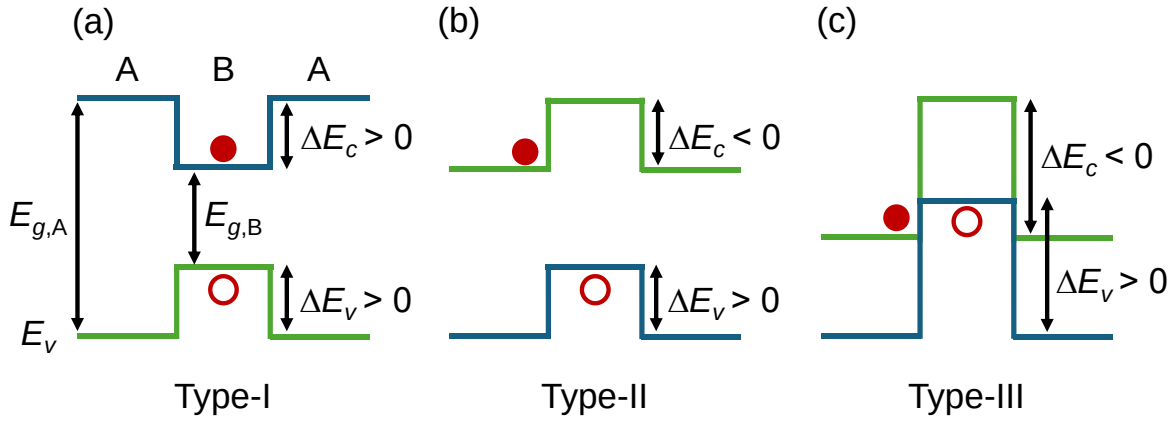

Fig. 2.2: Schematic band alignments at a heterointerface. (a) Type-I (straddling gap): electrons and holes confined in the same material; strong overlap and high radiative rate. (b) Type-II (staggered gap): electrons and holes localise on opposite sides of the interface; reduced overlap and longer lifetimes; emission energy set by band offsets ΔE_C, ΔE_V plus strain/quantisation. (c) Type-III (broken gap): the conduction band of one material lies below the valence band of the other. (Schematic-not to scale.) [7].

2. 2.2. Lattice Matching and Strain Effects in III-V Heterostructures

The performance of epitaxially grown optoelectronic devices is strongly dependent on the crystalline quality of the layers and the integrity of their interfaces. One of the most

important factors influencing this quality is lattice matching between adjacent semiconductor materials. In ideal conditions, the lattice constants of the two materials in a heterojunction should be identical or nearly identical to allow coherent, defect-free epitaxial growth. When a mismatch exists, strain builds up at the interface, and if not carefully managed, it can relax through the formation of misfit dislocations, stacking faults, or other crystallographic defects that are highly detrimental to carrier mobility and radiative efficiency.

In III-V systems, the degree of mismatch is typically quantified by the relative difference in lattice constants:

$$Mismatch = \frac{a_{layer} - a_{substrate}}{a_{substrate}} \times 100\% \quad (2.7)$$

where a_{layer} and $a_{substrate}$ are the lattice constants of the epitaxial material and the substrate, respectively. A mismatch below ~0.1-0.2% is generally considered acceptable for the growth of many monolayers without the introduction of dislocations [22], [53]. However, when this threshold is exceeded, strain relaxation mechanisms are activated, leading to threading dislocations that propagate vertically through the structure and act as highly efficient non-radiative recombination centres [54]. In the case of GaSb-based heterostructures, lattice matching becomes a particularly relevant design constraint. GaSb has a relatively large lattice constant (~6.0959 Å at 300 K), which makes it incompatible with more commonly used III-V substrates like GaAs (~5.6533 Å) with a mismatch of over 7.83% (Fig. 2.3) [11], [12], [55]. Growing GaSb directly on such substrates would result in highly defective interfaces unless thick buffer layers or metamorphic grading techniques are employed. On the other hand, InAs, with a lattice constant of ~6.058 Å, is almost lattice-matched to GaSb (with less than 1% mismatch) (Fig. 2.3) and forms the basis for high-quality Type-III broken-gap heterostructures widely used in mid-infrared and telecom optoelectronics [23], [51], [52], [56], [57].

The strain induced by lattice mismatch is not always purely detrimental. In low-dimensional structures such as quantum wells, dots and rings, pseudomorphic, i.e., below the critical thickness where misfit dislocations form, strain can be exploited to engineer electronic structure, and to tune band edges via deformation potentials and to adjust effective masses, thereby increasing low-field mobility when m^* is reduced. When the epitaxial layer is thin enough to avoid relaxation (typically <5-10 nm), the strain modifies the band edges via deformation potentials, allowing for bandgap tuning without changing material composition [58], [59], [60].

In quantum ring (QR) structures, which inherently rely on a fine balance between lateral confinement and vertical (barrier/well) confinement, the strain distribution and surface curvature can subtly influence carrier localisation, recombination rates and emission wavelength.

From a device perspective, the cumulative strain in multilayer stacks, such as those found in distributed Bragg reflector (DBRs) structures, poses additional challenges. DBRs typically consist of tens of alternating layers with different refractive indices. Each interface must be

optically and structurally coherent to maintain high reflectivity and prevent scattering losses. In the GaAs materials system, DBRs are typically realised as GaAs/AlGaAs or AlGaAs/AlGaAs stacks with a tailored Al fraction, which provides index contrast while keeping the layers close to lattice match, hence their robustness and widespread use [61], [62], [63], [64]. Unlike GaAs/AlAs DBRs, which benefit from nearly perfect lattice matching, GaSb-based DBRs, used in devices operating within the 1.3-3 μm range, require precise engineering of alloy pairs such as AlAsSb/InAsSb. Due to lattice mismatch and the need for optical contrast, these structures often incorporate strain-balancing techniques to maintain crystalline integrity and mirror performance over many epitaxial periods [65], [66].

In the devices developed in this work, material systems such as GaAs, GaSb and AlGaAs were selected based not only on optical performance but also on their lattice compatibility and strain relaxation behaviour. Quantum ring layers and DBR stacks were designed to minimise misfit strain, avoid relaxation during epitaxial growth and ensure optimal performance in the telecom C band (1.3- 1.55 μm).

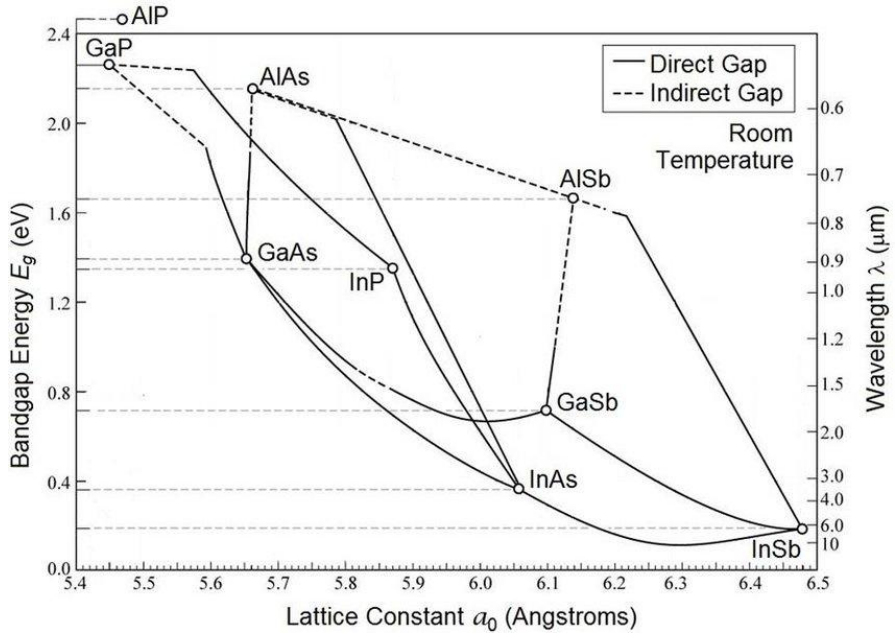

Fig. 2.3: Lattice constant and bandgap energy of various III-V semiconductors at room temperature (adapted from Tien, 1988) [3].

2.3. Quantum Wells, Quantum Wires, Quantum Dots and Quantum Rings

Quantum confinement is a foundational principle in modern optoelectronics and quantum photonics, referring to the restriction of carrier motion (electrons and holes) in one or more spatial dimensions. By engineering confinement geometries at the nanoscale, the electronic density of states and recombination dynamics of charge carriers can be precisely manipulated, enabling tunable emission wavelengths, enhanced quantum efficiency and control over photon emission statistics.

In this section, we explore three key confinement architectures, quantum wells (QWs), quantum dots (QDs) and quantum rings (QRs), highlighting their structural, electronic and optical differences. Special emphasis is placed on GaSb-based nanostructures due to their relevance in telecom-wavelength single-photon sources.

2. 3.1. Quantum Wells: 1D Confinement

Quantum wells are formed by sandwiching a low-bandgap semiconductor between two higher-bandgap barrier materials[67], [68], [69]. They confine carriers, resulting in discrete energy levels due to the potential barriers created by higher-bandgap materials [70]. This results in carrier confinement along the growth (z) axis while allowing free movement in the lateral (x-y) plane, yielding a quasi-two-dimensional (2D) system. The quantisation leads to discrete subband levels in the conduction and valence bands, and a first-order estimate for the confinement contribution to the transition energy can be written as

$$E_{transition} = E_g + \frac{h^2\pi^2}{2}\left(\frac{1}{m_e^* L_e^2} + \frac{1}{m_h^* L_h^2}\right), \quad 2.8$$

where L_e and L_h are the effective confinement widths for electrons and holes, respectively, and m_e^*, m_h^* are their effective masses [71]. Equation (2.8) is intended as a first-order estimate of the confinement-induced energy shift using an idealised single-particle effective-mass picture (parabolic bands and an infinite/rectangular well approximation). In real quantum wells the barriers are finite, so electron and hole wavefunctions penetrate into the barriers and the confinement energies can deviate from the simple $1/L^2$ scaling; strain and valence-band mixing (heavy-/light-hole character) can further modify the subband energies. In addition, because carriers are free to move in the x-y plane, each subband has an in-plane dispersion by

$$E_n(k_\parallel) = E_n(0) + \frac{\hbar^2 k_\parallel^2}{2m^*}, \quad 2.9$$

Finally, the experimentally observed optical transition is often excitonic, such that the emitted photon energy is reduced by the exciton binding energy,

$$E_{opt} \approx E_g + E_{conf,e} + E_{conf,h} - E_B. \quad 2.10$$

For type-II wells, where electrons and holes are spatially separated across the interface, the transition is spatially indirect and quantitative predictions generally require heterostructure-specific modelling that includes offsets, strain and excitonic corrections.

Type-II quantum wells (e.g., GaSb/GaAs, InAs/GaAsSb, InGaAs/GaAsSb) provide strong hole confinement with emission set by the offsets and strain; GaSb/GaAs on GaAs is often engineered near 1.3-1.6 μm, whereas other stacks can reach >2 μm or shorter wavelengths depending on composition and layer thickness.[69], [72], [73], [74], [75], [76]. However, they often suffer from carrier escape, inhomogeneous broadening and multi-exciton generation, limiting their application in deterministic single-photon emission [77], [78].

2. 3.2. Quantum Wires: 2D Confinement

A quantum wire confines carriers in two spatial directions (e.g., *y,z*) and leaves motion free along one axis (the wire axis, *x*). The spectrum is discrete in the confined directions and continuous along *x*, forming a 1D electron/hole gas with a one-dimensional density of states. Optical transitions occur between quantized electron and hole subbands; transition energies are set by lateral dimensions (wire width/height), band offsets and strain. Both type-I (co-localised carriers) and type-II (spatially indirect) alignments are possible depending on the material system [79], [80], [81], [82]. Wire structures are noted here for completeness; they are not investigated experimentally in this work.

2. 3.3. Quantum Dots: 3D Confinement

Quantum dots (QDs) are semiconductor nanostructures that confine electrons or holes within all three spatial dimensions, effectively creating a zero-dimensional (0D) quantum system. This pronounced quantum confinement results in discrete, atom-like energy levels and a delta-function-like density of states [83],[84], [85] . As a consequence, QDs exhibit sharp emission linewidths, high oscillator strengths, and size-tuneable optical transitions, making them highly promising candidates for applications such as single-photon sources and quantum information processing [86]. It is noteworthy that for the GaSb/GaAs system, this transition typically occurs after deposition of approximately 1.5-2.0 monolayers (0.9-1.2 nm) of GaSb [87].

GaSb/GaAs QDs offer particularly interesting opportunities due to their emission wavelengths lying in the telecom bands. These QDs are typically grown using techniques such as conventional molecular beam epitaxy (MBE), migration-enhanced epitaxy (MEE), or droplet epitaxy as well as by metal-organic chemical vapor deposition (MOCVD) [87], [88], [89], [90], [91], [92], [93], [94].

Self-assembled QDs commonly form during epitaxial growth processes, where thin crystalline layers are deposited onto a substrate. In heteroepitaxy, when the deposited and substrate materials have different lattice constants, strain builds up at the interface. To minimise the total system energy, growth can transition from a two-dimensional film to the nucleation of three-dimensional islands via the Stranski-Krastanow (SK) mode [87], [88], [89]. AFM studies reveal that the resulting QDs are relatively flat (~2-12 nm height, ~30-60 nm width) with densities typically around $2\text{-}3\times10^{10}$ cm^{-2} [95], [96].

Despite substantial progress, GaSb/GaAs type-II QDs still face important challenges. Size dispersion, strain inhomogeneity and spectral diffusion broaden emission, complicating integration into high-coherence device [90]. The carrier localisation depends on the interplay of band offsets, strain-induced band shifts (deformation potentials), piezoelectric fields and composition/intermixing. In general, smaller dots experience higher elastic strain for a given lattice misfit, which can modify effective masses and offsets and may push electrons away from the dot region in type-II systems, thereby reducing e-h overlap and radiative rate; larger dots, being more relaxed, need not show this repulsion, although the outcome remains material- and geometry-dependent [4]. Consequently, the relative contribution to

photoluminescence does not map monotonically to “small vs large”: emission is often dominated by those dots whose local strain/composition maximise overlap and minimise non-radiative channels, irrespective of absolute size.

Strong quantum confinement modifies many-body processes. In type-II heterostructures the spatial separation of electrons and holes reduces wave-function overlap, which tends to suppress overlap-controlled Auger channels compared with type-I [97], [98], [99]. Nevertheless, because Auger recombination scales steeply with carrier density, it can still become significant under high injection, especially where carriers pile up in one region. Thus, confinement does not inherently exacerbate Auger; it usually lowers the Auger coefficients, but does not eliminate Auger-limited performance at high n_e/p [99], [100]. This limitation diminishes the performance of electrically driven devices such as single-photon light-emitting diodes (SPLEDs), particularly under non-cryogenic operating conditions.

From a band structure perspective, eight-band k·p simulations reveal that strain lifts the degeneracy between heavy and light holes, favouring heavy-hole dominated optical transitions [4]. Reported conduction band offsets for GaSb/GaAs QDs vary widely from as low as 80 meV [101] to as high as 800 meV [4], reflecting differences in material purity, strain state [4] and growth conditions.

2. 3.4. Quantum Rings: Topology-Enhanced Confinement

QRs represent a topological evolution of QDs, characterised by the presence of a central hole that fundamentally alters the carrier confinement landscape. This distinctive geometry introduces both radial and azimuthal confinement components, leading to unique electronic states not achievable in conventional QDs Whether the electron-hole overlap is reduced depends on the material system and localisation pattern: in type-II stacks and/or when carriers localise on opposite sides of the ring (e.g., electron outside the GaSb region and hole within the GaSb rim), the spatial separation can lower overlap and hence the exchange interaction; however, in GaSb/GaAs rings the heavy hole is strongly confined in GaSb and the electron is only quasi-bound in neighbouring GaAs and structural asymmetry/disorder often dominates, so overlap (and fine-structure splitting) is not uniformly reduced and varies device to device. Likewise, Aharonov-Bohm-type phase effects require high circular symmetry and long phase-coherence around the ring [86], [102]; in practical GaSb QRs, with heavy-hole localisation and appreciable disorder, such oscillations are not expected in this work.

In the GaSb/GaAs material system, QRs exhibit a type-II band alignment, where holes are confined within the GaSb ring body while electrons remain delocalised in the GaAs matrix. This spatial separation reduces wave-function overlap and prolongs radiative lifetimes (often to the μs range under low excitation)[103], [104], [105],

Fabrication of these nanostructures typically involves molecular beam epitaxy (MBE), where self-assembled GaSb QDs initially form via the Stranski-Krastanow (SK) mode, with typical areal densities ranging from 1×10^{10} cm^{-2} to 5×10^{10} cm^{-2}, as inferred from cross-sectional scanning tunnelling microscopy and atomic force microscopy measurements

[103], [106]. Upon deposition of a thin GaAs "cold" capping layer, an exchange between arsenic and antimony occurs, driving outward diffusion of Sb and inducing the transformation from dot to ring morphology [103], [107].

Interestingly, the GaSb/GaAs material system exhibits a stronger tendency for true ring formation compared to InAs/GaAs. This can be attributed to the larger lattice mismatch (~7.8%) and higher strain energy density in GaSb/GaAs, which drives stronger antimony diffusion during capping [103], [106]. This efficient redistribution leads to sharp, well-defined ring structures while the strain relaxation that results from it reduces the introduction of dislocations or extended defects, crucial for scalable device applications. [108].

The type-II GaSb/GaAs alignment provides a hole well depth on the order of 0.6-0.8 eV (VBO), ensuring strong confinement; the precise value is strain-dependent. Electrons, while Coulombically attracted to the ring, remain spatially separated as the strain in the GaSb from the GaAs matrix raises the SBM such that GaSb nanostructures in GaAs are strongly type-II (Fig. 2.4) [4], [105], [109]. As additional holes are introduced into the ring, capacitive charging leads to a linear blue-shift of the emission energy, without significant involvement of higher quantized states, i.e. electrons continue to recombine with the holes in the ground state [36], [110]. Consequently, the photoluminescence spectrum of GaSb QRs and QDs is broad, spanning key telecom bands including the O-band and C-band, as well as transparency windows relevant for mobile sensing applications[105].

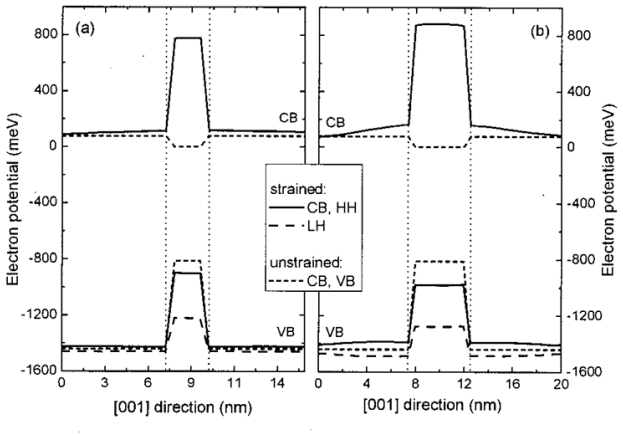

Fig. 2.4: Calculated conduction-band minimum (CBM) and valence-band maximum (VBM) profiles along the growth axis through the center of GaSb/GaAs quantum dots: (a) a “thin” dot (height ≈ 2.2 nm, base width 25 nm) and (b) a “thick” dot (height ≈ 4.4 nm, base width 22 nm). Both structures are truncated pyramids; vertical dashed lines mark the upper and lower dot interfaces. Strain lifts the heavy-hole (HH) / light-hole (LH) degeneracy. *(Reproduced from* [4] *with permission.)*

Overall, GaSb quantum rings efficiently accommodate lattice strain without introducing threading dislocations or lateral defects, preserving material quality essential for scalable integration. This combination of strain management, prolonged carrier lifetime, deep hole confinement and telecom-wavelength emission on GaAs positions GaSb/GaAs QRs as a robust platform for advanced photonic devices, including lasers, quantum memories,

bioimaging agents and particularly, telecom-band single-photon light-emitting diodes (SPLEDs) [46], [111].

2.4. Optical Properties of III-V Semiconductors

The optical behaviour of semiconductors arises from the interaction between charge carriers and the electromagnetic field, primarily governed by radiative and non-radiative recombination mechanisms. In III-V materials, these processes are influenced by the direct nature of the bandgap, strong spin-orbit coupling and the ability to form high-quality quantum heterostructures. Understanding these mechanisms is essential for designing efficient light-emitting devices, particularly in the context of quantum rings and single-photon sources operating in the telecom regime.

2. 4.1. Radiative Recombination

Radiative recombination is the desired process in light-emitting devices, where an electron from the conduction band recombines with a hole in the valence band and a photon is emitted. This process is dominant in direct bandgap III-V semiconductors, such as GaAs, InP and InGaAs, where the conduction band minimum and valence band maximum are aligned in momentum space, enabling efficient optical transitions. The recombination rate is proportional to the product of electron and hole concentrations:

$$R_{rad} = B\,(n_e p - n_i^2), \tag{2.9}$$

where n_i is the intrinsic carrier concentration, B is the radiative recombination coefficient, typically material-dependent. Radiative recombination is highly desirable in light-emitting applications, as it contributes directly to photon generation [112].

In nanostructures such as quantum wells (QWs), quantum dots (QDs) and superlattices, radiative recombination can be enhanced due to quantum confinement effects, which increase the overlap of electron and hole wavefunctions. This results in higher radiative efficiency, making quantum-confined structures ideal for high-performance optoelectronic applications. However, the efficiency of radiative recombination can be significantly reduced by competing non-radiative processes, particularly at high carrier densities and in defect-limited materials.

2. 4.2. Non-Radiative Recombination Mechanisms

Non-radiative recombination refers to any carrier annihilation process that does not result in photon emission and instead disperses energy through alternate mechanisms such as phonon emission or carrier-carrier scattering. These operations have a significant negative impact on the internal quantum efficiency of III-V semiconductor-based light-emitting devices.
There are three main methods of non-radiative recombination in III-V materials:

2. 4.2.1. Shockley-Read-Hall (SRH) Recombination

SRH recombination, also known as trap-assisted recombination, occurs when defects or impurities introduce energy states within the bandgap, providing intermediate states that

facilitate electron-hole recombination without photon emission. These defects can arise from unintentional doping, lattice mismatches in heterostructures or fabrication-induced damage. The SRH recombination rate is given by

$$R_{SRH} = \frac{(n_e p - n_i^2)}{\tau_{p0}(n_e + n_{e1}) + \tau_{n0}(p + p_1)}, \tag{2.10}$$

where $n_{e1} = n_i exp\left(\frac{E_t - E_i}{kT}\right)$ and $p_1 = n_i exp\left(\frac{E_i - E_t}{kT}\right)$ depend on the trap energy (*Et)* (relative to the intrinsic level (E_i)). Also, τ_{p0} and τ_{n0} are the trap-limited lifetimes given by

$$\tau_{p0} = \frac{1}{\sigma_p \upsilon_{th} N_t}, \qquad \tau_{n0} = \frac{1}{\sigma_n \upsilon_{th} N_t}, \tag{2.11}$$

with N_t the trap density $\sigma_{p,n}$ capture cross-sections, and υ_{th} the thermal velocity. SRH is maximised for mid-gap traps and when n and p are comparable [31], [113].

In nanostructured geometries with high surface-to-volume ratio (e.g., quantum rings, nanowires, etched photonic structures), trap-assisted recombination is often dominated by surface/interface states, the boundary form of SRH. This loss is commonly parameterised by the surface recombination velocity (*S*); surface passivation (e.g., dielectric/ALD) reduces S, while heterostructure design that minimises defect formation remains the primary lever for lowering SRH-related losses [114].

2. 4.2.2. Auger Recombination

Auger recombination is a non-radiative three-carrier process wherein the recombination energy and momentum of an electron-hole pair is transferred to a third carrier, either another electron or hole, which is thus excited to a higher energy state (Fig. 2.5) [32], [115], [116]. The excited carrier subsequently relaxes via phonon emission, converting the recombination energy into heat rather than light. The Auger recombination rate follows the relation formula:

$$R_{Auger} = C_n {n_e}^2 p + C_p n_e p^2, \tag{2.12}$$

where C_n and C_p are the Auger coefficients for electrons and holes, respectively [99].

Owing to its great dependency on carrier density, Auger recombination represents a significant loss mechanism at high current densities, contributing to the so-called efficiency droop in III-V LEDs [117].

Auger recombination is highly sensitive to the material's bandgap and temperature. Higher bandgap materials exhibit lower Auger rates at room temperature due to stricter conservation requirements for energy and momentum. However, at elevated temperatures, thermally populated higher energy states facilitate Auger transitions, leading to an exponential increase in the Auger rate with temperature[32]

Importantly, in type-II heterostructures, such as GaSb-based quantum wells and superlattices, Auger recombination can be suppressed by engineering band alignment to

reduce carrier overlap and weaken Auger transition probabilities [97], [118], [119]. Theoretical work suggests that in type-II structures, destructive interference of carrier tunnelling pathways can further suppress Auger processes, leading to power-law rather than exponential temperature dependence of the recombination rate [97] . This intrinsic suppression of Auger recombination is one of the key advantages exploited in devices based on type-II band alignment, such as interband cascade lasers (ICLs), where lower non-radiative losses contribute to higher efficiency and lower threshold currents compared to type-I quantum well devices [120], [121].

Overall, engineering dimensionality, band structure and spatial carrier separation offer a powerful toolkit for mitigating Auger recombination, pushing the performance limits of optoelectronic devices operating in high-density and mid-infrared regimes.

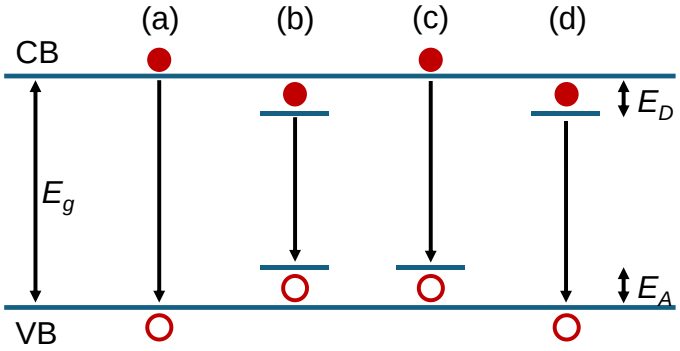

Fig. 2.5: Schematic band diagram showing possible radiative recombination pathways: (a) band-to-band transition, (b) donor-to-acceptor transition, (c) conduction band to acceptor transition and (d) donor to valence band transition. E_A and E_D represent the shallow acceptor and donor energy levels relative to the band edges.

2. 4.3. Impact of Recombination Mechanisms on Optoelectronic Devices

The interplay between radiative and non-radiative recombination mechanisms directly affects the efficiency, operational stability and thermal management of optoelectronic devices. In LEDs, minimising non-radiative recombination is essential for achieving high internal quantum efficiency (IQE) and mitigating efficiency drop at high current densities [122]. In laser diodes, non-radiative processes such as Auger recombination and Shockley-Read-Hall (SRH) recombination at defect sites contribute to increased threshold currents and reduced operational lifetimes [123], [124]. Moreover, temperature plays a significant role, with higher operating temperatures accelerating both Auger and SRH processes, further degrading device performance.

In mid-infrared photonic devices, such as GaSb-based type-II heterostructures, suppressing Auger recombination has been a major focus in optimising laser efficiency. The development of interband cascade lasers (ICLs) has demonstrated significant improvements over conventional quantum cascade lasers (QCLs) by leveraging type-II band alignment to achieve lower threshold currents and reduced non-radiative losses [120], [121]. Similarly, in

photodetectors, minimising surface recombination through proper passivation strategies is critical for improving signal-to-noise ratios and extending detection wavelengths [51], [125].

As semiconductor device design advances, the ability to engineer recombination processes through band structure modifications, heterostructure engineering and material passivation will continue to play a pivotal role in pushing the limits of optoelectronic efficiency and performance. The suppression of non-radiative losses remains a key challenge in achieving next-generation high-efficiency infrared emitters, high-power laser diodes and ultra-sensitive photodetectors.

2.5. Light-Emitting Diodes (LEDs): Theory and Operation

Light-emitting diodes (LEDs) are semiconductor devices that convert electrical energy into optical radiation through radiative recombination of injected carriers. Their operation hinges on key physical processes: carrier injection, transport, confinement and recombination, as well as structural considerations that enhance light extraction and emission efficiency. In III-V material systems, especially those incorporating quantum heterostructures like GaSb/GaAs quantum rings, LEDs can be optimised for telecom-wavelength emission, room-temperature operation and even single-photon purity [126], [127]. This section outlines the core physical principles behind LED operation and elaborates on architectural strategies to maximise their performance.

2. 5.1. Basic LED Physics

The operational core of an LED lies in the p-n or p-i-n junction. In a p-i-n LED, an intrinsic active region is placed between the p-type and n-type layers, creating a wide depletion region across which a built-in electric field is established at thermal equilibrium. Under these conditions, a single Fermi level is constant throughout the structure, while the band slope reflects the internal electric field that opposes further carrier diffusion. When a forward bias is applied, the junction barrier is reduced and the electron and hole quasi-Fermi levels split, promoting carrier injection into the active region. Electrons are injected from the n-type side into conduction-band states, while holes are injected from the p-type side into valence-band states, enabling radiative recombination. In the GaSb/GaAs type-II QR-LED considered here, holes become localised in the GaSb quantum-ring valence-band well, whereas electrons occupy nearby conduction-band states on the GaAs side, so that recombination occurs across the heterointerface.[31], [128]. This generic operating principle is illustrated schematically in Fig. 2.6.

In quantum-confined structures, such as GaSb quantum rings, confinement and interface engineering allow fine-tuning of the recombination energy and enable emission at specific wavelengths, notably within the telecom range (~1.3-1.55 μm) [46]. In type-II GaSb/GaAs configurations, electrons and holes are spatially separated, which modifies the recombination pathway and extends the carrier lifetime. A schematic of carrier injection and radiative recombination in the type-II GaSb/GaAs QR p-i-n LED is shown in Fig. 2.6(b) [46], [129], [130].

The injection efficiency, carrier recombination rate and photon extraction efficiency determine the overall performance. In Type-II configurations, such as GaSb/GaAs, spatial separation of carriers extends lifetimes and enables recombination at telecom-relevant wavelengths. Carrier confinement in a quantum ring structure ensures that recombination occurs preferentially at designed locations, improving spatial coherence and emission directivity [46], [129], [130].

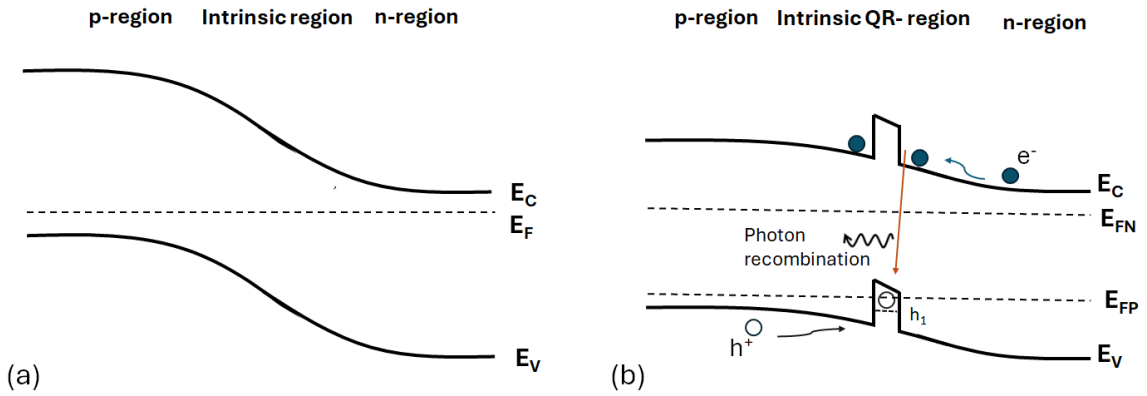

Fig. 2.6: Energy band diagrams of p-i-n QR-LED. (a) Equilibrium (V = 0 V) Single Fermi level E_F spans the wide intrinsic depletion region. Built-in field (band slope) separates carriers across p-i-n junction. (b) Under forward bias (V > 0): Quasi-Fermi levels split: E_{FP} (p-region) and E_{FN} (n-region) with $\Delta E_F \approx qV$ enabling radiative recombination. Electrons are injected from the n-region conduction band (blue arrow), while holes are injected from the p-region into the GaSb QR valence-band well (black arrow). The confined hole ground state h_1 in the QR valence-band well is indicated schematically. Type-II radiative recombination occurs across the GaAs/GaSb heterointerface (orange arrow), accompanied by photon emission (wavy arrow).

The overall efficiency of an LED is determined by the carrier injection efficiency, radiative recombination probability and photon extraction efficiency. Non-radiative mechanisms, notably Auger recombination and surface/interface recombination, impose limitations that must be carefully managed.

2. 5.2. Photon Extraction Efficiency in LEDs

Photon extraction represents a major bottleneck for LED efficiency. Due to the high refractive index (n_r) contrast between III-V semiconductors (e.g. n_r is near 3.86 at 1310 nm for GaSb) and air (n_r is near 1) a significant fraction of emitted photons undergoes total internal reflection and becomes trapped [131]. Several strategies are employed to overcome this:

- Surface Texturing: Random or periodic surface roughening increases scattering and outcoupling.
- Photonic Crystals: Modify the local photonic density of states to direct emission into desired modes. [132]

- Microcavities and distributed Bragg reflectors (DBRs): These structures form vertical resonant cavities, enhancing directional emission through constructive interference and narrowband spectral filtering.

SPLEDS within a DBR cavity can significantly enhance vertical light emission and improve EQE at telecom wavelengths.[129], [130], [133].

2. 5.3. Carrier Injection Dynamics and Biasing Effects

The forward bias applied across the p-n junction defines the carrier injection regime. At low injection levels, the LED operates in a spontaneous emission mode suitable for single-photon operation with minimised multi-exciton generation. At higher injection currents, non-radiative losses (Auger, thermal) increase, degrading efficiency and emission purity [126]

In Type-II QR-SPLEDs, biasing also influences the electric field across the interface, affecting the wavefunction overlap and quasi-Fermi level separate ion, both critical for emission energy and recombination probability [134].

Accurate modelling of the potential landscape and carrier transport under bias is essential, often using drift-diffusion or Poisson-Schrödinger self-consistent solvers [32].

The spontaneously emitted photon interacts with the surrounding optical environment. In free space, emission is isotropic and partially lost to total internal reflection. In confined structures like vertical-cavity QR-SPLEDs, the emission couples into optical modes supported by the cavity, defined by:

$$\lambda_m = \frac{2n_r L}{m}, \tag{2.13}$$

where L is the cavity length and m is the mode order [26]. Furthermore, in cavity-integrated QR devices, emission is filtered by the resonator's discrete longitudinal modes. The quality factor quantifies spectral selectivity,

$$Q \equiv \frac{\omega_o}{\Delta\omega} = \frac{f_0}{\Delta f} = \frac{\lambda_0}{\Delta\lambda}, \tag{2.14}$$

where f_0 is the resonance(centre) frequency of the mode and Δf ($or\ \Delta\omega, \Delta\lambda$) is the FWHM linewidth. Thus higher Q gives a narrower linewidth and a longer photon storage time $\tau_{ph} = Q/\omega_o$ [135], [136].

Incorporating DBRs enhances spontaneous emission via the Purcell effect, offering radiative rate control essential for integrated quantum photonic circuits [135].

2. 5.4. Advantages of GaSb Quantum Structures for Telecom Applications

GaSb offers a rare combination of material properties that position it as a strategic choice for telecom-wavelength quantum emitters:

- Telecom-band access on the GaAs platform: GaSb offers deep hole confinement and type-II alignment with GaAs, enabling emission engineered around 1.3-1.6 μm on GaAs substrates, compatible with GaAs/(Al)GaAs photonic stacks (e.g., DBR cavities) [46], [111], [137].
- Longer radiative lifetimes (type-II): Spatial separation of electrons (in GaAs) and holes (in GaSb) reduces wave-function overlap, yielding long exciton lifetimes that are useful for single-photon timing control [36], [48], [138].
- Spin-orbit and valence-band engineering**.** Strong spin-orbit coupling in GaSb can reduce valence-band mixing and help stabilise polarisation selection rules in certain geometries; the net effect is device-dependent [91], [139].
- Cavity compatibility and spectral control: On GaAs, GaAs/(Al)GaAs DBRs can be designed at telecom wavelengths to form Fabry-Pérot/ Vertical-Cavity Surface-Emitting Laser (VCSEL)-type cavities that (i) select the desired optical mode and suppress out-of-band background, (ii) narrow the linewidth with higher Q and (iii) improve extraction via directionality.
- Room-temperature operation: GaSb/GaAs type-II emitters can show room temperature electroluminescence/photoluminescence; however, single-photon purity and coherence still depend on device design, background suppression (e.g., DBR filtering), and drive conditions. Hence it is removing cryogenic cooling instead of InAs QDs.

In our (i.e. GaAs/ GaSb) devices, holes are confined in GaSb while electrons are supplied from neighbouring GaAs, forming a type-II active region. Such devices demonstrate:

- Enhanced photon purity due to reduced multi-exciton recombination.
- Longer coherence times, crucial for quantum key distribution (QKD) and on-chip quantum optics.
- Electrical control of injection conditions (current and bias), making them compatible with active photonic integrated circuits (PICs).

Ultimately, GaSb-based Type-II QR structures serve as electrically driven, telecom-compatible, room-temperature emitters, which are rare and highly valuable in practical quantum communication systems.

2.6. Distributed Bragg Reflectors (DBRs)

Distributed Bragg reflectors (DBRs, or Bragg mirrors) are one-dimensional photonic crystals formed by a periodic stack of high- and low-refractive-index films. They act as dielectric mirrors by exploiting thin-film interference: for the textbook design, each layer has quarter-wave optical thickness is given by

$$t_k = \frac{\lambda_0}{4n_k}, \tag{2.15}$$

where n_k is the refractive index of the k-th layer and λ_0 is the design wavelength. This ensures that the phase accumulated on propagation plus the π phase flips at higher-index reflections make the interface reflections add in phase at the design wavelength λ_0 [26], [140].

The result is a high-reflectivity stopband centred on λ_0, flanked by sidebands. Increasing the index contrast $\Delta n=|n_{r2}-n_{r1}|$ both raises the peak reflectivity and broadens the stopband, reducing the number of periods needed for a given R.

While quarter-wave stacks are often analysed at normal incidence, real devices radiate over an angular spread. DBR stopbands persist for moderate angles (with s/p splitting) but narrow and shift spectrally; cavity designs (e.g., VCSELs, RCLEDs) therefore use top and bottom DBRs to confine the vertical mode and to shape the far-field so that spontaneous emission couples efficiently to the desired, near-normal direction [26], [32], [140]. Multilayer geometry and build-up of coherent back-reflections are shown in fig 2.7.

The straight-line optical path length Λ in a homogeneous medium is given by

$$\Lambda = n_r d, \tag{2.16}$$

where n_r is the refractive index in the medium and d is the geometric length of the path in a homogeneous medium[140].

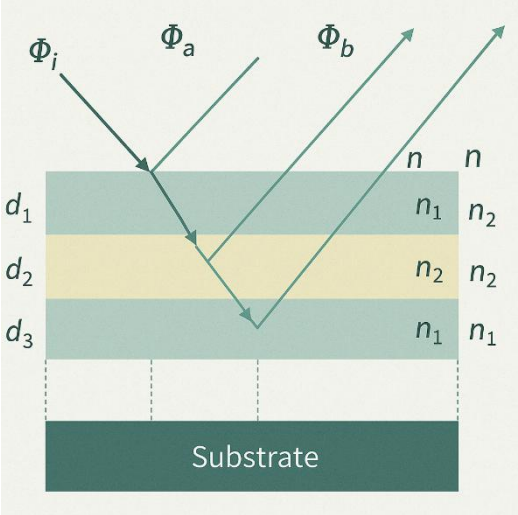

Fig. 2.7: Schematic of a distributed Bragg reflector (DBR): a multilayer stack of alternating high- and low-refractive-index films (n_{r1}, n_{r2}) with thicknesses d_1, d_2, d_3,…on a substrate. An incident wave Φ_i undergoes partial reflections at each interface; the optical phase accumulated in each layer causes the reflected waves Φ_a, Φ_b,… to add constructively at the design wavelength. The arrows indicate representative internal reflections and the build-up of the coherent back-reflected field.

When each layer is precisely λ/4 thick, the reflected waves remain in phase and produce a standing wave with nodes at low-to-high index interfaces. This can be illustrated by comparing the optical path differences:

$$\Phi_a = \frac{\lambda}{2}, \tag{2.17}$$

$$\Phi_b = 2(n_1 d_1 + n_2 d_2) + \frac{\lambda}{2}. \tag{2.18}$$

Setting $n_1 d_1 = n_2 d_2 = \lambda/4$, the total optical path becomes:

$$\Phi_b = 2\left(\frac{\lambda}{4} + \frac{\lambda}{4}\right) + \frac{\lambda}{2} = \frac{3\lambda}{2}. \tag{2.19}$$

Hence, the path difference is equal to λ as shown in equation (2.20);

$$\Phi_b - \Phi_a = \frac{3\lambda}{2} - \frac{\lambda}{2} = \lambda. \tag{2.20}$$

A path difference of λ implies that the reflected waves are constructively interfering, resulting in high reflectance at the design wavelength.
The Fresnel reflection and transmission coefficients at each interface are given by:

$$r = \frac{n_{r1} - n_{r2}}{n_{r1} + n_{r2}}, \tag{2.21}$$

$$t = \frac{2n_{r1}}{n_{r1} + n_{r2}}, \tag{2.22}$$

where n_{r1} and n_{r2} are the refractive indices of the incoming and transmitted wave media, respectively.

- If $n_{\mathrm{r2}} > n_{\mathrm{r1}}$ (into a higher-index medium), then r<0: the reflected electric field undergoes a π phase flip (equivalently, a half-wavelength phase shift).
- If $n_{\mathrm{r2}} < n_{\mathrm{r1}}$ (into a lower-index medium), then r>0: the reflected field has no phase flip.

At oblique incidence the same rule applies to the phase (the sign of the Fresnel coefficients), though the magnitudes differ for s- and p-polarizations. Metals have complex indices, so the phase upon reflection is generally not exactly 0 or π. In a DBR, you must add this interface phase to the propagation phase picked up in each layer. For a quarter-wave layer ($d = \lambda_0/4n$), the round-trip propagation phase is π; together with the interface phase flips, this makes reflections from successive interfaces add in phase at λ_0, yielding high reflectivity over the stopband[26], [140].

For multilayer stacks, optical interactions can be rigorously computed using the 2 × 2 transfer matrix formalism. The transmission matrix at a single interface is:

$$T_{interface} = \frac{1}{t}\begin{pmatrix} 1 & r \\ r & 1 \end{pmatrix}. \quad (2.23)$$

Graded or non-abrupt interfaces can be modelled by subdividing the transition regions into multiple thin layers and applying equations (2.21)-(2.23) iteratively across each sub-layer.

Finally, the overall reflectivity, R, of a DBR with N repeating layer pairs at the centre wavelength λ_0 is

$$R = \left(\frac{1 - \frac{n_{rs}}{n_{r0}} \left(\frac{n_{r1}}{n_{r2}} \right)^{2N}}{1 + \frac{n_{rs}}{n_{r0}} \left(\frac{n_{r1}}{n_{r2}} \right)^{2N}} \right)^2, \quad (2.24)$$

where n_{r0} is the refractive index of the originating medium, and n_{rs} the refractive index of the substrate, all at the centre wavelength λ_0 [31], [128], [140]

Material selection must balance optics and epitaxy/device constraints: (i) large Δn_r and low absorption at the target wavelength, (ii) lattice matching/low strain for many periods, (iii) adequate thermal conductivity, and, when the mirror also carries current, (iv) dopability with low series resistance.

There are two primary types of DBRs used in LEDs: dielectric DBRs and semiconductor DBRs. DBRs, which consist of layers of alternating materials with different refractive indices, are used to create highly reflective mirrors that significantly improve an LED's light extraction efficiency [126], [141].

Dielectric DBRs (e.g., TiO_2/SiO_2, Ta_2O_5/SiO_2) are ex-situ stacks of insulating high/low-index films. Their large index contrast gives very high peak reflectivity and broad stopbands with negligible absorption at the design wavelength. They are excellent optical mirrors and can be added after epitaxy (useful in flip-chip layouts). The trade-off is that they are non-conductive and their reflectance is angle dependent (stopband blue-shifts and narrows at oblique incidence), so they are poorly suited as current-carrying mirrors in electrically driven devices [142], [143], [144], [145].

Semiconductor DBRs (e.g., GaAs/AlAs or GaAs/ $Al_xGa_{1-x}As$ near 1.3-1.55 μm; InP/InGaAsP at 1.55 μm) are grown in situ with the active region and can be n/p-doped to conduct current. Index contrast is lower than dielectrics, so more periods are needed for a given R, and heterojunction band offsets introduce transport barriers, series resistance remains a key design constraint even with doping. The upside is monolithic integration, lattice compatibility, and simultaneous optical plus electrical functionality, which is why semiconductor DBRs are the default in VCSELs/RCLEDs/SPLEDs [46], [137], [146], [147], [148].

Electrical resistance in semiconductor DBRs stems from (i) the bulk resistivity of wide-bandgap layers (AlAs/AlGaAs, low intrinsic carrier density) and (ii) heterointerface barriers from GaAs/ $Al_xGa_{(1-x)}As$ band offsets that impede carrier flow. Even when n/p-doped, GaAs/$Al_xGa_{(1-x)}As$ DBRs remain heterobarrier-limited: $\Delta E \gtrsim k_B T$ at 300 K keeps

tunnelling/thermionic-field emission dominates, not drift-diffusion; p-type stacks are thus more resistive than n-type, reflecting heavier, low-mobility holes [137]. However, the effectiveness of doping differs by polarity: p-type DBRs generally show higher resistance due to the heavier effective mass and lower mobility of holes compared to electrons.

In electrically driven SPLEDs the DBR is part of the current path, so excess series resistance causes Joule heating, lowers electrical-to-optical efficiency, broadens linewidths, and can degrade single-photon purity under CW bias. Hence DBR design must jointly optimise doping profiles, material choices and thermal management alongside the optical reflectance [46].

2.7. Single-Photon Sources for Telecom Band

Single-photon sources (SPSs) are the workhorses of photonic quantum information: information is carried by individual photons, and their quantum features enable provably secure communication and interference-based computation. Moving to all-electrical single-photon emission removes bulky, alignment-sensitive pump lasers in favour of compact diodes that deliver one photon per clock cycle on chip, a decisive step for scalable photonic circuits in which sources, switches, filters, and detectors share the same substrate and are driven by integrated electronics [5], [149], [150], [151].

For quantum applications, an SPS must meet three core requirements: single-photon purity**,** indistinguishability and efficiency. Purity is quantified by the second-order autocorrelation at zero delay, $g^{(2)}(0)$, with values approaching zero indicating strong antibunching. Indistinguishability is assessed via two-photon interference (Hong-Ou-Mandel visibility) between sequential emissions. Efficiency (brightness) refers to the detected photons per trigger, and in cavity/waveguide-QED implementations is governed by the spontaneous-emission coupling factor (the β-factor into the desired mode) and the out-coupling efficiency of that mode to the collection optic. Together, these metrics, measured under the intended operating conditions (temperature, drive and photonic environment), set the practical usefulness of a source in telecom-band quantum networks.

2. 7.1. Pure single-photon emission

The essential criterion is one photon at a time. This is quantified with a Hanbury Brown-Twiss (HBT) measurement: pulses from the source are split by a beam splitter and detected on two channels while a variable delay (τ) aligns arrival times at $\tau=0$ (Fig. 2.8). The second-order autocorrelation $g^{(2)}(\tau)$ is then recorded.

If a pulse sometimes contains more than one photon, one photon can be transmitted and another reflected, producing coincidences at zero delay and yielding $g^{(2)}(0) >0$. For an ideal single-photon pulse, the photon exits only one port, so no coincidences occur and $g^{(2)}(0) =0$. Experimentally, the coincidence histogram shows peaks at multiples of the pulse period (from different pulses) and a strongly suppressed central bin at $\tau=0$ when true single-photon emission is achieved (e.g., for a source pulsed every 12 ns).

2. 7.2. Indistinguishability

When two single-photon wave packets meet at a 50:50 beam splitter, there are two indistinguishable quantum pathways for the photons to leave in different output arms: both

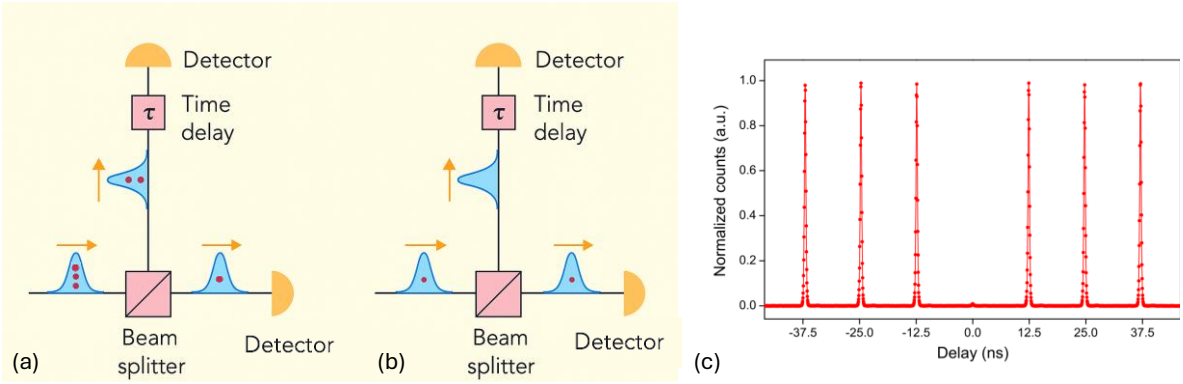

Fig. 2.8: Schematic of the Hanbury Brown-Twiss (HBT) measurement for input pulses containing (a) multiple photons and (b) a single photon. (c) Corresponding $g^{(2)}(\tau)$ autocorrelation trace recorded from a micropillar single-photon source. (Adapted from [5], [6], used with permission.)

reflected or both transmitted. For indistinguishable photons arriving simultaneously, the corresponding probability amplitudes have the same magnitude but opposite phase and cancel, suppressing the "separate-ports" outcome [5], [152].

In most Hong-Ou-Mandel (HOM) measurements the two photons are produced by the same source in consecutive pulses. A mode-locked laser (e.g., 80 MHz) excites the SPS, producing a pulse train of single photons separated by 12.5 ns. An unbalanced interferometer with a "short" and a "long" arm is adjusted so that a photon from one pulse traversing the long arm arrives at the same time as the next photon in the train traversing the short arm. With the delays set this way, the two photons overlap at the beam splitter [5], [149].

If the photons are made distinguishable (e.g., orthogonal polarisations), the destructive interference is lifted and coincidences at zero delay reappear, so $g^{(2)}(0)>0$. With parallel polarisations (and good temporal/spectral overlap), the HOM effect suppresses the central coincidence bin and ideally yields $g^{(2)}(0)=0$. The coincidence histogram shows satellite peaks at delays equal to integer multiples of the pulse period, originating from photons that do not meet at the beam splitter and therefore do not interfere. The indistinguishability is quantified as one minus the normalised area of the central ($\tau=0$) peak; an ideal source gives a value approaching unity [5], [153].

More generally, indistinguishability requires the emitted photons to be identical in all relevant degrees of freedom, spectrum, temporal phase, polarisation, spatial mode and arrival time, so that the two-photon amplitudes at the beam splitter interfere perfectly and force both photons to exit the same output port.

2. 7.3. Efficiency

The third central figure of merit is efficiency (brightness) [5], [154]. An ideal SPS is deterministic: every trigger event yields exactly one photon launched into the collection optics, a "single-photon gun." The generation efficiency was defined as the number of detected photons per trigger [149].

Within cavity/waveguide quantum electrodynamics (QED) frameworks, two parameters govern this efficiency. The first is the spontaneous-emission coupling factor (the β-factor), i.e. the fraction of spontaneous emission funnelled into the desired optical mode,

$$\beta = \frac{\Gamma_{mode}}{\Gamma_{mode}+\Gamma_{rad}}, \tag{2.25}$$

where Γ_{mode} is the emission rate into the targeted mode and Γ_{rad} accounts for leakage into unwanted radiation modes. If necessary, non-radiative channels can be included via

$$\beta = \frac{\Gamma_{mode}}{\Gamma_{mode}+\Gamma_{rad}+\Gamma_{nr}}, \tag{2.25}$$

where Γ_{nr} set by the emitter's intrinsic defects and thus not easily engineered, in contrast to Γ_{mode} and Γ_{rad}, which can be tailored by the photonic environment [5].

The second parameter is the out-coupling efficiency (η_{out}) measuring the fraction of power in the selected optical mode that is transmitted to the first collection optic (e.g., objective lens or fibre). In this simplified picture, the end-to-end single-photon efficiency is

$$\eta = \beta\eta_{out}. \tag{2.28}$$

In multi-photon interference experiments involving j photons, the overall success probability scales as η^j. Consequently, scalable photonic quantum information tasks impose stringent requirements: η must approach unity if large- j protocols are to be practical [5].

2. 7.4. Probabilistic Sources

A widely used route to single photons is spontaneous parametric down-conversion (SPDC). In a nonlinear medium the polarisation expands as

$$P = \varepsilon_0\left(\chi^{(1)}E + \chi^{(1)}E^2 + \chi^{(2)}E^3 + \ldots\right), \tag{2.29}$$

and the $\chi^{(2)}$ term enables a pump photon ($\hbar\omega_p$) to split into two lower-energy photons, the signal and idler, with energy conservation $\hbar\omega_p = \hbar\omega_s + \hbar\omega_i$ (and suitable phase matching)[155]. SPDC sources are simple and idler, but the process is inherently probabilistic: increasing pump power raises the single-pair rate and the multi-pair probability, so practical efficiencies are low and multi-photon contamination limits scaling to many photon experiments[5], [155].

A second one is the attenuated laser. Classical laser pulses are reduced to the "single-photon level" by controlled loss. This approach is also probabilistic (Poissonian photon-number

statistics): one trades low multi-photon probability for very low brightness, and the emitted photons are generally not indistinguishable. Despite these limitations, attenuated lasers remain useful in some commercial QKD systems where strict single-photon purity and indistinguishability are not required [151], [156], [157], [158].

2. 7.5. Quantum dot sources

Deterministic emission is provided by semiconductor quantum emitters, notably quantum dots acting as effective two-level systems. An excitation pulse (optical or electrical) promotes the system from the ground state $|g\rangle$ to an excited state $|e\rangle$; spontaneous relaxation emits a single photon with energy $\hbar\omega_0 = E_e - E_h$ [5], [159]. Because the excited state cannot host more than one excitation, multi-photon emission from a single trigger is intrinsically suppressed. Moreover, by engineering the photonic environment (cavities or waveguides) one can funnel emission into a single optical mode (high β) and out-couple it efficiently, approaching unity end-to-end efficiency under ideal conditions [5], [160].

Semiconductor QDs are leading solid-state candidates: self-assembled islands (e.g., Stranski-Krastanow) confine carriers in discrete, atom-like levels; under weak excitation a single exciton can be prepared and recombine radiatively to emit one photon [80, 107]. While optically pumped QDs can achieve excellent single-photon metrics, electrically driven implementations are especially attractive for integration, combining deterministic carrier injection with cavity-assisted extraction. For quantum networks, operation in the telecom O/C bands is essential to minimise fibre loss [161], [162].

2. 7.5.1. In(Ga)As quantum dots on GaAs

Self-assembled In(Ga)As dots embedded in GaAs photonic cavities (micropillars or photonic-crystal cavities) currently define the benchmark for simultaneous brightness, single-photon purity and indistinguishability under resonant pulsing. The platform benefits from decades of process maturity and from GaAs/(Al)GaAs DBR mirrors that afford large Purcell factors and efficient extraction. The principal limitation is spectral: even with strain and composition engineering the emission on GaAs can be extended only to the O-band (~1.3 μm); pushing further toward the C-band (1.55 μm) generally forfeits the GaAs/AlGaAs DBR stack or incurs performance penalties. High indistinguishability still typically requires cryogenic operation, and wafer-scale deployment is constrained by the persistent need to select a single dot at the correct frequency and position relative to the cavity, an alignment task that remains non-trivial at scale [163], [164], [165].

2. 7.5.2. InAs quantum dots on InP

Migrating to the InP materials system provides native 1.55 μm emission and immediate compatibility with fibre-optic components. The photonics, however, are less forgiving: the GaAs/AlGaAs DBR ecosystem that underpins many state-of-the-art GaAs micropillars does not transfer; one must rely on InP-family mirrors (e.g., InP/InGaAsP) or hybrid dielectrics, with tighter tolerances on loss and uniformity for high-Q cavities. The same single-emitter selection issue persists, now on a less-mature fabrication stack, and indistinguishability at

C-band likewise tends to be demonstrated at cryogenic temperatures. In short, the wavelength is ideal, but the cavity/mirror technology and spectral selection shift the engineering burden [166], [167], [168], [169].

2. 7.6. Colour centres in diamond and SiC

Point defects such as NV and SiV centres offer outstanding photostability and access to spin-photon interfaces; significant progress has been made in cavity coupling and in two-source interference. Their usefulness as telecom-band SPSs is tempered by strong phonon sidebands (especially for NV) that reduce the zero-phonon-line fraction, by the need for cryogenic operation to achieve narrow-line indistinguishability in many cases (e.g., SiV), and by the fact that telecom wavelengths are not native, necessitating frequency conversion or alternative centres. Electrical injection and wafer-level integration also remain challenging [170], [171].

2. 7.7. Defect emitters in hBN

Hexagonal boron nitride hosts bright, room-temperature single-photon emitters and supports deterministic placement and tuning (Stark, strain, or local dielectric engineering). Compact integrated demonstrations, even including QKD trials, have appeared. At present, however, the microscopic identity of many emitters is still being resolved; spectral diffusion and homogeneous broadening are significant at room temperature; and a full, pulsed-drive brightness- purity-indistinguishability benchmark on par with III-V dots is still emerging, which complicates strict like-for-like comparison [172], [173], [174].

2. 7.8. Rare-earth ions (e.g., Er^{3+})

Trivalent rare-earth ions provide intrinsically narrow optical transitions and long coherence times; Er^{3+} emits directly at 1.55 μm, making it attractive for telecom systems and CMOS-adjacent integration. The current limitation is brightness: radiative rates are low and coupling to nanophotonics must be carefully engineered to reach useful flux, while most high-coherence demonstrations are at cryogenic temperature. These sources are promising for memory-like roles; as primary SPSs, efficiency remains the central challenge [175], [176].

2. 7.9. Localised emitters in 2D

Strain- or defect-localised states in monolayer transition-metal dichalcogenides integrate naturally with planar photonics and can be positioned and tuned with high spatial control. Under pulsed excitation they can deliver good brightness and antibunching; however, rapid dephasing and spectral wandering presently limit indistinguishability, and long-term spectral stability is still being engineered. Telecom-band operation and robust electrical injection are active research areas rather than established capabilities [177], [178].

2. 7.10. GaSb/GaAs Quantum Rings

On the GaAs platform, GaSb/GaAs type-II quantum rings provide access to telecom-band emission while remaining compatible with GaAs/(Al)GaAs DBR cavities. The large valence-band offset yields deep hole confinement in GaSb and the spatially indirect alignment with electrons in GaAs extends the radiative lifetime, useful for timing control and background suppression in integrated links. Because emission on GaAs can be cavity-filtered and Purcell-enhanced, DBRs enable mode selection, linewidth narrowing ($Q=\lambda_0/\Delta\lambda$), and improved extraction. As with all type-II systems, the reduced electron-hole overlap that lengthens lifetimes also lowers oscillator strength, so device brightness relies on careful heterostructure quality (to suppress SRH and spectral diffusion) and on strong light-matter coupling in the chosen cavity or waveguide. Potential reductions in fine-structure splitting and stable polarisation can be achieved in well-engineered geometries, but are device- and disorder-dependent and should be verified experimentally in each structure [46], [110], [138], [179]. A comparison of major existing single-photon platforms is summarised in table 2.2.

Among various emitter architectures, type-II emitter systems, exhibit confinement geometries and band alignments that support deterministic single-photon emission in the telecom band, laying the physical foundation for electrically driven single-photon devices, such as SPLED, which will be discussed in the subsequent chapters.

Table 2.2 Comparison of existing single-photon source technologies

Platform	Emission Wavelength	Temperature	$g^{(2)}(0)$ Value	Integration Feasibility
In(Ga)As QDs (type-I) [223], [261]	900-980 nm (up to 1.3 μm with strain)	Cryogenic (4 K)	< 0.15	GaAs/(Al)GaAs DBR compatible; O-band reachable, C-band difficult on GaAs
InAs QDs on InP (type-I) [163], [374]	1.55 μm (C-band)	Cryogenic	< 0.05	InP/InGaAsP or dielectric mirrors; not GaAs-DBR
NV Centres in Diamond [375]	637 nm	Room Temp	< 0.1	Not telecom; needs frequency conversion; electrical injection hard
Defects in hBN [174], [376]	550-800 nm	Room Temp	~0.1-0.3	Easy integration; not telecom; electrical drive under development
Rare-earth ions [377]	1.55 μm	Cryogenic	< 0.5	CMOS-adjacent; needs strong cavity to raise brightness
Ion Traps [378]	Tunable	Cryogenic	~0.01	Complex, laboratory-scale
Weak Coherent Pulses (attenuated laser) [379]	Variable	Room Temp	> 0.5	Simple but non-deterministic
GaSb QR SPLEDs [46]	1310-1550 nm	Room Temp	-	High

2.8. Why Single-Photon Sources Matter for Quantum Key Distribution

Quantum key distribution (QKD) relies on transmitting quantum states whose measurement disturbances reveal eavesdropping. In practice, performance and security both hinge on the quality of the light source. Single-photon sources (SPSs) are preferred because they aim to deliver one photon per clock rather than a Poissonian pulse with a multi-photon tail. Lower multi-photon probability, quantified by a small second-order correlation $g^{(2)}(0)$ reduces an

eavesdropper's information and relaxes the overheads of decoy-state analysis used with weak coherent pulses. At the same time, brightness (detected photons per trigger) sets the raw key rate after channel loss, while temporal/spectral stability keeps the quantum bit-error rate low [151], [180], [181], [182].

The importance of additional source properties depends on the network architecture. In prepare-and-measure links (e.g. BB84 variants), source purity $g^{(2)}(0)$ and extraction to fibre dominate. In interference-based schemes (e.g. MDI-QKD or entanglement-assisted links), the indistinguishability of independently generated photons, often assessed via Hong-Ou-Mandel visibility, directly limits two-photon interference contrast and therefore the secure key rate. Across all cases, operation in the telecom O/C bands is crucial to minimise fibre attenuation and to interoperate with mature detectors and components [182], [183], [184], [185], [186]. We refer the reader to section 3.4 for a detailed review of the QKD literature and system-level considerations.

2.9. Conclusions and Outlook

This chapter established the physical and device framework used throughout the thesis: band structures and carrier statistics in III-V semiconductors, radiative and non-radiative recombination pathways and the operating principles relevant to light emission and extraction. Within this framework, type-II GaSb/GaAs quantum-ring structures were outlined as the target active medium for telecom wavelengths, highlighting their spatially separated electron-hole states, longer lifetimes, and the design need to control wavefunction overlap to sustain radiative efficiency. The Stranski-Krastanow dot-to-ring transition and associated strain/topology considerations were summarized with emphasis on preserving spectral reach while avoiding defect formation.

The role of photonic engineering, particularly GaAs/AlGaAs DBRs, was discussed in terms of both optical benefits (directionality, spectral selectivity) and electrical trade-offs (series resistance and current spreading), since these directly impact output power, thermal load and stability in SPLED architectures.

Finally, the link to quantum communication was made explicit: operation in the O/C bands, efficient fiber coupling, and source metrics aligned to protocol needs are prerequisites for practical QKD. These considerations clarify why GaSb/GaAs type-II QR-SPLEDs are strong candidates for telecom-compatible, electrically driven single-photon emitters.

In short, Chapter 2 integrated the essential physics from material to device and the key design variables for telecom-oriented QR-SPLEDs, establishing the theoretical basis for the subsequent chapters on device architecture, photonic cavity/DBR design and measurement methodology.

Chapter 3 Literature Review

This chapter presents a comprehensive literature review of the state of the art in single-photon source (SPS) technologies, with particular emphasis on devices operating in the low-loss telecommunication bands (1260-1675 nm) [130], [178], [187], [188], [189], [190], [191]. The objective is to situate GaAs/GaSb type-II QR emitters within the broader landscape of single-photon generation for quantum communication. The scope of the review encompasses the principal SPS families; semiconductor quantum structures, solid-state defect-based emitters and photon-pair sources, as well as the performance metrics and integration challenges relevant to their deployment in practical quantum networks. Special attention is devoted to electrically driven SPSs at telecom wavelengths, since electrical injection remains the key requirement for scalable, on-demand operation in quantum key distribution (QKD) and quantum networking.

By synthesising advances reported over the past two decades (2005-2025), the chapter positions the GaSb QR-SPLED approach relative to existing technologies, particularly the more established InAs quantum-dot platform. While InAs QDs remain highly successful for narrow-linewidth emission, photon indistinguishability and biexciton-based entangled-photon generation, GaAs/GaSb type-II QR emitters offer several advantages that are especially relevant to the goals of this thesis. Most importantly, they provide naturally long-wavelength emission in a GaAs-based material system, together with strong hole confinement and a device architecture that is well suited to monolithic processing. In addition, their compatibility with wafer-scale epitaxy and electrically injected device fabrication makes them particularly attractive for scalable telecom-band SPS arrays. The QR platform is therefore not presented here as universally superior to InAs QDs, but as a potentially more advanced and practical route for the specific challenge of robust, electrically driven single-photon emission at telecom wavelengths.

A balanced assessment must nevertheless recognise the trade-offs associated with type-II GaAs/GaSb QR emitters. The spatially indirect nature of the transition leads to slower radiative recombination than in type-I systems, although nanosecond-scale lifetimes are not, by themselves, prohibitive for single-photon operation. More significant limitations arise from the typically broader emission linewidths, which restrict photon indistinguishability, and from the difficulty of combining this material system with very high-Q optical confinement. Furthermore, QR emitters offer less direct scope for entangled-photon-pair generation than platforms based on biexciton-exciton cascades in InAs QDs or nonlinear processes. These considerations are important for defining the most suitable application niche of the QR-SPLED approach: robust, electrically injected, telecom-band single-photon emission with realistic prospects for scalability and integration.

A major gap in the current literature remains the combined demonstration, within a single electrically injected telecom-band SPS platform, of (i) operation at or near room temperature, (ii) wafer-scale scalability, and (iii) compatibility with fibre-based quantum networks. The thesis advances a GaSb/GaAs QR device architecture specifically to address this gap.

The role of this chapter is therefore to provide the conceptual and technological foundation for the experimental work that follows on GaSb QR-SPLED design, fabrication and characterisation. It concludes by distilling evaluation criteria from the literature review and outlining how the subsequent chapters apply these benchmarks to develop and assess the proposed devices.

3.1. Metrics & Definitions

Throughout this review, several key metrics are used to evaluate and compare single-photon sources (SPSs). Single-photon purity is quantified by the second-order autocorrelation at zero delay, $g^{(2)}(0)$ [192], [193], [194]. An ideal emitter yields $g^{(2)}(0)=0$, indicating perfect antibunching; experimentally, values below 0.5 confirm sub-Poissonian emission, while state-of-the-art solid-state SPSs routinely achieve $g^{(2)}(0) \ll 0.1$ [190], [195], [196].

Indistinguishability, the mutual coherence of successively emitted photons, is typically assessed through two-photon interference in a Hong-Ou-Mandel experiment [192], [197]. High photon indistinguishability, often quantified via Hong-Ou-Mandel two-photon interference visibilities exceeding 90%, is essential for interference-based quantum networking and has been demonstrated with QD sources in the near-infrared (around 800-900 nm), though achieving comparable performance at telecom wavelengths remains challenging due to dephasing processes [198], [199].

Other descriptors include spectral quality (linewidth and spectral diffusion) and timing jitter, which captures uncertainty in emission time [192], [194]. Under electrical excitation, brightness is commonly quantified either through external quantum efficiency (EQE), the probability that an injected carrier pair produces a collected photon, or, more pragmatically in SPS and LED-style devices, as detected photon counts per unit drive current within a defined numerical aperture (NA). Extraction efficiency refers to the fraction of generated photons coupled into a usable optical channel (e.g., fibre or detector) [192], [193], [194]. This parameter can be enhanced with optical microcavities or dielectric antennas [199], [200], [201], [202]. Reported values vary widely, for example, around 25% collection into single-mode fibre has been achieved for a telecom-band InAs/InP QD embedded in a nanowire waveguide at 80 MHz excitation [195], compared to $\ll 1\%$ in bulk samples lacking photonic structures.

In this chapter, the telecom bands are defined as the O-band (1260-1360 nm), valued for its low chromatic dispersion; the C-band (1530-1565 nm), corresponding to the minimum fibre loss; and the extended L-band (1565-1625 nm) [203]. On-demand refers to deterministic emission of a single photon at a user-defined time, triggered electrically or optically, in contrast to heralded photons generated probabilistically in in nonlinear optical processes such as spontaneous parametric down-conversion (SPDC) or four-wave mixing (FWM). A SPLED is a p-n or p-i-n junction device whose active region contains a quantum-emitting region (which may be a single emitter or an ensemble) and is operated such that it emits at most one photon per excitation event under forward bias [46], [191]. Two key performance metrics for SPLEDs are the single-photon purity and the photon-extraction efficiency under

electrical triggering at telecom wavelengths, conditions necessary for practical QKD [46], [204].

Finally, it is important to distinguish type-I and type-II band alignments (Fig. 3.1) [21], [47]. The fundamental band alignment types (detailed in Section 2.2.1). .Type-I structures confine both electrons and holes in the same material region, maximizing wavefunction overlap [53], [159], [205]. Type-II systems, by contrast, separate carriers across the interface, resulting in longer radiative lifetimes and enhanced sensitivity to local fields and charge environment [76], [118], [205], [206]. Consequently, ensemble PL from type-II GaSb QDs/QRs often appears broad and excitation-dependent, whereas single-emitter μ-PL can still show sharp spectral lines when charge configurations are well controlled [179], [105], [207], [35], [36], [208]. Similar single-emitter behaviour has been observed in strain-free GaSb/AlGaSb quantum dots, which operate in a type-I regime but still illustrate how strongly localised states can yield narrow lines and clear single-photon signatures in the telecom S-band [209]. This distinction between ensemble and single-emitter response becomes particularly relevant when evaluating purity, linewidth and radiance in electrically injected GaSb/GaAs QR-SPLEDs.

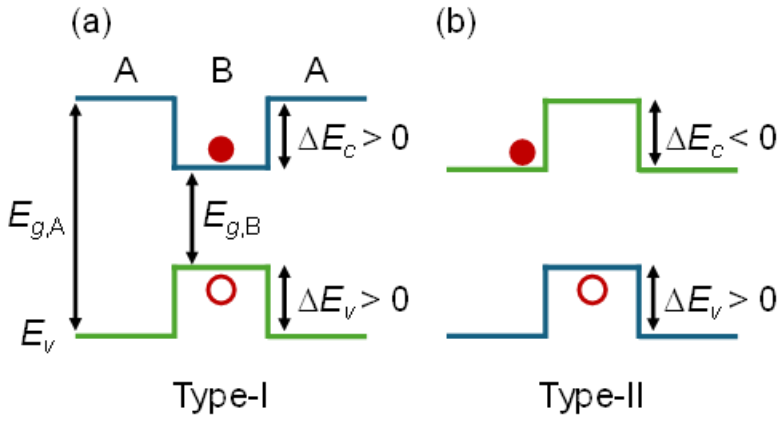

Fig. 3.1: Schematic band alignments at semiconductor heterointerfaces. (a) Type-I: electrons and holes confined in the same region. (b) Type-II: electrons and holes separated across the interface; emission set by ΔE_c, ΔE_v and confinement [7].

3.2. Classification of Single Photon Sources

Single-photon sources (SPSs) can broadly be divided into two categories: deterministic emitters, which ideally release one photon per excitation cycle and probabilistic sources, which rely on statistical processes and post-selection [149], [153], [192], [210]. Deterministic devices are typically based on solid-state quantum emitters such as semiconductor nanostructures or point defects in wide-bandgap crystals, whereas probabilistic approaches exploit nonlinear optical processes or attenuated lasers. A further distinction concerns how these sources are operated, optically or electrically driven and whether their photons fall natively within the telecom transmission bands or must be shifted there by frequency conversion.

3. 2.1. Semiconductor Sources

III-V semiconductor nanostructures represent the most mature deterministic platforms, combining atomic-like optical properties with wafer-scale reproducibility. III-V QDs, grown via Stranski-Krastanow, droplet epitaxy or site-controlled methods, confine carriers in all three dimensions and yield sharp, discrete transitions [110], [211], [212]. A wide range of epitaxial quantum-dot platforms has been explored, including III-V arsenide [213], [214], phosphide [215], [216] and nitride [217], [218]systems as well as II-VI telluride [219], [220] and selenide systems [221], covering emission from the ultraviolet through the telecom bands. While many epitaxial QDs require cryogenic operation, wide band-gap semiconductors can support high-temperature, even room-temperature, performance [150]. At near-infrared wavelengths (around 800-900 nm), InAs QDs routinely achieve near-ideal purity and indistinguishability [222], [223]. Extending this performance into the telecom bands has been achieved through materials engineering, either by growing InAs QDs directly on InP substrates [199], [224], [225], [226] or by employing metamorphic InGaAs buffers on GaAs [227], [228]. Along these routes, triggered single-photon emission at 1.3 and 1.55 µm with $g^{(2)}(0) \ll 0.5$ has been reported [21]. By the late 2010s, electrically pumped InAs/InP QD LEDs achieved $g^{(2)}(0) = 0.10 \pm 0.02$ [200], while biexciton-exciton cascades delivered entangled photon pairs with fidelities of near 87% up to 93 K[204]. InAs-based QDs thus define the state of the art for deterministic telecom-band SPSs, albeit typically at cryogenic temperatures [189], [166], [229], [230], [196]. Also, InAs-based QD sources have been deployed in intercity QKD experiments with fibre lengths up to 79 km, demonstrating strong performance [231].

III-Sb heterostructures offer a complementary pathway, since many GaSb-based structures can be engineered to exhibit type-II band alignment on GaAs-compatible platforms, although III-Sb systems can also realise type-I confinement depending on the barrier composition [209]. In GaSb/GaAs quantum wells (QWs), QDs and quantum rings (QRs), electrons and holes are spatially separated, allowing longer-wavelength emission on GaAs-compatible platforms. Sb-As exchange during capping often transforms GaSb dots into rings, confirmed by cross-sectional scanning tunnelling microscopy (STM) and scanning tunnelling spectroscopy (STS) [232], [233]. GaSb/GaAs QRs in photonic-crystal nanobeam cavities have even shown lasing under optical pumping [234].

3. 2.2. Crystal Defect and Dopant Sources

Defects and dopants in wide-bandgap crystals also act as “atomic-like” solid-state emitters. The nitrogen-vacancy (NV) centre in diamond is the archetype, offering room-temperature single-photon emission at 637 nm [235], [236]. While NV centres provide long-lived electronic spins, coherence is limited by spectral diffusion and cryogenic cooling is often required for interference protocols [235], [237]. Other diamond colour centres, such as SiV (738 nm) and GeV (602 nm), benefit from inversion symmetry, producing narrower optical lines at low temperature [238], [239], [240], [241]. Still, none of these centres natively emit in the telecom range.

In silicon carbide (SiC), divacancy and related defects emit around 1070-1130 nm, approaching the O-band but still outside the lowest-loss telecom windows, motivating either frequency conversion or alternative interfacing [171]. A significant advance came with the discovery of T- centres in isotopically purified silicon, which emit at 1326 nm directly in the O-band. Single T- centres have been optically isolated and even electrically driven in silicon diodes [242], making them promising spin-photon interfaces.

Rare-earth ions provide another route, notably Er^{3+} with an optical transition at 1530 nm in the C-band [175], [243]. Though single-ion emission is weak and requires high-Q cavities, experiments have demonstrated detection of individual photons and spin-photon interfaces with Er^{3+} qubits [176], [244]. Other rare-earths such as Pr^{3+} and Eu^{3+} emit outside the telecom bands and are better suited as quantum memories.

In summary, defect- and dopant-based SPSs offer exceptional spin coherence and spectral stability, but efficient telecom operation remains limited to a few cases such as T- centres and Er^{3+}.

While colour centres offer exceptional spectral stability and long spin coherence, challenges include faint emission, inhomogeneous broadening and the necessity for cryogenic temperatures. Nevertheless, their integration with CMOS-compatible hosts (like silicon and SiC) and potential for quantum memory make them valuable for future hybrid quantum networks.

3. 2.3. 2D Heterostructures

Atomically thin semiconductors host quantum emitters arising from defect states, strain-localized excitons and interlayer (Moiré) excitons [191]. hBN provides bright room-temperature single-photon emission (visible range) with large inhomogeneity [173], [174], [245], [246]; transition-metal (TMD)monolayers (e.g., WSe_2) and Moiré bilayers yield narrow lines at cryogenic temperatures with improving site control and on-chip integration [247], [248], [249]. Electrical driving and cavity coupling have been demonstrated in prototypes, but telecom-band operation and high indistinguishability remain outstanding challenges and issues with spectral diffusion/blinking are non-trivial [177], [250]. Consequently, 2D emitters are promising for integrated photonics but are not yet competitive for telecom-band, electrically driven QKD links.

3. 2.4. Probabilistic Sources

Probabilistic sources generate photons through statistical processes. The simplest example is an attenuated laser: a coherent telecom pulse is reduced to a mean photon number $\mu \ll 1$. In this regime, both single-photon and multi-photon emission probabilities are small, so most pulses are vacuum, and the source is intrinsically slow and inefficient. However, the multi-photon probability scales as $O(\mu^2)$), whereas the single-photon probability scales as $O(\mu)$, so choosing $\mu \approx 0.1$ suppresses multi-photon events well below the single-photon rate. Widely used in QKD testbeds, such weak coherent sources are simple to implement but require decoy-state protocols to monitor and mitigate the residual multi-photon component.

Widely used in QKD testbeds, these sources are simple but require decoy-state protocols to counter multi-photon events [183], [156], [157].

Nonlinear optical processes offer heralded single photons. In spontaneous parametric down-conversion (SPDC), a pump photon splits into a signal-idler pair; detection of one photon heralds the other. Phase-matched waveguides, such as periodically poled lithium niobate (PPLN) pumped near 770 nm, can produce telecom photons [251], [252], [253], [254]. Similarly, four-wave mixing (FWM) in optical fibres or micro-resonators generates photon pairs through a $\chi^{(3)}$ (third-order) nonlinear optical process, often operating in the telecom C-band [255], [256]. Both SPDC and FWM readily provide entanglement and high single-photon purity, but suffer from intrinsically low brightness and probabilistic emission.

Heralded sources routinely support GHz-class pump clocks, yet usable in-fibre rates are ultimately limited by the multi-pair trade-off: raising pump power increases heralding probability but also the multi-photon fraction, which impacts the quantum bit error rate (QBER) in QKD.

3. 2.5. Excitation & Telecom Compatibility (optical/electrical; native/converted)

Initial demonstrations of telecom-wavelength single-photon emission appeared in 2005 for both InAs/GaAs [257] and InAs/InP [258] material systems. In the intervening years, substantial gains have been realized for quantum dots on GaAs [163], [259], [260], [261], [262], [263], [264], [265], [266] and on InP [169], [204], [267], [268], [269], [270], [271], [272]. State-of-the-art devices now deliver first-lens brightness of 36% for InP implementations with photonic-crystal cavities [273] and 23% for GaAs implementations with circular Bragg gratings [266]. A critical distinction among SPSs lies in excitation method and telecom compatibility. Optical pumping is widely used in proof-of-principle experiments, offering precise quantum control and high indistinguishability [196], [199]. Yet, its reliance on external lasers hinders scalability. Electrical pumping, pioneered by Yuan *et al.* in 2002 [274], is essential for integration and has since enabled telecom-band QD-LEDs [204].

In terms of wavelength, many emitters lie outside the O- and C-bands. Two strategies exist: (i) native telecom emitters, such as InAs/InP QDs and GaSb QRs; and (ii) quantum frequency conversion (QFC), which shifts visible photons to telecom while preserving quantum properties. For example, QD photons at 711 nm have been converted to 1313 nm with >30% efficiency [275] and NV photons at 637 nm down-converted to 1588 nm [276]. Although conversion introduces loss and noise, antibunching and entanglement can be retained. As mentioned in section 3.3.2, T-centres (1326 nm) and Er^{3+} ions (1530 nm) are intrinsically telecom-compatible and provide routes toward integrated quantum photonics.

While InAs/InP QDs currently define the technological benchmark for electrically driven telecom SPSs, their reliance on cryogenic operation and stringent emitter-cavity alignment highlights remaining obstacles to scalable deployment. In this context, GaSb/GaAs quantum rings represent an emerging alternative: although less mature, they promise native telecom

emission on GaAs platforms, potential resilience to elevated temperatures and ensemble-based device concepts that could ease fabrication constraints. This thesis builds on these opportunities to explore GaSb QR-based SPLEDs as a complementary route toward the ideal electrically driven telecom SPS.

3.3. Type-II Telecom Wavelength Light Emitting Diode Technologies

Telecommunications networks rely on light sources operating at the low-loss fibre bands around 1.3-1.55 μm. Conventional InP-based type-I semiconductor lasers (e.g. InGaAsP active layers on InP) dominate these wavelengths, but suffer performance degradation at elevated temperatures due to Auger recombination and carrier leakage [277]. This necessitates power-hungry cooling in high-density optical interconnects. In response, researchers have explored type-II heterostructure LEDs and lasers on GaAs or GaSb platforms, aiming for thermally robust emission in the O- and C-bands. In type-II band alignment, electrons and holes reside in different layers, enabling staggered-gap emissions at longer wavelengths than each material's bandgap and offering potential suppression of Auger recombination [234], [277].

This section surveys experimental type-II LEDs at 1.3-1.55 μm across three platforms; GaSb/GaAs quantum dots (QDs), GaSb/GaAs QRs and "W-type" GaAsSb/InGaAs QWs. We compare MBE vs. MOCVD growth, interface/strain management (As/Sb abruptness, mismatch) and post-growth annealing; benchmark optical metrics (wavelength, brightness, temperature stability, confinement); and review device/integration schemes (multilayer stacks, DBRs, cascades, cavity coupling, biasing). We highlight key references, trends and open challenges toward telecom-grade type-II LEDs.

3. 3.1. Band Alignment and Carrier Separation

In type-II band alignment, electrons and holes are spatially separated across the heterointerface. In GaSb/(In)GaAs QDs and QRs, holes localise in GaSb while electrons reside in GaAs or GaInAs. Related GaSb/GaAsSb heterostructures exploit the tunability of the valence-band offset via the Sb content in $GaAs_{1-x}Sb_x$, allowing the "type-ness" of the alignment to be tuned from quasi-type-I to strongly type-II. This compositional control provides an additional handle on the radiative lifetime and emission wavelength in type-II GaSb-based emitters. This real-space separation lowers the electron-hole overlap, extends the radiative lifetime and renders the transition energy highly sensitive to local electrostatics, built-in fields, background acceptors and the instantaneous charge state [105], [48], [278].

Ensemble photoluminescence (PL) therefore exhibits a characteristic blueshift with increasing excitation. By contrast, micro-PL from single or few emitters shows narrow lines that shift only weakly, while charged and multiexciton transitions gain spectral weight so that the spectrum's centre of mass moves. The agreement between these micro- and macro-observations points to capacitive charging rather than a uniform Stark effect as the dominant mechanism. In GaSb/GaAs QRs, a per-hole energy increment of ~24 meV is consistent with

a simple nano-capacitor model; band bending contributes only a small, weakly state-dependent offset [36], [48], [105], [232], [233].

The same principles apply to planar type-II stacks such as InAs/GaSb superlattices and GaAsSb/GaInAs "W" quantum wells: interface chemistry (GaAs-like vs. InSb-like bonds), layer thickness and applied electric fields tune the effective gap and real-space separation, trading oscillator strength for spectral reach [279], [280], [281], [282]. Field-induced control of alignment between type-I and type-II further enables electrically reconfigurable emission.

3. 3.2. GaSb/GaAs Quantum Dots and Rings for 1.3 μm Emission

GaSb/GaAs forms a staggered type-II junction in which the GaSb valence band sits above GaAs, tightly confining holes in GaSb while electrons reside in the GaAs matrix or adjacent layers [234]. The resulting spatially indirect recombination emits below the GaAs bandgap (1.424 eV), giving infrared output, typically around 1.1-1.2 μm at room temperature and extendable >1.3 μm with appropriate design [46]. This same separation, however, reduces wavefunction overlap and radiative probability, constraining efficiency [234].

Turning to growth, GaSb/GaAs QDs and QRs are typically realized by molecular beam epitaxy (MBE), which provides the flux control needed to manage As-Sb interactions. Owing to the 7.8% lattice mismatch, deposition of a few monolayers of GaSb on GaAs triggers Stranski-Krastanow islanding, producing self-assembled nanostructures without the need for metamorphic buffers [283], [284], [48]. Substrate temperatures near 500 °C and carefully tuned Sb_2/As_4 flux ratios are commonly employed [283]. For vertically stacked structures, strain management becomes essential, often via thin InGaAs caps or spacers that partly relax the mismatch and adjust the band alignment [285]. Interface abruptness is particularly critical: uncontrolled Sb segregation can form GaAsSb interlayers with ambiguous composition, leading to mixed type-I/type-II character that broadens the optical transition and degrades radiative efficiency [232]. For well-engineered type-II systems, maintaining sharp interfaces and controlled Sb composition is essential for stable telecom-band emission and efficient radiative recombination. Lower growth temperatures suppress unintended segregation and interdiffusion, yielding sharper PL spectra with well-defined band alignment.

Optically and electrically pumped devices confirm these advantages. InGaAs-capped GaSb QRs have yielded strong room-temperature EL near 1.3 μm, with long radiative lifetimes that stabilize emission against thermal quenching [188], [286]. Indeed, type-II GaSb/GaAs quantum-ring structures have been reported to exhibit thermally assisted carrier capture and relatively weak Auger processes at telecom energies, leading to characteristic increases in PL intensity over moderate temperature ranges [287]. Electrically driven devices based on GaSb/GaAs type-II nanostructures have also been demonstrated in LED form, although achieving true single-photon operation under electrical injection remains challenging. In parallel, more advanced III-V nanophotonic platforms, such as photonic-crystal nanobeam cavities and DBR-based microcavities, have shown that high Q factors, Purcell enhancement and efficient extraction are achievable with appropriately engineered emitters [234]. Collectively, these studies motivate ongoing efforts to realise telecom-band, electrically

driven type-II single-photon devices, but a fully monolithic, on-chip type-II SPLED operating in this regime has yet to be demonstrated.

3. 3.3. Quantum Wells on GaAs

The W-quantum well is a type-II heterostructure in which an InGaAs layer confines electrons and an adjacent GaAsSb layer confines holes, creating a “W-shaped” band profile when sandwiched between GaAs/AlGaAs barriers. Radiative recombination occurs across the interface, yielding longer-wavelength emission than either material alone. Early demonstrations by Klem et al. at Sandia showed that ~4 nm $In_{0.2}Ga_{0.8}As/GaAs_{0.72}Sb_{0.28}$ bilayers grown by MBE could red-shift photoluminescence to ~1.43 μm at room temperature, well beyond conventional GaAsSb or InGaAs wells [288]. Growth challenges arise from strong compressive strain and interface intermixing (In-Sb or As-Sb exchange), requiring precise thickness control and low growth temperatures [281]. More recent MOVPE work, including Fuyuki’s low-temperature process (475 °C), has achieved abrupt interfaces and bright PL[277]. Wavelength extension strategies include higher In/Sb compositions and coupled “double-W” designs; the latter have reached ~1.36 μm emission on GaAs, the longest yet for a GaAs-based QW laser without N or Bi incorporation [277] . While the C-band (1.55 μm) remains just out of reach, these results highlight W-QWs as a promising path to native telecom emission on GaAs.

3. 3.4. Performance Trends & Limiters

In GaSb type-II nanostructures, excitation-dependent spectral shifts are typically dominated by capacitive hole charging rather than a uniform Stark effect.

For quantum rings, this behaviour has been described by a nano-capacitor model, though the precise energy increments per carrier remain device-dependent [232]. Hydrogenation experiments further support this picture, showing that passivating shallow acceptors suppresses spectral drift but also reduces emission intensity by limiting hole pre-filling [35].

Thermal performance is often limited by electron localisation and thinner caps or suitably engineered barriers have been shown to extend operation toward higher temperatures [46].

Since type-II transitions exhibit longer lifetimes than type-I counterparts, modulation speeds can be restricted; coupling to photonic crystal or nanobeam cavities provides Purcell enhancement that shortens lifetimes and improves extraction [289].

At the excitonic level, calculations and spectroscopy both indicate a dense manifold, with charged and multiexciton states lying only a few meV from the neutral exciton, explaining the rapid emergence of additional lines under strong drive [90].

In practice, interface abruptness, strain management, charge control and tight cavity/process tolerances determine whether the long-wavelength leverage of type-II physics can be realised in a stable, electrically pumped emitter on a GaAs photonics platform.

3.4. Quantum Key Distribution

Quantum Key Distribution (QKD) enables secure key exchange based on the principles of quantum mechanics, with single photons serving as the ideal carriers due to their sensitivity to eavesdropping [182], [184], [151]. While early and commercial systems predominantly use attenuated laser pulses (weak coherent pulses, WCPs) at telecom wavelengths (1310 nm, 1550 nm), these have intrinsic multi-photon probabilities, necessitating protocol-level corrections such as decoy states [156], [157], [290]. This has motivated significant research into true single-photon sources (SPSs) capable of telecom-band operation, aiming to enhance both security and performance [193], [223].

3.4.1. Quantum Key Distribution Protocols and Source Requirements

QKD is a cryptographic protocol in which two parties, Alice (sender) and Bob (receiver), establish a shared secret key using quantum properties of light, while a potential eavesdropper (Eve) cannot intercept this key without introducing detectable disturbances. The security of QKD stems from the no-cloning theorem: Eve cannot copy an unknown quantum state without disturbing it and any measurement attempt on quantum states leaves traces detectable by Alice and Bob [291], [292], [293]. The basic workflow involves:

1. State Preparation (Alice): Alice prepares and sends quantum states (typically single photons) encoding random bits, often using randomly chosen measurement bases or polarization states.
2. Measurement (Bob): Bob receives the photons and measures them in randomly chosen bases, recording outcomes.
3. Basis Reconciliation (Public Channel): Alice and Bob publicly compare their chosen bases (without revealing measurement results) and keep only events where bases matched.
4. Eavesdropping Check: If Eve attempted to measure or intercept photons, the error rate (Quantum Bit Error Rate, QBER) in Alice-Bob's shared key exceeds the threshold expected from legitimate noise, triggering detection of an eavesdropping attempt.

Photon source characteristics, such as single-photon purity, indistinguishability, brightness and timing stability, directly influence protocol feasibility, security levels and achievable key rates.

Quantum key distribution (QKD) protocols differ in their photon source requirements. Below is a summary of key protocols and their implications for source design:

- **BB84 (Prepare-and-Measure):** Requires single photons to ensure security. In practice, weak coherent pulses (WCPs) are used, with decoy-state methods to counteract multi-photon attacks [184]. Ideal sources are fast, stable and support state modulation. True single-photon sources (SPSs) with low $g^{(2)}(0)$ could simplify the protocol and strengthen security [294].

- **Decoy-State QKD:** Enhances WCP-based BB84 by interleaving signal and decoy pulses to estimate photon-number splitting attacks. It relies on precise intensity modulation and phase randomization. SPSs would eliminate the need for decoys, reducing complexity and loopholes [156].
- **Measurement-Device-Independent QKD (MDI-QKD):** Users send quantum states to a central, possibly untrusted node. High interference visibility between independent sources is crucial, requiring indistinguishable photons. SPSs could boost security and rates, though synchronizing two SPSs remains a technical challenge [186], [295].
- **Entanglement-Based QKD (E91, BBM92):** Uses entangled photon pairs, often via SPDC or quantum dots. Key metrics include entanglement fidelity, brightness and low multi-pair emissions. Telecom wavelengths are preferred for long-distance fibre transmission. Quantum dot-based entangled SPSs show promise for high performance [296], [297], [298].
- **Device-Independent QKD (DI-QKD):** The most demanding, requiring near-perfect entangled sources and detectors to close all loopholes. Though still experimental, deterministic SPSs like quantum dots are seen as enablers of practical DI-QKD [180], [299], [300].

In summary, QKD protocols differ in their demands on photon sources. Prepare-and-measure schemes focus on single-photon purity and fast modulation, while interference-based protocols like MDI-QKD and entanglement-based QKD require high photon indistinguishability and precise synchronization. Device-independent QKD sets the highest bar, relying on near-ideal entangled sources. Progress in deterministic single- and entangled-photon sources is therefore key to advancing secure and scalable quantum communication.

3.4.2. Integration in Quantum Key Distribution Systems

Integrating SPSs into QKD architectures depends on the protocol. In prepare-and-measure schemes, the source is placed at Alice's transmitter; in entanglement-based QKD, at a central node; and in MDI-QKD, at both ends [186], [301]. Replacing weak coherent pulses with SPSs often leaves the state-encoding optics unchanged, but can simplify setups by removing the need for decoy-state modulation or phase randomization [210], [290], [156]. SPSs have been successfully combined with both polarization and time-bin encoders, as demonstrated in recent field trials [186], [302], [303].

Synchronization follows similar principles as with lasers: SPSs are usually triggered by pulsed excitation, which naturally provides a clock. Timing jitter is typically small compared to detector resolution, though coincidence windows remain critical in entanglement-based schemes [304], [305]. On the receiver side, integration is straightforward; SPSs paired with low-noise superconducting detectors even allow free-running operation, improving detection efficiency [306], [307]. In interference-based protocols, however, indistinguishability between photons from different sources remains a major challenge [197], [273]

From a practical standpoint, SPSs must operate stably over long periods. Recent quantum dot demonstrations show day-long stable key exchange, though coupling drift and environmental fluctuations remain concerns. Integration into real telecom networks also requires careful filtering to suppress background and pump leakage, similar to laser-based systems [183], [308].

In essence, the integration of single-photon sources into QKD systems is rapidly transitioning from lab to field [309], [310]. Early QKD experiments with SPSs often had elaborate, delicate setups, but recent trials use more robust arrangements (fibre coupling, automated stabilization). The next step is likely combining such sources with integrated photonic encoders and possibly integrated detectors to realize a full QKD transmitter or transceiver on a chip. Reducing the footprint and increasing the reliability of SPS-based QKD transmitters will make them viable for deployment in telecommunications equipment racks alongside classical network gear [311].

3.4.3. Performance Comparison and Trade-offs

Evaluating photon sources for QKD involves balancing multiple performance metrics, since gains in one dimension often compromise another. The fundamental trade-off is between brightness and single-photon purity. Weak coherent pulses (WCPs) and SPDC sources can raise key rates by sending more photons, but this increases the probability of multi-photon events, limiting security. As a result, WCP systems typically operate with mean photon numbers $\mu \ll 1$ [158], [312]. Deterministic single-photon sources (SPSs), particularly quantum dots, offer a way around this dilemma: in principle, they can deliver both high brightness and low $g^{(2)}(0)$[183], [313]. Experiments support this advantage. Yamamoto's group (2015) achieved 27.6 bps over 100 km without decoy states, three times higher than comparable decoy-laser systems at 50 km [314]. More recently, Yang et al. (2024) demonstrated SPS-based QKD exceeding the theoretical decoy-state bound by combining high efficiency with low multi-photon probability [231].

Distance and loss tolerance represent another key trade-off. Fibre attenuation ultimately limits all QKD systems, but decoy-BB84 has extended secure operation up to 150-200 km [141], [143]. Twin-field QKD (TF-QKD), in which Alice and Bob send photons simultaneously to a central measurement node for phase-matching interference, has reached >500 km by mitigating fiber loss penalties; however, this comes at the cost of extreme phase stability requirements and very low key rates [316], [317], [318]. SPS systems are rapidly closing this gap. In 2015, a quantum dot QKD experiment achieved 0.3 bps at 120 km with modest source brightness and gated InGaAs detectors [314]. By 2024, a German intercity trial using a deterministic SPS reached 144 km with 28.1 dB channel loss, achieving a secret key rate of 4.8×10^{-5} bits per pulse [231].

Quantum bit error rate (QBER) further illustrates these performance trends. SPSs remove errors associated with multi-photon pulses but may introduce small penalties from timing jitter or spectral mismatch [181]. Reported QBERs include near 3-4% in the Copenhagen trial (2024)[183], approximately 0.65% in the German intercity demonstration (2024) [231]

and 5-10% in traditional SPDC entanglement experiments [319]. All are within protocol thresholds, but only deterministic SPSs offer both low error and low multi-photon leakage simultaneously, an essential property for device-independent QKD, which demands low error in Bell-violation terms [180], [185], [320].

Different QKD protocols favour different sources: WCPs achieve the highest raw rates (tens of Mbit/s) but rely on decoy-state modulation, while SPS-based BB84 operates at lower rates yet simplifies security by eliminating decoys. Deterministic SPSs are especially valuable for interference-based schemes like MDI-QKD and future entangled SPSs could replace SPDC in entanglement-based and device-independent protocols.

In terms of scalability, WCP transmitters remain inexpensive and suitable for multi-user networks, whereas SPSs, currently limited by cryogenic operation, are best suited for backbone or trusted-node links. As integration matures, SPSs are expected to follow the trajectory of lasers, evolving into compact, deployable components that will ultimately surpass WCPs in both performance and trust.

A number of companies worldwide are actively developing or commercializing quantum key distribution (QKD) systems, each leveraging different photon source technologies as seen in table 3.1. ID Quantique (Switzerland) and Toshiba Quantum Technology (Japan/UK) are among the leaders, offering weak-coherent pulse and entangled-photon QKD devices, with Toshiba also demonstrating entangled QKD protocols. In the United States, firms such as MagiQ Technologies and Qubitekk provide attenuated-laser BB84 systems and entangled photon pair sources for infrastructure security, while Quantum Xchange integrates third-party QKD hardware into network services.

Other regions have also become active players: QuintessenceLabs (Australia) explores quantum vacuum and continuous-variable QKD, QuantumCTek (China) and Qasky (China) develop fibre and satellite QKD platforms and QNu Labs (India) offers indigenous fibre-based systems. QRate (Russia) has demonstrated decoy-laser QKD over hundreds of kilometres, whereas UK-based startups like KETS Quantum and Nu Quantum focus on chip-scale QKD transmitters, on-chip single-photon sources and ultra-sensitive detectors. Collectively, these companies illustrate the diversity of technological approaches, from weak-coherent pulses to entangled and deterministic single-photon sources, that are shaping the path toward commercial quantum-secure networks.

Table 3.1 Examples of QKD / SPS / Field Trials with responsible institutions or companies

Experiment / Project	Institutions / Companies	Notes / Key Features	True SPS Used?
Intercity deterministic SPS QKD (2024, Germany) [231]	Leibniz University of Hannover; PTB; University of Stuttgart	First intercity QKD with deterministic SPS; with 28.1 dB channel loss. Emphasized deterministic SPS deployment in field QKD using GaAs QD in circular Bragg grating resonator emitting at telecom wavelength, cryogenic temperature (~10K) operation and record 144 km	Yes
ID Quantique & UNIGE- Detector speed record [321]	ID Quantique; University of Geneva	Faster superconducting nanowire detectors; critical for SPS-based QKD performance.	Not source-related (detector improvement)
IM-QKD Field Trial (Padova University Network) [322]	University of Padova; INFN Legnaro	Three-node field trial with fibre/free-space links; no deterministic SPS reported.	No
Toshiba- “Quantum key >10 Mb/s” [323]	Toshiba	Record 13.7 Mb/s QKD using improved electronics and detectors.	No (WCP/decoy states)
Toshiba- Semiconductor SPS diode [204]	Toshiba	Developed diode with quantum dot emitting single photons at telecom wavelengths; operating temperature up to 93 K (liquid nitrogen compatible);	Yes (lab demo, not full field QKD)
Toshiba - 600 km fibre QKD [324]	Toshiba	Longest fibre QKD (600 km) using dual-band stabilization.	No (WCP-based)
Toshiba - Twin-Field QKD [325]	Toshiba	Demonstrated TF-QKD to extend secure distance via central measurement node.	No (coherent sources with decoys)

3.5. Open Challenges: Gaps and Research Questions

Despite recent progress, key gaps remain before telecom-band single-photon sources can be widely deployed in quantum networks. Fibre-coupling efficiencies are still modest and

improving them without degrading purity or indistinguishability requires new cavity-QED and nanophotonic designs. Coherence remains limited by phonon and charge noise, particularly at telecom wavelengths and high-temperature operation. Scalability is constrained by growth inhomogeneity and device variability, while long-term stability is challenged by blinking, spectral diffusion and material degradation. On the system level, seamless integration with modulators, converters and classical channels introduces crosstalk and reliability concerns. Furthermore, entangled pair generation in semiconductors at telecom bands remains at an early stage and theoretical models for type-II systems are underdeveloped, leaving multi-particle dynamics poorly understood. Together, these challenges define the central research questions: how to realize efficient, high purity, indistinguishable and stable emission at or near room temperature, how to reproducibly scale device arrays and how to generate entanglement in electrically driven architectures suitable for real-world quantum communication.

Chapter 4 Experimental Methods

The realisation of high-performance GaSb/GaAs quantum-ring light-emitting diodes and single-photon light-emitting diodes demands precise control over material composition, layer thickness and device geometry at the nanometre scale. This chapter outlines the experimental techniques employed throughout this thesis to achieve such control, from epitaxial growth through device fabrication and comprehensive characterisation.

The chapter is organised into three principal sections. Section 4.1 describes the epitaxial growth methodology, focusing on molecular beam epitaxy (MBE), the cornerstone technique used to grow all heterostructures, including quantum-ring active layers, distributed Bragg reflector (DBR) mirrors and doping-engineered carrier-transport layers. MBE's atomic-scale control over layer thickness, composition and doping makes it indispensable for achieving the structural precision required for both optical cavity performance and quantum confinement effects.

Section 4.2 presents the device fabrication techniques, spanning photolithographic patterning (both mask-based and direct laser writing), dry and wet etching (reactive ion etching and inductively coupled plasma etching), thin-film deposition (thermal evaporation and plasma-enhanced chemical vapour deposition) and post-fabrication annealing. These methods collectively translate the epitaxial wafers into functional devices with defined mesa geometries, electrical contacts and surface passivation.

Section 4.3 details the characterisation techniques used to evaluate device performance and material quality. These include optical spectroscopy (photoluminescence and electroluminescence), non-destructive optical metrology (spectrophotometry and ellipsometry) and high-resolution structural imaging (transmission electron microscopy). Together, these tools provide both macroscopic performance metrics and microscopic insight into layer quality, interface sharpness and defect structures.

The methodologies described here form the complete workflow from design to characterisation, ensuring that the optical, electrical and structural properties of the fabricated devices can be rigorously evaluated and correlated with theoretical predictions and device performance models presented in earlier chapters.

Unless stated otherwise, the device fabrication, optical spectroscopy (PL/EL), electrical characterisation and data analysis reported in this thesis were performed by the author. Epitaxial growth of the wafers by molecular beam epitaxy was carried out in the Lancaster University Physics Department MBE facility by Dr Peter Hodgson, based on layer designs and device requirements defined for this project. Transmission electron microscopy (TEM) characterisation was performed at the University of Warwick by Francisco Alvarado-Cesar; the author prepared and supplied the samples for TEM, specified the regions/structures of interest, and carried out the interpretation and analysis of the microscopy data presented here.

4.1. Epitaxial Growth Technique

4. 1.1. Molecular Beam Epitaxy (MBE)

Molecular beam epitaxy (MBE) is a cornerstone epitaxial technique employed in this study for the fabrication of distributed DBR LEDs and SPLEDs. The method offers atomic-scale control over layer thickness, composition and doping, all of which are critical for achieving high-reflectivity optical structures and well-defined quantum emitters [326]. The general layout of the MBE system is illustrated in Fig. 4.1, highlighting key operational components and their interactions.

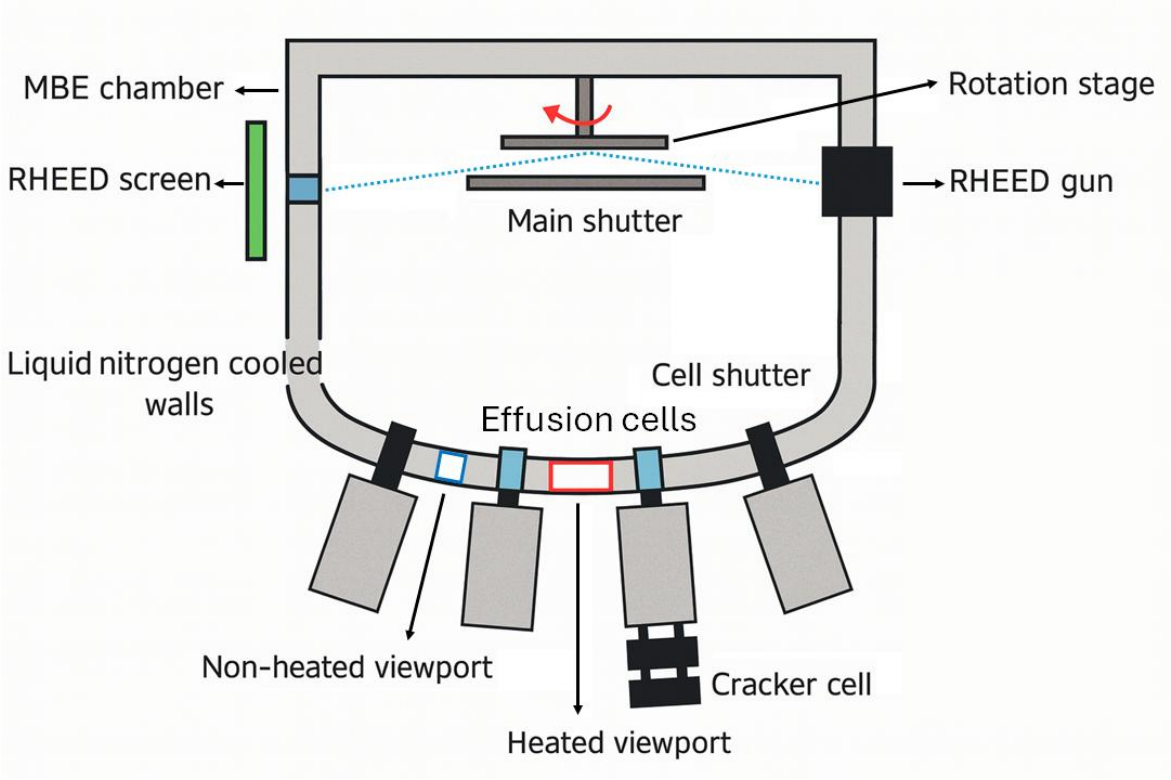

Fig. 4.1: Schematic diagram of a typical molecular beam epitaxy (MBE) system. The system operates under ultra-high vacuum (UHV) and includes effusion cells, shutters, beam modulation, substrate temperature and rotation control and reflection high-energy electron diffraction (RHEED) monitoring.

Growth is conducted under UHV conditions (typically reaching pressures as low as 10^{-11} mbar), which are essential for maintaining material purity and minimising the incorporation of defects [327], [328]. In MBE, the constituent elements are evaporated thermally and directed towards the heated substrate in the form of molecular beams. These beams travel along line-of-sight paths from a series of independently controlled effusion and cracker cells located at the base of the growth chamber.

The MBE system utilised in this work is a Veeco GENxplor, equipped with solid-source effusion cells for group-III elements and dopants (e.g., gallium, aluminium, indium, beryllium and silicon), as well as valved cracker cells for group-V sources such as arsenic and antimony. Each cell is fitted with a dedicated shutter to enable precise control of the

material flux. The chamber walls are cooled using liquid nitrogen cryopanels to trap residual gases and sustain UHV conditions.

Substrates are mounted on a rotating stage and heated to several hundred degrees Celsius to ensure appropriate surface diffusion and adhesion of adatoms [329]. This thermal control is particularly crucial when growing DBR structures, which rely on periodic refractive index variations and uniform layer thicknesses, as well as for SPLED structures, where quantum confinement and emitter quality are highly sensitive to interface roughness and material uniformity.

RHEED is employed as an in-situ diagnostic tool to monitor surface morphology and crystal quality in real time [330], [331]. An electron beam is directed at a glancing angle onto the substrate surface and the resulting diffraction pattern, observed on a phosphorescent screen, provides immediate insight into the growth mode. Streaked patterns typically indicate smooth, two-dimensional growth, which is ideal for optical cavity structures, while spotty patterns may suggest rough or three-dimensional island growth, which is generally undesirable for optoelectronic device performance [329].

In this project, MBE was indispensable for achieving the structural and optical quality required for telecom-wavelength operation of DBR mirrors and quantum emitter layers. All epitaxial growths, including the GaSb-based quantum ring layers and GaAs/AlGaAs DBRs, were carried out by Dr Peter Hodgson at Lancaster University under growth conditions tailored specifically for high-performance SPLED applications.

4.2. Device Fabrication Techniques

Lithographic patterning was an essential step in the fabrication of DBR LEDs and single-photon LEDs (SPLEDs), enabling the definition of etch masks and contact regions with lateral features ranging from millimetre to micron scale. Two complementary lithography methods were employed, which are optical mask UV photolithography and direct laser writer (DLW) lithography, depending on the specific processing step and design flexibility required.

4. 2.1. Mask Lithography

Optical mask UV lithography was primarily used for high-throughput patterning [332]. The process involved spin-coating the sample with positive photoresists, specifically S1813 for etch patterning and S1813/LOR3A bilayers for metal lift-off in this work. Following spin-coating and soft baking, the resist-coated samples were exposed to near-UV light (365 nm) using a SUSS MicroTec MJB4 mask aligner, which allowed for precise alignment of the photomask to the sample via an integrated microscope and micrometre-controlled stage.

The general steps of the UV lithography process including spin-coating, UV exposure through a patterned mask and development are illustrated schematically in Fig. 4.2. Exposure was carried out in soft contact mode under a high-pressure mercury arc lamp (~260 W) and the desired patterns were transferred to the resist based on the photomask geometry.

After development, the patterned resist acted either as a mask for dry/wet etching or as a stencil for subsequent lift-off of deposited metals.

This method was used throughout the fabrication flow due to its high reliability and ability to support both large and micron size features, especially when fine alignment was required across multiple lithography steps.

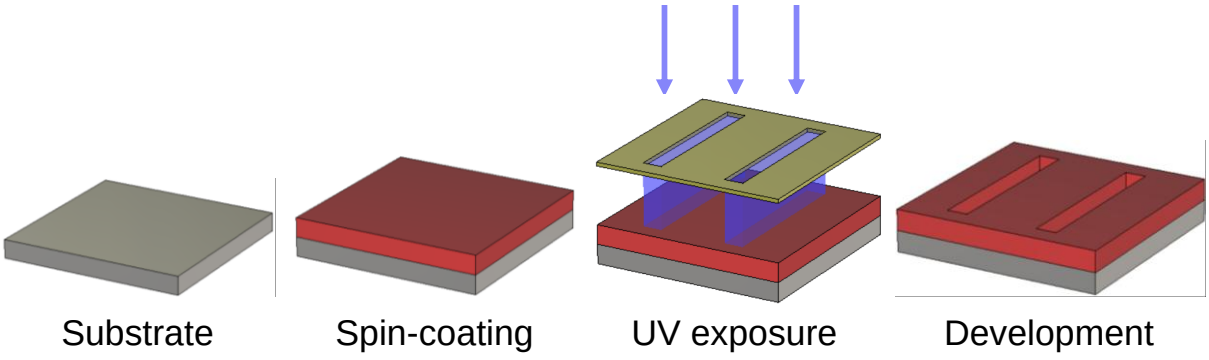

Fig. 4.2: Process flow of positive photoresist lithography: spin-coating, UV exposure through a photomask and development of exposed regions.

4. 2.2. Direct Laser Writer Lithography

A Picomaster 100 Direct Laser Writer (DLW) (4Pico, now Raith), in addition to mask-based photolithography, was employed for rapid and flexible pattern generation without the need for physical masks as shown in Fig. 4.3. This was especially useful for prototyping, single-device exposures and situations requiring design changes without the delay or expense of new chrome masks.

The DLW process followed a similar resist preparation protocol to optical mask lithography: resist was spin-coated (either S1813 or S1813/LOR3A) at optimised parameters, followed by soft bake. The sample was then loaded into the laser writer, where autofocus calibration was performed using a 635 nm red laser and four-quadrant detection system. Proper focussing ensured that the 405 nm exposure laser would write with optimal resolution and dose within the resist layer.

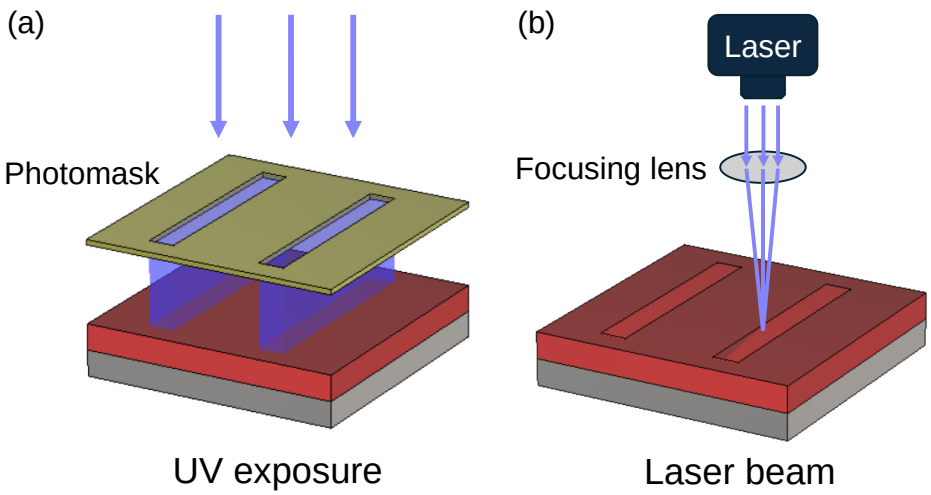

Fig. 4.3: Comparison of mask-based lithography and direct laser writing (DLW). (a) A photomask defines the pattern and UV light selectively exposes the photoresist. (b) In DLW, a focused laser beam directly writes the pattern into the photoresist without the need for a physical mask.

Once focus was achieved, optical alignment was performed using an integrated camera system. A virtual mask, created in the DLW control software, was used to raster the laser beam across the resist surface, selectively exposing the desired pattern. The ability to edit digital mask layouts in real-time and directly write them onto the sample provided significant flexibility, especially during development phases and one-off designs.

Although DLW generally has lower throughput than mask-based lithography, it complements it by offering unmatched design flexibility, making it a valuable tool in the patterning workflow of this project.

4. 2.3. Plasma Ashing

Plasma ashing was used in this study as a dry-cleaning method to eliminate photoresist residues remaining after lithographic and etching steps [333]. The process involves generating a reactive oxygen plasma, typically by applying high-frequency radio waves to an O_2 gas flow. This breaks molecular oxygen into reactive atomic species, which chemically degrade the organic resist into volatile by-products. The general mechanism of oxygen plasma ashing, involving the interaction between reactive oxygen species and carbon-based photoresist residues, is illustrated in Fig. 4.4.

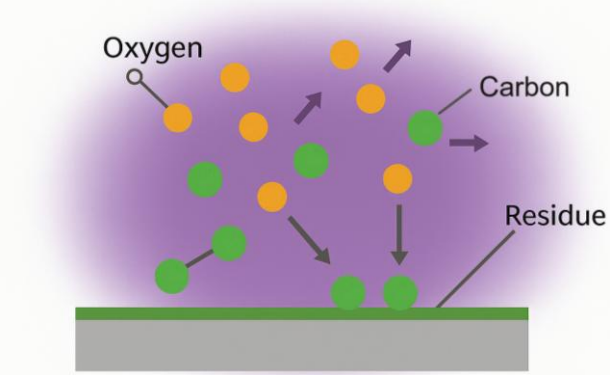

Fig. 4.4: Representation of a O_2 plasma ashing process. Reactive oxygen species attack the polymer chains in the photoresist, breaking them into volatile compounds that are evacuated from the chamber.

The ashing mechanism is based on oxidative reactions that disrupt polymer chains within the resist, converting them into gaseous compounds that are pumped away. While effective, plasma ashing must be carefully controlled to avoid surface damage, particularly on III-V materials, as high plasma power or prolonged exposure can lead to unwanted oxidation or material modification [334].

In this work, ashing was primarily used before metal deposition or after etching steps, where a clean surface is essential for adhesion and pattern fidelity and also applied after each lithography process to remove residual photoresist and ensure surface cleanliness for subsequent processing. Low-power, oxygen-rich plasma conditions were selected to ensure compatibility with DBR and SPLED device layers.

4. 2.4. Reactive Ion Etching (RIE)

Reactive ion etching (RIE) is a plasma-based dry etching technique widely used in micro- and nano-fabrication for defining fine features with vertical sidewalls. It combines chemical etching, driven by reactive species, with physical sputtering induced by ion bombardment. This hybrid approach enables anisotropic material removal while maintaining selectivity to different layers in the device stack [333].

In a typical RIE process, gases such as CF_4, CHF_3, or O_2 are introduced into a vacuum chamber and excited into plasma using radio-frequency (RF) power [31]. The plasma breaks the gas molecules into a mixture of neutral radicals and positively charged ions. These species interact with the sample surface where reactive radicals chemically modify the target material to form volatile by-products, while ions are accelerated towards the surface, enhancing etch directionality by physically assisting in material removal. The basic schematic if the RIE system is illustrated in Fig.4.5.

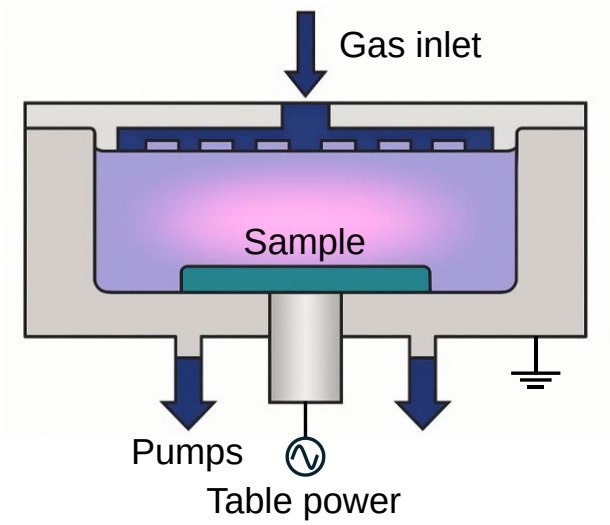

Fig. 4.5: Schematic diagram illustrating the RIE process. The RIE system operates with an RF-powered sample plate and utilises both reactive ions and neutrals to etch desired layers.

The system used in this work is the Oxford Instruments PlasmaPro 80, a parallel-plate RIE tool with a grounded chamber wall and an RF-powered electrode beneath the substrate. This configuration ensures a uniform electric field and stable plasma, where a single RF source governs both ion energy and density.

RIE was employed primarily to etch silicon nitride (Si_3N_4) passivation layers in DBR and SPLED structures. These dielectric layers, used for surface protection and electrical isolation, required clean and controlled etching to avoid damage to underlying semiconductor materials. Process conditions, including RF power, gas flow and pressure, were tuned to achieve reliable anisotropic etching with minimal surface roughness or residue.

4. 2.5. Inductively Coupled Plasma (ICP) Etching

Inductively coupled plasma (ICP) etching is a high-density plasma process widely used for material removal in semiconductor fabrication. Unlike conventional reactive ion etching (RIE), where the plasma is sustained primarily between two electrodes, ICP systems generate plasma through electromagnetic induction. A radio-frequency (RF) antenna, typically in a coil geometry around the chamber, creates an oscillating electromagnetic field that accelerates free electrons, causing ionisation of the process gases and forming a dense, uniform plasma [333], [335]. The general structure of an ICP system and the principle of operation are illustrated schematically in Figure 4.6.

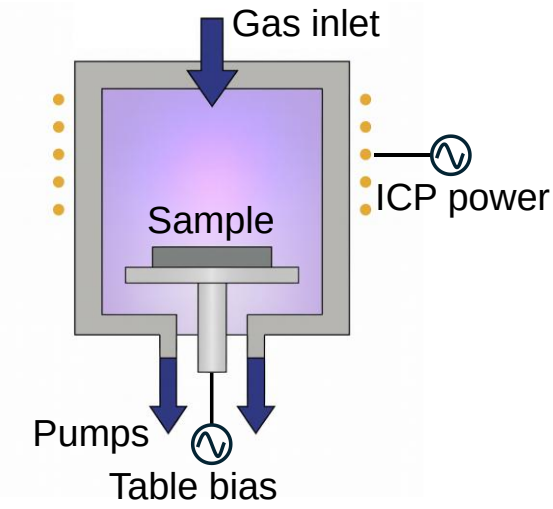

Fig. 4.6: Schematic illustration of an ICP etching system. An RF coil generates a dense plasma via electromagnetic induction, while independent RF biasing of the substrate allows controlled ion acceleration for highly anisotropic etching.

In an ICP system, ions are accelerated toward the sample surface due to the self-bias potential that develops between the plasma and the substrate electrode. This creates a strong electric sheath, allowing ions to impact the surface at near-vertical angles and enabling highly anisotropic etching [335]. Importantly, the plasma density (ion generation) and the ion energy (acceleration) can be controlled independently by adjusting the RF powers applied to the coil and the platen, respectively. This decoupled control offers greater process flexibility compared to traditional RIE [336].

Etching in an ICP tool typically relies on a combination of chemical reactions, where reactive radicals modify the surface and physical sputtering by energetic ions. In the absence of ion bombardment, purely chemical etching rates are very low, highlighting the critical role of ion assistance in most plasma processes.

In this work, ICP etching was preferentially used for removing III-V semiconductor materials where high anisotropy and real-time process control were required. The ICP system available was equipped with in-situ laser reflectometry, which enabled real-time monitoring of the etch depth by observing reflectivity changes during the process [337]. This capability was particularly advantageous because III-V semiconductor layers exhibited variations in composition and thickness from sample to sample, making time-based etch termination unreliable. By contrast, for Si_3N_4 passivation layers, RIE tools equipped with CHF_3-based chemistries and pre-calibrated etch rates were sufficient. However, due to the selective etching properties and the ability to accurately control depth, halogen-based precursors (e.g., Cl_2 and BCl_3) used in the ICP chamber were essential for etching the critical semiconductor layers in DBR and SPLED device fabrication.

A representative III-V ICP mesa-etch used chlorine-based chemistry with independently controlled coil/platen RF powers to decouple plasma density from ion energy. In-situ laser reflectometry (Horiba system) was used for endpoint control; with a typical 1 Hz sampling

rate, the reflectance trace provides ~15 nm depth resolution per sample and prevents over-etch into the lower claddings.

4. 2.6. Thermal Evaporation

Thermal evaporation is a physical vapour deposition (PVD) method widely used for depositing metal thin films onto a substrate. It operates by heating a solid source material, typically a metal, until it vaporises within a high-vacuum chamber. The vapour then travels through the chamber and condenses onto the cooler surface of the target substrate, forming a uniform film [338].

The heating is achieved via Joule heating where an electric current passes through a resistive filament or metal boat containing the source material. Once the temperature exceeds the material's evaporation point, atoms or molecules are released in the form of vapour [339]. Under high-vacuum conditions (typically less than 3×10^{-6} mBar), the vapour follows line-of-sight trajectories toward the substrate with minimal scattering, ensuring that most particles reach the substrate at near-normal incidence. The basic layout of a thermal evaporation chamber is shown schematically in Fig. 4.7.

In this study, a Moorfield MiniLab thermal evaporator was used to deposit metal contacts including titanium (Ti), gold (Au), nickel (Ni) and gold/germanium (AuGe). The samples were mounted upside down on a rotating substrate holder above the source, ensuring uniform coverage during deposition. A mechanical shutter positioned between the source and substrate was used to control the exposure, enabling precise start/stop control of film growth. A quartz crystal monitor tracked the deposition rate in real time, which was typically maintained between 3-4 Å/s to ensure film quality and reproducibility [340].

The thermal evaporation process was critical for patterning ohmic contacts and reflective metal layers in both DBR LED and SPLED devices fabricated in this work.

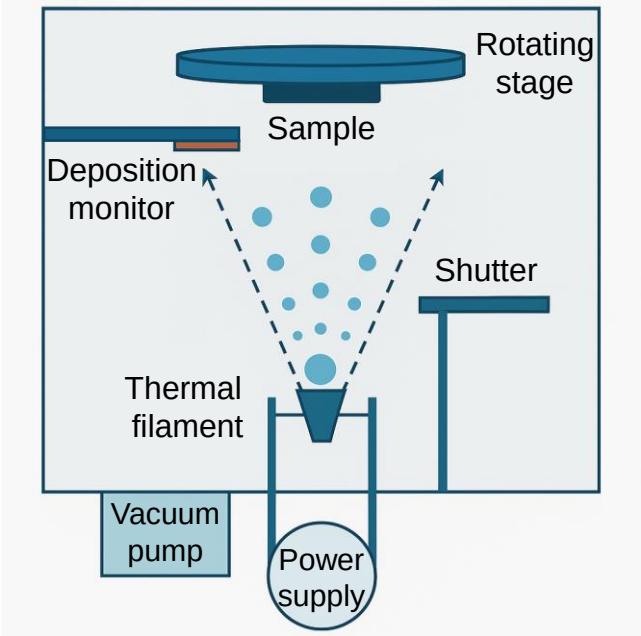

Fig. 4.7: Schematic of a thermal evaporation system. Vapourised metal atoms travel from the heated source material to the rotating substrate under high vacuum. A shutter and deposition monitor are used to control and measure the film thickness.

4. 2.7. Plasma-Enhanced Chemical Vapour Deposition (PECVD)

Plasma-enhanced chemical vapour deposition (PECVD) is a widely used thin-film deposition technique, particularly suited for forming dielectric layers such as silicon nitride (Si_3N_4) and silicon dioxide (SiO_2) in semiconductor processing. Unlike conventional thermal CVD, PECVD operates at significantly lower substrate temperatures by using plasma to activate the chemical reactions necessary for film growth [341].

In a typical PECVD system, gaseous precursors are introduced into a low-pressure vacuum chamber, where an RF-powered electrode generates an electric field between itself and a grounded electrode, usually the sample stage. The applied field excites the process gases into a plasma state, producing ionised species and reactive radicals. These chemically active components undergo surface reactions upon contacting the heated substrate, leading to the continuous, non-self-limiting deposition of material [342]. A simplified schematic of the PECVD process is shown in Fig. 4.8.

The PECVD process is well suited for the deposition of conformal, electrically insulating films and for surface passivation. In this work, an Oxford Instruments PlasmaPro 80 ICP-CVD system was used to deposit Si_3N_4 passivation layers on DBR LED and SPLED structures. This system features an additional RF coil, allowing separate control of plasma density and ion energy, thus improving the process tunability for delicate III-V substrates. High deposition rates (~70 nm/min) were achieved while maintaining process temperatures compatible with prior device layers.

By operating at millibar-range pressures and using mass flow controllers to precisely control gas flow rates, PECVD enabled the formation of smooth, isotropic dielectric films essential for electrical isolation and environmental protection of the fabricated devices

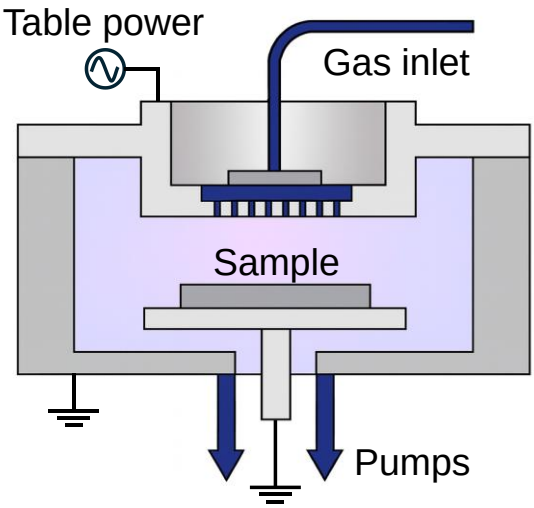

Fig. 4.8: Schematic of a PECVD system. Reactive gases enter the chamber and are ionised by RF-generated plasma. The ionised species deposit on the heated substrate surface, forming a uniform dielectric layer.

4. 2.8. Rapid Thermal Annealing (Annealer)

Rapid thermal annealing (RTA) is a post-processing technique used to activate dopants, improve metal-semiconductor contact properties, or repair damage induced during fabrication [31], [333]. In this work, all thermal treatments were conducted using an Allwin21 AccuThermo AW 610 system, which employs infrared lamps to rapidly heat the sample.

The samples were placed inside a SiC-coated graphite susceptor, designed to provide efficient thermal transfer and uniform heating. Heating was achieved through a set of high-intensity lamps and the temperature was closely monitored using a thermocouple located within the susceptor, near the sample position. This setup assumes thermal equilibrium between the susceptor and the sample throughout the annealing process. A mass-flow controller regulated the process gas composition and flow rate. The system layout is illustrated in Fig. 4.9.

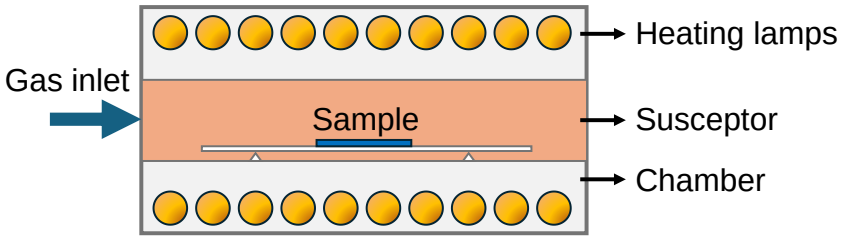

Fig. 4.9: Schematic of the Allwin21 AccuThermo AW 610 RTA system. Samples are placed in a SiC-coated graphite susceptor, heated by infrared lamps. A thermocouple monitors temperature near the sample and process gases are introduced through a mass-flow controller.

Although the system lacks active cooling, temperature ramp-down was achieved through passive radiation and convective heat transfer from the flowing process gases. Variability in annealing conditions was mitigated by preheating the system to the target temperature and allowing it to cool to 50 °C prior to sample loading. An additional warm-up step to ~60 °C before ramping helped further stabilise conditions. The annealing process played a vital role in activating contact layers and ensuring reproducible electrical behaviour in DBR LED and SPLED devices.

4.3. Characterisation Techniques

4. 3.1. Photoluminescence (PL) Measurement

Photoluminescence (PL) spectroscopy is a non-destructive optical technique used to investigate the electronic and optical properties of semiconductors. In PL measurements, a light source with photon energy above the bandgap excites electron-hole pairs, which subsequently recombine and emit photons. Analysis of the emitted spectrum provides insight into material composition, bandgap energy, defect states and interface quality, making PL an essential characterisation method for epitaxial layer structures and optoelectronic devices [343].

PL characterisation was performed using the optical setup shown in Fig. 4.10, specifically configured for optical excitation of the devices rather than electrical injection. A continuous-wave 532 nm laser served as the excitation source, providing photons with energy above the bandgap of the active material to generate electron-hole pairs. The excitation beam was directed into the setup via silver-coated mirrors, an optical periscope and a partial reflector before being focused onto the sample surface.

The emitted PL from the sample was collected by a 3″ off-axis parabolic mirror positioned to maximise the collection angle. Collected light was transferred to the upper beamline through a beam reducer formed by a matched pair of off-axis parabolic mirrors with coincident focal points. Polarisation optics, mounted on flip stages, were available in the upper beamline to enable or bypass polarisation-resolved measurements. A final parabolic mirror focused the collected emission into a multimode optical fibre, which fed an Acton SpectraPro 2300i spectrometer coupled to an Andor iDus 492A InGaAs array detector.

Samples were mounted on a motorised x-y-z-θ stage with an optional temperature-controlled holder for measurements between 15 °C and 85 °C. Alignment was optimised using a low-power green alignment laser on a flip mount, allowing for fine positioning of the sample at the focal point of the collection mirror. A grid search method was used to adjust the stage position until the maximum detector signal was achieved.

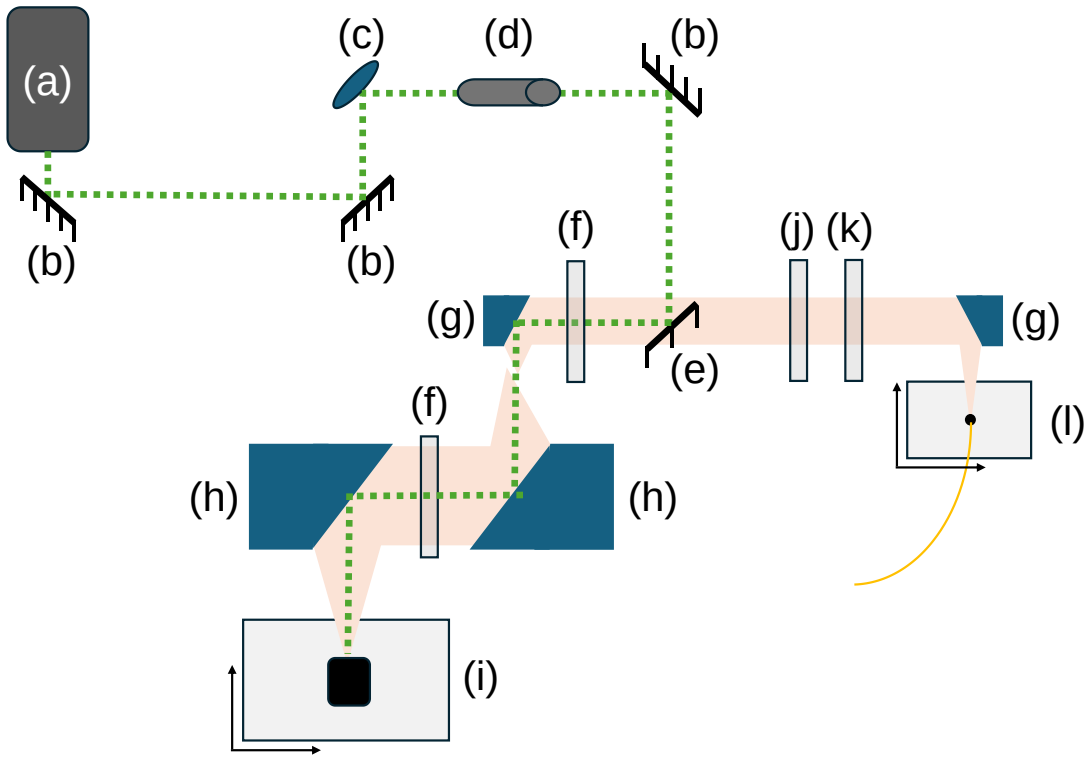

Fig. 4.10: Optical setup used for EL and photoluminescence measurements. a) 1 W, 532 nm excitation laser, b) silver-coated mirrors, c) optical periscope, d) low-power green alignment laser mounted on a flip stage, e) Thorlabs MLP650L partial reflector, f) adjustable apertures, g) 1″ off-axis parabolic mirrors, h) 3″ off-axis parabolic mirrors, i) motorised sample stage with x-y-z-θ control (compatible with temperature-regulated mounts), j) motorised rotation stage with linear polariser (flip-mounted), k) second motorised polariser on flip mount and l) collection fibre on manual x-y-z stage. Emission is focussed by the final parabolic mirror (g) into the fibre (l), which delivers light to an Acton SpectraPro 2300i spectrometer coupled to an Andor iDus 492A InGaAs array detector.

The beamline used 3″ off-axis parabolic collection optics, a Thorlabs DMLP650L partial mirror in the upper line and coupled to an Acton 2300i + Andor iDus 492A detection chain; the same optical geometry was used for EL.

For low-temperature measurements at 77 K, a cryostat-compatible “cold stick” was used. In this configuration, the sample was mounted at the base of the stick and both excitation and emission light were coupled through the same optical fibre. The cold stick was immersed in liquid nitrogen during measurements, enabling temperature-dependent PL analysis.

This PL setup provided a consistent and highly reproducible method for evaluating the optical properties of DBR LED and SPLED devices fabricated in this study, enabling direct comparison with Electroluminescence (EL) results obtained using the same optical geometry.

4. 3.2. Time-Resolved Photoluminescence (TRPL) Measurement

Time-resolved photoluminescence (TRPL) spectroscopy is a time-domain optical technique used to investigate carrier recombination dynamics in semiconductor materials and

nanostructures. Unlike steady-state photoluminescence, TRPL directly probes the temporal evolution of photoluminescence following pulsed optical excitation, enabling the extraction of characteristic carrier lifetimes associated with different recombination pathways.

In TRPL measurements, the sample is excited using short optical pulses with photon energy above the bandgap, generating a transient population of electron-hole pairs. Following excitation, the photoluminescence intensity decays as carriers recombine through radiative and non-radiative channels. By recording the arrival time of emitted photons relative to the excitation pulse, photoluminescence decay transients can be reconstructed with nanosecond-scale temporal resolution. This temporal resolution enables reliable measurement of carrier lifetimes in the nanosecond regime, with decay curves accumulated over typical acquisition times sufficient to achieve high signal-to-noise ratios.

In this work, TRPL measurements were performed at room temperature under ambient conditions using a 405 nm pulsed laser for above-bandgap excitation. The excitation power was kept constant throughout the measurement series to maintain a consistent excitation density and avoid carrier-density-dependent artefacts. The emitted photoluminescence was spectrally selected using the monochromator to isolate the quantum ring emission band, thereby minimising contributions from the GaAs substrate and higher-energy emission channels.

Time-resolved detection was achieved using a time-correlated single-photon counting (TCSPC) scheme. The excitation laser signal served as the start trigger, while emitted photons were detected using a photomultiplier-based single-photon counting detector and registered as stop events. Photon arrival times were recorded using a Time Tagger Ultra (Swabian Instruments), and decay transients were constructed as photon arrival time histograms.

The measured decay curves exhibited bi-exponential decay kinetics and were analysed using weighted least-squares fitting of the form

$$I(t) = A_1 exp\left(\frac{-t}{\tau_1}\right) + A_2 exp\left(\frac{-t}{\tau_2}\right), \quad (4.2)$$

where *I(t)* is the time-dependent photoluminescence intensity, *t* denotes time, and τ_1 and τ_2 are the characteristic decay lifetimes expressed in the same temporal units as *t*. Such behaviour is characteristic of type-II GaSb/GaAs quantum ring systems, where spatial separation of electrons and holes gives rise to multiple recombination channels with distinct characteristic lifetimes.

4. 3.3. Electroluminescence (EL) Measurement

Electroluminescence (EL) is the process by which a material emits light in response to an applied electric field or current injection. In semiconductor devices such as LEDs, EL arises from the radiative recombination of electrons and holes in the active region when the device is forward biased. The emitted spectrum reflects the electronic band structure, recombination mechanisms and efficiency of the device, making EL spectroscopy a key tool for evaluating optoelectronic performance [344]. In this work, EL measurements were performed to

characterise the emission wavelength, spectral linewidth and intensity of DBR LED and SPLED devices under controlled operating conditions.

Electroluminescence (EL) characterisation was performed using the same customised optical setup as PL designed for efficient spectral collection and alignment control, as illustrated in Fig. 4.10. Devices were packaged on TO-46 headers using either conductive silver epoxy or electrodag and mounted on a thermoelectrically cooled stage. This stage enabled precise temperature regulation between 15 °C and 85 °C, ensuring consistent device behaviour during measurement.

The devices were electrically biased using a Keithley 2400 Source Measure Unit (SMU), which simultaneously recorded current and voltage during operation. Emission spectra were collected via an optical beamline aligned to focus the emitted light into a spectrometer coupled with an InGaAs linear-array detector (Andor iDus 492A). The detector was connected to the collection path via a multimode optical fibre.

Precise optical alignment was achieved by positioning the device at the focal point of a 3″ off-axis parabolic mirror, using a motorised stage with x-y-z translational control and rotational adjustment in the azimuthal direction. A grid-based spatial search was employed to optimise alignment, whereby the stage was scanned around the focal volume and the position yielding the maximum detector response was selected as the optimal alignment.

The spectra are presented as measured (counts versus wavelength); no full wavelength-dependent correction for the combined spectrometer throughput and detector responsivity was applied.

This setup, which shares its beamline geometry with the PL system described previously, ensured accurate and repeatable EL measurements across devices. It was particularly important for evaluating emission efficiency and spectral characteristics of both DBR LED and SPLED structures fabricated in this study.

4. 3.4. Spectrophotometry (Transmission)

Optical transmittance and reflectance measurements were performed to evaluate the spectral characteristics of the epitaxially grown DBR LED and SPLED structures. These measurements provide a rapid, non-destructive means of assessing the accuracy of layer thicknesses and refractive index profiles by comparing the measured spectra with simulated designs [345]. The position and width of the DBR stopband can be used to verify growth precision where a shift of the central wavelength to shorter values indicates layers that are too thin, while a shift to longer wavelengths suggests layers that are too thick.

Measurements were carried out using an Agilent Cary 5000 spectrophotometer. This instrument employs a broadband halogen light source directed through a monochromator and split into two beams before entering the sample compartment. In double-beam transmission mode, one beam passes through the sample while the other serves as a reference. The ratio of these signals compensates for temporal fluctuations in the lamp intensity, improving measurement stability. Calibration is performed by leaving the sample

beam unobstructed for the 100% transmission reference and by blocking the beam with an opaque plate to set the 0% baseline. Two acquisition modes were used: fast scans = 0.5 s per point, slow scans = 10 s per point. For diffuse-reflectance measurements with the integrating sphere, a PTFE reference defined nominal 100 % reflectance; as the PTFE albedo in the SWIR is slightly <100 %, occasional apparent values >100 % were normalised in post-processing

Reflectance measurements were performed using a diffuse reflectance accessory (DRA) with an integrating sphere ash shown in Fig. 4.11.

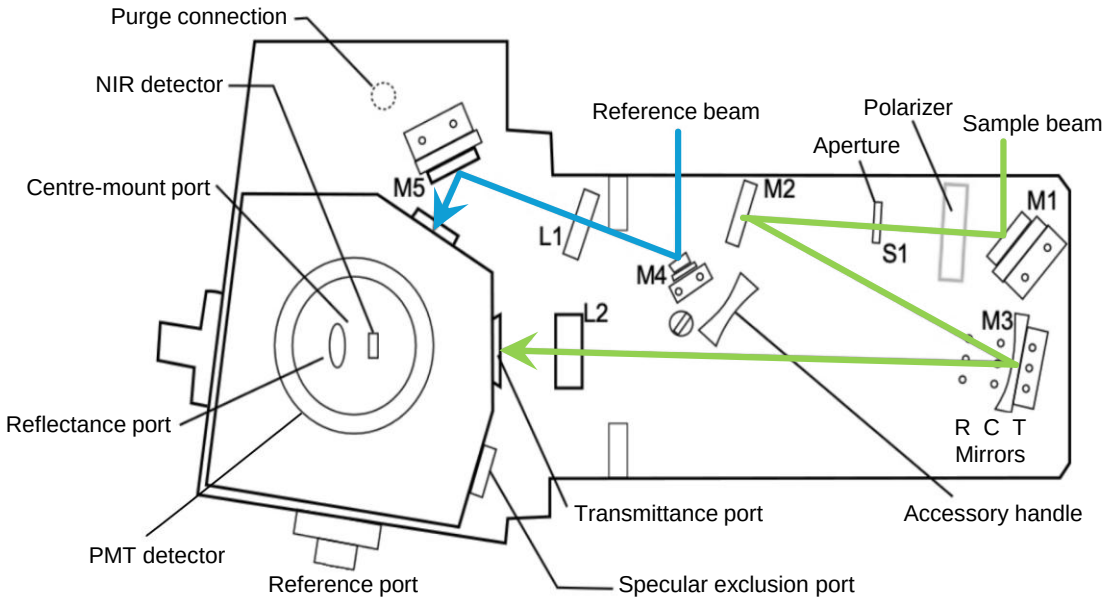

Fig. 4.11: Internal optical layout of the Cary 5000 spectrophotometer with an integrating sphere accessory [8].

This setup collects both specular and diffuse components of reflected light, enabling rapid identification of the DBR stopband. However, because the measurement is not purely normal-incidence, the recorded spectrum may appear broadened. To ensure consistency, reflectance values slightly above 100%, arising from the sub-unity albedo of PTFE in the SWIR, were normalised during post-processing.

For uniformity mapping, the same transmittance measurement configuration was used, with the sample moved in discrete steps across the aperture to measure spectra at multiple positions. This approach provided a spatial profile of the stopband position and width across the wafer, allowing identification of any non-uniformities in the growth of DBR LED and SPLED structures prior to device fabrication.

4. 3.5. Variable Angle Spectroscopic Ellipsometry

Variable-angle spectroscopic ellipsometry (VASE) is a non-contact optical technique for determining thin-film thicknesses and their optical constants, namely the refractive index (n) and extinction coefficient (k). The method relies on measuring the change in polarisation state of light upon reflection from the sample surface. When polarised light interacts with a

multilayer film, the reflected beam experiences a change in both amplitude ratio (Ψ) and phase difference (Δ) between the p- and s-polarised components. These changes are characteristic of the optical properties and thicknesses of the layers [346], [347].

In this work, a J.A. Woollam M-2000XI spectroscopic ellipsometer was used to characterise dielectric and semiconductor layers in DBR LED and SPLED structures. The system employs a rotating compensator to provide high-precision Ψ and Δ measurements across a broad spectral range. Measurements were taken at multiple angles of incidence (from 45° to 75° with 5° steps) to improve sensitivity and minimise parameter correlation in the fitting process. A schematic representation of the VASE principle is shown in Fig. 4.12.

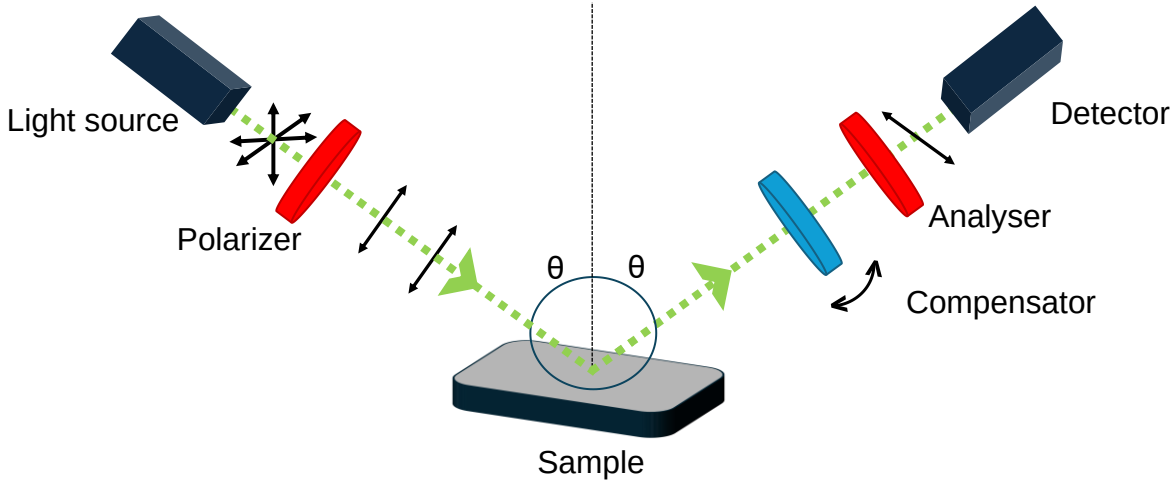

Fig. 4.12: Schematic representation of VASE. Polarised light is directed at the sample at an oblique angle and changes in the amplitude ratio (Ψ) and phase difference (Δ) between p- and s-polarised components after reflection are measured and analysed.

The M-2000XI system was operated over a spectral range covering the visible to near-infrared region, encompassing the emission wavelengths of the devices studied. Before measurement, the instrument was calibrated using a reference wafer to ensure baseline accuracy. Measurements were taken at 45° to 75° in 5° steps, and data were fitted in CompleteEase using a Cauchy (+EMA surface-roughness) model where appropriate; fit quality was reported via MSE. Extracted n, k(λ) and thicknesses were cross-checked against design and corroborated by TEM thickness where available.

Data analysis was carried out using CompleteEase software. The measured Ψ and Δ spectra were fitted to optical models based on known dispersion relations (e.g., Cauchy or Gen-Osc models, depending on material type). For DBR structures, the extracted layer thicknesses and refractive indices were compared with design values to confirm the accuracy of epitaxial growth. This allowed identification of any deviations and ensured consistency with the TEM thickness results.

4. 3.6. Transmission Electron Microscopy (TEM)

Transmission electron microscopy (TEM) is a high-resolution imaging method that enables direct observation of material structure at the atomic scale. In this technique, a highly

focused electron beam is transmitted through an ultra-thin specimen and the transmitted and diffracted electrons are collected to form an image. Because electrons have much shorter wavelengths than visible light, TEM offers sub-nanometre resolution, making it ideal for examining crystalline quality, interface sharpness and defect structures [348]. A simplified schematic of the TEM operating principle is shown in Fig. 4.13.

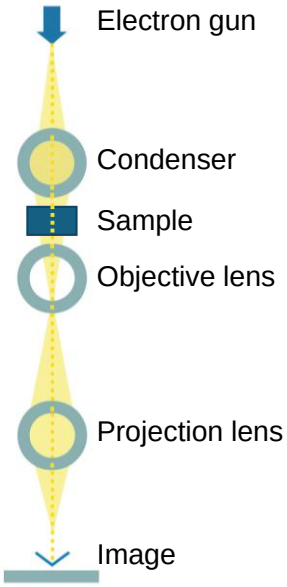

Fig. 4.13: Schematic diagram of a TEM. An electron beam from the electron gun is focused by condenser lenses onto a thin sample. The transmitted and diffracted electrons are collected and further magnified by the objective and projection lenses to produce the final image.

Electrons generated by the electron gun are focused by electromagnetic condenser lenses to form a fine beam, which passes through the sample. Interactions between the beam and the material alter the electron trajectories and the resulting signal is used by the objective lens to form the first magnified image. This image is further enlarged by projection lenses before being recorded by the imaging system.

In this study, TEM was used to examine the epitaxial structures of DBR LEDs and SPLEDs, focusing on verifying DBR periodicity, layer thickness uniformity and the integrity of interfaces. The technique is particularly valuable for identifying abruptness between alternating high and low refractive index layers in DBRs and for assessing quantum emitter regions in SPLEDs.

Sample preparation for TEM requires the creation of electron-transparent lamellae, typically less than 100 nm thick, using methods such as focused ion beam (FIB) milling or mechanical polishing. While TEM provides unparalleled spatial resolution and detailed localised analysis, its field of view is limited to small sample regions and cannot evaluate large-area uniformity.

TEM imaging for this work was performed by Francisco Alvarado-Cesar at Warwick University using a JEOL 2100 transmission electron microscope. These measurements

provided critical confirmation of growth quality and interface sharpness, ensuring that device performance could be correlated with the structural properties of the epitaxial layers.

4.4. Conclusions and Outlook

This chapter has presented a comprehensive account of the experimental and characterisation techniques employed in the design, fabrication and evaluation of GaSb/GaAs quantum-ring LEDs and SPLEDs. The multi-step workflow, encompassing epitaxial growth, lithographic patterning, plasma-based etching, metal deposition, annealing, and diverse characterisation modalities, demonstrates the integrated approach required to realise complex semiconductor nanostructures at telecom wavelengths.

Molecular beam epitaxy provided atomic-scale control over layer composition, thickness and doping profiles, enabling the realisation of high-reflectivity DBR stacks and well-defined quantum-ring active regions. Photolithography and direct laser writing offered complementary patterning capabilities, supporting both high-throughput production and flexible prototype development. Plasma-based etching techniques, particularly inductively coupled plasma with in-situ reflectometry, ensured precise mesa definition and depth control, critical for maintaining optical and electrical performance in nanoscale devices.

Optical characterisation, combining photoluminescence, electroluminescence and spectrophotometric measurements, yielded quantitative data on emission wavelength, spectral linewidth and efficiency across a range of device geometries and operating conditions. These measurements directly informed assessment of device functionality and performance relative to design targets. Transmission electron microscopy and ellipsometry provided complementary structural and optical validation, confirming DBR periodicity, layer thickness accuracy and interface quality.

The techniques described represent current best practice in III-V semiconductor optoelectronics and quantum nanophotonics. Their successful application across multiple device architectures (conventional LEDs, DBT-integrated LEDs and cavity-enhanced SPLEDs) demonstrates both the maturity and versatility of the fabrication and characterisation platforms. The availability of such comprehensive capabilities at Lancaster University, combined with expertise in MBE growth and device physics, enabled the ambitious experimental programme undertaken in this thesis.

Looking forward, emerging techniques, such as in-situ cathodoluminescence during device operation and advanced pump-probe spectroscopy for carrier dynamics, could provide additional mechanistic insight. However, the current toolkit is sufficient to advance understanding of type-II GaSb/GaAs nanostructure optoelectronics and to support the development pathway toward practical quantum-light sources.

Chapter 5 GaSb Quantum Ring Light Emitting Diodes

GaSb quantum-ring (QR) light-emitting diodes (LEDs) are promising light sources in the telecommunications bands, offering compatibility with low-cost and compact optical systems[46], [349], [111]. This chapter focuses exclusively on devices fabricated from a single MBE-grown wafer; full epitaxial and process details are provided.

The epitaxial design of wafer QPH473 follows an established GaSb/GaAs type-II quantum-ring p-i-n LED platform previously developed in our group, and is used here as a fixed baseline to study geometry-dependent device behaviour. The novelty of the work in this chapter lies in demonstrating and documenting the type-II electro-optical signatures of GaSb/GaAs quantum-ring LEDs across multiple device geometries and lateral sizes, using a consistent epitaxial design and processing flow.

The expected telecom-wavelength operation is motivated by the type-II band alignment of GaSb/GaAs quantum rings and is verified experimentally through electroluminescence measurements in Section 5.2.

The epitaxial structure comprises a GaAs/GaSb/GaAs active region enclosed by $Al_{0.6}Ga_{0.4}As$ cladding layers and graded AlGaAs spacers. Be-doped and Te-doped layers provide the p-type and n-type contacts, respectively.

All devices were processed following a standard flow comprising mesa etching, Si_3N_4 passivation and multi-step metallisation.

Although the fabrication process steps were identical for both finger-shaped and ring-shaped devices, they were processed in separate fabrication runs and characterised at different times. This ensures independent validation of the process flow, but any potential environmental or equipment-related variations between runs should be considered when comparing results.

The primary aims of this work are:

1. To assess the influence of device lateral dimensions on current-density uniformity, thermal management and spectral stability.
2. To evaluate the transport and EL characteristics of finger-shaped and ring-shaped device layouts.

Section 5.1 describes the design and fabrication. Section 5.2 presents the electrical and optical characterisation results, including I-V behaviour and EL spectra under varying drive conditions.

5.1. Device Design and Fabrication

All devices were fabricated from the MBE-grown QPH473 wafer, which incorporates three GaSb QR layers in a GaAs/GaSb/GaAs active region bounded by $Al_{0.6}Ga_{0.4}As$ cladding and graded $Al_xGa_{(1-x)}As$ spacers. Be-doped p-type and Te-doped n-type layers provide the electrical contacts.

5. 1.1. Device geometries

Two distinct device size categories were fabricated to investigate geometry-dependent effects:

- **Large-area devices:** Lateral dimensions of 1 mm × 1 mm and 0.5 mm × 0.65 mm, fabricated using finger-shaped layout.
- **Small-area devices:** Diameters ≤ 200 μm (nominally 200 μm, 150 μm and 70 μm), realised in a ring-shaped layout. These smaller devices were designed to enable evaluation of area scaling, current crowding, series/differential resistance and spectral stability under high current densities.

The detailed fabrication process of the ring-shaped geometry is presented in Chapter 7, whereas the present section focuses exclusively on the finger-shaped layout. For the ring-shaped devices, only EL and IV measurement results are reported.

The devices were fabricated using photolithography masks to accommodate multiple geometries on a single die. Large devices employed a *finger-shaped* top-contact geometry, in which the p-contact metallisation is patterned into multiple narrow "fingers" extending across the device surface. This design improves current distribution across the active region, thereby promoting more uniform carrier injection. It also assists with thermal management by reducing localised current crowding (Fig. 5.1(a)) [350]. The photomask comprises mesa-etch, passivation-opening and bond-pad layers and implements finger-shaped top-contact geometries for the large-area devices (D1-D2) (Fig. 5.1(b)). In addition, ring-shaped devices were incorporated into the mask layout. In this geometry, the p-contact forms a continuous annular ring surrounding a central aperture above the active region. This design confines current injection to an annular region, which can reduce current crowding effects in small devices and facilitate uniform carrier distribution at high current densities. The central aperture also enables direct optical access to the emission region, which is advantageous for high-resolution optical characterisation [46], [137].

The purpose of including multiple mesa sizes was to establish a baseline across geometries and to check whether down-scaling introduced any obvious issues under like-for-like conditions. Large, medium and small devices were patterned on the same wafer to enable direct comparisons where possible. Given that only one device of each size was, we do not attempt to identify an 'optimum' geometry or to draw scaling laws; the comparisons are descriptive and intended to document operating ranges.

The complete photomask layout incorporates the lithographic patterns required for multiple processing steps. Each colour corresponds to a different mask layer:

- Yellow (top left quadrant): Mesa definition mask for isolating devices of various lateral sizes. Larger mesas are located in the upper rows, with progressively smaller geometries arranged below.
- Green (top right quadrant): Dielectric opening mask for etching contact windows through the Si_3N_4 passivation layer.

(a) 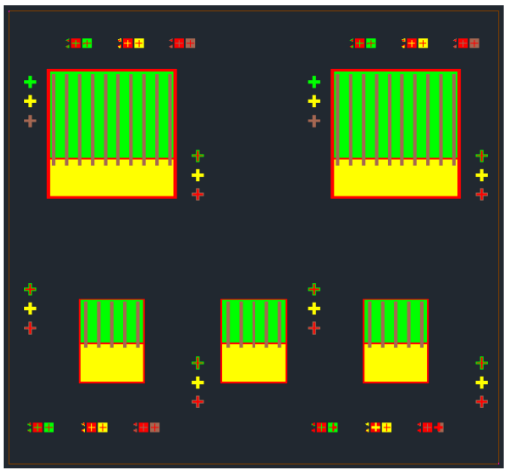 (b) 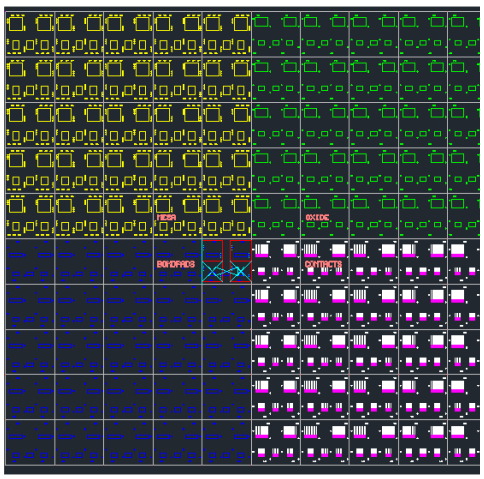

Fig. 5.1: Photomask layout for GaSb QR LED devices of varying lateral dimensions. Large devices (1 mm × 1 mm) are at the top, intermediate devices (0.5 mm × 0.65 mm) at the bottom. (b) Multi-layer photomask layout showing the lithography masks for mesa etching, passivation openings and bond pad contact patterns, including finger-shaped top contacts.

- Blue (bottom left quadrant): Bond pad layer, providing large-area metal pads for probing and wire bonding.
- White and magenta (bottom right quadrant): Metallisation masks for defining p-type and n-type contact pads, along with interconnect features. The arrangement allows fabrication of large- and medium-area LEDs on the same wafer, enabling direct comparison of geometry-dependent performance.

Table 5.1: Epitaxial layer structure of GaSb QR LED wafers (QPH473). Both structures are identical except for the number of GaSb QR layers in the active region.

Layer	**Material**	**Al content (*x*)**	**Thickness**	**Doping**	**Dopant**
Top contact	GaAs	-	100 nm	p 5×10^{19} cm^{-3}	Be
p-region	Al*x*Ga*(1-x)*As	0.6	1000 nm	p 2×10^{18} cm^{-3}	Be
Spacer	Al*x*Ga*(1-x)*As	0.6→0.3	275 nm	-	-
Active region (3 QR layers)	GaAs		50 nm		
	GaSb QR				
	GaAs			-	-
Spacer	Al*x*Ga*(1-x)*As	0.3→0.6	275 nm	-	-
n-region	Al*x*Ga*(1-x)*As	0.6	1000 nm	n 2×10^{18} cm^{-3}	Te
Substrate	GaAs	-	-	n 1-5×10^{18} cm^{-3}	Si

The epitaxial structure, summarised in table 5.1, was designed to optimise carrier injection, optical confinement and radiative recombination in the QR active region [36], [232]. The heavily Be-doped GaAs top contact ensures low-resistance ohmic connection to the p-type region [351], [352]. The p-type $Al_{0.6}Ga_{0.4}As$ layer provides hole injection and contributes to vertical optical confinement due to its higher bandgap [353], [354]. Two composition-graded $Al_xGa_{(1-x)}As$ spacers flank the active region: on the p side, the Al content decreases from $Al_{0.6}$ to $Al_{0.3}$ toward the active region, whereas on the n side it increases from $Al_{0.3}$ to $Al_{0.6}$ away from it. This monotonic band-edge grading smooths the heterointerfaces and funnels carriers into the active region, suppressing back-diffusion and reducing interfacial scattering [354]. The result is more uniform injection and improved thermal robustness.

The active region consists of GaAs/GaSb/GaAs layers, where the GaSb layer contains 3 quantum ring layers responsible for the device's electroluminescence [46], [58]. Owing to the type-II GaSb/GaAs band alignment, holes are confined in the GaSb-rich quantum-ring states while electrons reside predominantly in GaAs, so the radiative transition is spatially indirect and its energy is set by the band offsets together with confinement and excitonic corrections. A qualitative prediction of telecom-band emission follows from literature band parameters and band-offset models (Chapter 2) and is verified experimentally by the electroluminescence spectra presented in Section 5.2. A second graded spacer ($Al_{0.3}\rightarrow Al_{0.6}$) provides similar strain management and optical confinement on the n-side [355]. The n-type $Al_{0.6}Ga_{0.4}As$ layer, doped with Te, facilitates electron injection, while the Si-doped GaAs substrate provides mechanical support and serves as the growth platform for the epitaxial layers [356], [357].

5. 1.2. Fabrication process

The QPH473 wafers were grown by molecular beam epitaxy (MBE) on n-type GaAs substrates, with layer structures designed for emission in the 1.3-1.55 μm telecommunications band (Fig. 5.2).

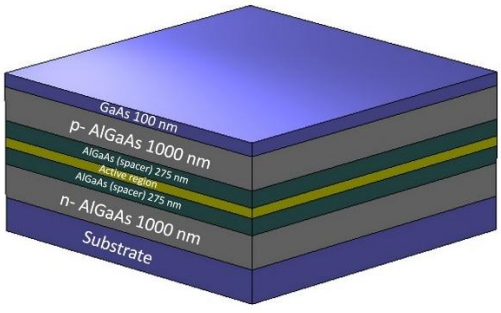

Fig 5.2: Schematic representation of the as-grown GaSb QR-LED wafer structure after MBE growth. The design comprises p- and n-doped $Al_{0.6}Ga_{0.4}As$ cladding layers, $Al_xGa_{(1-x)}As$ spacers, a GaAs/GaSb/GaAs active region and a GaAs cap layer.

Following growth, the wafers were processed into LED devices using a four-mask, top-down photolithography sequence. This flow, comprised mesa definition, dielectric passivation with contact window opening, bond pad formation and ohmic contact metallisation.

(1) Mesa definition: Mask layer 1 (yellow)

Finger-shaped devices with lateral dimensions of 1 mm × 1 mm and 0.5 mm × 0.65 mm, as well as ring-shaped devices with nominal diameters of 200 µm, 150 µm and 70 µm, were patterned in S1813 positive photoresist. The photoresist was spin-coated at 4000 revolutions per minute (rpm) to achieve a nominal film thickness of near 1.3 µm, followed by a soft-bake at 118 °C for 120 s and a 3 min cool-down to room temperature. UV exposure was carried out in soft-contact mode for 2.5 s, providing high resolution and accurate alignment, using a contact mask aligner. Development was performed in MF-CD-26 developer (2.4% TMAH) for 60 s with gentle agitation, followed by a 60 s rinse in deionised (DI) water and drying under a nitrogen gun

Prior to etching, the target etch depth was determined using an in-house MATLAB-based ICP etch simulation tool (*SimEtch*) (Fig. 5.3.). This software models the in-situ 670-nm reflectance signal from the Horiba® monitoring system integrated in the ICP tool, based on the known epitaxial layer sequence. By simulating the reflectance versus etch depth, the stopping point could be precisely identified to ensure full device isolation while avoiding over-etch into lower cladding layers.

Mesa etching was then performed in an inductively coupled plasma (ICP) reactor using Cl_2/Ar chemistry. Chlorine radicals reacted with GaSb and GaAs to form volatile species, which were evacuated from the chamber. Co-flowed Ar ions enhanced sidewall quality by physically sputtering residual etch products. The process yielded smooth mesa floors and near-vertical sidewalls suitable for subsequent dielectric passivation.

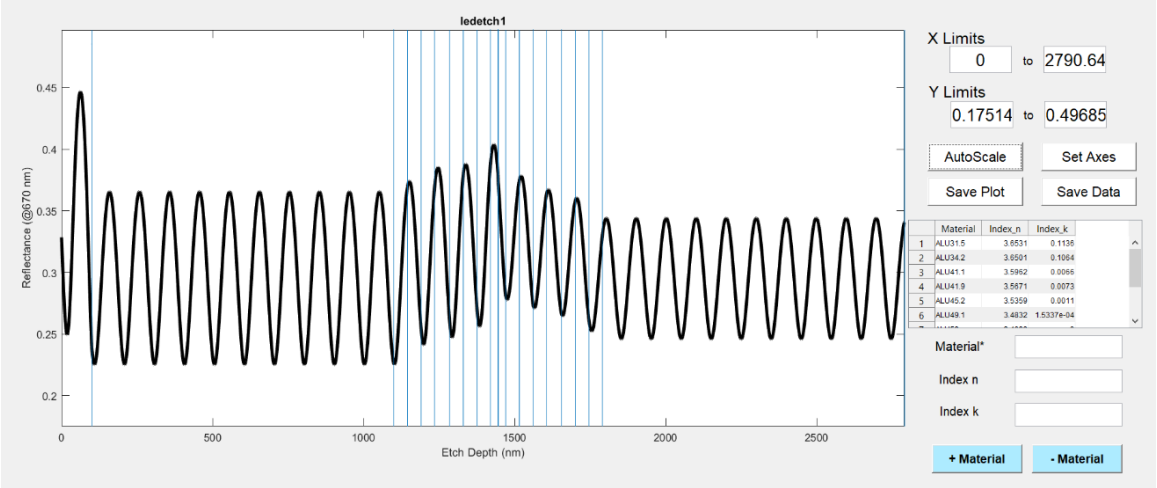

Fig. 5.3: SimEtch prediction of the in-situ 670-nm reflectance during ICP mesa etch of the QR-LED stack. The black curve shows calculated reflectance versus etch depth from the top surface (nm) using a transfer-matrix model and the layer n,k inputs listed at right.

The resulting mesa structures, including finger shaped layouts, are illustrated in Fig.5.4, which shows the schematic device cross-section after etching and representative optical microscope images of fabricated mesas.

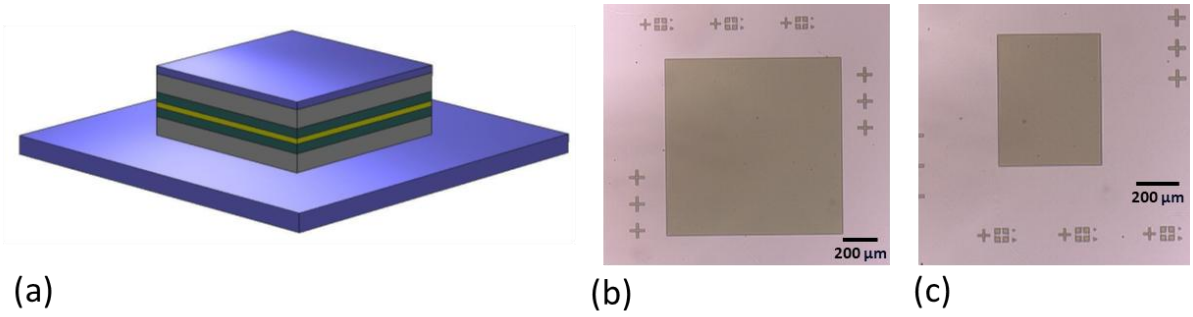

Fig 5.4: (a) Schematic of the device cross-section after mesa etching, showing isolation of the active region from the surrounding material. Optical microscope images of (b) 1 mm × 1 mm and (c) 0.5 mm × 0.65 mm (right) mesas after ICP etching.

(2) Dielectric passivation and window opening- Mask layer 2 (green)

Following mesa formation, both finger-shaped and ring-shaped devices were passivated with a silicon nitride (Si_3N_4) dielectric layer to provide electrical isolation between the top p-contact metallisation and the mesa sidewalls. A 150-nm-thick Si_3N_4 film was deposited by plasma-enhanced chemical vapour deposition (PECVD) using an Oxford Instruments PlasmaPro NGP80 system.

The contact windows were then defined using a second photolithography step (Fig. 5.5). S1813 positive resist was spin-coated at 4000 rpm (near 1.3 µm thickness), soft-baked at 118 °C for 120 s and exposed for 2.5 s in soft - contact mode with an optimised dose for this resist thickness. Development was performed in MF-319 for 60 s with gentle agitation, followed by a DI rinse (60 s) and nitrogen dry.

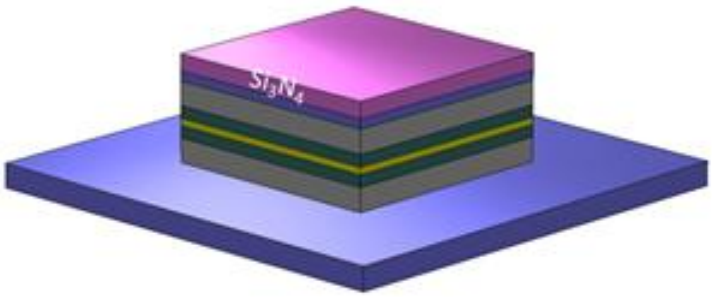

Fig 5.5: Schematic representation of the device after PECVD deposition of the Si_3N_4 passivation layer, covering the mesa sidewalls and top surface prior to window opening.

The exposed Si_3N_4 was removed using reactive ion etching (RIE) in an Oxford Instruments PlasmaPro 80 RIE tool with CHF_3/O_2 chemistry. This process opened precise windows in the dielectric above the intended contact areas/emission surface, while maintaining full passivation of the mesa sidewalls (Fig. 5.6). The CHF_3 process provides good selectivity of

Si_3N_4 over GaAs, ensuring clean exposure of the semiconductor surface. Following etching, the resist was stripped in acetone and IPA and any residues were removed with an oxygen plasma ash. These windows allow electrical contact to the p-side of the device while maintaining sidewall passivation.

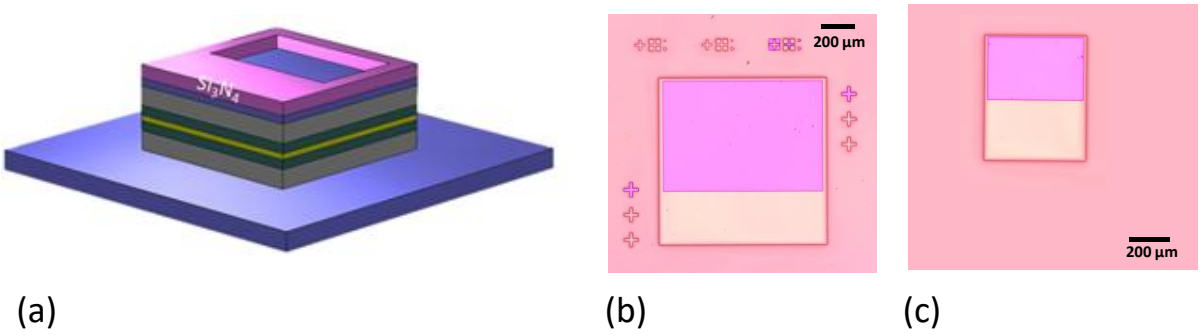

Fig 5.6: (a) Schematic representation of the device after RIE etching of the Si_3N_4 passivation layer to open the top contact window. (b) Optical microscope image of a 1 mm × 1 mm device after window etching. (c) Optical microscope image of a 0.5 mm × 0.65 mm device after window etching.

(3) Bond pad metallisation - Mask layer 3 (blue)

Following window etching, a third photolithography step was carried out to define the bond pad regions for electrical connection to the p-side of the devices (Fig. 5.7). The bond pad geometry was designed to ensure low-resistance ohmic contact, mechanical robustness during subsequent wire-bonding and compatibility with both on-wafer probing and packaged device testing. For larger finger-shaped devices, bond pads were positioned to minimise series resistance and to align with the main current injection area, while for smaller ring-shaped devices, pad placement and connection lines were optimised to maintain symmetry and minimise parasitic resistance along the annular top contact.

A bilayer resist approach was adopted, as it is well-documented that the undercut profile produced in such stacks facilitates high-fidelity lift-off by preventing metal bridging and preserving sharp feature edges. A bilayer resist stack was used to facilitate a clean lift-off profile: LOR-3A (MicroChem) was spin-coated at 500 rpm for 5 s (spread) and 3000 rpm for 45 s (thickness about 300 nm), followed by a hotplate bake at 170 °C for 5 min. After baking, S1813 was spin-coated on top at 500 rpm for 5 s (spread) and 4000 rpm for 45 s (thickness ~1.3 µm), then soft-baked at 118 °C for 2 min.

UV exposure was performed in contact mode using a mask aligner, with an exposure time of 2.5 s. The sample was then developed in MF-319 developer for 60 s with gentle agitation, rinsed in DI water and dried under N_2. The differential dissolution rates of LOR-3A and S1813 in the developer generated a controlled lateral undercut in the LOR-3A layer,

improving the reliability of the lift-off process by reducing the risk of residual metal 'stringers' at feature edges.

Metallisation of the bond pads was performed by thermal evaporation (Edwards Auto 306 system) of a Ti/Au stack (10 nm / 200 nm) at a base pressure < 1×10^{-6} mbar. Titanium served as an adhesion layer to the underlying GaAs surface, while gold provided low resistivity and chemical stability. Lift-off was achieved by immersing the sample in Microposit Remover 1165 at 75 °C for 10 min, followed by sequential acetone and IPA rinses to ensure complete removal of resist residues.

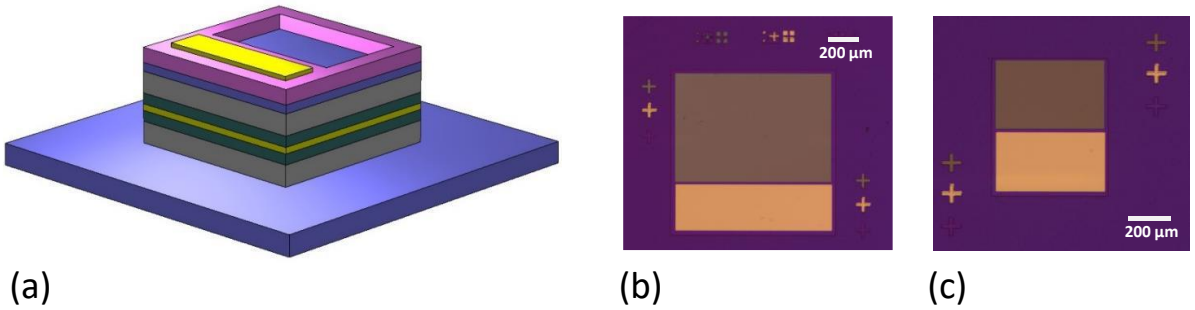

Fig. 5.7: (a) Schematic representation of the device after metallisation of Ti/Au bond pads (10 nm / 200 nm) defined using bilayer LOR-3A/S1813 photolithography. (b) Optical microscope image of a 1 mm × 1 mm device after bond pad deposition and lift-off. (c) Optical microscope image of a 0.5 mm × 0.65 mm device after bond pad deposition and lift-off.

(4) Contact metallisation- Mask layer 4 (magenta/white)

The final top-contact metallisation step was used to define the p-contact geometries for both finger-shaped devices.

A bilayer resist photolithography process, identical to that used for bond pad definition, was implemented. LOR-3A (MicroChem) was spin-coated at 500 rpm for 5 s (spread) and 3000 rpm for 45 s, yielding a nominal thickness of ~300 nm. This layer was baked at 170 °C for 5 min to ensure full solvent removal and mechanical stability. Without cooling, improving adhesion between layers, S1813 was spin-coated at 500 rpm for 5 s (spread) and 4000 rpm for 45 s, achieving a thickness of about 1.3 µm, followed by a soft-bake at 115 °C for 2 min.

UV exposure was conducted in contact mode for 2.5 s using the fourth mask layer, ensuring accurate alignment of the finger structures with the underlying active region. Post-exposure development in MF-319 for 60 s, followed by DI water rinse and N_2 drying, revealed the bilayer pattern. The undercut profile in the LOR-3A ensured clean lift-off of the finger metallisation by eliminating edge bridging effects.

Metallisation was carried out by thermal evaporation (Edwards Auto 306) of an Au/Ni/Au stack (15/30/100 nm) at a base pressure < 1×10^{-6} mbar. The initial Au layer provides a low-resistivity interface; the Ni interlayer serves as a diffusion barrier and enhances adhesion; the top Au layer improves chemical stability and bondability for subsequent wire-bonding.

Lift-off was completed in Microposit Remover 1165 at 75 °C for 10 min, followed by acetone and IPA rinses to remove residual resist (Fig. 5.8).

For large-area devices (1 mm × 1 mm and 0.5 mm × 0.65 mm), the p-contact metallisation was patterned into multiple narrow "fingers" connected to the main bond pad. The finger geometry was optimised to balance current spreading and optical shading. The pitch p and finger width w determined the metal fill factor $f_{metal} = w/p$ and thus the optical aperture $\eta_{ap} = 1 - f_{metal}$ [350]. This design ensured low-resistance p-side injection, uniform carrier distribution across the active region and stable mechanical and chemical performance suitable for device packaging. The fabricated structure, an array of narrow, parallel Au/Ni/Au finger electrodes connected to the main bond pad, also promoted efficient heat dissipation, which is critical for maintaining device performance and reliability under high-power operation [358].

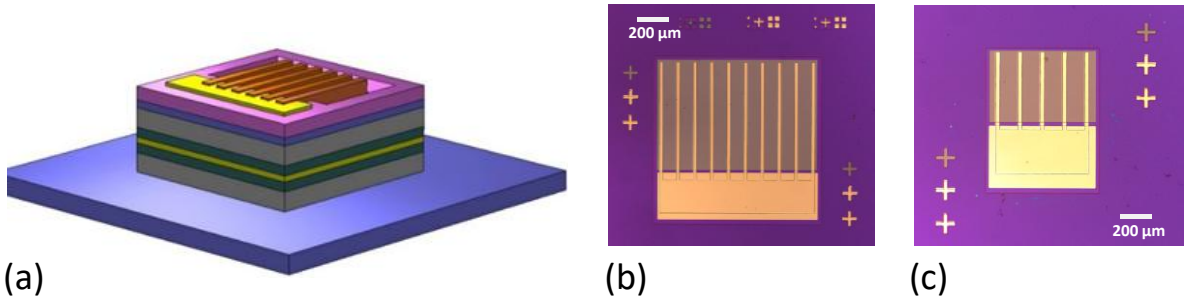

Fig. 5.8: (a) Schematic representation of the device after metallisation of the finger-shaped p-contact using an Au/Ni/Au stack (15 nm / 30 nm / 100 nm) defined by bilayer LOR-3A/S1813 photolithography. (b) Optical microscope image of a 1 mm × 1 mm device after finger contact deposition and lift-off. (c) Optical microscope image of a 0.5 mm × 0.65 mm device after finger contact deposition and lift-off.

(5) Backside metallisation

Following completion of the p-side metallisation, the wafer pieces were prepared for deposition of the n-type ohmic contact on the backside of the GaAs substrate. The backside surface was first cleaned to remove any native oxides and residual contaminants, ensuring uncontaminated interface for metallisation.

The n-type contact stack was deposited by thermal evaporation (Edwards Auto 306) of AuGe/Ni/Au with thicknesses of 80 nm/ 35 nm/ 80 nm, respectively (Fig. 5.9). The AuGe layer was chosen due to its well-established ability to form low-resistance ohmic contacts to n-type GaAs through the formation of a AuGe eutectic alloy. The intermediate nickel layer served as both a diffusion barrier, preventing excessive intermixing of the AuGe with the top Au layer and as an adhesion promoter. The top gold layer provided chemical stability and an inert surface suitable for subsequent device handling.

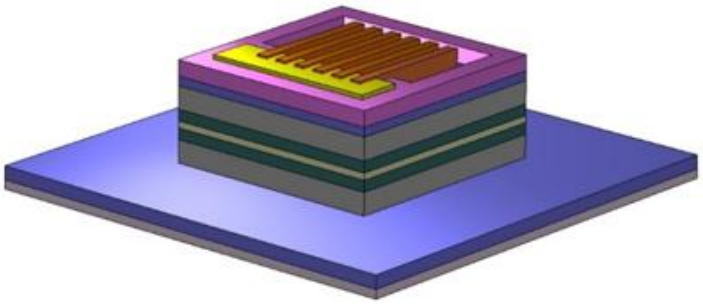

Fig. 5.9: Schematic representation of the device after deposition of the backside n-type ohmic contact (AuGe/Ni/Au, 80 nm / 35 nm / 80 nm) onto the GaAs substrate. This contact provides a low-resistance electrical pathway to the n-side of the device.

(6) Annealing of Contacts

Following metallisation, rapid thermal annealing (RTA) was carried out to form low-resistance ohmic contacts. The devices were annealed at 300 °C for 3 min in a nitrogen ambient using a rapid thermal annealer. This thermal process facilitated interdiffusion between the contact metal layers and the semiconductor surface, leading to the formation of a heavily doped interfacial region. Such a microstructure enables efficient carrier tunnelling across the contact-semiconductor interface, thereby yielding stable, low-resistance ohmic contacts to the n-type GaAs substrate.

(7) Device Mounting and Wire Bonding

Fabricated devices were cleaved from the processed wafer using a diamond scribe. Individual dies were mounted onto TO-46 headers with conductive silver epoxy, ensuring both good thermal conduction and low-resistance electrical connection between the device backside and the package header. After curing, p-side bond pads were connected to the package leads via gold ball wire bonding. This packaging configuration provided mechanical stability, efficient heat dissipation and reliable electrical access for subsequent optical and electrical characterisation.

5.2. Device Characterisation and Optical Results

This section presents the electrical and optical characterisation of GaSb QR-LEDs with two different p-contact geometries. Current-voltage (I-V) and electroluminescence (EL) measurements were first carried out on finger-shaped, large-area devices (D1-D2). For comparison, EL spectra as a function of injection current and temperature were subsequently obtained from ring-shaped, small-area devices (D3-D5).

The ring-shaped devices were fabricated in a separate processing run from the larger finger-contact devices. Differences in fabrication time, storage period and measurement setup mean that absolute resistance and optical intensity values are not directly comparable between these two geometries. The analysis here therefore focuses on relative trends within each device size, rather than on cross-geometry comparisons.

By comparing EL results, correlations between the intrinsic optical quality of the quantum ring structure and its electrically-driven performance could be established. This combined approach also allowed evaluation of how device geometry (finger-shaped vs. ring-shaped) influences current spreading, thermal management and spectral stability at varying current densities. The following sections present the results and discussion for each characterisation method in detail.

The optical characterisation of the GaSb QR-LEDs was performed using a configurable bench-top system capable of both continuous-wave EL measurements. The setup was explained in detail in chapter 4.

5. 2.1. Electrical and Optical Performance

EL spectroscopy was employed to investigate the emission characteristics of the QR-LED devices under electrical injection. The objective was to evaluate their optical output behaviour, spectral stability and correlation with electrical transport parameters.

Individual LEDs were mounted on a temperature-controlled stage and wire-bonded to TO-46 header, enabling direct electrical access to the p- and n-contacts. Current injection was supplied by a precision source-measure unit (Keithley 2400) operated in constant-current mode, with a compliance voltage set to prevent device damage.

The emitted light was collected from the top surface of the device using a 50× microscope objective in a normal-incidence configuration. The light was then coupled into a multimode optical fibre connected to a grating spectrometer (Andor Shamrock 303i) equipped with a thermoelectrically cooled InGaAs array detector (Andor iDus). Neutral density filters were inserted when necessary to prevent detector saturation at high injection currents.

Spectral calibration was performed using reference emission lines and the system's wavelength-dependent response was corrected using a calibrated tungsten-halogen lamp. EL spectra were recorded over a range of injection currents to quantify integrated EL intensity, peak-wavelength shifts, linewidth evolution and spectral stability. Electrical characteristics, including I-V and L-I curves, were measured simultaneously to enable direct correlation between optical emission and carrier transport performance.

5. 2.2. Current-Voltage Characteristics of Large Devices (D1, D2)

The current-voltage characteristics of the fabricated QPH 473 LEDs were investigated for two different device geometries: a large-area device (Device D1, $1.0 \times 1.0\ mm^2$) and a smaller-area device (Device D2, $0.65 \times 0.50\ mm^2$), both incorporating finger-shaped p-contact metallisation. Measurements were conducted under continuous-wave (CW) conditions at room temperature (~300 K) using a Keithley 2400 source-measure unit.

- **D1** (1 mm × 1 mm): A=0.01 cm^2 (i.e. J=1.0 A cm^{-2} for 10 mA).
- **D2** (0.5 mm × 0.65 mm): A=0.00325 cm^2 (i.e. J=3.08 A cm^{-2} for 10 mA).

Both devices display clear rectifying behaviour with negligible reverse leakage (≤ 0.3 µA at −5 V), consistent with high-quality p-i-n junctions and minimal parasitic paths. Under forward bias, defining the turn-on as the voltage at I = 100 µA, the turn-on voltages are V_{on}=1.02±0.02 V for both D1 and D2 (Fig. 5.10).

The electrical turn-on voltage extracted from the I-V curve marks the onset of efficient carrier injection through the p-i-n junction, i.e. the bias at which the diode current starts to rise steeply. A common rule-of-thumb is to compare qV_{on} with the photon energy E_{ph} ; however, in real LEDs this correspondence is only qualitative because the measured I-V characteristics include voltage drops from series and contact resistances, as well as any injection barriers, so that not all of the applied bias contributes to the quasi-Fermi-level splitting in the active region.

Above turn-on, electroluminescence becomes observable once the separation of the electron and hole quasi-Fermi levels across the active region is sufficient to sustain radiative recombination and exceeds leakage and non-radiative channels. Consequently, the apparent threshold in the I-V curve indicates where efficient injection is achieved, while the detailed relation between that voltage and the optical emission is modified by resistive losses and leakage paths.

From the quasi-linear region of the forward I-V (I ≥ 5 mA), a weighted fit to $V=V_0+IR_s$ gives an average series resistance of R_s=29.4±0.2 Ω for D1 and 20.95±0.04 Ω for D2. The higher R_s in D1 points to stronger device-internal contributions (current spreading/contact resistance) in that diode. Because the resistances are not similar within uncertainty, the data do not support a dominant external series contribution; any common external component is limited to the 0.1-0.2 Ω range at most in this setup.

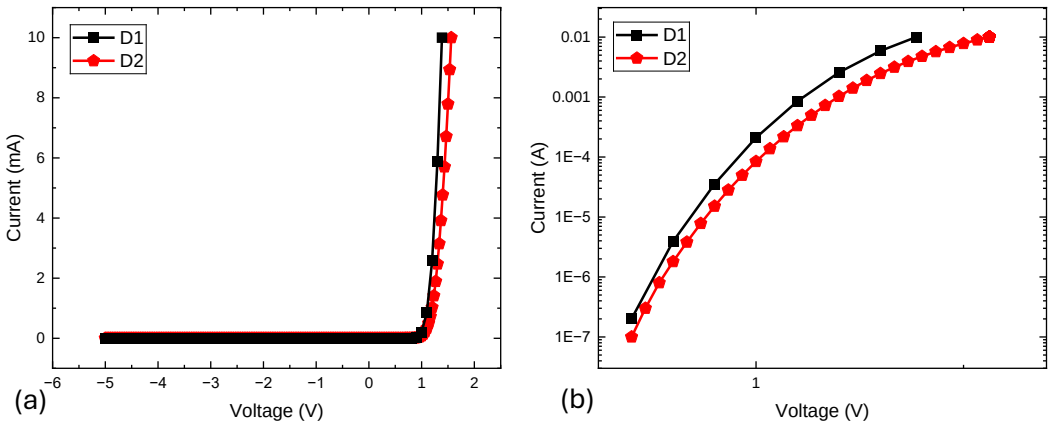

Fig. 5.10: (a) Forward I-V characteristics of devices D1 and D2 measured under continuous-wave bias at room temperature, showing typical diode behaviour with turn-on voltages around 1.1-1.3 V. D1 exhibits a steeper turn-on and higher current due to its larger active area and lower series resistance. (b) The same I-V characteristics plotted on a semi-logarithmic scale, highlighting the exponential current increase in the low-bias regime and confirming diode-like behaviour.

Comparative I-V plots show that, within the plotted forward-bias range (up to 1.4 V for D1), D1 consistently supports higher forward current than D2 at identical voltages. Near 1.4 V the curves become ohmic-like, consistent with increasing series-resistance contributions; for D2 this behaviour continues into high-injection range, whereas D1 is not plotted above 1.4 V in Fig. 5.10. These results confirm the effective performance of the implemented metallisation scheme, comprising finger-patterned p-side contacts Au/Ni/Au and AuGe/Ni/Au n-side contacts, which supports low specific contact resistance (ρ_c) and robust ohmic behaviour at both interfaces.

5. 2.3. Current-Voltage Characteristics of Small Devices (D3, D4, D5)

The forward current-voltage characteristics of the small-area QR LEDs (nominal diameters of 70 μm, 150 μm and 200 μm) were measured at room temperature under CW electrical injection. Measurements were performed using a Keithley 2400 SourceMeter connected to a Cascade probe station, with a voltage sweep range of 0-3 V and a step size of 10 mV. The devices are called D3, D4 and D5, corresponding to nominal diameters of 70 μm, 150 μm and 200 μm, respectively.

At higher injection the curves become ohmic-like as series-resistance contributions grow. To quantify this, the series resistance R_s was extracted by a weighted linear fit to $V=V_0+I\,R_s$ over a defined high-injection window. Using the device-appropriate windows (and excluding compliance-limited flat-V points where relevant) we obtain:

- D3 (70 μm): R_s=690±30 Ω
- D4 (150 μm): R_s =450±40 Ω
- D5 (200 μm): R_s =860±60 Ω.

Series resistance was extracted from straight-line fits applied to the high-injection region (2.5-3.8 V), where the dV/dI slope is approximately constant. Within this window the fits yield R^2 > 0.995, indicating numerically stable fits and a consistent Rs estimate. The ordering D4 < D3 < D5 in R_s is consistent with their relative current levels in Fig. 5.11(a). Because only one device per nominal diameter is included here and measurements were acquired in separate runs, no geometry-scaling conclusions are drawn beyond this qualitative consistency. The data simply show that all three devices operate cleanly, reach an ohmic-like regime at high injection and that R_s can vary substantially between nominally similar structures, underscoring sensitivity to process non-uniformities (e.g., contact resistance and wafer-scale non uniformity).

On the semi-log plot (Fig. 5.11b), shown solely to illustrate the measurement dynamic range, the <~2 V region is sparsely sampled; therefore, no low-current analysis or precise turn-on assignment is presented.

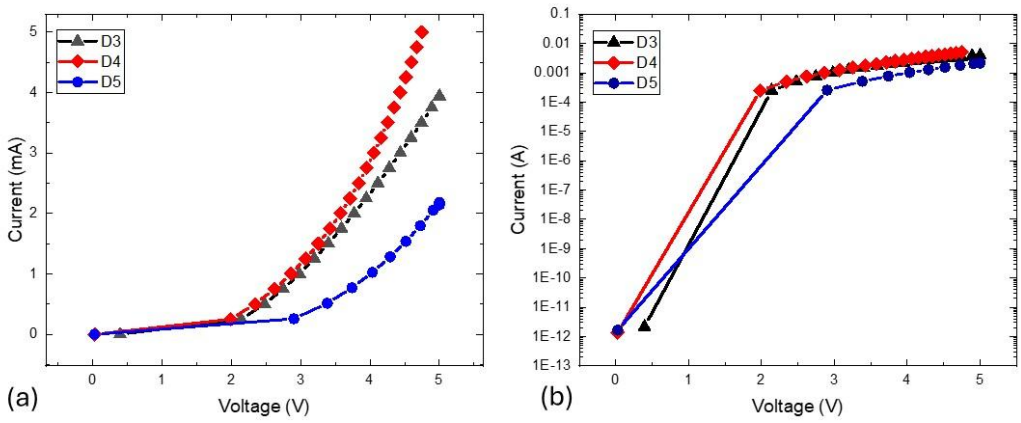

Fig. 5.11: Room temperature forward I- QR LEDs: D3 (70 µm), D4 (150 µm), D5 (200 µm). (a) Linear scale: devices rectify; the <~2 V region is sparsely sampled, so no turn-on is assigned. (b) Semi-log (log(I)-V) plot, room-temperature CW**.** Shown to illustrate measurement dynamic range; the <~2 V region is sparsely sampled, so no low-current analysis or precise turn-on is assigned.

5. 2.4. Electroluminescence Spectra for Large Devices (D1, D2)

Room-temperature CW EL spectra were measured for both large-area (Device D1, 1.0 × 1.0 mm²) and small-area (Device D2, 0.50 × 0.65 mm²) QR light-emitting diodes. Measurements were performed using the optical bench described in Section 4.3.1 with devices operated in constant-current mode. At each bias point, a steady-state spectrum was acquired with identical spectrometer settings to ensure comparability. Injection currents ranged from 10 mA to 100 mA for D1 and from 1 mA to 100 mA for D2, enabling the analysis of both low- and high-current regimes.

The recorded EL spectra represent the product of the true device emission and the wavelength-dependent response of the measurement chain (collection optics, grating efficiency and InGaAs detector responsivity). Since no full system-response correction was applied, detailed comments on spectral asymmetry are treated as qualitative. Peak wavelength and relative shifts with current are expected to be less sensitive to this instrumental response than the absolute lineshape.

Device D1 - Large area (1.0 × 1.0 mm²)

The EL spectrum is dominated by a broad emission peak centred at 1238.6 nm at 10 mA, blue-shifting to 1228.2 nm at 100 mA characteristic of radiative recombination across the type-II GaAs/GaSb QR heterointerface (Fig. 5.12(a)) [105], [110]. The emission intensity increases monotonically with current and indicating that recombination is confined to the QR active region.

The peak wavelength blue-shifts systematically with drive current, reaching 1228.2 nm (≈1.010 eV) at 100 mA, corresponding to an energy increase of approximately 8.5 meV, i.e., ≈0.094 meV/mA over 10-100 mA (Fig. 5.12(b),(c)). This behaviour is consistent with carrier-induced screening of the built-in field and state filling in type-II GaAs/GaSb quantum

rings; from these spectra alone, any contribution from inhomogeneous broadening cannot be isolated.

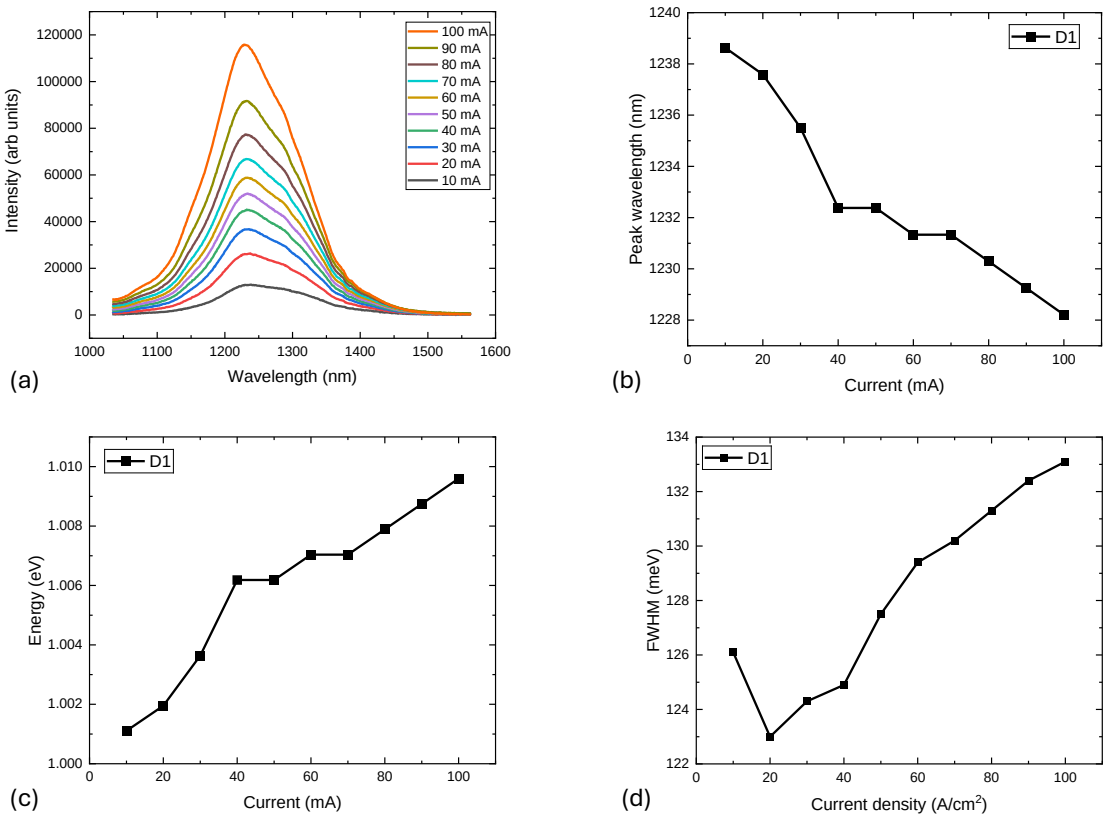

Fig 5.12: Room-temperature CW EL characteristics of Device D1 (1.0 × 1.0 mm² active area). a) EL spectra for injection currents from 10 mA to 100 mA. (b) Peak wavelength as a function of injection current. (c) Corresponding photon energy versus current, exhibiting a monotonic increase consistent with carrier-induced state-filling and partial screening of the built-in electric field. (d) The FWHM as a function of current density, showing a modest broadening from 122 meV to 133 meV across the tested bias range.

Within the measured range, the EL spectra are dominated by a single broad band; however, a weak asymmetry and a small shoulder/tail on the high-energy (short-wavelength) side are visible, particularly at higher injection. With the present spectral resolution and signal-to-noise ratio, these features are not analysed as distinct peaks, but they indicate that the emission is not perfectly symmetric. In Fig. 5.12(d) the FWHM (meV) varies only weakly with current density: from ≈126 meV at J≈1 A cm^{-2} (10 mA), dipping slightly to near 123-124 meV around J=2-3 A cm^{-2} (20-30 mA), then increasing gradually to 133 meV at J≈10 A cm^{-2} (100 mA). The total change is ~7 meV (≈5-6%) and the apparent non-monotonicity is largely driven by the first point; given the limited sampling at low current and the absence of formal uncertainty bars on FWHM, we do not assign a definitive trend.

The broad linewidth is largely attributed to inhomogeneous broadening of the quantum-ring ensemble (size/composition variations) and to carrier redistribution among a manifold of localised states under injection. The observed asymmetry/shoulder is consistent with state filling and band-tail contributions, where higher-energy states contribute increasingly at higher carrier density; additional contributions from carrier heating cannot be excluded without a dedicated power- and temperature-dependent lineshape study.

We simply note that the concurrent blue-shift with drive current is consistent with established type-II GaAs/GaSb behaviour, where the dominant mechanism is capacitive charging, as reported previously by our group [105], [110]; a dedicated temperature-/power-dependent line shape study would be required to separate possible contributions such as inhomogeneous broadening or carrier heating.

The integrated EL output increases nearly linearly with current within 10-100 mA and no efficiency roll-over is observed in this range.

Device D2 - Small area (0.50 × 0.65 mm²)

D2 exhibits a broad peak centred at 1284.4 nm (0.965 eV) at 10 mA, again consistent with type-II QR emission. With increasing current, the peak blue-shifts systematically, reaching 1273.0 nm (0.974 eV) at 100 mA (Fig. 5.13). This corresponds to an energy increase of 8.65 meV, i.e. 0.096 meV/mA over 10-100 mA.

For D2, the dominant emission band is accompanied by small sub-features/shoulders that become more apparent with increasing current; these are treated here as fine structure on top of the broad ensemble emission rather than as separate resolved bands. The total shift is comparable to D1 measured under similar conditions (near 8.5 meV). With the present dataset we do not infer a different underlying mechanism between devices; the observed blue-shift is consistent with capacitive charging, field screening and band-filling effects in type-II GaAs/GaSb structures [105], [110]. A separation of possible additional contributions (e.g. charge-state distributions or inhomogeneous broadening) would require dedicated temperature-/power-dependent lineshape analysis and is not attempted here.

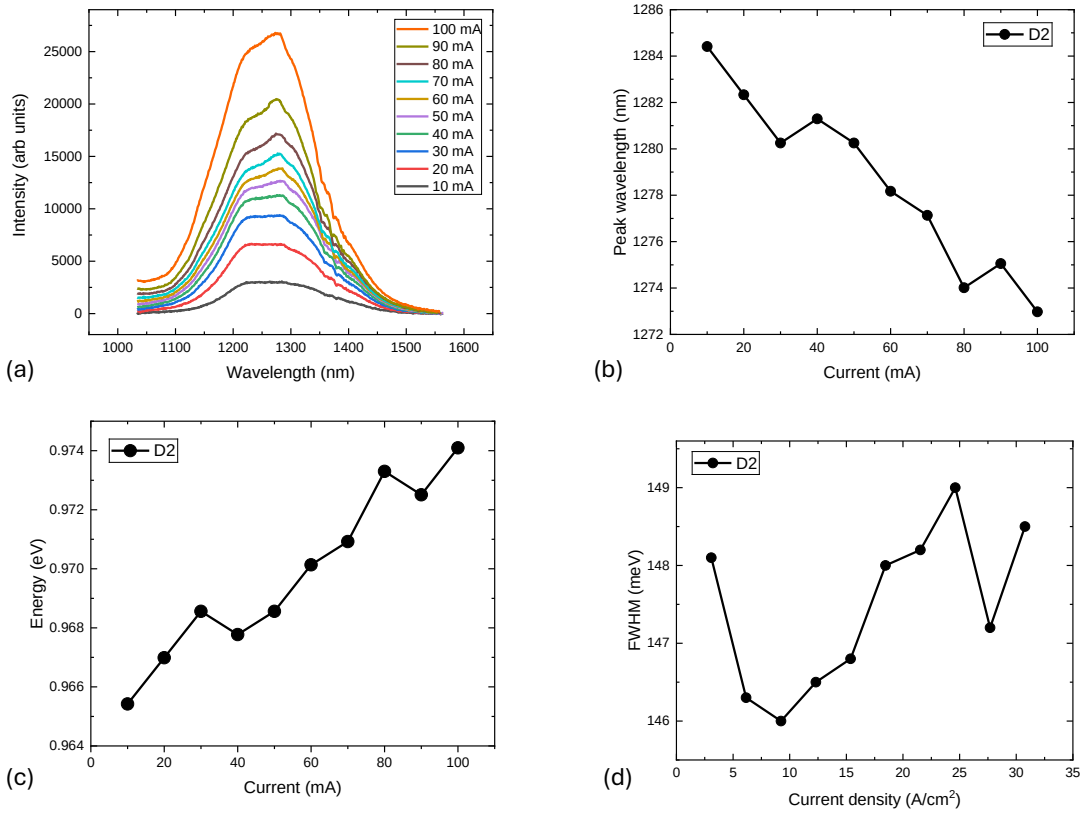

Fig 5.13: Room-temperature CW EL characteristics of Device D2 (0.5 × 0.65 mm² active area). a) EL spectra for injection currents from 10 mA to 100 mA. (b) Peak wavelength as a function of injection current. (c) Corresponding photon energy versus current, exhibiting a monotonic increase consistent with carrier-induced state-filling and partial screening of the built-in electric field. (d) FWHM as a function of current density, showing a modest broadening from 146 meV to 149 meV across the tested bias range.

5. 2.5. Comparative Analysis and Discussion for Large Devices (D1, D2)

Both devices show the expected blue-shift with increasing drive and a monotonic rise in EL intensity, consistent with established type-II GaAs/GaSb QR behaviour. Over 10-100 mA, the peak energy increases by between 8.5 and 8.7 meV in each case (0.094-0.096 meV/mA). Linewidth changes are small: for D1 the FWHM in energy grows by ≈5-6%, while for D2 it is nearly constant (≈2% variation) across the same current range. Given that only one sample of each design was measured, we do not ascribe different underlying mechanisms or claim geometry-scaling trends here; separating possible contributions (e.g., field screening, band filling, charge-state effects) would require a dedicated temperature/power-dependent line shape study. Within this limitation, both devices operate stably up to 100 mA with no observable roll-off; D1 reaches higher absolute optical power, whereas D2 yields higher power per area due to its smaller aperture (Fig 5.14). A comprehensive overview of the device-dependent trends in emission behaviour, linewidth, and power output is provided in table 5.2. Overall, the results are consistent with prior observations for type-II QR LEDs and indicate no significant issues between these large-device format.

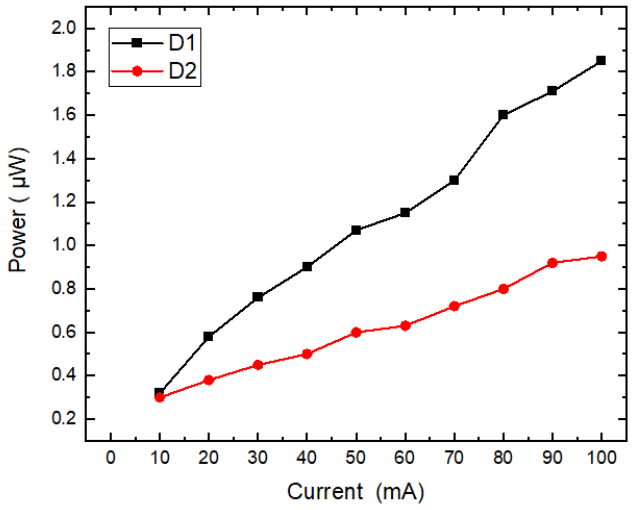

Fig 5.14: Integrated optical output power versus injection current for D1 and D2 under room-temperature operation.

Table 5.2. Summary of main spectral and electrical characteristics of devices D1 and D2.

Parameter	Device D1	Device D2	Remarks
Device Area A	1.0 × 1.0 mm² = 0.01 cm²	0.50 × 0.65 mm² = 0.00325 cm²	D2 is appr. 3× smaller
Current Range	10 - 100 mA	10 - 100 mA	Same current span
Current Density Range J	1.0 - 10.0 A·cm^{-2}	3.08 - 30.77 A·cm^{-2}	Higher J for D2 due to smaller area
Initial Peak Wavelength	1238.6 nm (1.001 eV)	1284.4 nm (0.965 eV)	D1 starts at higher photon energy
100 mA Peak Wavelength	1228.2 nm (1.01 eV)	1273.0 nm (0.974 eV)	Both blue-shift with drive
Total Blue-shift (ΔE)	8.5- 9 meV	9 meV	Similar
FWHM (energy)	Appr. 126 to 133 meV (5-6% increase)	Appr. 146 to 149 meV (2% variation, near-constant)	D2 broader across range; changes are small
EL Power at 100 mA	~1.85 μW	~0.95 μW	D1 > D2 in absolute power
Output Power per Unit Area	Lower	Higher	Higher for D2 due to smaller area

5. 2.6. Electroluminescence Spectra for Small Devices (D3, D4, D5)

This section presents a comprehensive analysis of the EL behaviour of GaSb QR-LED devices fabricated with three devices with varying circular mesa diameters: 70 µm (D3), 150 µm (D4) and 200 µm (D5). They were fabricated using the same epitaxial structure and characterised under pulsed electrical current at a constant substrate temperature of 20°C. Figure 5.15 (a-c) shows the raw EL spectra for 1-10 mA. All three devices exhibit broadband emission centred around 1180-1220 nm, consistent with type-II transitions. The measured intensity increases with current for each device. Because measurements were taken in separate sessions and only one sample of each size is shown, while optical coupling and current density differ, absolute intensity is not compared across devices.

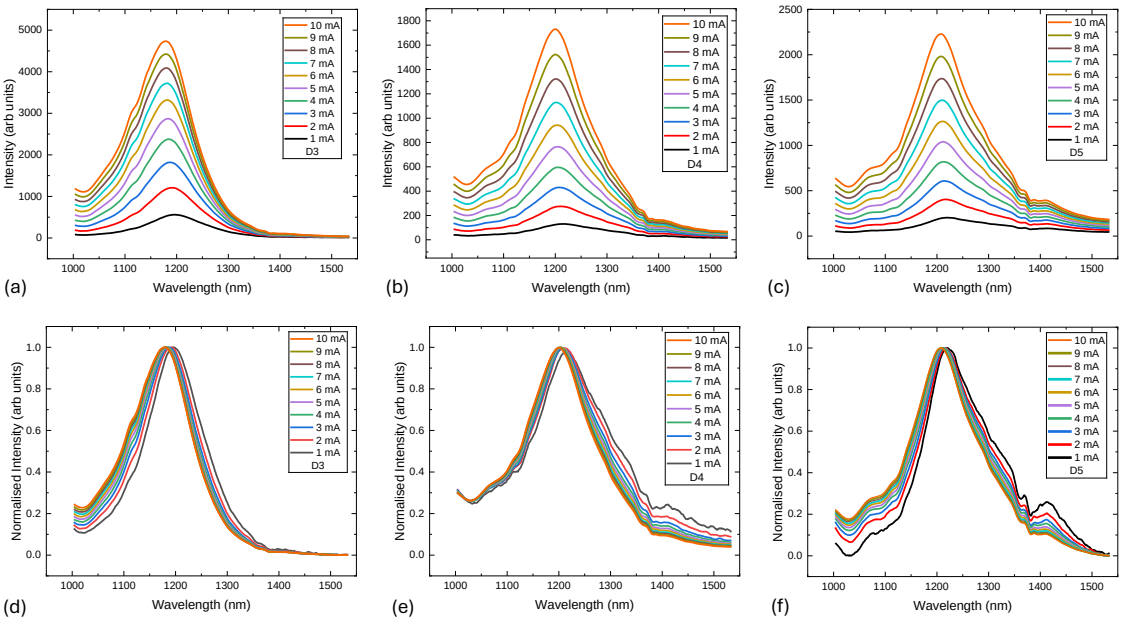

Fig 5.15: EL spectra of (a) D3, (b) D4 and (c) D5 at various injection currents (1-10 mA). Normalised EL spectra of (d) D3, (b) D4 and (c) D5, highlighting differences in spectral symmetry and broadening. The 70 µm device, D3, shows the cleanest and narrowest emission.

To compare spectral shapes, peak-normalised spectra are shown in Fig. 5.16 (d-f). In this view, all devices show a gradual short-wavelength shift with increasing current and a moderate broadening of the line shape. D4 and D5 display more fine-scale structure at higher currents; we do not quantify asymmetry here, and note that small features can be influenced by the measurement path and session-to-session conditions like lab humidity.

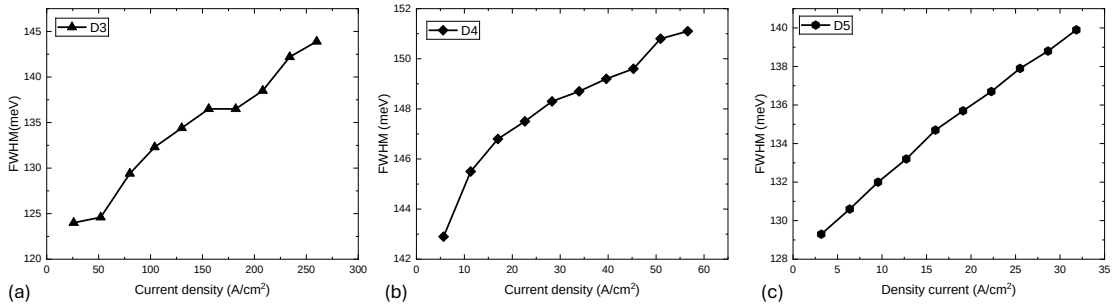

Fig. 5.16: FWHM plotted against injection current density of (a) D3, (b) D4, (c) D5. The D3 (70 µm) device consistently exhibits narrower spectra, suggesting enhanced inhomogeneous broadening.

Across 1-10 mA linewidth changes are modest in all three devices: D3 increases from nearly 124 to 144 ± 2 meV (about 16%), D4 from ~143 to 151 ± 2 meV (about 5-6%) and D5 from 129 to 140 ± 2 meV (about 8%) (Fig. 5.16). Within this limited dataset we do not assign a mechanism for the small differences in linewidth; separating device-intrinsic effects from session-to-session measurement factors would require dedicated temperature-/power-dependent lineshape studies. We simply note that a gradual increase in linewidth with current is commonly observed in type-II structures and may reflect general carrier heating (Joule heating) and enhanced carrier-phonon scattering under higher injection. We therefore treat Fig. 5.16 as documentation of operating ranges rather than evidence for a specific broadening process.

Over 1-10 mA the total blue-shifts are similar in magnitude: D3 about 13.1 ±0.5 meV, D4 about 8.9 ±0.5 meV and D5 about 11.4 ±0.5 meV (Fig. 5.17). The current-dependent increase in transition energy is consistent with the established picture for type-II GaAs/GaSb nanostructures; we do not infer different underlying mechanisms between devices from these data alone.

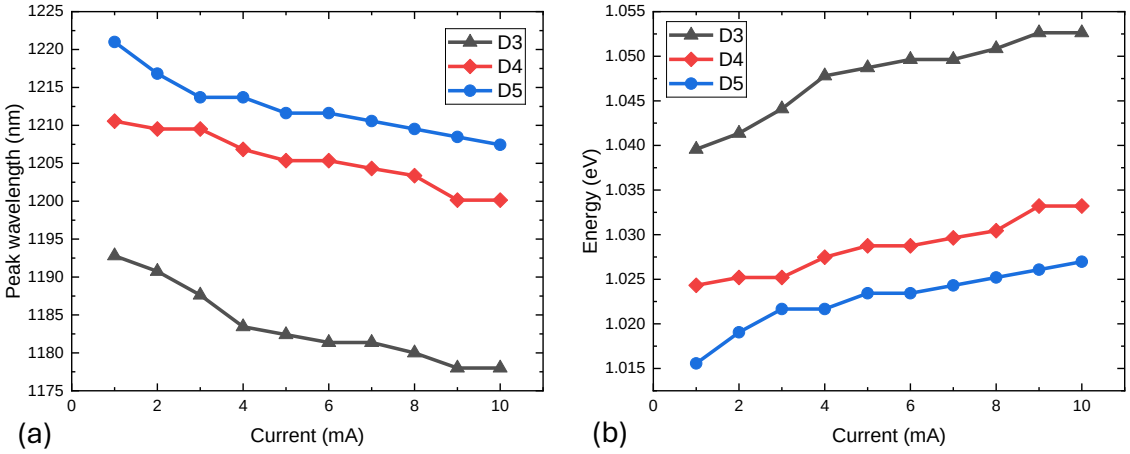

Fig. 5.17: (a) Peak emission wavelength as a function of injection current for all devices. A clear blue shift is observed, attributed to band-filling. (b) Corresponding photon energy shift with increasing current. Smaller devices show a larger energy shift, indicating stronger carrier confinement effects.

Integrated EL intensity (1000-1550 nm) increases monotonically with current for each device. Absolute comparisons between devices are not made because only one sample of each size was measured and optical coupling/collection can differ between sessions. When values are normalised by the nominal aperture area, the area-scaled intensities diverge; however, without identical coupling this should be viewed as descriptive rather than proof of differing injection or spreading physics.

In summary, the small-device set shows broadband single-peak EL near 1.18-1.22 μm, a modest increase in linewidth with current, and meV-scale blue-shifts of comparable size across devices under the present conditions as shown in table 5.3. Given the single-sample, separate-session limitation, we do not claim geometry-scaling trends or differences in homogeneous versus inhomogeneous broadening. The observations are consistent with prior results on type-II QR LEDs and show no significant issues when moving from 200-μm down to 70-μm apertures.

Table 5.3. Comparison of EL metrics for small-mesa devices (D3-D5)

Parameter	**D3 (70 μm)**	**D4 (150 μm)**	**D5 (200 μm)**	**Remarks**
Device Area A	3,848 μm² (3.85×10^{-5} cm²)	17,671 μm² (1.77×10^{-4} cm²)	31,416 μm² (3.14×10^{-4} cm²)	D4 ≈ 4.6×, D5 ≈ 8.2× larger than D3
Current Range	1-10 mA	1-10 mA	1-10 mA	Same for all devices
Current density J	26-260 A cm^{-2}	5.7-56.6 A cm^{-2}	3.2-31.8 A cm^{-2}	At 10 mA: D3 reaches ~8× (vs D5) higher J, stronger state filling/field screening expected.
Peak Wavelength at 1 mA	1192.8 nm (≈1.0397 eV)	1210.56 nm (≈1.0244 eV)	1221.0 nm (≈1.0156 eV)	-
Peak Wavelength at 10 mA	1178.0 nm (≈1.0530 eV)	1200.139 nm (≈1.0333 eV)	1207.44 nm (≈1.0270 eV)	All blue-shift with current
FWHM (energy)	124 to 144 ± 1.8 meV (≈16% change)	143 to 151 ± 1.8 meV (≈5-6% change)	129 to 140 ± 1.8 meV (≈8% change)	D3 ≳ D5 ≫ D4
Energy shift ΔE	13.1 ±0.5 meV	8.9 ±0.5 meV	11.4 ±0.5 meV	Similar meV-scale shifts; no mechanism assigned
Integrated EL	803,227 a.u.*	346,352 a.u.*	477,523 a.u.*	*derived from area×(per-area)

5. 2.7. Temperature-Dependent Electroluminescence Analysis for Small Devices (D3, D4, D5)

The temperature-dependent EL was measured at a constant drive of 5 mA from 20 to 80 °C in 10 °C steps for devices with circular mesas of 70 µm (D3), 150 µm (D4) and 200 µm (D5) (Fig. 5.18). We analyse the temperature evolution of peak position (reported as photon energy), integrated intensity (1000-1550 nm) and linewidth (FWHM in meV). No model fitting is attempted in the main text.

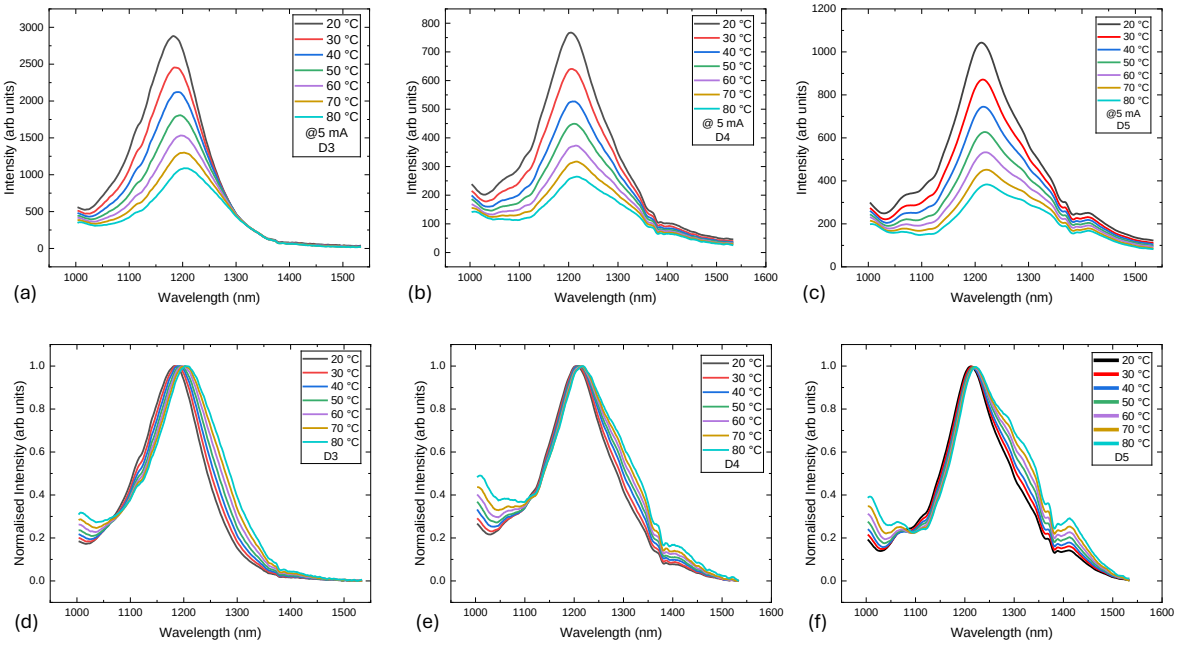

Fig. 5.18: EL spectra of (a) D3 (70 µm), (b) D4 (150 µm) and (c) D5 (200 µm) devices under increasing temperature across 20-80 °C. Normalised EL spectra for (d) D3, (e) D4, (f) D5 across 20-80 °C.

Across all devices, EL intensity decreases with increasing temperature at fixed current, which is consistent with an increased contribution from non-radiative channels. The peak shifts to longer wavelength; in energy units the transition energy decreases monotonically with temperature, consistent with band-gap narrowing over this range. Peak-normalised spectra show this systematic red shift with only modest change in overall line shape (Fig. 5.19).

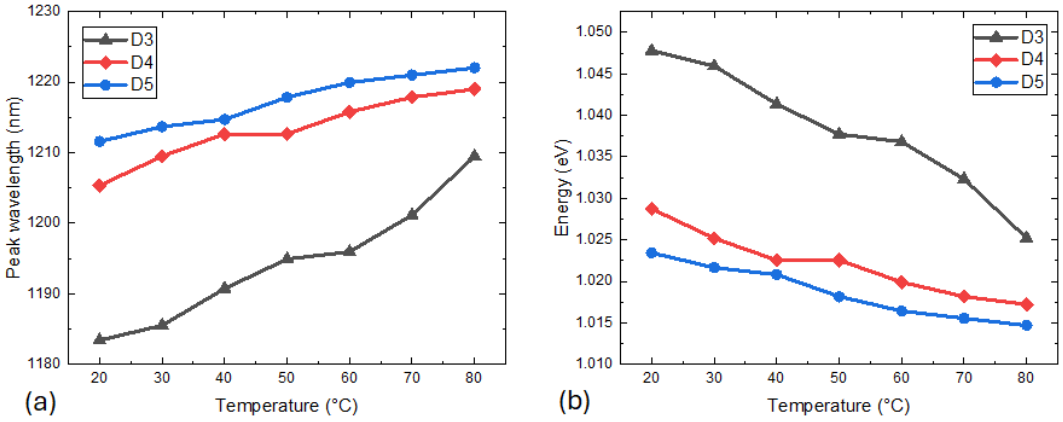

Fig. 5.19: Temperature dependence of the (a) peak emission wavelength and (b) photon energy for D3, D4 and D5 devices.

Here, a simple linear description over 20-80 °C captures the trends at 5 mA. The peak photon energy decreases with temperature with fitted slopes of -0.36 meV/K for D3, -0.18 meV/K for D4 and -0.15 meV/K for D5, giving total drops of 22.6 ± 0.5 meV, 11.5 ± 0.5 meV and 8.7 ± 0.5 meV between 20 and 80 °C (Fig. 5.19 (b)). Peak intensity (normalised to its 20 °C value) decreases monotonically for all devices over 20-80 °C (Fig. 5.20 (a)). Over the same range the FWHM in energy increases approximately linearly: +0.26 meV/K for D3, +0.42 meV/K for D4 and +0.05 meV/K for D5, corresponding to total increases of 15 ± 3 meV, 26 ± 3 meV and 3 ± 3 meV (Fig 5.20(b)). Uncertainties are obtained by propagating a wavelength calibration of ±0.2 nm to energy (giving ±0.17 meV per peak point near 1.2 µm) and an FWHM fit uncertainty of ±1.0 nm to energy (±0.9 meV per point) and then using standard least-squares error formulas for the slope; the corresponding slope uncertainties are about ±0.006 meV/K for peak-energy fits and ±0.034 meV/K for FWHM fits. These values document the temperature dependence over the measured range; no model fitting beyond linear trends is attempted and we do not attempt to quantitatively separate the underlying mechanisms for the linewidth changes.

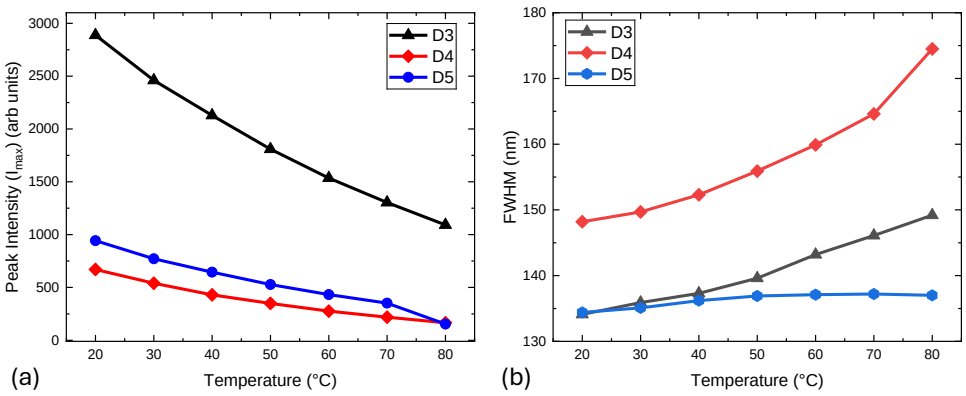

Fig. 5.20: (a) Temperature dependence of peak EL intensity for devices D3, D4 and D5 at 5 mA injection. D3 maintains higher peak intensity across all temperatures, indicating by the rate of change. (b) Evolution of the FWHM with temperature.

Nevertheless, the observed increase in FWHM with temperature is expected and is commonly attributed to enhanced carrier-phonon scattering, thermally activated hopping between localised states and additional inhomogeneous broadening.

Within this limitation, there is no evidence that the smaller device (D3) performs worse than the larger ones over 20-80 °C. Any claims about geometry-dependent confinement or thermal resistance would require a controlled study with multiple devices per size, identical coupling and temperature/power sweeps.

The behaviour reported here with increasing temperature, intensity quenching at fixed current, a red shift due to band-gap narrowing and increasing linewidth (except D5), is consistent with prior observations for type-II GaAs/GaSb nanostructures.

5.3. Conclusions and Outlook

This chapter has demonstrated that GaSb/GaAs type-II quantum-ring LEDs operate reliably as broadband near-infrared emitters in the 1.18-1.28 μm (peak wavelength) range across the measured devices. The emission covers part of the telecom O-band, and the broad spectra suggest that cavity-enhanced operation at 1310 nm, and potentially longer wavelengths, should be feasible with appropriate optical design. The devices exhibit the characteristic signatures of type-II heterostructures: a current-induced blue-shift dominated by capacitive charging and a temperature-induced red-shift consistent with band-gap reduction, accompanied by a gradual increase in linewidth with temperature.

Some differences between nominal device geometries were observed, but given that only one device per diameter was measured and the data were acquired in separate sessions, these variations cannot be interpreted as systematic size effects. The present dataset therefore documents operating ranges rather than establishing quantitative structure-property trends.

Even so, the results establish a solid baseline for subsequent optimisation. The emission wavelengths overlap the lower telecom O-band, confirming relevance for fibre-compatible applications. A natural next step is a controlled geometry study with multiple devices per size and uniform optical coupling, enabling rigorous assessment of confinement, surface-related recombination and thermal behaviour. Further refinement of the heterostructure, or integration with engineered optical stacks such as DBR-based cavities, offers clear routes to improved extraction efficiency and spectral stability. Collectively, these findings provide both a validated starting point and concrete directions for advancing type-II quantum-ring LEDs toward high-performance, telecom-relevant light sources.

Chapter 6 GaSb Quantum-Ring Light Emitting Diodes with Distributed Bragg Transmitters

Building upon the optoelectronic device characterisation and fabrication methodologies discussed in Chapter 5, this chapter addresses a fundamental challenge in semiconductor light-emitting diodes (LEDs): improving light extraction efficiency. Conventional LEDs face significant photon loss due to internal reflections at the semiconductor/air interface, a consequence of the large refractive index contrast between the active material and its surrounding medium. These internal reflections reduce the number of photons that escape the device, thus lowering overall efficiency, an issue that becomes particularly critical in devices operating at telecommunication wavelengths. In high-index III-V materials such as GaAs ($n \approx 3.4$), only a small fraction of internally generated photons lie within the escape cone, so most undergo total internal reflection and are lost [130]. In QKD, the detected-photon rate sets the achievable key rate, so improving external efficiency from a few percent to tens of percent has a direct and proportional impact on performance [271], [359]. For SPLEDs, higher extraction efficiency increases the probability that each electrically triggered cycle yields one usable photon in the fibre, which is crucial for maintaining key rates over long-distance links [130], [271]. Thus, integrating efficient light extraction structures such as distributed Bragg reflectors (DBRs) or photonic crystal cavities becomes essential for realizing practical, deployment-ready telecom-band single-photon sources [359], [360], [361].

III-V compound semiconductor quantum dots (QDs) embedded in p-i-n diode structures have emerged as promising candidates for scalable and efficient light sources, owing to their compatibility with standard laser-diode fabrication platforms. For emission around 1550 nm, InP substrates are typically preferred because their smaller lattice mismatch with narrow-band-gap III-V materials such as InAs reduces the strain, thereby limiting strain-induced band-gap shifts and enabling emission in the telecom C-band. In contrast, for ~1310 nm emission, GaAs substrates offer a robust, cost-effective and DBR-friendly platform: GaAs/ $Al_xGa_{(1-x)}As$ forms a nearly lattice-matched material pair with a useful refractive-index contrast, supporting high-quality epitaxial distributed Bragg reflectors. At the same time, the substantial lattice mismatch between narrow-band-gap materials like InAs and GaAs is exploited to drive Stranski-Krastanow self-assembly of QDs [362], [363] .

Among potential candidates for telecommunication-wavelength light sources, type-II GaSb nanostructures are of particular interest due to their capability for infrared emission and suitability for room-temperature operation. Compared to GaSb QDs, GaSb quantum rings (QRs) grown via molecular beam epitaxy (MBE) exhibit reduced strain and fewer defects, along with deep hole-confinement potentials, attributes that enhance their performance in the target wavelength range. These properties make GaSb QRs strong candidates for cost-effective, high-performance LEDs.

The work presented in this chapter investigates the integration of a novel distributed Bragg anti-reflection stack, termed a distributed Bragg transmitter (DBT), with GaSb QR LEDs. The DBT is specifically engineered to minimise surface reflection at the target emission wavelength, thereby maximising the transmission of photons from the active region into free space. Using the transfer matrix method (TMM), alternating layers of GaAs and $Al_xGa_{1-x}As$ were optimised to achieve near-zero reflectivity at the designed wavelength, while

maintaining full lattice compatibility with the underlying GaSb QR structures. This approach provides a scalable, monolithic solution for enhancing light extraction efficiency without introducing complex post-growth processing steps.

The specific objectives of this chapter are:

1. To design and optimise a DBT structure tailored to the emission characteristics of GaSb QR-LEDs.
2. To fabricate both standard and DBT-integrated GaSb QR-LEDs and compare their performance.
3. To experimentally validate the predicted improvements in photon extraction efficiency through electroluminescence (EL) measurements and structural verification via transmission electron microscopy (TEM).
4. To assess the thermal stability of the DBT-enhanced devices for potential telecommunication and quantum photonic applications.

A conventional DBR is designed for high reflectivity to form a resonant cavity (e.g., VCSELs), whereas the goal of the DBT is the opposite: to minimise reflectivity and maximise transmission at the emission wavelength for improved out-coupling. Achieving stimulated emission would require a high-Q cavity (typically two DBRs), sufficient modal gain and low optical loss, which is not targeted in this chapter and can be particularly challenging for type-II emitters with reduced oscillator strength. DBR-based cavity spectral selection is instead explored in Chapter 7.

The remainder of this chapter is organised as follows: Section 6.1 describes the device design and simulation methodology; Section 6.2 presents growth, fabrication and structural/optical validation; Section 6.3 details the electrical and optical device characterisation; and Section 6.4 summarises the findings and identifies directions for future work.

6 .1. Device Design and Simulation

The distributed Bragg transmitter (DBT) structure was developed as an optical engineering solution to minimise Fresnel reflection losses while maximising photon extraction at the designed emission wavelength of the GaSb QR active region. As discussed in Chapter 2, conventional DBRs employ alternating high- and low-refractive-index layers to achieve high reflectivity through constructive interference. In contrast, the DBT design presented here inverts this functional objective by tailoring the interference condition for destructive reflection at the emission wavelength, thereby enabling near-unity forward transmission. The design process was carried out using the transfer matrix method (TMM) implemented in TFCalc software, enabling precise calculation of transmission and reflection spectra for multilayer dielectric stacks.

6. 1.1. Optical Design Principles

Unlike conventional DBRs, which are designed to reflect light within a narrow spectral band, the DBT functions as a narrowband high-transmission filter, suppressing reflections at a specific wavelength. This selective transmission is achieved via destructive interference of backward-propagating waves at λ_0, while subsidiary stop-bands emerge near $2\lambda_0$ due to second-order interference effects, i.e., the usual DBR narrowband reflector centred at $2\lambda_0$.

In this study, each period of the DBT comprises GaAs (≈λ/2n), $Al_{0.9}Ga_{0.1}As$ (≈λ/4n) and two $Al_{0.45}Ga_{0.55}As$ (each ≈λ/8n) sub-layers. Here, n_r denotes the refractive index (not electron density, which was used in Chapter 2). The phase budget of the quad-layer is chosen such that the back-reflections cancel at λ_0 (destructive interference) with secondary reflection features appearing near $2\lambda_0$. We therefore refer to a quad-layer, phase-engineered period rather than a literal "λ/2 per half-period" stack, and this period is repeated over a number of, e.g., seven periods. At the target wavelength λ_0 ≈1310 nm, the optical-thickness targets are ;

$n_{GaAs}.d_{GaAs} = {}^{\lambda_0}/_{2}$, $n_{Al_{0.9}Ga_{0.1}As}.d_{Al_{0.9}Ga_{0.1}As} = {}^{\lambda_0}/_{4}$,

$n_{Al_{0.45}Ga_{0.55}As}.d_{Al_{0.45}Ga_{0.55}As} = {}^{\lambda_0}/_{8}$ (for each of the two sub-layers), so that $\sum_i n_i.d_i \approx \lambda_0$ within one period (total phase ≈ 2π).

With these separations, the phase advances between successive interfaces at λ_0 (π, π/2, π/4, π/4) make the vector sum of first-order interface reflections ≈ 0, thereby minimising R and maximising T at λ_0; away from λ_0 the phases detune and stop-band ripples appear. This deliberate phase inversion ensures that reflections from successive interfaces arrive 180° out of phase at the design wavelength, cancelling one another and thereby suppressing the net reflection coefficient R while maximising transmission T.

Material selection was driven by three considerations:

1. Refractive index contrast: GaAs (n≈3.4036 at 1310 nm) and $Al_{0.9}Ga_{0.1}As$ (n≈2.946 at 1310 nm) provide the necessary index difference for effective interference control.
2. Electrical resistance reduction: The intermediate $Al_{0.45}Ga_{0.55}As$ (n≈3.156 at 1310 nm) layers are included primarily to reduce series resistance in the p-i-n diode structure during forward bias operation [137]. The thickness of these layers is engineered to preserve optical properties, maintaining destructive interference at λ_0 without introducing additional spectral distortion.
3. Lattice compatibility and stability**:** All chosen compositions are (almost) lattice-matched to GaAs within <0.15% (GaAs-AlAs mismatch ≈ 0.12%), enabling defect-free molecular beam epitaxy (MBE) growth while maintaining thermal and chemical stability during fabrication.

This quad-layer λ/2 DBT configuration departs significantly from the λ/4-λ/4 DBR arrangements arrangements primarily in its functional objective, destructive versus

constructive interference, making it well-suited for integration with type-II GaSb QR-LEDs aimed at telecommunication wavelength operation.

6. 1.2. Transfer Matrix Method (TMM) Modelling

The optical performance of the DBT structure was modelled using the transfer matrix method (TMM), a formalism derived from the continuity of the electric (E) and magnetic (H) field components at each material interface. Each layer in the DBT is represented by a 2×2 characteristic matrix M_i of the form as follows:

$$M_i = \begin{bmatrix} cos\delta_i & \frac{j}{n_i}\sin\delta_i \\ jn_i\sin\delta_i & cos\delta_i \end{bmatrix}, \tag{6.1}$$

where n_i is the refractive index of the layer, $\delta_i = \frac{2\pi}{\lambda} n_i . d_i$ is the phase thickness, and j is the imaginary unit.

For a multilayer stack of N layers, the overall transfer matrix is given by:

$$M_{total} = \prod_{i=1}^{N} M_i . \tag{6.2}$$

The complex transmission (t) and reflection (r) coefficients at the design wavelength are obtained from M_{total}, and the corresponding power transmission and reflection spectra are calculated as $T=|t|^2$ and $R=|r|^2$, respectively.

The TMM modelling was implemented in TFCalc software, which offers built-in dispersion models for refractive index and allows direct optimisation of multilayer designs for specified spectral targets. The refractive index dispersion for GaAs, $Al_{0.45}Ga_{0.55}As$ and $Al_{0.9}Ga_{0.1}As$ was defined using literature-derived Sellmeier equations [131] and verified against spectroscopic ellipsometry measurements on calibration samples grown under identical MBE conditions. The optimisation process in TFCalc involved:

1. Setting the target wavelength λ_0=1310 nm.
2. Iteratively varying the layer thicknesses to achieve R<1% at λ_0 and T>95% across the LED emission bandwidth.
3. Performing a tolerance analysis for ±5 nm deviations in layer thickness to assess manufacturability robustness.

The final design utilised seven pairs of quad-layer sequence, achieving simulated peak transmission of 99.8% at λ_0.

6. 1.3. Optimisation of Layer Repetitions

The number of repetitions in a multilayer interference structure directly impacts its optical performance, bandwidth and manufacturability. In a DBT, increasing the number of repetitions sharpens the spectral transmission peak and deepens the reflection minimum, but at the cost of a narrower bandwidth and increased fabrication complexity. For molecular

beam epitaxy (MBE)-grown devices, additional periods also translate to longer growth times, higher accumulated strain and greater risk of interface roughness.

Initial TMM simulations were performed for DBT structures ranging from three to ten repetitions of the quad-layer λ/2 configuration. The results indicated that:

- Fewer than five repetitions produced insufficient suppression of surface reflection, with R_{min} exceeding 2% at the target wavelength.
- More than eight repetitions provided negligible additional reflection suppression (<0.2% improvement) while narrowing the high-transmission bandwidth, risking partial spectral clipping.
- Growth times beyond seven repetitions approached the upper limit for strain-free monolithic integration with the active region, as determined from prior MBE calibration runs.

A seven-repetition configuration was therefore selected as the optimum design, yielding a simulated reflection minimum of $R_{min}\approx0.2\%$ at $\lambda_0=1310$ nm, a transmission exceeding 99% across a ±20 nm bandwidth centred on λ_0 and a total stack thickness compatible with high-quality epitaxial growth (Fig 6.1.).

This choice represents a balance between optical performance and manufacturability, ensuring both high photon extraction efficiency and reproducible device fabrication. The influence of this optimised repetition number on the final device performance is evaluated experimentally in Section 6.3.

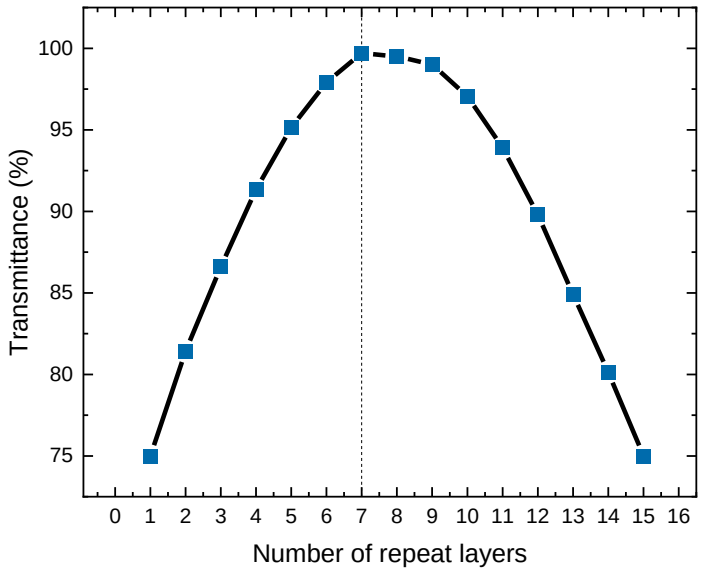

Fig. 6.1: Simulated dependence of maximum transmittance on the number of DBT repeat layers. Peak transmission is achieved for 7-8 repetitions, with performance degrading for higher values due to sideband and phase mismatch effects.

6. 1.4. Sensitivity to Cap-Layer Thickness (Tolerance Analysis)

To quantify fabrication tolerances, we specifically investigated the sensitivity of the DBT's transmission to the GaAs cap-layer thickness. The cap layer is unique among the structure components because it directly affects the boundary condition at the semiconductor/air interface, whereas variations in the DBT repeat layers primarily affect the internal resonance condition. This distinction makes cap-layer thickness a process-relevant degree of freedom for optimisation. The simulations reveal a modulated (oscillatory) dependence of both the peak wavelength and the on-target transmittance at λ_0=1310 nm as the cap thickness is varied (Fig. 6.2). In particular, the transmittance at 1310 nm exhibits clear extrema at fractional optical thicknesses, with a maximum close to 3λ/8 and two distinct minima approximately near λ/4 and 5λ/8-3λ/4. The peak transmission wavelength appears to show related behaviour, shifting by ≈20-30 nm over a 0-300 nm cap sweep, consistent with the additional phase accumulated in the cap layer (Fig 6.2.).

These results provide two practical guidelines for growth:

(i) targeting the cap thickness near the 3λ/8 condition to maximise forward transmission at 1310 nm, and

(ii) recognising that modest thickness errors (tens of nanometres) mainly shift the resonance but do not catastrophically degrade the maximum transmission, provided the cap is not close to a transmittance null. This complements our ±5 nm layer-by-layer tolerance study (Section 6.1.5), extending it to a process-relevant top-layer degree of freedom.

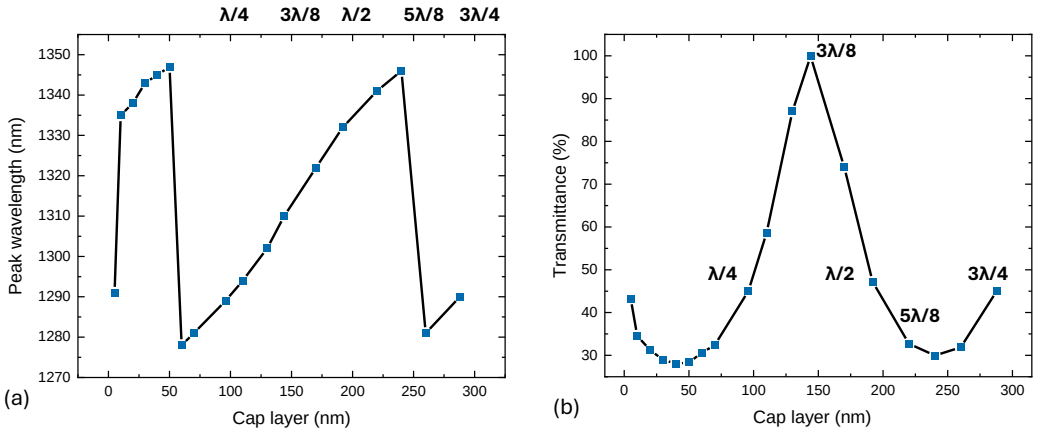

Fig. 6.2: (a) Peak transmission wavelength vs cap-layer thickness, showing modulated/oscillatory tuning of the resonance. (b) Transmittance at 1310 nm vs cap-layer thickness, highlighting extrema near fractional optical thicknesses (λ/4, 3λ/8, λ/2, 5λ/8, 3λ/4).

The observed modulation of the peak wavelength and transmittance is solely attributed to variations in the GaAs cap layer thickness, rather than the DBT repeat layers themselves. The repeat layers establish the intrinsic resonance of the DBT stack, whereas the cap layer (the topmost interface) modulates the phase matching condition at the semiconductor/air interface. Adjusting the cap thickness modifies the effective optical path and

reflection/transmission boundary condition, thereby shifting the spectral position and amplitude of the transmission peak. However, it should be noted that the optimal value of 3λ/8 is an empirical result of the simulation; the underlying physical reasons for this particular value remain incompletely understood and warrant further investigation.

6. 1.5. Final Layer Design

The optimised DBT device structure is summarised in table 6.1, including the active region and buffer/substrate layers. The GaSb QR active region is embedded within GaAs spacers and is positioned within the p-i-n diode such that the vertical optical field at the DBT anti-reflection resonance is maximised. In practice, the active region is placed at a point where the calculated intensity profile of the DBT transmission mode at λ_0 = 1310 nm exhibits an antinode, thereby improving extraction efficiency. This spatial alignment ensures that spontaneous emission from the quantum rings couples efficiently into the high-transmission mode of the DBT: backward-propagating components are effectively suppressed by destructive interference, while the forward-propagating photons experience a transmission maximum at the semiconductor/air interface. The layer stack was defined to satisfy the dual requirements of;

(i) achieving the optical interference conditions predicted by TMM simulations, and
(ii) maintaining lattice-matched growth conditions to ensure structural quality and minimise defect propagation.

Table 6.1. Final DBT LED layer structure and target thicknesses

	Material	Target Thickness (nm)	Doping	
Cap Layer	GaAs	145	p	$1x10^{19}$
DBT x6 (λ/2)	$Al_{0.45}Ga_{0.55}As$	50.64	p	$2x10^{18}$
	$Al_{0.9}Ga_{0.1}As$	109.91	p	$2x10^{18}$
	$Al_{0.45}Ga_{0.55}As$	50.64	p	$2x10^{18}$
	GaAs	192.42	p	$2x10^{18}$
DBT x1 (λ/2)	$Al_{0.45}Ga_{0.55}As$	50.64	p	$2x10^{18}$
	$Al_{0.9}Ga_{0.1}As$	109.91	p	$2x10^{18}$
	$Al_{0.45}Ga_{0.55}As$	50.64	p	$2x10^{18}$
	GaAs	192.42	i	-
Ring Layers x3	GaAs	15	i	-
	GaSb	5	i	-
	GaAs	15	i	-
	GaAs	192.42	i	-
Buffer	GaAs	~500	n	$4x10^{18}$
Substrate	GaAs	substrate	n	$\sim 3x10^{18}$

The emission layer comprises three layers of GaSb quantum rings embedded within GaAs spacers. Each QR layer is nominally ~5 nm thick, self-assembled via the Stranski-Krastanow growth mode, with 15 nm GaAs spacers separating successive QR layers. The type-II band alignment between GaSb and GaAs provides strong hole confinement and enables emission in the 1.3 μm telecom window at room temperature.

Below the active region, around 700 nm GaAs buffer layer is included to separate the active region from the substrate, smoothen the surface and reduce dislocation propagation. This buffer also forms part of the p-i-n diode structure, ensuring electrical confinement of carriers within the active region.

The uppermost layer is a GaAs cap with a target physical thickness of 145 nm, corresponding to an optical thickness of approximately $3\lambda/8$ at λ_0= 1310 nm. As demonstrated in the cap-thickness sensitivity analysis (Section 6.1.3), this choice of thickness provides optimal phase alignment between the emission from the active region and the DBT resonance, maximising transmission at the target wavelength. The cap also serves as a protective layer during processing, preventing oxidation of the high-Al content layers beneath.

The device is grown on a commercial (100)-oriented GaAs substrate, doped n-type, with a thickness of ~350 μm. The substrate provides mechanical stability and serves as the lower electrical contact layer after thinning and metallisation during device processing.

Figure 6.3. presents the simulated normal-incidence transmission spectrum of the optimised seven-period DBT stack, as calculated using the transfer matrix method with the target layer thicknesses listed in table 6.1. The spectrum exhibits a pronounced transmission maximum exceeding 99% centred close to the design wavelength λ_0=1310 nm, confirming that the quarter-/half-wave optical thickness conditions have been correctly implemented in the multilayer structure. This high-transmission peak is flanked by oscillatory sidebands, characteristic of Fabry-Pérot interference within the finite-period Bragg stack.

At longer wavelengths, a deep transmission minimum is observed near $2\lambda_0 \approx 2620$ nm, consistent with the stopband behaviour expected for a conventional DBR. This feature further validates that the structure behaves as a DBT at the fundamental wavelength while exhibiting DBR-like reflection at its second-order resonance, in agreement with the design principle. The relatively modest sideband suppression, compared with idealised infinite-period DBRs, arises from the deliberate limitation to seven Bragg periods in order to maintain a total epitaxial thickness compatible with high crystalline quality.

This result demonstrates that the DBT structure selectively suppresses reflection at the desired emission wavelength without compromising the overall spectral integrity of the device. Importantly, the GaAs substrate contribution to the transmission spectrum remains flat over the measured range, confirming that the observed enhancement is solely attributable to the engineered DBT multilayer.

In order to verify that the enhanced transmittance observed at λ_0=1310 nm originates exclusively from the DBT multilayer design and not from the substrate itself, a control simulation was performed using only a bare GaAs substrate without any additional layers.

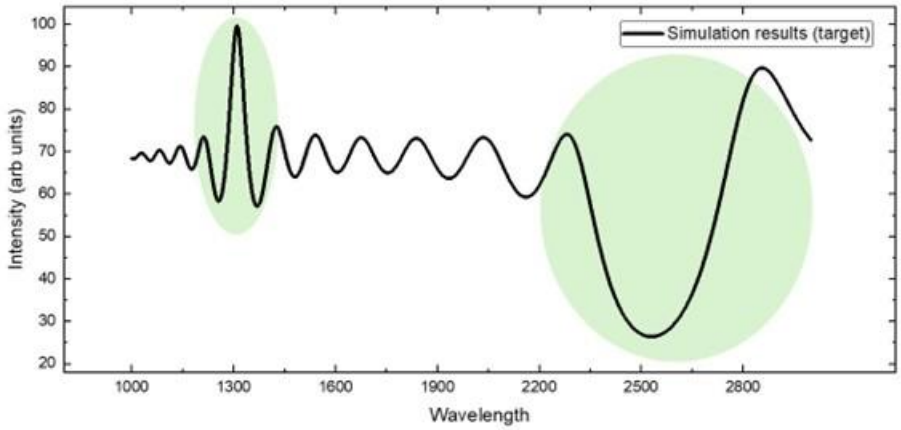

Fig. 6.3: Simulated transmittance spectrum of the optimised DBT structure showing near-unity transmission at λ_0=1310 nm and the second-order DBR stopband at $2\lambda_0$. The design comprises seven periods of GaAs/$Al_xGa_{1-x}As$ layers, tailored using the transfer matrix method to maximise transmission at the target wavelength while suppressing unwanted reflection bands.

The resulting spectrum exhibited a flat transmittance response across the investigated wavelength range, with no spectral features or resonances (Fig 6.4.). This behaviour is expected for a homogeneous material of uniform thickness, as there are no periodic refractive index contrasts to induce constructive or destructive interference.

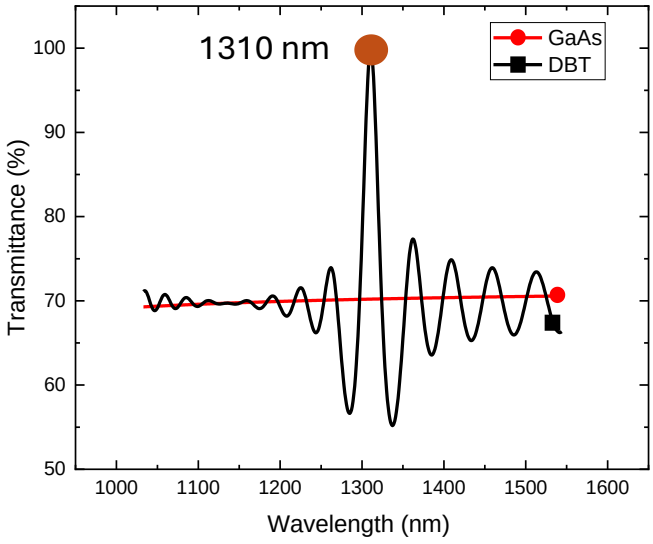

Fig 6.4: Simulated transmittance spectra for a bare GaAs substrate (red dashed line) and the optimised DBT structure (black solid line). The GaAs substrate exhibits a flat, featureless spectrum, confirming that it does not contribute to wavelength-selective transmission. In contrast, the DBT structure shows a pronounced transmission peak near 1310 nm, demonstrating that the enhancement is entirely due to the interference effects of the multilayer design.

When the same analysis is applied to the optimised DBT structure, a pronounced transmission peak of nearly 100% appears at the design wavelength. The direct comparison

between the flat GaAs response and the DBT-enhanced spectrum confirms that the transmittance improvement is entirely attributable to the engineered interference effects of the DBT layers. This result validates the effectiveness of the DBT approach for wavelength-selective transmission control while maintaining high off-band transparency.

The simulation results confirmed that the optimised DBT structure can achieve near-unity transmittance at the target wavelength of 1310 nm, while maintaining a compact total thickness suitable for epitaxial growth. With the optical design principles validated, the next stage involved realising the structure through molecular beam epitaxy (MBE) growth and evaluating its performance through experimental characterisation. In this section, the growth parameters, structural analysis (including TEM) and a comparison between simulated and measured optical responses are presented.

6 .2. Growth, Fabrication and Experimental Characterisation

6. 2.1. Growth of the devices and optimisation

The DBT-integrated GaSb quantum ring LED structures were grown by solid-source molecular beam epitaxy (MBE) by Dr Peter Hodgson on (100)-oriented n-type GaAs substrates. The active GaSb quantum ring layers were formed using the Stranski-Krastanow self-assembly method, in accordance with the design parameters listed in table 6.1. The DBT layers, spacer layers and active region sequence followed the optimised design described in Section 6.1.

Following epitaxial growth, the layer thicknesses and interface quality were assessed using cross-sectional transmission electron microscopy (TEM). This analysis provided direct visual confirmation of the DBT periodicity and allowed quantitative measurement of individual layer thicknesses. The experimentally measured values were then compared with those from the optical design simulations, enabling an evaluation of fabrication accuracy and its impact on the optical response.

High-resolution cross-sectional transmission electron microscopy (TEM) analysis was performed by Francisco Alvarado Cesar at the University of Warwick, UK, using a JEOL JEM-2100F operating at 200 kV. Samples were prepared in the [110] crystallographic orientation to provide a clear view of the multilayer sequence from the GaAs cap through the DBT stack and into the active region.

A schematic representation of the target structure is shown in Figure 6.5(a), comprising seven repetitions of the GaAs/$Al_{0.45}Ga_{0.55}As$-$Al_{0.9}Ga_{0.1}As$- $Al_{0.45}Ga_{0.55}As$ quad-layer stack, a λ/2 GaAs spacer, and three GaSb QR planes embedded within GaAs spacers. The low-magnification TEM image in Figure 6.5(b) reveals the overall periodicity of the DBT stack, with clearly resolved alternating high- and low-contrast layers corresponding to the GaAs and $Al_xGa_{1-x}As$ compositions. No evidence of gross structural defects such as cracks or delamination was observed.

At intermediate magnification (Figure 6.5(c)), the DBT interfaces appear sharp and well-defined, with minimal contrast smearing indicative of interdiffusion. Layer thickness measurements performed across ten consecutive periods show a mean deviation from the design values of less than 3%, confirming the accuracy and stability of the MBE growth process. A slight systematic drift (<1 nm per period) towards increased layer thickness was observed from the substrate upwards, consistent with minor growth rate variation over time.

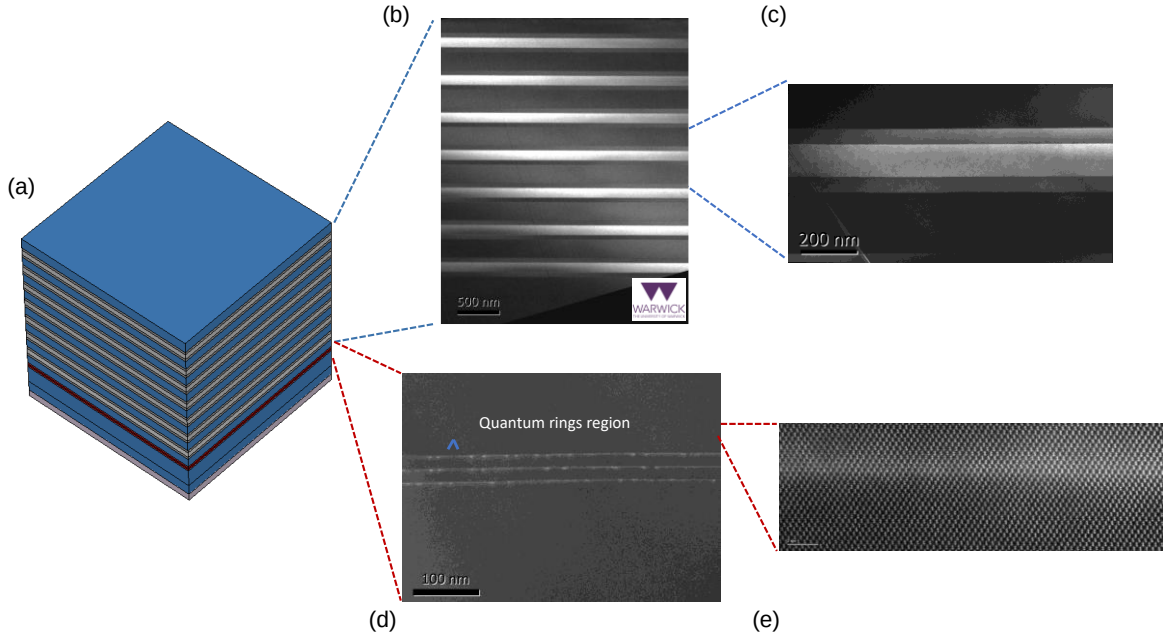

Fig. 6.5: Structural characterisation of the DBT QR-LED by cross-sectional TEM. (a) Schematic representation of the target layer sequence, showing seven repetitions of the GaAs/$Al_{0.45}Ga_{0.55}As$-$Al_{0.9}Ga_{0.1}As$- $Al_{0.45}Ga_{0.55}As$ quad-layer DBT stack, a λ/2 GaAs spacer and three GaSb QR layers embedded within GaAs spacers. (b) Low-magnification TEM image showing the full DBT stack with clear periodic contrast between GaAs and $Al_xGa_{1-x}As$ layers. (c) Intermediate-magnification view of the DBT section highlighting sharp, well-defined interfaces and uniform layer thicknesses. (d) Active region containing three GaSb quantum ring layers (indicated by arrows) separated by 15 nm GaAs spacers, with no evidence of discontinuities or dot coalescence. (e) High-resolution TEM (HRTEM) image resolving the atomic lattice at a GaAs/$Al_xGa_{(1-x)}As$ interface, showing coherent epitaxy and the absence of misfit dislocations.

The active region, shown in Figure 6.5(d), contains three distinct GaSb QR layers (highlighted by arrows) separated by 15 nm GaAs spacers. The QR planes appear continuous across the field of view, with no evidence of discontinuities or coalescence into dot-like structures. This confirms that the intended ring morphology was preserved during overgrowth.

High-resolution TEM (HRTEM) imaging (Figure 6.5(e)) resolves the atomic lattice at the GaAs/$Al_xGa_{1-x}As$ interfaces. Fast Fourier Transform (FFT) analysis of the HRTEM images shows no detectable misorientation between layers and the absence of misfit dislocations indicates that strain is adequately accommodated within the structure. Interface roughness, quantified via intensity profile analysis across multiple boundaries, was found to be less than 2 nm root mean square (RMS), which is sufficiently low to avoid significant optical

scattering losses. The TEM-derived thickness values for each constituent layer were compiled and compared against the target design in table of figure 6.6.

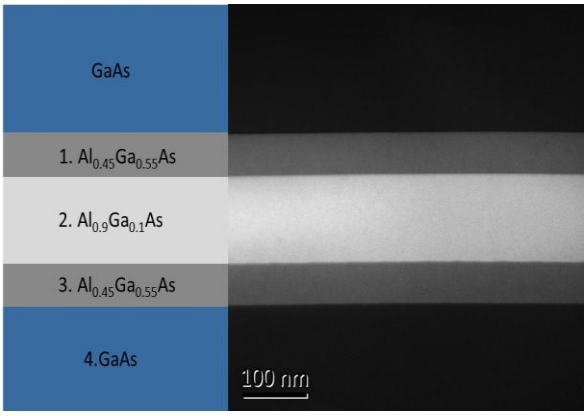

	Target thickness	TEM thickness
CL	150 nm	149.2 nm
1	50.6 nm	51 nm
2	109.9 nm	107.2 nm
3	50.6 nm	51.8 nm
4	192 nm	203 nm

Fig 6.6: Cross-sectional TEM micrograph of one period of the GaAs/ $Al_xGa_{(1-x)}As$ DBT stack (left) alongside a comparison of target and measured layer thicknesses (right).

To see the effect of the small differences between the target design layer thicknesses and those measured from the TEM cross-sections, the measured values were incorporated into the transfer matrix method (TMM) model to evaluate their impact on the optical performance. This approach allowed a direct comparison between the "as-designed" and "as-grown" DBT structures, enabling us to assess whether typical MBE growth tolerances could significantly alter the transmission spectrum and peak wavelength position.

The updated simulation (Fig 6.7. and Fig 6.8.) shows that the DBT resonance peak experiences a slight redshift of approximately 30-40 nm compared with the original design, shifting from 1310 nm to 1349 nm.

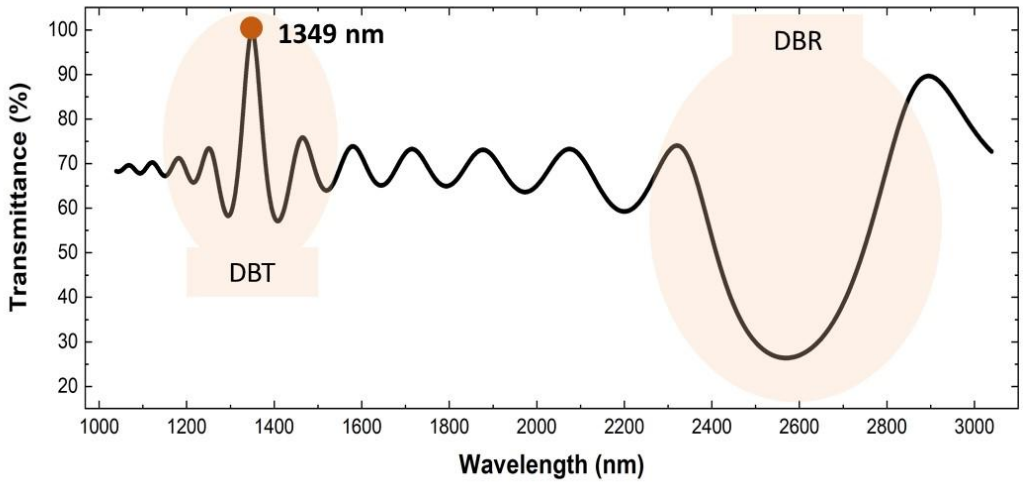

Fig. 6.7: Simulated DBT transmission spectra using TEM-measured thicknesses. A slight redshift of ~39 nm is observed in the TEM-based simulation, while the high-transmittance resonance and sideband structure are preserved, confirming the robustness of the DBT optical design to growth-induced thickness variations.

Importantly, the maximum transmittance remains above 98% and the sideband structure is preserved. This confirms that the DBT design is robust to small thickness deviations within typical MBE tolerances for the intended 1300-1350 nm emission window and the ~1 nm cap-layer variation does not catastrophically degrade performance. Notably, the same redshift is also observed in the experimental electroluminescence spectra presented in Section 6.2.7, providing strong evidence that the spectral shift originates from the measured structural deviations. Thus, TEM-informed simulations act as a bridge between idealised optical design and experimental characterisation, demonstrating the predictive reliability of the DBT modelling approach.

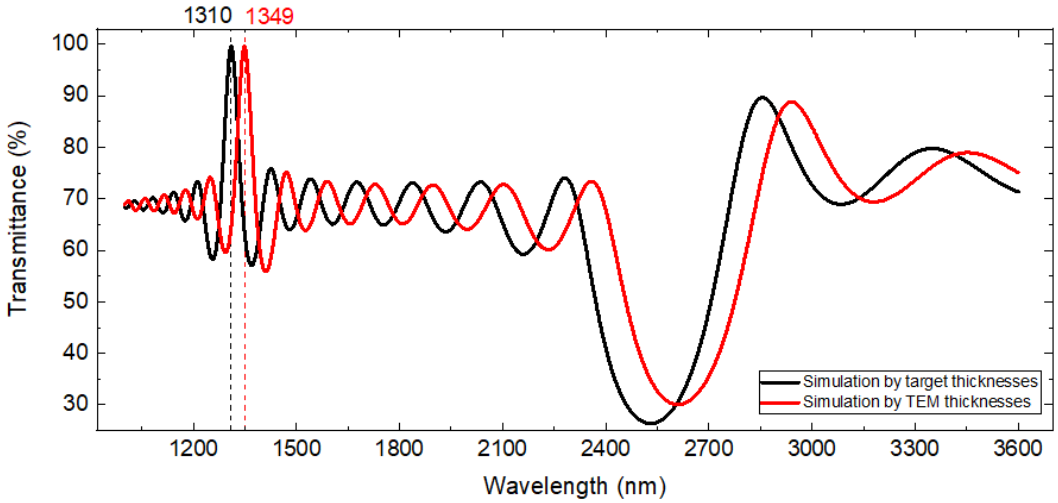

Fig. 6.8: Comparison of DBT transmission spectra. Black line: TMM simulation using targeted design layer thicknesses (λ_0 = 1310 nm). Red line: TMM simulation using TEM-measured layer thicknesses (λ_0 = 1349 nm).

6. 2.2. Structural and Optical Validation of DBT Layers by Ellipsometry

To ensure that the distributed Bragg transmitter (DBT) operates as designed, we carried out a combined structural and optical validation using cross-sectional transmission electron microscopy (TEM), spectroscopic ellipsometry (SE) and transmission spectroscopy. Ellipsometry measurements were taken in CSIC-IMN, Spain. Together, these techniques confirm both the accuracy of the epitaxial growth and the intended optical functionality of the multilayer stack.

(i) **TEM thickness calibration:** Table 6.2 compares the nominal design with TEM measurements. The agreement is excellent, with deviations below ~3% across all DBT layers. For example, the 110 nm $Al_{0.9}Ga_{0.1}As$ target was realized as 107.4 nm and the 51 nm $Al_{0.45}Ga_{0.55}As$ layers averaged 51.2-51.4 nm. This level of accuracy verifies that the quarter-wave design condition was reliably achieved during growth.

Table 6.2 Structural parameters of the DBT layers: TEM thickness and ellipsometry composition fits

	Material	TEM thickness	Al composition fitting by ellipsometry	Thickness values by ellipsometry
Cap layer	GaAs	149.2 nm		149 nm
DBT Repeat layers X 7	$Al_{0.45}Ga_{0.55}As$	51 nm	$Al_{0.45}Ga_{0.55}As$	51.2 nm
	$Al_{0.9}Ga_{0.1}As$	107.2 nm	$Al_{0.90}Ga_{0.10}As$	107.4
	$Al_{0.45}Ga_{0.55}As$	51.8 nm	$Al_{0.45}Ga_{0.55}As$	51.4
	GaAs	203 nm		203 nm

(ii) **Optical constants from SE:** Figure 6.9 shows variable-angle ellipsometry (Ψ, Δ at 60-70° incidence), fitted using transfer-matrix simulations constrained by the TEM thicknesses. The retrieved alloy compositions were $Al_{0.45}Ga_{0.55}As$ and $Al_{0.90}Ga_{0.10}As$, with estimated composition uncertainties of ±0.02 (Al fraction) from spectroscopic ellipsometry fitting, in excellent agreement with the nominal design values. The fit reproduces the oscillatory phase and amplitude with high fidelity (mean squared error (MSE) ≈ 19.4) and the extracted interface roughness of 1.96±0.03 nm indicates excellent epitaxial quality. These results confirm that the high index contrast essential for strong DBT interference is preserved in the actual structure.

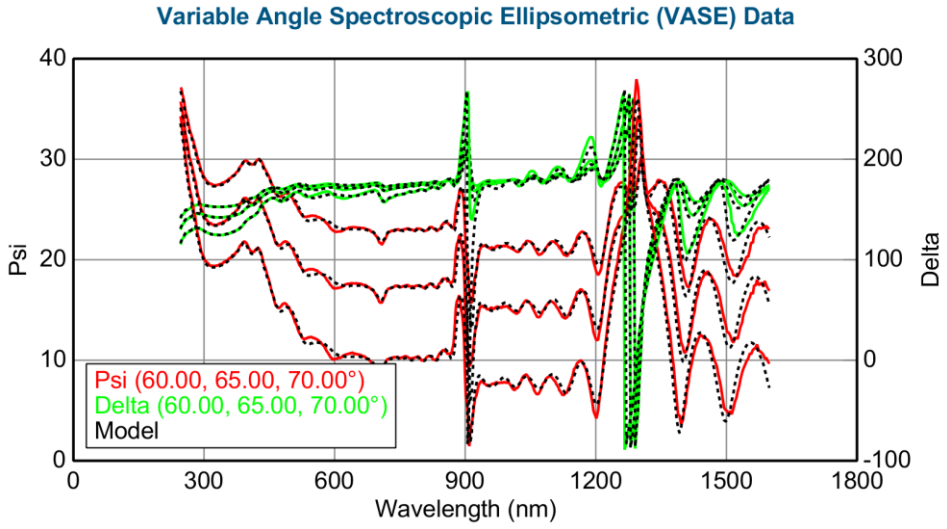

Fig. 6.9: Variable-angle spectroscopic ellipsometry (Ψ, Δ at 60-70°) fitted with transfer-matrix simulations constrained by TEM thicknesses. The retrieved Al compositions are close to design values; fitted roughness ≈ 2 nm confirms high interface quality.

By combining TEM thickness calibration, SE-derived optical constants and transmission validation, we show that the fabricated DBT closely matches its intended design both structurally and optically. The agreement between experiment and simulation validates the integrity of the multilayer stack and explains the spectral modulation pattern observed in

DBT-integrated LEDs. Consistent with this, the DBT acts as a wavelength- and angle-dependent transmission element that not only imprints fringes on the broadband QR emission but can also increase the collected EL intensity by reducing effective surface reflection within the escape cone (as quantified in Section 6.3.2.3). However, the measured modulation amplitude significantly exceeds the predictions of normal-incidence transfer-matrix simulations (few % at 1310 nm vs observed factor-of-two variation), indicating that additional effects such as finite-angle collection and angle-dependent interference contribute beyond a simple normal-incidence filtering picture.

6. 2.3. Device Fabrication

Following the MBE growth of the DBT-integrated and reference GaSb QR-LED wafers, 1 mm × 1 mm LED devices were fabricated for electrical and optical testing. Ohmic contacts were deposited on both the p-type top surface and the n-type substrate. For the top contact, an Au/Ni/Au metallisation stack was patterned into a finger-shaped geometry (Fig. 6.10) in order to ensure uniform current spreading across the device area while leaving sufficient aperture for light emission. The n-type backside contact was formed using an AuGe/Ni/Au stack.

Both contacts were annealed to promote interdiffusion and achieve low-resistance ohmic behaviour. Devices were then isolated by cleaving and mounted onto TO headers, with wire bonding used to provide electrical connection to the finger contacts. This process produced test-ready devices suitable for I-V and EL measurements.

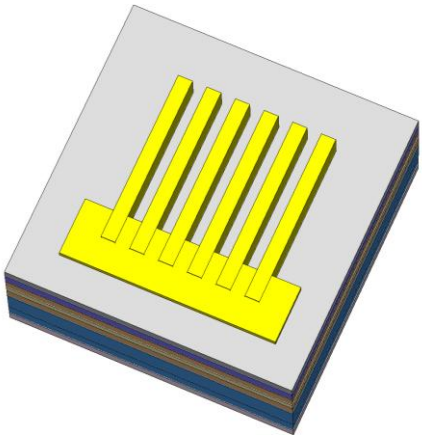

Fig. 6.10: Schematic of the fabricated GaSb QR-LED device structure with finger-shaped top contact (yellow) for uniform current distribution and enhanced optical emission.

6. 2.4. Photoluminescence Measurement: Normal vs DBT LEDs

Photoluminescence spectra were recorded at five positions (four corners and the centre) for both the reference GaSb QR-LEDs and the DBT-integrated devices under identical conditions (5 mW excitation, 3 s integration A narrow feature near ~0.80-0.82 μm is observed in all spectra; this originates from GaAs-related luminescence from the cap/substrate region and is not associated with the GaSb quantum-ring transition. The DBT is designed to minimise reflection near 1.3 μm and is not optimised for 820 nm; accordingly,

the 0.82 µm feature is used only as a qualitative check of the measurement chain and is not interpreted as a DBT-enhanced emission channel.

Normal LED devices are dominated by a broad peak centred at around 1.1-1.2 µm, attributable to type-II GaSb/GaAs QR transitions. A weak long-wavelength tail extends towards the 1.3 µm telecom region, but no distinct telecom-band peak is observed. The spectral shape and intensity are uniform across the device (corner ≈ centre), indicating good wafer-scale homogeneity (Fig. 6.11.)

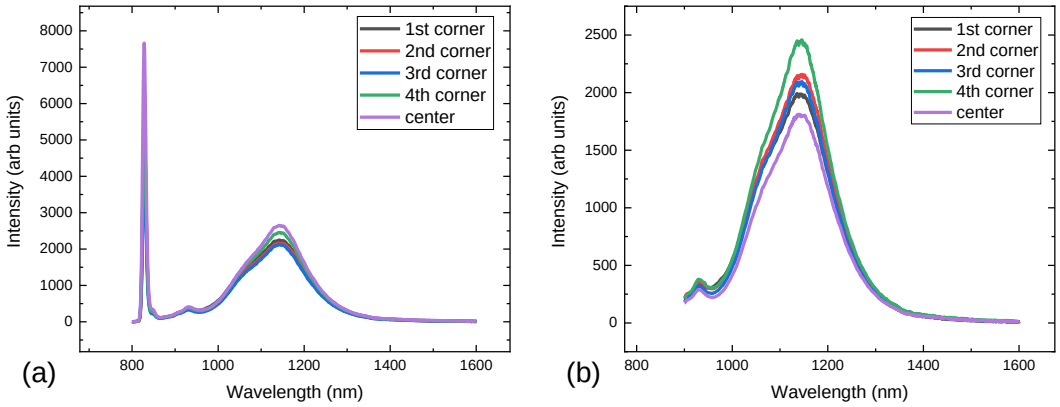

Fig. 6.11: Room-temperature PL of the reference GaSb QR-LEDs under 5 mW excitation. (a) Full 0.8-1.6 µm range: broad type-II peaks at around 1.1-1.2 µm; narrow feature at 0.80 µm is a GaAs-related artefact. (b) 0.9-1.6 µm zoom: telecom emission appears only as a weak long-wavelength tail towards ~1.3 µm; spectra are spatially uniform across the device.

DBT-integrated devices exhibit the same underlying type-II GaSb/GaAs quantum-ring emission band as the reference LEDs, with a relatively narrow maximum around 1.1-1.2 µm (Fig 6.12).

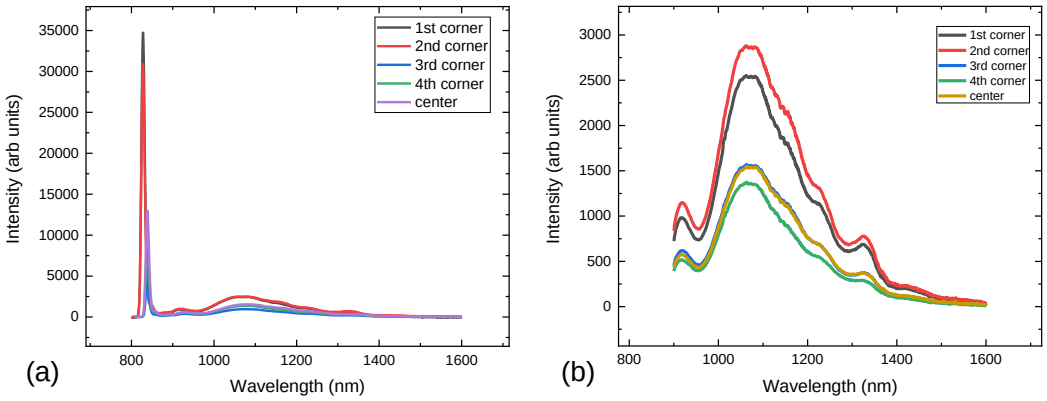

Fig. 6.12: Room-temperature PL spectra of DBT-integrated GaSb QR-LEDs (5 mW excitation). (a) Full 0.8-1.6 µm range. A broad type-II GaSb/GaAs emission band centred at ~1.1-1.2 µm is observed at all positions; the narrow feature near ~0.80 µm is attributed to GaAs-related background luminescence. (b) Zoom into the 0.9-1.6 µm region. All five locations (four corners and centre) exhibit similar spectral shape and intensity. Gentle ripples between 0.95 and 1.35 µm are consistent with thin-film interference in the DBT stack.

Spectra recorded at the four corners and the centre of the die show only modest spatial variation: all positions display the same spectral shape and comparable intensities, indicating that the DBT does not introduce strong spatial non-uniformity in the optically excited emission. In the 0.95-1.35 µm region, gentle spectral ripples are visible. These features are attributed to thin-film interference within the DBT multilayer and do not correspond to additional radiative transitions.

Overall, the PL spectra of the DBT devices demonstrate that the DBT preserves the intrinsic type-II emission of the quantum rings. Under optical excitation, any DBT-induced enhancement of the telecom-band out-coupling is subtle at the PL level, with the more significant DBT-related effects becoming evident in the electroluminescence measurements presented in Section 6.3.

6. 2.5. Time-Resolved Photoluminescence: Normal vs DBT LEDs

Time-resolved photoluminescence (TRPL) measurements were performed at low temperature (15K) using a 405 nm pulsed-excitation setup with a repetition period of T=200 ns. Emission was spectrally filtered around the peak of the type-II GaSb/GaAs quantum-ring band (1.1-1.2 µm) and temporal decays were recorded for both the reference LEDs and the DBT-integrated devices (Fig. 6.13.). Data were analysed over a fixed window (10-200 ns) chosen to exclude the prompt instrument-response region.

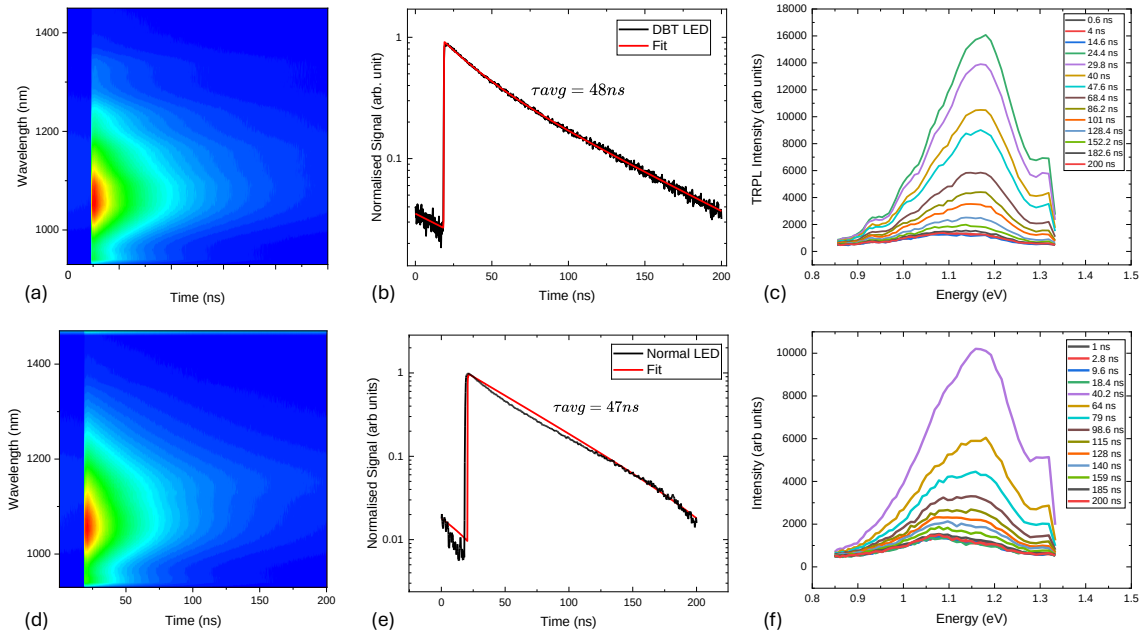

Fig. 6.13: TRPL characterisation of the DBT-LED (top) and normal LED (bottom) at 15K (a), (d) False-colour time-wavelength maps of the PL transient under periodic excitation (repetition period T= 200 ns). (b), (e) Semi-log decays at the PL-peak photon energy, normalised and fitted with a single exponential model; amplitudes are corrected for incomplete decay between pulses (repumping), which does not affect the extracted time constants. The photon-weighted mean lifetimes are τavg≈ 48 ns ±2 ns (DBT) and τavg≈47 ns ±2 ns (normal LED). (c), (f) Time-sliced spectra illustrating a mild red-shift and narrowing with increasing delay, consistent with carrier

cooling in the GaSb quantum-ring ensemble. The near identical kinetics and spectral evolution confirm that integration of the DBT stack does not alter the intrinsic recombination dynamics of the active region.

For both device types, the PL transients exhibit predominantly double-exponential decay, with photon-weighted mean lifetimes of τ_{avg}= 47- 48 ±2 ns. The fitting uncertainty (estimated from the standard errors returned by the least-squares optimisation) is typically within ±2 ns and within this range the decay times of the normal and DBT LEDs are indistinguishable.

The DBT is designed to reduce the reflection rather than to form a resonant cavity; therefore, no Purcell-type change in radiative lifetime is expected. Consequently, the near-identical TRPL kinetics primarily indicate that DBT integration does not introduce additional non-radiative recombination pathways in the optically pumped regime.

Time-wavelength maps and time-sliced spectra show the expected early-time carrier cooling (mild red-shift and narrowing) and no evidence of slow defect-related tails within the 200 ns observation window. The measured decay times of 47-48 ns are much slower than the sub-nanosecond lifetimes typical of type-I In(Ga)As quantum dots, yet still a factor of 4-6 shorter than the ≈200-300 ns values reported at room temperature for type-II GaSb/GaAs quantum rings from our group by Peter *et al.* [105] and by Jones [137]. This indicates that, under the present measurement conditions (room temperature and high-power pulsed excitation), the effective decay time is significantly influenced by non-radiative channels in addition to the intrinsic radiative lifetime. In this non-radiative-limited regime, TRPL primarily probes the combined radiative and non-radiative decay rate and becomes relatively insensitive to modest changes in the radiative component alone; any DBT-induced modification of the radiative rate that is small compared with the dominant non-radiative contribution would therefore produce only a minor change in the total decay constant.

Taken together, the TRPL results show that (i) both devices share the same effective non-radiative decay pathway under pulsed excitation, (ii) DBT integration does not introduce a resolvable change in the observed decay constant and (iii) within the sensitivity of these measurements, the recombination kinetics appear unaffected by the presence of the DBT stack. This is consistent with the DBT functioning primarily as an optical out-coupling structure rather than modifying carrier recombination [364], [365], [199]. Device-level differences arising from DBT integration manifest more clearly in the electroluminescence characteristics (Section 6.2.6) than in TRPL.

6 .3. Electrical Characterisation of Normal LEDs and DBT LEDs

6. 3.1. I-V Characteristics: Comparative Overview

Forward current-voltage (*I-V*) measurements were obtained at room temperature for four reference GaSb/GaAs quantum-ring LEDs (N1-N4) and four DBT-integrated devices (D1-D4). Measurements were taken over the accessible voltage range for each device; in several

cases the range was truncated to avoid irreversible electrical or thermal damage (for example, N2 was not driven above 1.5 V and D1 above 1.7 V). Linear and semi-logarithmic plots for the normal and DBT LED devices are shown in figures 6.14 and 6.15, respectively.

All devices exhibit clear rectifying behaviour. Within the low-bias region, leakage currents lie below the measurement floor ($\leq 10^{-8}$-10^{-7} A) over the range inspected, although this sub-threshold region is not fully plotted for every device due to acquisition limits. Forward conduction becomes appreciable between approximately 1.05 V and 1.6 V, with some device-to-device variation in the "knee" voltage. This variation is not specific to the DBT architecture: for example, N1 shows a noticeably higher knee voltage than the other normal LEDs, whereas D3 and D4 turn on at comparable biases to the better reference devices.

On semi-logarithmic current–voltage axes, both normal and DBT devices exhibit a clear exponential diode regime over approximately 0.9-1.3 V, characteristic of standard forward-biased III–V LEDs operating at room temperature. The overall slopes and turn-on behaviour are comparable across the two device sets, indicating that incorporation of the DBT multilayer does not significantly perturb the underlying diode transport mechanism. Variations between individual devices are attributed to differences in mesa definition and contact quality rather than to systematic effects associated with the DBT structure.

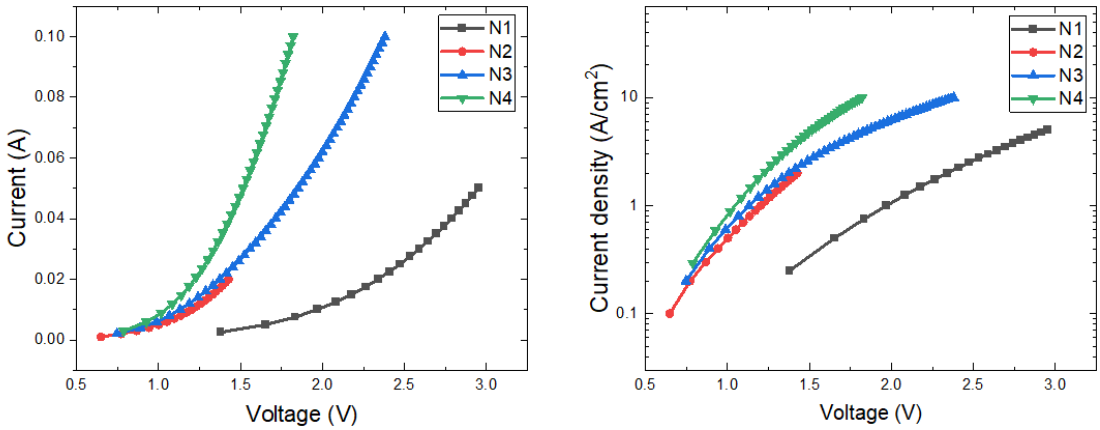

Fig. 6.14: Electrical characteristics of normal GaSb/GaAs QR-LEDs (N1-N4) at room temperature. (a) Forward current-voltage (*I-V*) curves on a linear scale. All devices show diode-like rectifying behaviour, with some variation in the accessible voltage and current ranges due to device-to-device differences and current-compliance limits. (b) Corresponding current-density-voltage (*J-V*) curves on a semi-logarithmic scale, calculated using an active area of 1 mm × 1 mm.

The high-bias deviation from ideality is governed by the series resistance R_s. To enable a fair comparison across devices with different turn-on voltages, R_s was extracted from the clearly linear high-current region of each *V(I)* curve, using a current window rather than a fixed voltage interval. For each LED, a least-squares linear fit was applied to the portion of the *JV* curve where the behaviour is locally ohmic.

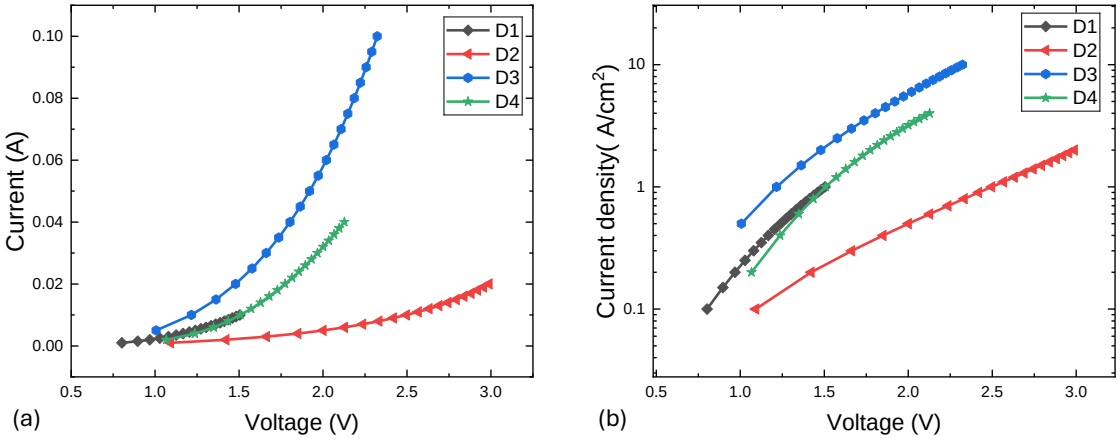

Fig. 6.15: (a) Forward current-voltage (*I-V*) characteristics of the DBT-integrated GaSb/GaAs QR-LEDs (D1-D4), plotted on a linear scale. All devices show diode-like rectifying behaviour, with differences in the accessible bias range arising from device-specific current handling (e.g., early termination of D1 to avoid damage). (b) Semi-logarithmic current-density-voltage (*J-V*) characteristics for the same devices. The exponential region and subsequent high-bias curvature illustrate the variation in dynamic series resistance across the DBT cohort. Data gaps at higher bias reflect conservative measurement limits rather than intrinsic device behaviour.

The uncertainty ΔR_s reflects the standard error of the fit together with the variation obtained when expanding or contracting the fit window by ±2 data points. This procedure avoids over-estimating R_s from low-current or non-ohmic regions and provides a consistent basis for comparing normal and DBT devices.

The resulting series resistances are summarised in table 6.3. Across the reference devices, the extracted values yield an average Rs = 14 ± 10 Ω. The DBT-integrated cohort gives Rs = 20 ± 10 Ω. Within the overlapping uncertainty ranges (3.9-23.7 Ω for normal; 8.7-37.6 Ω for DBT), the two cohorts are statistically indistinguishable. Devices such as D2 show elevated resistance, while N1 and D1 have truncated traces due to conservative current limits; these outliers are most plausibly attributed to mesa definition, contact quality or local layer-thickness variations rather than the DBT concept itself. Crucially, the best-performing DBT LEDs (D3-D4) achieve series resistances comparable to the best reference devices (N3-N4), indicating that DBT integration does not impose an intrinsic electrical penalty and allowing a direct comparison of optical performance in the following sections.

Table 6.3: Extracted series resistance R_s for normal and DBT LEDs

Normal LED Device	Fit window (A)	R_s (Ω)	DBT LED Device	Fit window (A)	R_s (Ω)
N1	0.033-0.050	24.4 ± 0.3	D1	0.0065-0.010	28.0 ± 5
N2	0.015-0.02	20.0 ± 0.3	D2	0.014-0.020	40.7 ± 1
N3	0.094-0.1	6.8 ± 0.1	D3	0.060-0.100	7.3±0.5
N4	0.088-0.100	4.0 ± 0.07	D4	0.026-0.040	16.6 ± 1.0
Normal mean± SD	-	14 ±10	Normal mean± SD	-	23 ± 10

6. 3.2. Current-Dependent Electroluminescence of Normal LEDs (N1-N4) and DBT LEDs (D1-D4)

EL spectra were recorded under continuous wave (CW) drive from 10 to 100 mA for eight devices: four normal LED samples (N1-N4) and four DBT-integrated devices (D1-D4). All measurements were conducted at room temperature using nominally identical optical collection and alignment settings to ensure consistency in comparative analysis.

6. 3.2.1. Normal LEDs (N1-N4)

The EL spectra of the reference devices exhibit a smooth, broadband emission envelope spanning 0.95-1.35 μm, dominated by the type-II transition in GaSb-based quantum rings (QRs), with a central peak typically located near 1.1-1.2 μm (Fig 6.16.). This emission feature is consistent across all reference devices and remains qualitatively unchanged as current increases, indicating spontaneous-emission-dominated operation with no evidence of lasing or stimulated emission up to 100 mA.

With increasing drive current, the emission intensity scales proportionally without any emergent structure or spectral narrowing. A slight blue shift and modest spectral broadening are observed with increasing current, attributed to capacitive charging effects within the type-II quantum ring ensemble consistent with observations reported in Chapter 5 (section 5.2.1). These phenomena are consistent with the carrier redistribution and recombination dynamics typical of spatially indirect transitions in type-II heterostructures. The spectral

shape remains effectively identical across devices N1-N4, suggesting uniform underlying radiative recombination dynamics.

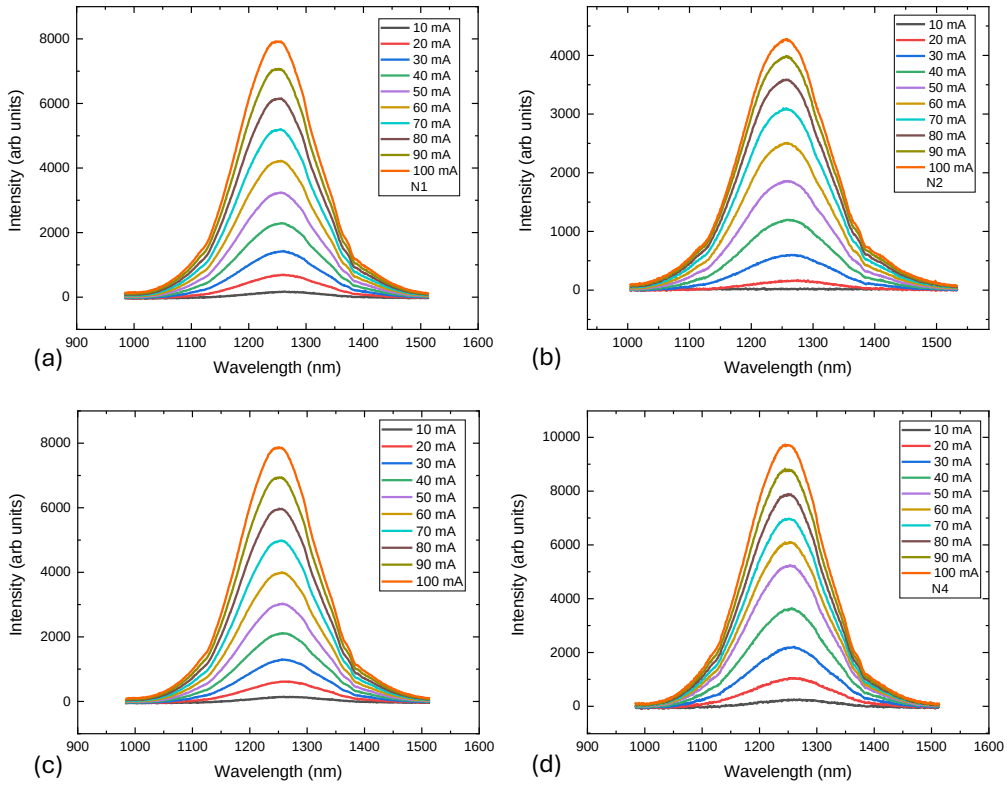

Fig. 6.16: (a-d) Current-dependent electroluminescence spectra of the GaSb QR-LEDs (N1-N4), measured from 10 mA to 100 mA at room temperature. All four devices exhibit a single, broad band centred at ~1.1-1.2 µm, characteristic of type-II recombination in GaSb QRs.

Minor differences in amplitude are noted between devices, which can be ascribed to variations in series resistance, thermal dissipation and current spreading. Because the optical collection was held constant across the cohort, these amplitude disparities are best interpreted as electrical or thermal in origin. Devices with higher series resistance are expected to dissipate more power as heat, leading to elevated junction temperatures and reduced radiative efficiency.

6. 3.2.2. DBT LEDs (D1-D4)

The DBT-enhanced devices similarly display the broadband QR emission envelope but superimposed with a distinct spectral modulation (Fig 6.17.). Sharp peaks and notches are present at fixed wavelengths and persist across the entire current range, increasing in amplitude with current but maintaining stationary spectral positions. This behaviour is indicative of thin-film interference effects originating from the DBT stack.

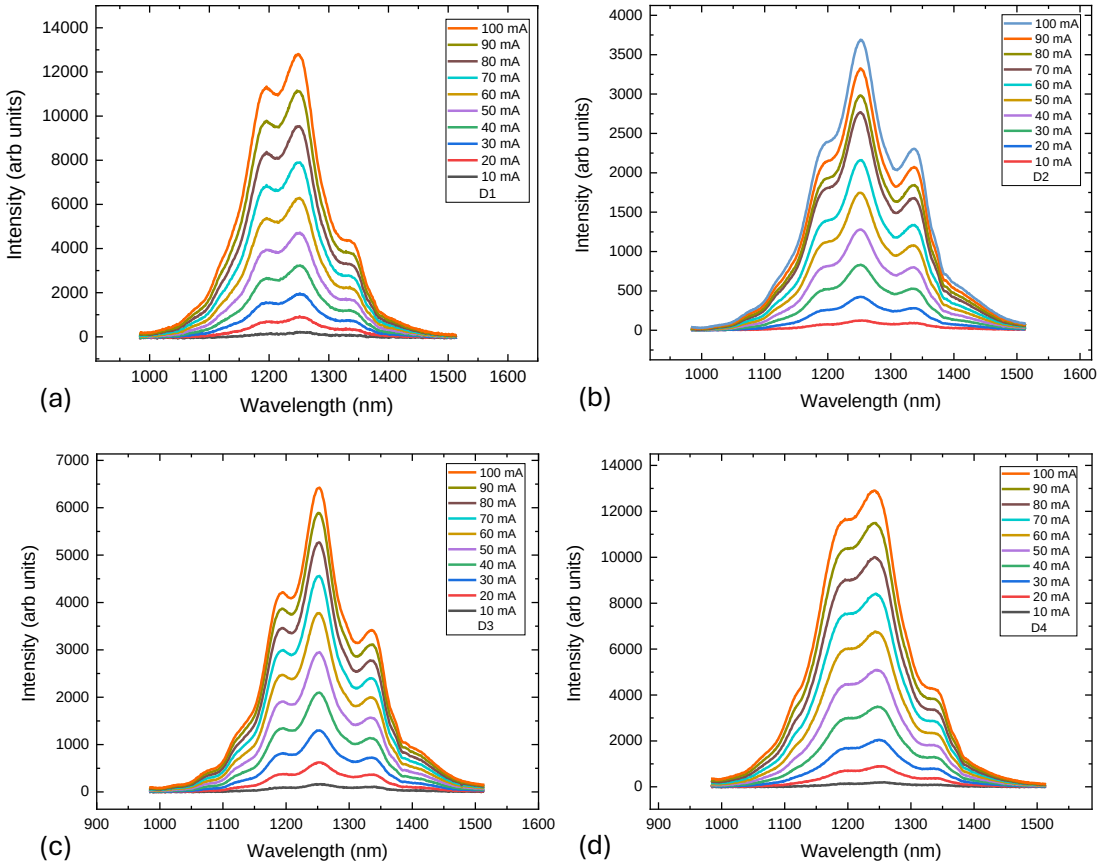

Fig 6.17: (a-d) Current-dependent electroluminescence spectra of the DBT-integrated GaSb QR-LEDs (D1-D4), measured from 10 mA to 100 mA under room temperature. In all devices, the broadband type-II emission is accompanied by a stable interference ripple imposed by the dielectric Bragg structure. The overall intensity scales with drive current, while the fringe positions remain spectrally fixed, confirming their optical rather than electronic origin.

The DBT structure introduces a wavelength- and angle-dependent transmission function, $T\_DBT(\lambda,\theta)$, which acts as a passive optical filter. This modulation subtly reshapes the broadband spontaneous emission spectrum without affecting the underlying carrier recombination dynamics, as demonstrated in Section 6.2.5. Crucially, the interference fringes imposed by the DBT remain spectrally stationary with increasing current, supporting their purely optical origin rather than arising from electronic transitions. While the spectral ripple remains fixed, the underlying broadband envelope exhibits a slight blue shift with current, consistent with capacitive charging effects associated with the type-II quantum ring system. This dynamic behaviour overlays the static optical modulation, highlighting the independent contributions of electronic and optical mechanisms to the observed electroluminescence.

6. 3.2.3. Comparative Analysis of Normal LEDs and DBT LEDs

To assess the impact of the distributed Bragg transmitter (DBT) in a statistically meaningful manner, a comparative analysis was performed across all fabricated devices: four reference

GaSb/GaAs quantum-ring LEDs (N1-N4) and four DBT-integrated LEDs (D1-D4). All measurements were conducted under nominally identical optical collection and alignment conditions to enable direct comparison.

The apparent "multi-peaks" in DBT-integrated EL arise from the wavelength-dependent transmission of the DBT stack (thin-film interference fringes) superimposed on the intrinsically broad QR emission band. In this thesis, the "peak wavelength" is defined as the wavelength of the global maximum of the measured EL spectrum at each drive current. For DBT devices, this definition can be influenced by the fringe pattern (i.e., by which fringe happens to be highest), so peak-based comparisons are interpreted together with the band-integrated EL intensity, which is treated as the more robust metric for overall collected output.

Figures 6.18(a) and 6.18(b) show the evolution of the peak emission wavelength and corresponding photon energy as a function of injection current for all devices. Across both normal and DBT-integrated LEDs, a systematic blueshift is observed with increasing current. This behaviour is consistent with canonical type-II recombination in GaSb/GaAs heterostructures and is commonly attributed to electric-field screening and the resulting increase in electron-hole wavefunction overlap under higher carrier injection.

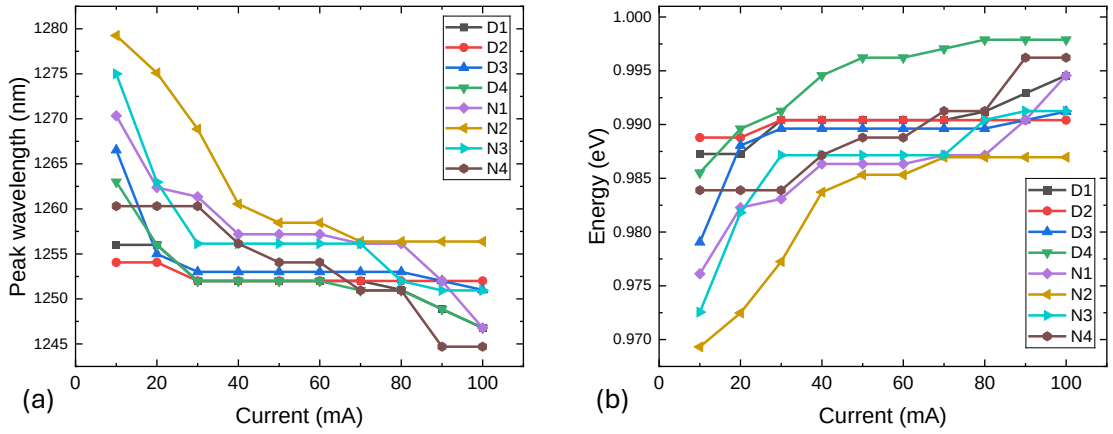

Fig. 6.18: (a) Peak emission wavelength as a function of injection current for all normal (N1-N4) and DBT-integrated (D1-D4) GaSb/GaAs quantum-ring LEDs. (b) Peak emission energy versus injection current for reference (N1-N4) and DBT-integrated (D1-D4) devices. The energy blueshift mirrors the wavelength trends and follows a comparable magnitude and functional form across all devices.

Importantly, no qualitative distinction is observed between normal and DBT devices in either peak wavelength or peak energy trends. While device-to-device variations are present, the overall magnitude and functional form of the blueshift are comparable across all eight devices. This indicates that incorporation of the DBT does not fundamentally alter the band structure or carrier recombination pathways within the quantum-ring active region.

The evolution of the FWHM is shown in Fig. 6.19, plotted against current density to allow comparison across devices with different mesa sizes. For all devices, the emission linewidth

lies in the range of approximately 155-185 nm and varies only weakly with increasing drive. Minor narrowing is observed in several devices at moderate current densities, while others remain effectively constant within experimental uncertainty.

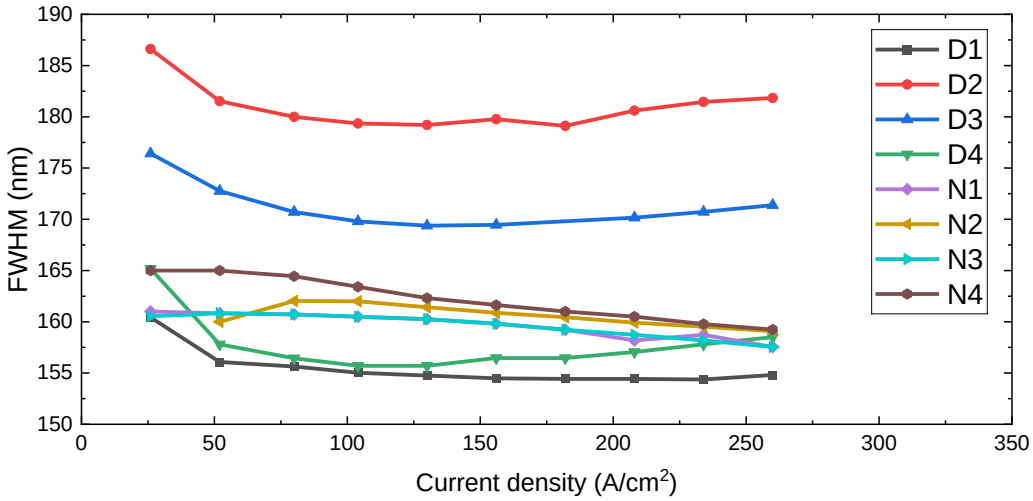

Fig. 6.19: FWHM of the electroluminescence spectra plotted against current density for all devices.

An isolated outlier previously observed for D3 around $J \approx 180$ A cm^{-2} (attributed to FWHM extraction sensitivity in the presence of DBT-induced fringes / limited SNR) was excluded from the dependence plot for clarity; this does not affect the overall trends.

Crucially, DBT-integrated LEDs do not exhibit any systematic linewidth broadening or narrowing relative to reference devices. The similarity in FWHM evolution confirms that the DBT does not introduce additional inhomogeneous broadening or modify the intrinsic recombination linewidth of the quantum-ring ensemble. The dominant spectral changes with current therefore arise from the redistribution of spectral weight rather than modification of the emission bandwidth itself.

Figure 6.20(a) compares the peak electroluminescence intensity as a function of injection current for all devices. In linear scale, DBT-integrated LEDs consistently exhibit higher collected peak intensity than reference LEDs across the full current range. However, the magnitude of this enhancement is strongly current dependent.

To highlight this behaviour, the same data are replotted on a semi-logarithmic scale in Fig. 6.20(b). This representation reveals that at low injection currents (≈10-30 mA), DBT-integrated devices outperform normal LEDs a factor of 4-5 in peak intensity at low injection (≈10–20 mA). As the current increases, the relative enhancement progressively diminishes, converging toward a factor of approximately two at the highest injection levels.

To quantify the DBT effect, we compare both the peak spectral intensity and the band-integrated EL intensity (983–1514 nm) at matched drive currents under nominally identical collection settings. Here, the peak intensity is defined as the global maximum detector counts within the measured EL spectrum at each drive current (within the plotted EL range). For DBT LEDs this maximum typically corresponds to the highest interference-fringe

maximum, whereas for reference LEDs it corresponds to the maximum of the smooth broadband envelope. Since the DBT introduces spectral fringes, peak intensity can be sensitive to which fringe maximum dominates; therefore, the integrated intensity is treated as the more robust indicator of overall collected output. This trend is consistent with the band-integrated analysis shown in Fig. 6.21. The injection-dependent behaviour is observed across multiple devices and is not driven by a single outlier, suggesting that it is not solely attributable to trivial device-to-device variation, although collection sensitivity and electrical/thermal differences remain contributing factors.

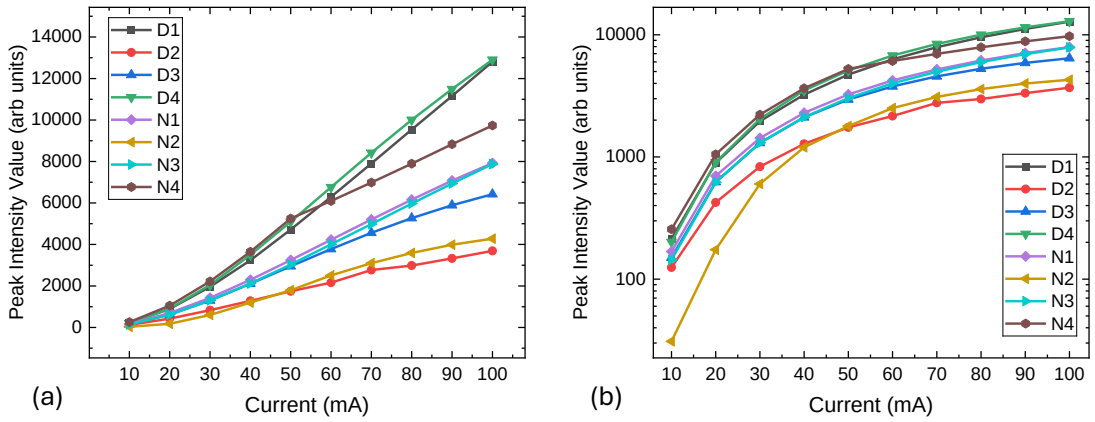

Fig. 6.20: (a) Peak electroluminescence intensity as a function of injection current (linear scale) for normal and DBT-integrated LEDs. (Peak intensity is taken as the global maximum of the measured EL spectrum at each current; for DBT LEDs, this is typically the highest fringe maximum) (b) Peak electroluminescence intensity replotted on a semi-logarithmic scale to emphasise relative enhancement at low injection currents.

Figure 6.21 shows the integrated electroluminescence intensity over the 983-1514 nm spectral range as a function of current. The integrated intensity trends mirror those observed in the peak intensity data: DBT devices consistently yield higher collected output, with the strongest relative enhancement at low injection and reduced contrast at high injection.

The agreement between peak and integrated intensity analyses confirms that the enhancement is not limited to a narrow spectral feature but reflects a global increase in collected emission within the telecom-relevant wavelength range.

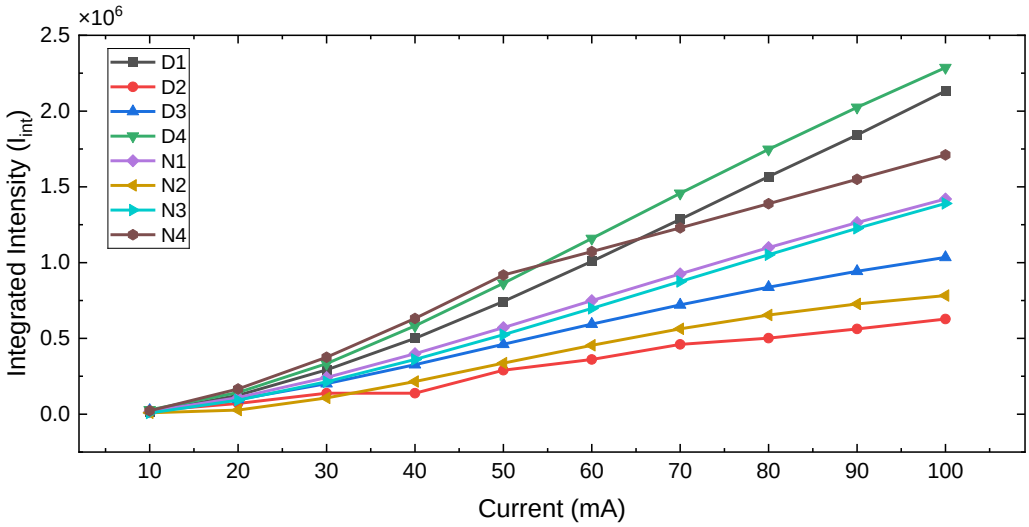

Fig. 6.21: Integrated electroluminescence intensity (983-1514 nm) as a function of injection current for all devices.

Taken together, these results demonstrate that incorporation of the DBT does not significantly affect the intrinsic spectral position, linewidth, or current-induced blueshift behaviour of GaSb/GaAs quantum-ring LEDs. Instead, the primary impact of the DBT is to increase the collected emission intensity.

Using the peak intensity metric, the DBT devices show an enhancement factor

$$G = \frac{I_{peak}^{DBT}(I)}{I_{peak}^{normal}(I)} \tag{6.4}$$

of 5.4× at 10 mA and 4.0× at 20 mA, reducing towards almost 1.85× at 100 mA (Fig. 6.20).

Since the DBT introduces spectral fringes, peak intensity can be sensitive to the DBT fringe pattern (i.e., which fringe maximum dominates) and to small variations in collection geometry; therefore, the band-integrated intensity (Fig. 6.21) is treated as the more robust indicator of overall collected output.

The strong enhancement observed at low injection, followed by convergence at higher current, cannot be straightforwardly explained by a purely geometrical out-coupling argument alone, as geometrical factors are invariant with carrier density. While the DBT transmission profile clearly imposes a static spectral modulation, the injection-dependent intensity enhancement suggests that additional mechanisms, potentially involving carrier dynamics or radiative recombination efficiency, may contribute, particularly in the low-current regime.

Time-resolved photoluminescence measurements performed under high-excitation conditions do not reveal measurable differences in carrier lifetime between reference and DBT devices; however, such measurements probe a regime more representative of high

injection, where the relative enhancement is already reduced. Consequently, the low-current enhancement observed here remains an open question and motivates further investigation.

Overall, the comparative analysis across eight devices establishes a consistent and reproducible trend: DBT integration yields a substantial improvement in collected emission, most pronounced at low injection currents, while preserving the fundamental optical characteristics of the underlying type-II quantum-ring active region.

6. 3.3. Temperature-Dependent Electroluminescence of Normal LEDs (N1-N4) and DBT LEDs (D1-D4)

6. 3.3.1. Normal LEDs (N1-N4)

The temperature response of the reference GaSb QR-LEDs is shown in figure 6.22 (a-d). As we increase the stage temperature from 20 °C up to 80 °C at a fixed injection of 50 mA, two things consistently happen: the peak emission wavelength shifts to longer values (a redshift) and the overall emission intensity steadily drops. The spectra remain smooth and broadband, without any signs of ripple or modal features, which is exactly what we would expect from a type-II QR-LED dominated by spontaneous emission.

The redshift arises from bandgap shrinkage according to the Varshni empirical relation [366]:

$$E_g(T) = E_g(0) - \frac{\alpha T^2}{T+\beta}, \tag{6.3}$$

where $E_g(T)$ is bandgap energy (in eV) at temperature T(in K), $E_g(0)$ is bandgap energy at 0 K, α is temperature coefficient and β is the Debye temperature. The bandgap reduction between 20 °C and 80 °C corresponds to several tens of meV, which in the 1.1-1.2 μm region produces a red-shift of order ~40-80 nm. The exact value depends not only on the intrinsic bandgap shift but also on band offsets in the GaSb/GaAs interface and the type-II spatial separation of carriers, a geometry where electrons are confined primarily to the GaAs layer and holes to the GaSb layer, thereby modulating the effective recombination energy. The shift observed experimentally is therefore consistent with expectations for GaSb/GaAs type-II emission, without requiring additional mechanisms beyond the Varshni-driven bandgap shrinkage.

A secondary contribution may come from thermally assisted redistribution of carriers within the inhomogeneously broadened quantum-ring ensemble. At elevated temperatures some carriers may access shallower states, subtly modifying the ensemble-averaged transition energy. However, this effect cannot be isolated unambiguously in the present data and is expected to be smaller than the dominant Varshni-driven bandgap shrinkage.

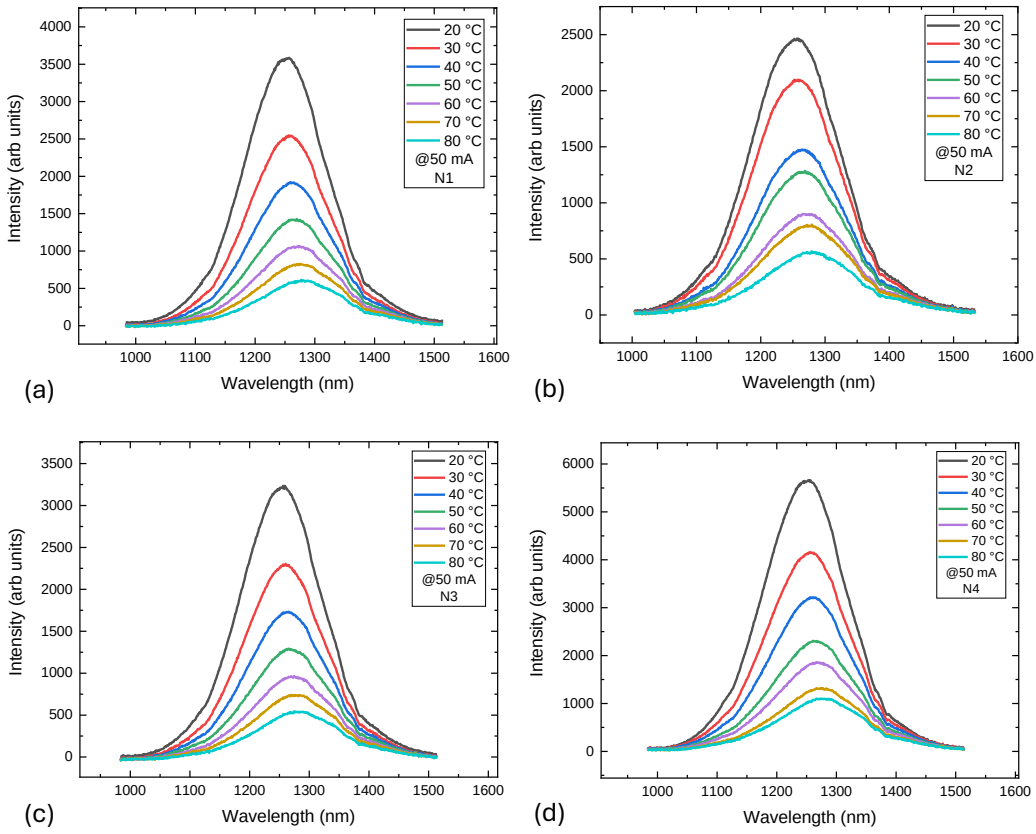

Fig. 6.22: Temperature-dependent electroluminescence spectra of the normal GaSb QR-LEDs (N1-N4) measured at a fixed injection current of 50 mA. All devices exhibit a monotonic redshift of the emission peak and a reduction in intensity as the stage temperature is increased from 20 °C to 80 °C. The smooth, broadband line shapes remain featureless across all devices, consistent with spontaneous-emission-dominated type-II recombination and thermally activated non-radiative losses.

The reduction in EL intensity with increasing temperature is likewise expected. Higher temperatures activate additional non-radiative recombination channels, including Shockley-Read-Hall (SRH) and Auger processes where a recombining carrier transfers its energy to another carrier, a process that becomes increasingly significant at elevated temperature and higher carrier densities and can modify the charging configuration of the quantum rings. Previous studies of GaSb/GaAs type-II nanostructures have shown that thermally assisted rearrangement or escape of excess holes can shift the emission energy and reduce quantum efficiency [367]. The relatively small differences among N1-N4 are therefore attributed mainly to device-level variations such as thermal impedance and series resistance, not to intrinsic differences in the active region.

The evolution of the FWHM with temperature provides additional information (Sec. 6.2.7.5). As the lattice temperature increases, enhanced carrier-phonon scattering and thermal redistribution within the quantum-ring ensemble led to a modest broadening of the emission spectrum. In the normal LEDs this broadening is clearly resolvable in the data,

indicating that their emission is sensitive to thermal fluctuations, even though the line shape remains smooth and featureless across the measured range.

6. 3.3.2. DBT LEDs (D1-D4)

The DBT-integrated LEDs exhibit the same fundamental temperature response as the reference devices: the broadband background redshifts and the intensity decreases as the temperature is increased from 20 °C to 80 °C at a fixed current of 50 mA (Fig 6.23). These changes reflect the same bandgap shrinkage and thermally activated non-radiative processes discussed above.

From 20 °C to 80 °C, the positions of the peaks and notches stay locked in place, even as the broadband emission underneath drifts steadily to longer wavelengths.

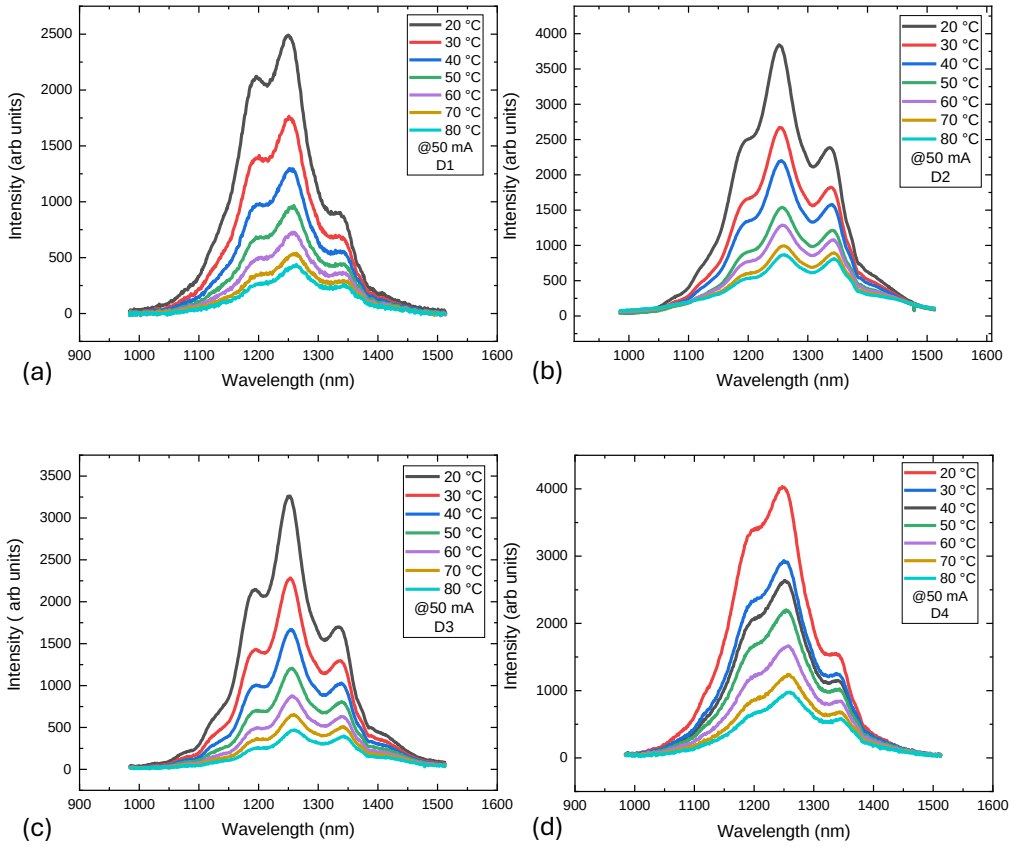

Fig. 6.23: (a-d) Temperature-dependent electroluminescence spectra of the DBT-integrated GaSb QR- LEDs (D1-D4), measured at a fixed current of 50 mA. As the stage temperature increases from 20 °C to 80 °C, the broadband emission undergoes a progressive redshift and intensity reduction, consistent with bandgap shrinkage and enhanced non-radiative recombination.

However, the DBT introduces a qualitative difference: the interference-fringe pattern remains fixed in wavelength across the entire temperature range. The positions of the spectral maxima and minima, defined by the optical thickness of the DBT layers, are essentially temperature-independent over this range because the refractive-index variations in the multilayer are small compared with the bandgap shrinkage of the active medium. For

typical III-V materials, dn/dT is on the order of 10^{-4} K^{-1}, so over a 60 K change the fractional index change is only a few $\times 10^{-3}$, corresponding to a shift of only a few nanometres in the DBT resonances. In contrast, the type-II emission band shifts by several tens of nanometres. Thus, while the underlying broadband emission drifts to longer wavelengths, the DBT continues to act as a fixed spectral and angular filter.

Notably, the temperature-dependent spectral linewidth (FWHM) evolution differs between the two device cohorts. While both normal and DBT LEDs show linewidth broadening with temperature, the DBT devices broaden more than the normal LEDs (Fig. 6.24(c)). This indicates that the fixed DBT transmission profile does not suppress the underlying thermal broadening of the spontaneous-emission spectrum. Instead, the combination of a thermally broadening type-II emission band with a static DBT transmission function can lead to an apparent enhancement of the effective linewidth in the transmitted spectrum compared to the intrinsic active-region broadening, particularly if the DBT resonance width and the emission broadening have comparable scales. In this sense, the DBT's spectral shaping is effective for static out-coupling enhancement at room temperature but does not mitigate thermal effects on the emission linewidth. The ripple contrast weakens slightly at high temperature due to the reduced overall signal, but the structured spectral profile remains visible throughout the measured range.

6. 3.3.3. Comparative Discussion on Temperature-Dependent EL

To further assess the impact of DBT integration on device behaviour and to distinguish intrinsic material effects from optical filtering and device-to-device variability, the temperature dependence of the electroluminescence (EL) was analysed across the full set of normal (N1-N4) and DBT-integrated (D1-D4) GaSb/GaAs quantum-ring LEDs. Measurements were performed over the temperature range 20-80 °C at fixed injection current and under identical optical collection conditions.

This ensemble-based approach avoids over-interpretation of individual devices and enables identification of systematic trends relevant to practical operation at and above room temperature.

Figure 6.24 (a,b) summarises the evolution of the EL peak wavelength and peak emission energy as a function of temperature for all eight devices. In all cases, increasing temperature produces a monotonic redshift of the emission peak, corresponding to a reduction in peak energy. This behaviour is consistent with bandgap narrowing and thermally induced changes in carrier confinement in type-II GaSb/GaAs heterostructures.

While the absolute magnitude of the redshift varies between individual devices, no systematic separation between the reference and DBT-integrated cohorts is observed. Both device classes exhibit comparable temperature coefficients, indicating that DBT integration does not modify the intrinsic temperature dependence of the quantum-ring emission. Differences previously observed in individual devices therefore reflect device-specific spectral alignment and optical filtering effects rather than a fundamental change in recombination physics.

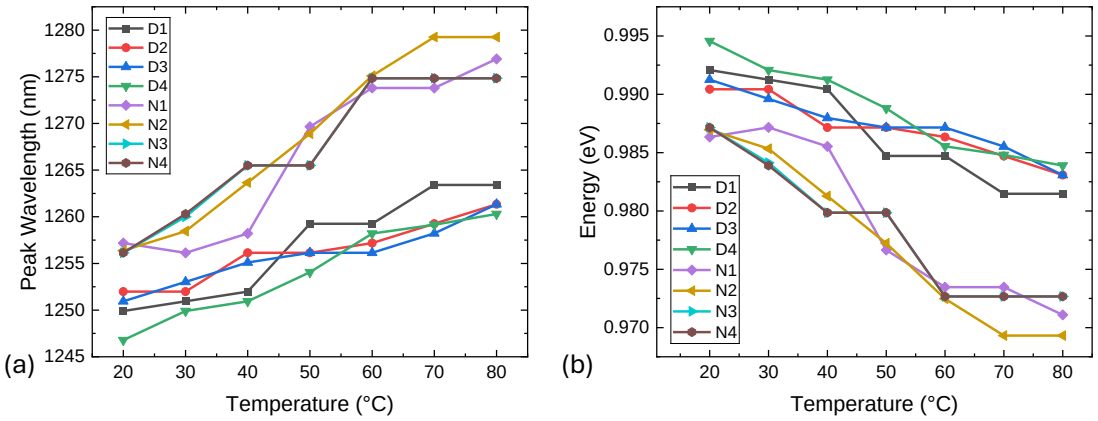

Fig. 6.24: (a) Temperature dependence of the peak electroluminescence wavelength for reference (N1-N4) and DBT-integrated (D1-D4) GaSb/GaAs quantum-ring LEDs measured at a fixed injection current. (b) Peak emission energy as a function of temperature for reference and DBT-integrated GaSb/GaAs quantum-ring LEDs.

The temperature dependence of the spectral linewidth, quantified by the full width at half maximum (FWHM), is shown in Fig. 6.25. All devices exhibit linewidth broadening with increasing temperature, as expected from enhanced carrier-phonon interactions, thermal population of higher-energy states, and increased inhomogeneous broadening in type-II systems.

Although some DBT-integrated devices display larger absolute linewidths at elevated temperatures, this behaviour is not universal across the DBT cohort and comparable broadening trends are observed among the reference LEDs. The observed spread in FWHM therefore reflects substantial device-to-device variability. The data are consistent with convolution between a thermally evolving broadband emission spectrum and the fixed spectral transmission profile of the DBT, rather than a systematic degradation of recombination quality induced by DBT integration.

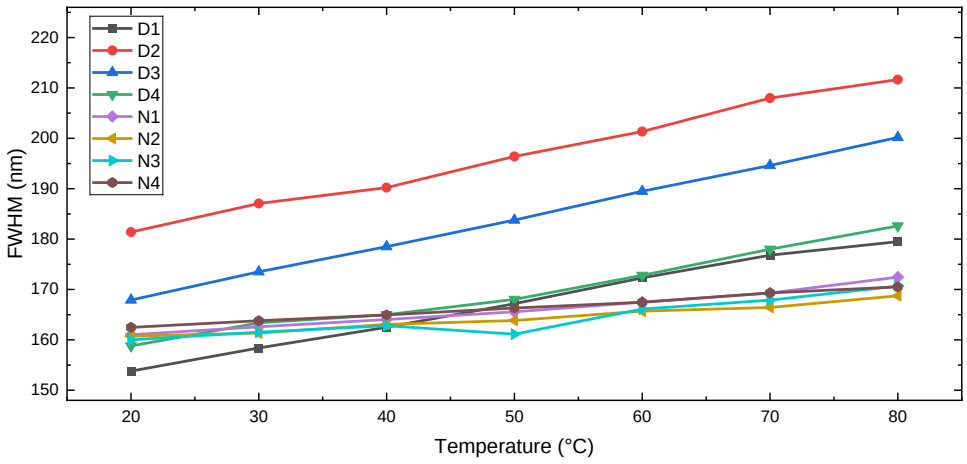

Fig. 6.25: FWHM of the electroluminescence spectra as a function of temperature for reference (N1-N4) and DBT-integrated (D1-D4) devices.

The integrated EL intensity decreases monotonically with increasing temperature for all devices, reflecting thermally activated non-radiative recombination processes. To quantify thermal quenching, Arrhenius analysis was performed by plotting ln(I_{int}) as a function of inverse temperature (1/T, with T in Kelvin), as shown in Fig. 6.26 (a,b). The data were fitted with a linear model of the form

$$ln(I_{int}) = \alpha + b\left(\frac{1}{T}\right), \tag{6.1}$$

from which an activation energy Ea is extracted via the slope. Across the reference devices (N1-N4), the fitted slopes cluster in the range b≈2.41×10^3 to 3.06×10^3 (in the units defined by the chosen 1/T scaling), corresponding to comparable activation energies within experimental uncertainty. Similarly, the DBT-integrated devices (D1-D4) exhibit slopes that are broadly consistent with the reference set for three devices (D1, D3) but show increased scatter for others (e.g. D4), as reflected by the reduced goodness-of-fit (lower R^2).

Across the full device set, several LEDs from both cohorts (N1, N3, D1 and D3) yield activation energies clustered around Ea ≈ 0.25-0.26 eV, consistent with strong hole confinement in GaSb quantum rings and thermally assisted carrier escape processes reported for similar type-II systems are summarised in Table 6.4. Other devices (e.g. N2, D2 and D4) exhibit increased scatter and reduced goodness-of-fit, particularly for D4, where the uncertainty in the fitted slope is large. The lower apparent activation energy extracted for D2 may reflect limited signal-to-noise ratio and increased sensitivity to alignment at elevated temperatures, rather than a distinct physical quenching mechanism. These variations highlight the sensitivity of intensity-based analysis to device-specific factors and experimental alignment.

Table 6.4. Activation energies extracted from Arrhenius analysis of integrated EL intensity

Device	Structure	Ea (meV)	Fit range (°C)	R^2
N1	Normal	255 ± 20	20-80	0.999
N2	Normal	208 ± 11	20-80	0.986
N3	Normal	264 ± 6	20-80	0.998
N4	Normal	235 ± 6	20-80	0.997
D1	DBT	264 ± 2	20-80	0.999
D2	DBT	124 ± 11	20-80	0.963
D3	DBT	257 ± 3	20-80	0.999
D4	DBT	173 ± 40	20-80	0.792

Taken as an ensemble, the Arrhenius analysis therefore does not provide evidence for a systematic change in the dominant thermally activated loss pathway upon DBT integration. Instead, any differences between devices are primarily expressed through the prefactor α and through device-to-device variability in the fit quality, which is most plausibly driven by differences in signal-to-noise at elevated temperature and by small variations in optical

collection/alignment during temperature sweeps. This is most naturally interpreted as the DBT modifying the collected emission through spectral and angular weighting, while leaving the underlying thermal quenching behaviour broadly comparable across the two cohorts. However, given the sensitivity of absolute intensity to experimental alignment/collection conditions (and, for DBT devices, additional spectral/angular weighting by the stack), the Arrhenius results are interpreted conservatively: they support similarity of quenching energetics across devices, but do not uniquely identify the microscopic origin of the enhanced low-current intensity observed in the DBT devices.

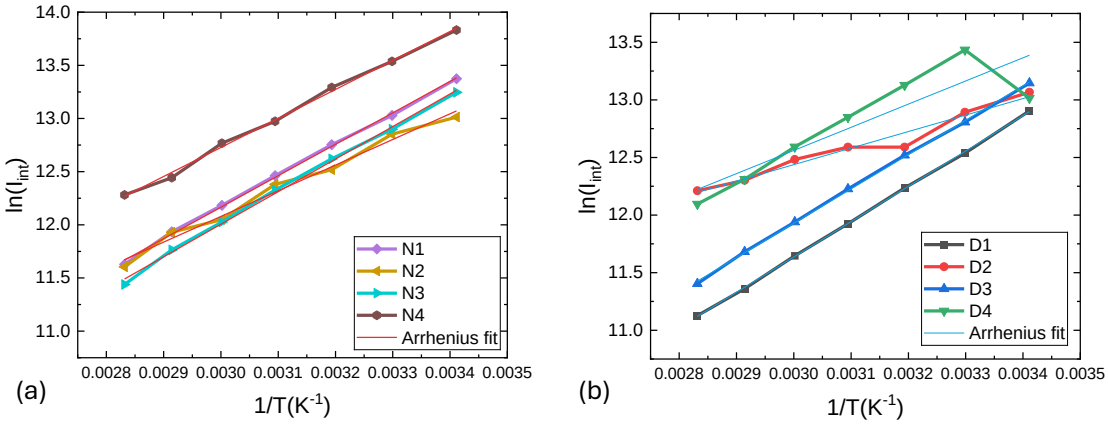

Fig. 6.26: Activation energies extracted from Arrhenius fits for (a) normal and (b) DBT-integrated GaSb/GaAs quantum-ring LEDs. Devices N1, N3, D1 and D3 cluster around Ea ≈ 0.25-0.26 eV, while others show larger uncertainties or reduced goodness-of-fit. The spread reflects device-to-device variability rather than a systematic effect of DBT integration.

6. 3.4. Transmission Characteristics and Spectral Modulation of the DBT

To clarify the optical role of the distributed Bragg transmitter (DBT) and to provide an appropriate reference for the device-level electroluminescence (EL) measurements, the transmission characteristics of the DBT stack were first investigated independently and compared with transfer-matrix-method (TMM) simulations based on experimentally determined layer thicknesses.

Transmission spectra were measured using a double-beam spectrophotometer (Cary 5000) at nominally normal incidence with unpolarised light, employing a spectral step of 1 nm and integration times between 0.5 s and 10 s depending on signal-to-noise ratio. Integration time (0.5–10 s) and detector gain/settings were adjusted between scans to optimise signal-to-noise and avoid saturation, depending on the sample transmission level. These settings affect the absolute scaling and noise floor, but not the spectral positions of maxima/minima, which are the quantities compared with the TMM model and used to identify DBT-induced modulation. The measured percent transmittance was referenced to an open-beam baseline and corrected for instrumental response. The resulting transmission spectrum is shown in Fig. 6.27 (blue trace), alongside the corresponding TMM simulation (black trace) calculated using layer thicknesses extracted from transmission electron microscopy.

The DBT exhibits a pronounced transmission maximum of approximately 50% in the wavelength range 1.34-1.38 μm, in close agreement with the simulated peak transmittance of ≈52%. The correspondence between the measured and simulated spectra confirms both the structural fidelity of the grown multilayer stack and the validity of the optical model used in its design. Minor discrepancies in fine spectral features are expected due to the simplifying assumptions of the simulation, including idealised layer interfaces and strict normal-incidence conditions.

A striking difference between DBT-integrated LEDs and reference devices is the presence of strong spectral modulation in the EL spectra of the DBT LEDs, as illustrated in Fig. 6.27 (red trace). This modulation closely mirrors the oscillatory sideband structure observed in the DBT transmission spectrum and is absent in the emission from reference LEDs without the DBT. The correspondence in spectral periodicity indicates that the DBT imposes its interference-based transmission profile onto the emitted light, acting as a wavelength-dependent optical filter.

However, the magnitude of the modulation observed in EL exceeds that expected from the normal-incidence TMM simulation alone. While the simulated and measured transmission spectra show modulation on the order of several percent, the EL modulation can approach a factor-of-two variation in collected intensity. This discrepancy indicates that the DBT-LED system cannot be fully described as a simple normal-incidence optical filter acting on a static emission spectrum.

It is important to note that both transmission measurements and EL collection inherently integrate over a finite angular range. In high-refractive-index III-V semiconductors, total internal reflection already restricts emission to a narrow escape cone even in the absence of a DBT. As such, purely geometric arguments based on angular redistribution are insufficient to fully account for the observed spectral modulation and its magnitude. In particular, the fixed geometry of the DBT stack cannot, by itself, explain the strong current-dependent modulation amplitude observed in EL.

The data therefore suggest that while the DBT transmission function clearly shapes the spectral envelope of the emitted light, additional effects may contribute to the observed behaviour. In particular, the interaction between the DBT optical environment and the emitting active region under electrical injection may influence how spontaneous emission is spectrally redistributed and collected, especially at low injection levels. At present, the available measurements do not allow this effect to be uniquely attributed to a specific mechanism.

Importantly, the DBT transmission peak itself is not observed as a sharp, isolated feature in the EL spectra; rather, the emission reflects a convolution of the broadband type-II GaSb/GaAs quantum-ring emission with the DBT transmission profile. As the intrinsic emission spectrum shifts with current and temperature, different portions of the DBT transmission function are sampled, leading to the observed modulation without implying wavelength locking or intrinsic spectral stabilisation.

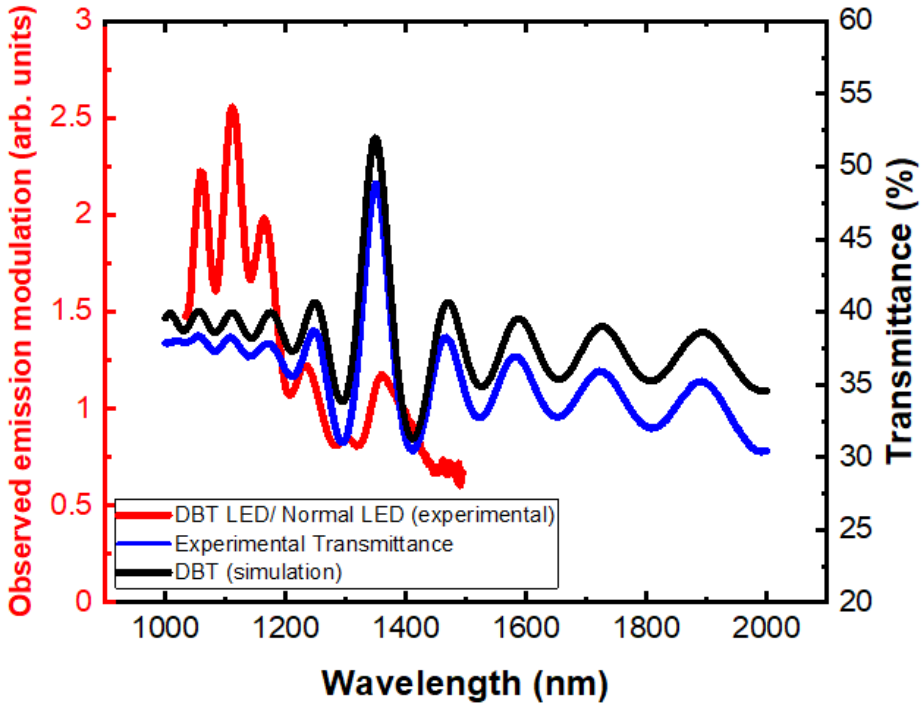

Fig. 6.27: A striking difference was the strong modulation of the DBT LED emission compared to the normal LED (red line). This modulation is a direct result of the 'sidebands' either side of the DBT transmission peak (black line). This is corroborated by comparing measured (blue line) and simulated (black line) transmission through the DBT wafer, showing remarkable consistency in both the intricate structure and the magnitude of the transmission.

Taken together, the transmission measurements establish that the DBT behaves as designed in terms of its optical response and interference structure. The pronounced modulation observed in EL confirms that this response is imprinted onto the electrically driven emission. However, the magnitude and injection dependence of the modulation indicate that a purely passive, geometric filtering model is insufficient to explain all observed features. These results motivate a cautious interpretation of the DBT as an optical element that strongly influences the collected emission spectrum, while leaving open the possibility that it also modifies the effective emission dynamics under certain operating conditions. Further experimental and theoretical work would be required to isolate and quantify any such effects.

6 .4. Conclusions and Outlook

This chapter investigated the distributed Bragg transmitter (DBT) as a monolithic multilayer structure intended to improve photon extraction from GaSb/GaAs type-II quantum-ring LEDs operating in the 1.3 µm region. The study combined transfer-matrix design, structural verification (TEM and ellipsometry), current-dependent electroluminescence (EL) at room temperature, and temperature-dependent measurements over 20-80 °C.

The most unambiguous and reproducible outcome of DBT integration is the spectral modulation imprinted on the EL, consistent with the measured/simulated DBT transmission.

While increases in collected EL are observed, attributing a definitive extraction-efficiency gain is limited by device-to-device variation and collection sensitivity; therefore, the net extraction enhancement is treated as suggestive rather than conclusive.

The DBT was realised as a seven-period GaAs/$Al_xGa_{(1-x)}As$ multilayer stack designed for high transmission near the target wavelength. Structural characterisation confirmed that the as-grown layer sequence closely matched the intended design, supporting the validity of the optical model and indicating good reproducibility of the epitaxial growth. Optical measurements of the DBT wafer further showed that the measured transmission spectrum is well captured by TMM simulations when TEM-informed thicknesses are used.

In device operation, DBT-integrated LEDs exhibit a characteristic spectral modulation in EL that is absent in reference devices. The modulation follows the DBT transmission sideband structure, indicating that the multilayer optical response is imprinted onto the collected emission. While the periodicity is consistent with interference in the DBT stack, the observed modulation depth in EL can be substantially larger than expected from normal-incidence modelling alone, pointing to the importance of measurement geometry (finite angular collection) and/or additional injection-dependent effects that are not captured in a simple passive filtering picture.

The strongest relative improvement occurs at low injection, where DBT-integrated devices can show up to 10× higher collected intensity (depending on device pairing and metric), reducing towards higher injection where the curves partially converge. This pronounced injection dependence suggests that the DBT influence is not straightforward to interpret as a purely geometrical out-coupling gain alone. A passive angular-selection mechanism may contribute, but the strong injection dependence, together with the large EL modulation depth, suggests that additional factors may be involved. In this respect, the DBT should be treated as an optical element that clearly reshapes the collected spectrum and intensity, while the degree to which it also affects effective recombination under low-injection electrical operation remains an open question.

Time-resolved photoluminescence (TRPL) measurements at low temperature showed comparable decay times for DBT and reference wafers under pulsed optical excitation. This is expected because the DBT is designed to anti-reflection rather than to form a resonant cavity, so no Purcell-type lifetime change is anticipated. These results provide useful constraints, but they should not be over-interpreted as ruling out injection-dependent changes in electrically driven operation, because TRPL probes a high-excitation, optically pumped regime that differs from the low-injection electrical conditions where the largest DBT enhancements are observed.

Temperature-dependent EL measurements across the full device cohort showed that both reference and DBT-integrated LEDs redshift and quench with increasing temperature, consistent with bandgap narrowing and thermally activated non-radiative loss. Ensemble Arrhenius analysis of the integrated EL intensity yielded activation energies that cluster around ~0.25-0.26 eV for several devices from both cohorts, indicating that the dominant thermally activated quenching pathway is broadly similar across the set. This activation

energy is relatively high for an LED active region and is consistent with comparatively weak thermal quenching in the 20-80 °C range. Scatter in extracted values for some devices (notably those with poorer fit quality) highlights the sensitivity of intensity-based analysis to device-specific factors and experimental signal-to-noise, and the Arrhenius results are therefore interpreted conservatively.

Overall, the key conclusion of this chapter is that the DBT can be reproducibly grown and that it strongly influences the collected EL spectrum and intensity of GaSb/GaAs type-II QR LEDs by imprinting a characteristic interference structure and enhancing the measured output. However, the large modulation depth and the pronounced injection dependence of the enhancement indicate that a simple “purely optical, purely geometrical” interpretation is not sufficient to explain all observed features. The DBT is therefore best viewed as a powerful optical component whose full impact on the electrically driven emission process warrants further dedicated investigation.

Future work should prioritise experiments that can disentangle optical collection effects from possible changes in effective recombination under electrical injection. The most direct routes include: (i) angle-resolved EL (or Fourier-plane imaging) to quantify the emission angular distribution with and without DBT; (ii) angle-dependent transmission/reflectance modelling and measurement to compare with the EL modulation depth; (iii) time-resolved EL (electrical pulsing) in the low-injection regime to test for changes in effective radiative dynamics under conditions relevant to the observed enhancement; and (iv) systematic statistics over multiple device pairs to separate DBT-driven trends from device-to-device variability and alignment sensitivity. In parallel, combining the DBT concept with cavity designs that provide genuine spectral locking and/or Purcell enhancement offers a clear pathway for moving beyond extraction control towards improved quantum-light performance in future device generations.

Chapter 7 Introduction to GaSb/GaAs Quantum-Ring SPLEDs: Device Architecture, Fabrication and Experimental Characterisation

This chapter presents a single-photon light-emitting diode (SPLED) architecture that combines type-II GaSb/GaAs quantum rings (QRs) with a GaAs quantum-dot (QD) single-electron filter embedded in $Al_xGa_{(1-x)}As$ and an optical cavity defined by distributed Bragg reflectors (DBRs). The approach follows a micro-LED-style process and dispenses with selecting individual emitters by wavelength, because the optical cavity provides the spectral selection. We detail the growth and micro-fabrication sequence and report electroluminescence (EL), current-voltage (*IV*) and temperature-dependent measurements that demonstrate a strong, stable cavity peak with diode-like injection and a suppression of off-resonant background emission as temperature is increased in the practical 20-80 °C range.

The vertical stack comprises n-GaAs/ $Al_xGa_{(1-x)}As$ with embedded GaAs-QD single-electron filter/GaSb-QR active layer/p-GaAs, sandwiched between top and bottom DBRs to define the optical cavity [368].

- Single-electron filter (GaAs QDs in $Al_xGa_{(1-x)}As$): A deliberately broad size distribution of GaAs QDs forms an injection filter that favours resonant tunnelling of single carriers into the active QR layer, enabling controlled electron delivery.
- Type-II GaSb/GaAs QR emission: Holes are strongly confined in GaSb while electrons are more weakly localised in GaAs, resulting in type-II radiative recombination. The optical cavity subsequently enhances a narrow spectral window from the inhomogeneously broadened emission of the QR ensemble within the aperture.
- DBR cavity: The cavity defines a dominant peak and can imprint sidebands associated with cavity-system interactions.

A concise version of this device architecture and concept has been reported previously in a SPIE conference proceeding [46]. In this thesis, the original contribution is the full epitaxial design optimisation for telecom O-band operation, the micro-LED fabrication flow (maskless direct-write process), and the systematic electrical/optical characterisation across mesa diameters and 20-80 °C operation. In particular, we quantify cavity locking, spectral-cleanliness trends and device-geometry-dependent series resistance in a way not previously reported for this platform.

7. 1. Device Architecture

We implement an electrically driven SPLED using type-II GaSb/GaAs QRs as the active medium, a GaAs QD single-electron injection filter embedded in $Al_xGa_{(1-x)}As$ and a DBR-defined optical cavity that selects a narrow emission band.

The device consists of a vertically-stacked heterostructure grown on an n-type GaAs substrate, with layers designed to enable controlled single-electron injection, efficient radiative recombination and directional photon extraction. A schematic of the device architecture is shown in Figure 7.1.

Layered structure and key components from bottom to top (Fig. 7.1)

- Lower DBR mirror ($Al_xGa_{(1-x)}As$/GaAs): Multilayer reflector defining the bottom of the Fabry-Pérot cavity.
- Electron-filter layer (GaAs QDs in $Al_xGa_{(1-x)}As$): A QD ensemble providing an energy-selective injection pathway (filter) for electrons under forward bias via resonant tunnelling.
- Active region (GaSb QRs in GaAs): Self-assembled rings with type-II alignment; holes are strongly confined in GaSb and electrons weakly localised in the surrounding GaAs.
- Cladding layers (GaAs/$Al_xGa_{(1-x)}As$): Provide carrier and optical confinement; set the effective index for the cavity.
- Upper DBR mirror ($Al_xGa_{(1-x)}As$ /GaAs): Completes the cavity and enhances vertical extraction.

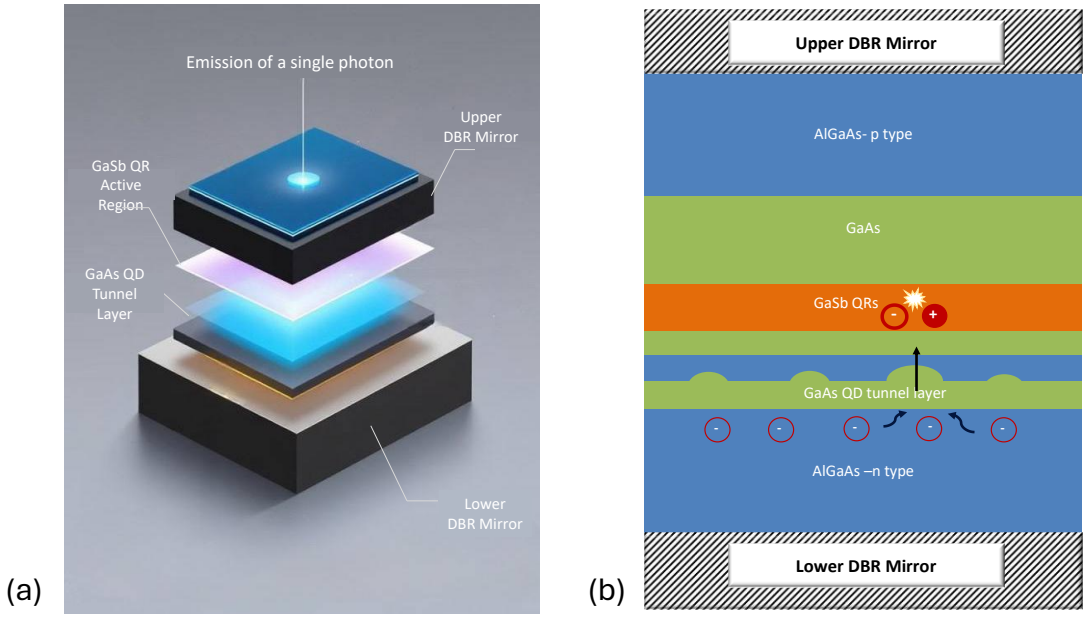

Fig. 7.1: Architecture and operating principle of the QR-SPLED. (a) Exploded view of the vertical stack: lower/upper DBR mirrors, GaAs QD tunnel layer (electron filter) and GaSb QR active region. (b) Cross-sectional cartoon of carrier injection: electrons tunnel through the GaAs QD filter into the QR layer, where radiative recombination is intended to enable a single photon; the DBR cavity enhances extraction (not to scale).

Active Region: GaSb Quantum Rings

The active region comprises GaSb quantum rings embedded within GaAs. These structures exhibit a type-II band alignment, confining holes within GaSb while electrons are localised in adjacent GaAs. Though strain-induced conduction-band bending typically repels electrons, the ring geometry alters the potential profile compared to dots. As a result, electrons are localised above or below the GaSb ring, leading to spatially indirect transitions

with small electron-hole overlap and long radiative lifetimes [46]. Emission occurs near 1300 nm, within the telecom O-band, without requiring bandgap engineering. The deep hole confinement provided by GaSb also enhances thermal stability, making these structures well suited for near-room-temperature operation.

Electron Injection: GaAs QD Tunnel Layer

Below the active region, a layer of non-uniform GaAs quantum dots embedded in $Al_xGa_{(1-x)}As$ forms an energy-selective electron-injection filter. In the intended operating regime, the QD layer is designed to restrict injection such that (ideally) a single electron is delivered per electrical excitation, thereby suppressing multi-electron injection and reducing multi-photon probability. Under forward bias, only a subset of (typically the largest) QDs are expected to align within the transport window, enabling resonant tunnelling of individual electrons towards the QR region[368], [369], [370].

This filtering mechanism:

- Can limit electron injection to approximately one electron per tunnelling event under suitable bias and temperature conditions, thereby helping to suppress multi-photon emission and preserve quantum purity,
- Is designed to support high-speed electrical injection via fast tunnelling; however, the optical modulation bandwidth has not yet been experimentally verified,
- Enhances device scalability by avoiding reliance on lithographic isolation of single emitters.

Figure 7.2 is based on one-dimensional nextnano simulations of the proposed QR-SPLED structure, carried out in collaboration with Lucie Leguay at the Technical University of Berlin. The structure is including the n-doped region, the GaAs QD electron-filtering layer, the GaSb QR active region and the p-doped region. In this simplified 1D treatment, both the GaAs QD and the GaSb QR are represented as effective quantum wells in order to capture the essential transport and confinement physics.

At zero bias, the confined Γ(gamma)-state in the GaAs QD region lies above the Fermi level, indicating that electrons are not injected through the filtering layer. Under forward bias, the electron quasi-Fermi level shifts relative to the confined state, and at sufficiently high bias the QD level enters the transport window, enabling electron tunnelling through the GaAs QD layer towards the GaSb QR region. In the proposed operating regime, this electron-filtering layer is intended to promote bias-selective, ideally single-electron injection into the QR active region, where radiative recombination can occur with holes that remain strongly confined in the GaSb QRs due to the type-II band alignment.

Pre-filling of the QRs with holes (via modulation doping or unintentional background doping) can reduce capture and transit delays and shorten the effective recombination timescales; however in type-II GaSb/GaAs the radiative lifetime remains long in the absence of a cavity; a bias-dependent blueshift is also expected [371], [105].

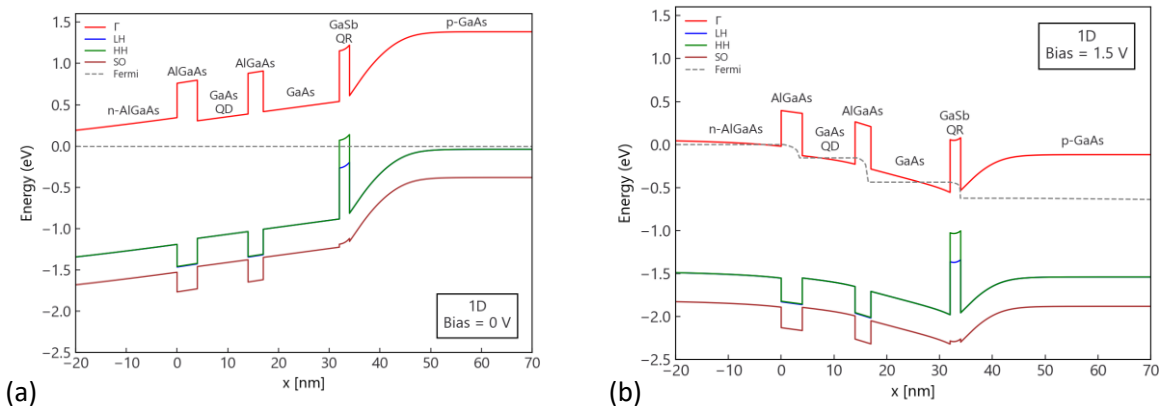

Fig. 7.2: Local band edges of the one-dimensional nextnano++ model of the proposed GaSb/GaAs QR-SPLED structure, including the n-doped region, the GaAs QD electron-filtering layer, the GaSb QR active region and the p-doped region: (a) at zero bias and (b) at an applied bias of 1.5 V. In the 1D approximation, both the GaAs QD and the GaSb QR are represented as effective quantum wells. Under forward bias, the confined Γ-state in the GaAs QD region enters the transport window, enabling electron tunnelling towards the GaSb QR region, where recombination with strongly confined holes can occur (Adapted from Acar, 2024 [46]).

Optical Cavity and Emission Control

The device incorporates top and bottom DBR mirrors formed from alternating layers of GaAs and $Al_xGa_{(1-x)}As$, defining a vertical Fabry-Pérot cavity centred at the emission wavelength [111], [137],. This cavity provides:

- Spectral filtering / cavity-mode weighting: Preferentially enhances emission near the cavity resonance (and within the collection cone) while suppressing off-resonant background.
- Improved outcoupling: Directs photons predominantly in the vertical direction, improving collection into free space or optical fibre.
- Purcell-driven emission control: For QRs that are spectrally matched to a cavity mode, the enhanced local density of optical states can narrow the emission linewidth and increase the radiative rate, potentially enabling brighter and faster single-photon emission in suitably optimised devices.

This cavity-enhanced approach avoids the need for single-emitter isolation and is compatible with micro-LED fabrication. Although fast tunnelling may help reduce injection latency, the high-speed modulation performance of the device has not yet been demonstrated. At this stage, the devices are evaluated primarily in terms of cavity-defined spectral shaping and extraction enhancement, while direct verification of single-electron injection and single-photon emission (e.g., pulsed operation and HBT $g^{(2)}(0)$ remains future work. Consequently, the observed electroluminescence remains broadband and ensemble-like, consistent with emission from multiple quantum rings under multi-carrier injection.

Under forward bias, a single electron tunnels via a large GaAs QD in the filter layer into a pre-hole-filled GaSb QR, where it recombines radiatively with the confined hole. This process produces one photon per injection event, which is spectrally refined and extraction-enhanced by the DBR cavity. The full sequence of the SPLED working mechanism is illustrated in Fig. 7.1.

This architecture provides room-temperature, telecom-band emission, and is intended to enable fast-injection and single-photon-like behaviour; its ensemble-based design remains compatible with scalable III-V fabrication processes. Devices were fabricated with circular mesas of 10, 30, 70, 100, 150 and 200 μm diameters to assess current spreading and size-dependent effects under fixed current density condition.

7. 2. Device Fabrication

The fabrication of GaSb/GaSb QR SPLEDs was carried out on n-type GaAs (100) substrates, following MBE growth of a vertically structured heterostructure. The epitaxial stack was composed of, from bottom to top: a lower DBR, GaAs/$Al_xGa_{1-x}As$ claddings, a droplet-epitaxy GaAs quantum dot (QD) tunnel layer acting as an electron filter, the self-assembled GaSb QR active region and an upper DBR. Growth conditions were optimised for telecom-wavelength emission (~1.3 μm) and for resonant-tunnelling electron injection through the filter layer.

All lithographic steps were conducted using a direct-write laser lithography system, eliminating the need for photomasks. The laser writer enabled flexible patterning of circular mesas, bond pads and contact openings, with overlay accuracies better than 1, 2 μm, sufficient for concentric annular structures and mesa-to-contact alignment. A bilayer resist process (LOR-3A / S1813) was employed throughout to enable clean lift-off. An overview of the fabrication flow is shown in Fig. 7.3 and the corresponding materials, tools and key parameters are summarised in table 7.1. The full process consisted of ten main steps, described below:

7. 2.1. Top Contact Metallisation (p-side, Au/Ni/Au)

A bilayer resist stack (LOR-3A ~300 nm / S1813 ~1.3 μm) was spin-coated and soft-baked (170 °C / 115 °C). Patterns for p-type contacts were directly written using the laser lithography tool and developed in MF-319. An Au/Ni/Au (15/30/50 nm) was thermally evaporated (base pressure < 10^{-6} mbar) and lifted-off in Remover 1165 at 75 °C, followed by acetone/IPA rinse and N_2 dry. Defining the p-contact on a planar surface improves clean edges; ohmic behaviour was achieved after the final RTA (Section 7.2.7).

7. 2.2. Dielectric Isolation (PECVD) and Contact Window Opening (RIE)

To mitigate nitride blistering after RTA, a vacuum dehydration hold (~110 °C, ≥ 1 h) preceded deposition. ~200 nm Si_3N_4 was deposited by PECVD at ~300 °C (SiH_4/NH_3). Emission apertures and p-contact vias were re-opened using CHF_3/O_2 RIE (Oxford PlasmaPro 80), defined by laser-writer lithography. The process provided clean re-access to the semiconductor while maintaining mesa sidewall passivation.

7. 2.3. Bond Pad Metallisation (Ti/Au)

Bond pads were defined using the same bilayer resist and laser-writer lithography process. A Ti/Au stack (~20/180 nm) was deposited via thermal evaporation or sputtering. Pads overlapped the underlying Au/Ni/Au contacts, with a narrow bridging track crossing the future mesa area to ensure electrical continuity and maintain planarity. Lift-off was performed in heated Remover 1165 as described above.

7. 2.4. Mesa Definition (ICP-RIE)

Circular mesas of 10, 30, 70, 100, 150 and 200 μm were defined by laser-writer S1813 resist. Any residual field nitride was first cleared by CHF_3/O_2 RIE. The III-V stack was then etched using ICP-RIE ($BCl_3/Cl_2/Ar$), for example in an Oxford Instruments system, with typical settings of 500 W ICP and 100 W RF powers, respectively, at a chamber pressure of 3 mTorr. In-situ reflectometry at ≈670 nm was used to monitor the etch depth, and the process was terminated within the upper GaAs layer of the lower DBR to ensure electrical isolation while preserving mirror. Typical etch rate was 200-300 nm min^{-1} with ± 10-20 nm stop-depth tolerance.

7. 2.5. Passivation and Final Window Reopening

A second conformal Si_3N_4 passivation layer (~200 nm) was redeposited by PECVD to protect the etched mesa sidewalls. Bond-pad and emission openings were redefined by laser writer lithography and etched in CHF_3/O_2 RIE, restoring access for electrical probing and emission.

7. 2.6. Back Contact Metallisation (n-side, AuGe/Ni/Au)

The backside of the wafer was carefully cleaned using acetone and IPA solvents, followed by a deionised water rinse and nitrogen blow-dry, ensuring that the previously fabricated front-side layers remained unaffected. A metal stack of AuGe/Ni/Au (100/35/100 nm) was thermally evaporated to form the n type-ohmic contact. The AuGe layer provided n-type doping through interdiffusion during subsequent annealing.

7. 2.7. Rapid Thermal Annealing (RTA)

Ohmic contact formation was achieved by a single RTA step at 300 °C for 3 minutes under N_2 ambient. This simultaneously activated both the front-side Au/Ni/Au and the backside

AuGe/Ni/Au contacts, yielding low contact resistance. A 50-100 °C s^{-1} ramp and ~1-2 SLM N_2 flow were used, pre-calibrated on monitor pieces. Cooling was radiative to minimise thermal stress; nitride exposure to ambient moisture was limited prior to deposition to avoid blistering. A representative plan-view micrograph of a finished device is shown in Fig. 7.4: a GaSb QR-SPLED with a 100-µm mesa and a 50-µm annular emission aperture (scale bar: 50 µm). This layout is a representative of the series; only the mesa diameter is varied across devices (10-200 µm).

7. 2.8. Mounting and Wire Bonding

Following the fabrication, the wafer was cleaved into individual dies using a diamond scribe. Chips were mounted onto TO-46 headers using silver-loaded epoxy. After curing, the Ti/Au bond pads were wire-bonded to the package leads using Au ball bonding. This configuration enabled stable optical/electrical testing with efficient thermal dissipation. In addition to the main fabrication flow described above, several process optimisations were required to ensure uniform device operation:

- All lithography used a direct-write laser writer with $\lesssim$ 2 µm overlay.
- Ti/Au serves only as the bond-pad metal; the p-ohmic is Au/Ni/Au (activated by RTA).
- Thermal dehydration steps perform prior to each PECVD deposition significantly reduce Si_3N_4 blistering observed after rapid thermal annealing (RTA).
- Mesa stop-depth control preserves cavity performance while ensuring lateral isolation.

Throughout Chapter 7, devices are labelled as SXX, where xx denotes the circular mesa diameter in micrometres (e.g., S10 = 10 µm, S30 = 30 µm, …, S200 = 200 µm).

Table 7.1 Summary of the GaSb QR-SPLED fabrication flow, listing process steps, materials/tools and key parameters; notes include resist stacks, etch chemistries and RTA conditions

Step	Process	Material/Tool	Key Parameters	Notes
1	**Top contact metallisation (Thermal Evaporator)**	Au/Ni/Au	15/30/50 nm (thermal evap.)	Bilayer resist (LOR-3A/S1813); lift-off at 75 °C
2	**Dielectric isolation (PECVD)**	Si_3N_4	~200 nm @ 300 °C	SiH_4/NH_3 chemistry; pre-bake at 110 °C to prevent blistering
3	**Contact window opening (RIE)**	CHF_3/O_2	PlasmaPro 80 tool	Selective etch to GaAs; retains mesa sidewall protection
4	**Bond pad metallisation (Thermal Evaporator)**	Ti/Au	~20/180 nm	Overlaps p-contact; ensures wire-bond robustness
5	**Mesa etching (ICP-RIE)**	$BCl_3/Cl_2/Ar$	ICP 500 W / RF 100 W / 3 mTorr	Stop in upper GaAs of lower DBR; in-situ reflectometry used
6	**Final passivation (PECVD)**	Si_3N_4	~200 nm	Same chemistry as step 2; protects exposed sidewalls
7	**Window reopening (RIE)**	CHF_3/O_2	RIE etch for bond pad & aperture access	Same recipe as step 3
8	**Back contact metallisation (Thermal Evaporator)**	AuGe/Ni/Au	100/35/100 nm (thermal evap.)	Pre-clean with ashing; forms n-ohmic contact after RTA
9	**Annealing (RTA)**	N_2 ambient	~300 °C for 3 min	Activates both p- and n-ohmic contacts
10	**Mounting & wire bonding**	TO-46 header + Au ball bonds	Silver epoxy + bonder	Ensures stable probing & thermal contact

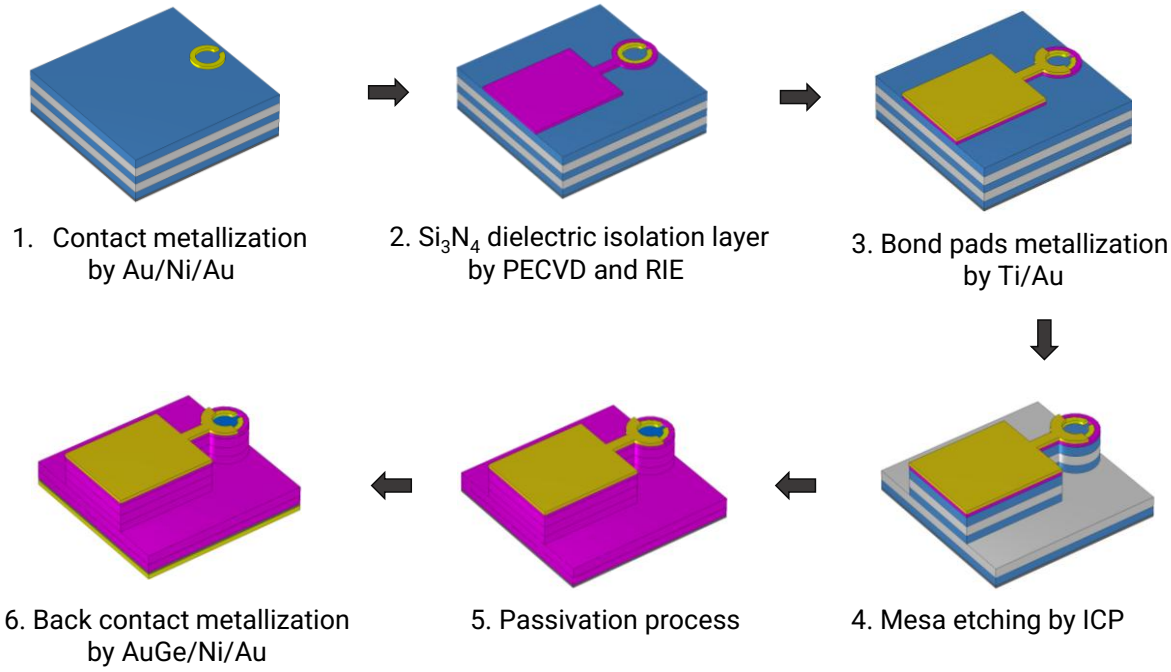

Fig. 7.3: Schematic fabrication sequence of the QR-SPLED (not to scale).

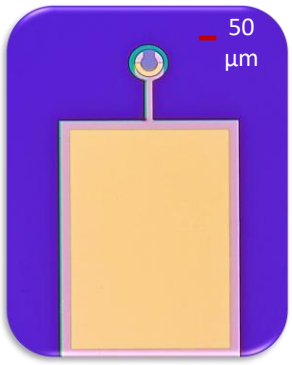

Fig. 7.4: Plan-view optical micrograph of a GaSb QR-SPLED used in the EL studies, showing a 100-µm-diameter mesa and a 50-µm annular emission aperture. Scale bar: 50 µm.

7. 3. Device Characterisation Results

This section reports the electrical and optical characterisation of the GaSb/GaAs QR-SPLEDs fabricated in Section 7.2. We study six circular mesa diameters (10, 30, 70, 100, 150 and 200 µm) to quantify size-dependent behaviour. Three complementary datasets are presented:

(i) Current-voltage (*IV*) measurements at room temperature;
(ii) EL spectra (intensity vs wavelength) at room temperature for increasing drive; and
(iii) Temperature-dependent EL spectra recorded at fixed current over a practical range (20-80 °C).

All EL/*IV*/temperature measurements in this chapter used the same apparatus described in Chapter 4 [137]. In brief: forward-bias drive from a source-measure unit; normal-incidence collection into a fibre-coupled grating spectrometer with an InGaAs detector; and a temperature-controlled stage operated between 20 and 80 °C. Wavelength and intensity calibrations followed the Chapter-4 protocol.

7. 3.1. Current-Voltage Results

The *IV* characteristics of the SPLED devices exhibit typical diode behaviour, resembling that of a conventional LED at room temperature. The characteristics are shown in three complementary views; a linear *IV* plot reporting absolute current (Fig. 7.5a), a linear *JV* plot highlighting high-current behaviour and series resistance (Fig. 7.45b), and a semi-log *JV* plot that resolves the exponential diode regime (Fig. 7.5c). Currents are normalised to the electrical area $A=\pi(d/2)^2$ so that the current density $J=I/A$ enable size-independent comparison across the six mesa diameters (10-200 µm).

All devices exhibit a clear turn-on around 3-3.5 V (Fig. 7.5a). The exponential transport window is most clearly resolved in the semi-logarithmic *JV* representation (Fig. 7.5b): for the 10 and 30 µm mesas, straight-line guides highlight an approximately exponential dependence over ~3.8-6.5 V and ~4.2-6.2 V, respectively, while deviations at lower and higher bias indicate the onset of weak-injection and series-resistance effects. In the linear J-V plot (Fig. 7.5c), the high-bias curvature becomes more pronounced with increasing mesa size, consistent with enhanced series resistance and current crowding in the larger devices.

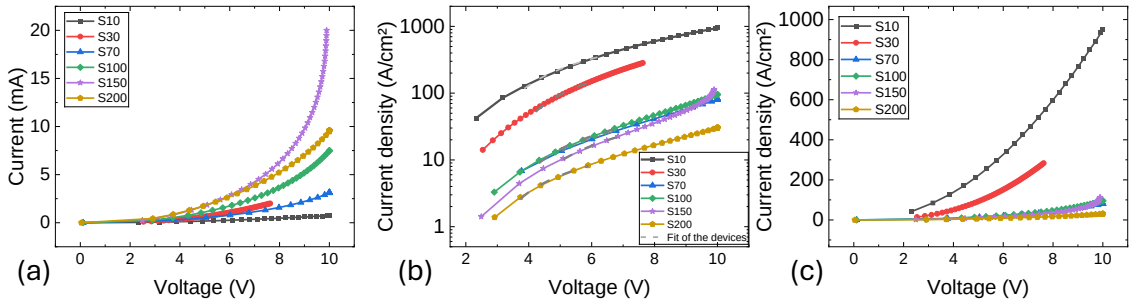

Fig. 7.5: Room-temperature *I*V characteristics of GaSb/GaAs QR-SPLEDs (10-200 µm). (a) *IV* (absolute current), (b) semi-log *JV* representation highlighting the exponential transport window; dashed straight-line guides mark the linear-in-log region, and (c) linear *JV* curves showing the high-bias roll-off associated with series resistance, which becomes more pronounced for larger mesas. Current density is defined as $J=I/A$.

The current density at fixed bias decreases systematically with diameter. Quantitatively:

- S10 reaches nearly 10^3 A cm^{-2} by V≈10 V.
- S30 reaches nearly (2-3) × 10^2 A cm^{-2} by V≈7.5-8 V.
- S70 -S200 lie in the 10^1-10^2 A cm^{-2} band at V≈10V.

This monotonic trend is consistent with diameter-dependent current spreading and access/series resistance. Since the mesas were passivated, surface-leakage currents are expected to be suppressed and are not required to explain the observed behaviour; instead, current crowding near the contact perimeter and series-resistance-limited transport at high bias are the most plausible contributors.

To quantify the resistive contribution within the log-linear (exponential) transport window, the effective series resistance R_s was extracted using Cheung's method. For a diode described by the ideality-factor model [372], [373],

$$I = I_0 exp\left(\frac{V - IR_s}{nV_T}\right). \tag{7.1}$$

Taking the derivative with respect to lnI gives

$$\frac{dV}{d(lnI)} = nV_T + IR_s. \tag{7.2}$$

Here n is the ideality factor, obtained from the slope of the semi-logarithmic *JV* curve in the exponential region identified in Fig. 7.5(b), and V_T=kT/q is the thermal voltage, fixed at V_T=25.85 mV for T=300 K and not treated as a free fitting parameter. Equation (7.1) was fitted to $^{dV}/_{d(lnI)}$ versus I only over this straight-line region in order to avoid weak-injection and high-bias series-resistance artefacts. The resulting Rs values were converted to an area-specific figure of merit, R_sA=R_s×A, enabling a geometry-independent comparison across mesa sizes (Table 7.2). remains valid and the parasitic series resistance first begins to influence the slope.

Table 7.2 Window-specific series resistance and area-specific figures

Sample (d, µm)	**Fit window (V)**	**R_s (Ω)**	**A (cm²)**	**R_s× A (Ω·cm²)**
S10 (10)	3.5-6.5	6100 ±300	7.85×10^{-7}	$(4.8 \pm 0.2)\times10^{-3}$
S30 (30)	3.5-6.5	2740 ± 70	7.07×10^{-6}	$(1.93 \pm 0.05)\times10^{-2}$
S70 (70)	5.0-9.0	2180 ± 40	3.85×10^{-5}	$(8.4 \pm 0.2)\times10^{-2}$
S100 (100)	4.5-8.5	1650 ± 30	7.85×10^{-5}	$(1.30 \pm 0.03)\times10^{-1}$
S150 (150)	4.5-7.0	710 ± 10	1.77×10^{-4}	$(1.25\pm 0.03)\times10^{-1}$
S200 (200)	3.7-6.0	1520± 30	3.14×10^{-4}	$(4.76\pm 0.09)\times10^{-1}$

Physically, R_sA represents the intrinsic resistive contribution of the current-carrying layers and contacts, with the trivial 1/A scaling of the device resistance removed. This means that

differences between devices reflect changes in material quality, interface properties and current-spreading behaviour rather than simple geometric effects. Unlike high-current "average" resistances taken from the fully ohmic regime, R_s and R_sA extracted in this way characterise the exponential/log-linear transport region, where the diode equation

The values in the table 7.2 were obtained using fit windows selected directly from the log-linear region of the semi-logarithmic *JV* curves (Fig. 7.5b). The lower boundary corresponds to the voltage at which weak-injection behaviour ends and the diffusion-dominated exponential regime becomes linear on a logarithmic scale. The upper boundary marks the onset of series-resistance-induced curvature, where the JV slope begins to deviate from ideality. To account for the sensitivity of R_s to the exact choice of fit window, uncertainties in R_s and R_sA were estimated by shifting the fit window by ±0.1 V and recalculating the parameters.

When the extracted R_sA values are considered together with their uncertainties (Table 7.2), a clear and systematic dependence on device diameter is observed. R_sA increases monotonically with increasing mesa size, reflecting the growing contribution of current spreading and series resistance in larger-area devices. Only the S100 and S150 devices exhibit overlapping R_sA values within uncertainty, indicating comparable effective resistance-area products for these two geometries. The smallest mesas (S10 and S30) exhibit clearly lower R_sA than all larger devices, consistent with reduced current-spreading distance and smaller effective series paths. At intermediate diameters (S100 and S150), the values overlap within uncertainty and therefore cannot be unambiguously ranked; these two devices should be regarded as statistically indistinguishable in R_sA. In contrast, S200 shows a significantly higher R_sA than all other samples, with a difference far exceeding the uncertainty range, confirming that the largest device is strongly limited by its long lateral current path underneath the top contact and bridge metal.

Overall, this analysis demonstrates a robust and physically meaningful dependence of R_sA on device geometry. While fitting uncertainties limit the unambiguous ranking of devices with similar intermediate diameters, the systematic increase in R_sA with mesa size is clearly preserved. In particular, the pronounced contrast between the smallest and largest mesas is statistically robust and highlights the dominant role of lateral current spreading in determining the series resistance of large-area SPLEDs.

For SPLED operation, small mesas are generally preferred, as they enable high current density at low absolute current, reducing self-heating and facilitating stable single-emitter excitation. Conversely, larger mesas serve characterisation purposes-probing ensemble behaviour and contact/process uniformity-but require careful current-spreading management and optimised contact geometry to mitigate resistive losses and non-uniform injection.

A brief note on the semi-log slope and the "ideality factor": In typical pn-junction diodes, the slope *M* of the semi-logarithmic *JV* curve in the exponential regime is commonly used to extract the ideality factor n, via the relation $n = 1/(0.0596\ \mathrm{M})$ at 300 K [31]. In our SPLEDs studied here, however, the GaAs-QD injection filter (resonant tunnelling) together with

access/series resistance and current spreading compresses the forward slope in the log-linear window. Consequently, converting M to n yields very large apparent values ($\gg 2$) that do not reflect a recombination mechanism. Therefore, we do not report ideality factors. Instead, we present the window-specific effective R_s (from Cheung's method) and R_sA as more appropriate comparative metrics for forward conduction behaviour. For completeness, apparent values of $n_{app}=1/(0.0596\,M)$ at 300 K is not used for mechanistic interpretation. This approach avoids over-interpreting the semi-log slope in a non-Shockley architecture while still enabling like-for-like comparison across diameters and bias ranges.

7. 3.2. Current-dependent EL Measurement Results at Room Temperature

Following the electrical characterisation (Sec. 7.3.1), room-temperature electroluminescence (EL) spectra were recorded from six circular mesas (10-200 μm diameter) while the injection current was systematically varied. The goal is to assess how effectively the DBR cavity isolates emission from the GaSb/GaAs QR ensemble and to track the cavity resonance as a function of drive.

Across all devices the same spectral fingerprint appears: a single, narrow cavity-selected line in the telecom O-band, superimposed on a broad QR background extending from roughly 1.05 to 1.5 μm. The raw spectra of the all devices showed a stable peak at ≈ 1242 nm (Fig. 7.6). This is the expected behaviour for a cavity-filtered type-II emitter in which the distributed Bragg reflectors define a vertical Fabry-Pérot cavity that amplifies one longitudinal mode while suppressing off-resonant emission. Within the spectrometer resolution the peak position is invariant with current; minor drifts hinted at the highest drives in the widest mesas are comparable to the fit uncertainty and are not over-interpreted here (a finer discussion appears in the temperature-controlled study).

At low-moderate injection the cavity-line intensity increases approximately linearly with current. At the highest drives, a gentle sub-linear trend appears in the larger mesas. This behaviour is consistent with increased lateral current spreading and drive-induced self-heating in wide-aperture devices, both of which reduce the fraction of carriers contributing to radiative recombination. While series resistance does not directly alter the light-current relationship, its contribution to Joule heating at high bias can indirectly enhance these effects. Consequently, performance metrics are re-expressed in terms of current density or power per unit area to enable size-independent evaluation.

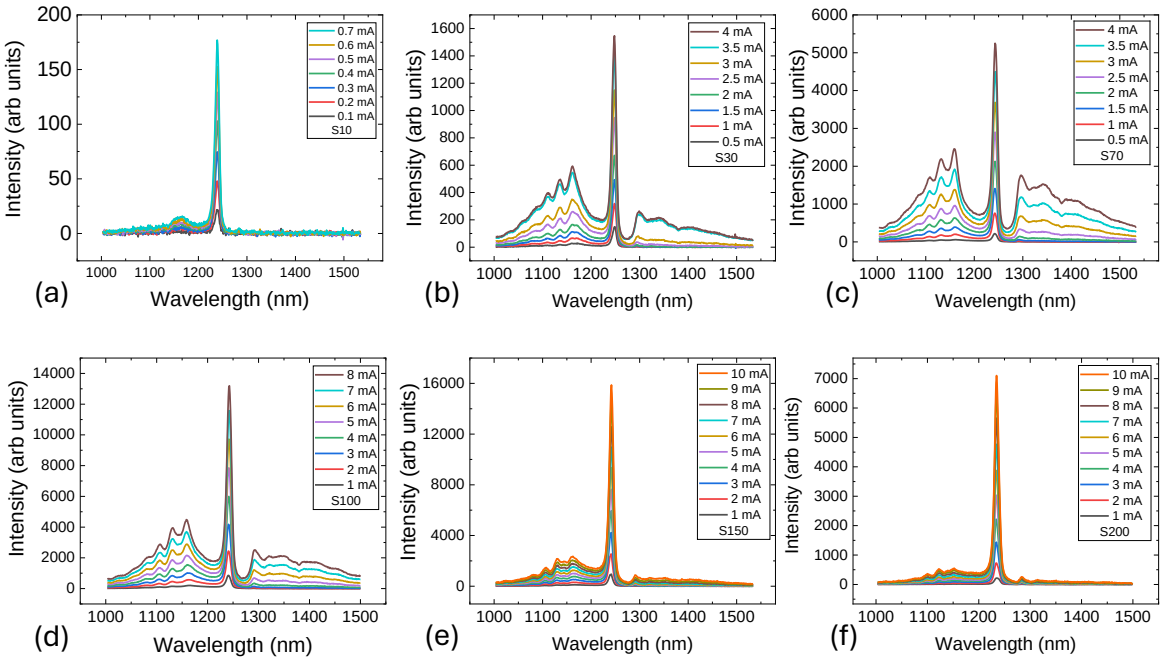

Fig. 7.6: Room-temperature EL spectra under increasing current for the diameter series. Cavity-mode peak wavelengths are: (a) S10 at 1238 nm, (b) S30 at 1248 nm, (c) S70 at 1242 nm, (d) S100 at 1241 nm, (e) S150 at 1241 nm and (f) S200 mesas at 1234 nm.

After peak normalisation, the spectral shape is nearly current-invariant for a given device; what changes with drive is the relative weight of the broad background (Fig. 7.7).

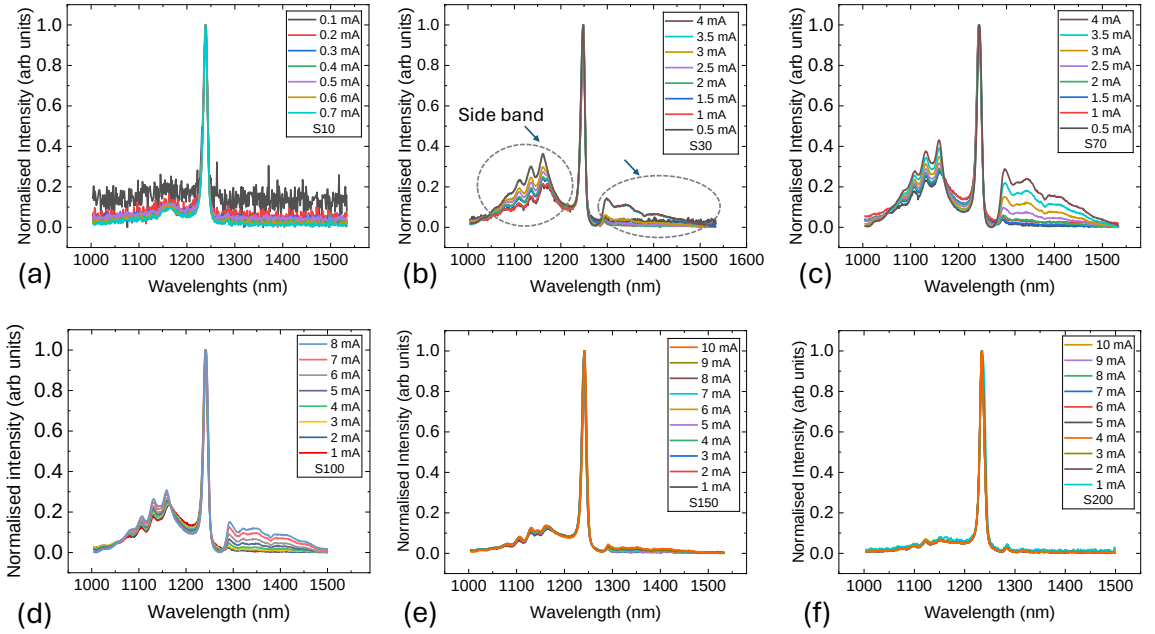

Fig. 7.7: Corresponding peak-normalised spectra; the sideband sampling point is indicated near 1.15 µm for (a) S10, (b) S30, (c) S70, (d) S100, (e) S150 and (f) S200 mesas.

At higher currents the background and weak short-wavelength sidebands become more visible, especially in wider mesas, whereas at reduced currents the cavity peak dominates.

Each spectrum is baseline-corrected using a linear fit to the far wings. We characterise the cavity line by its peak wavelength λ_{peak}, FWHM and integrated line intensity $I_{int}=\int I(\lambda)\, d\lambda$ over the feature. SSR is defined here as the ratio between the intensity of the cavity-selected peak and the average intensity of the short-wavelength sideband region. This provides a geometry-independent measure of how strongly the cavity filters QR emission: a larger SSR indicates a more cavity-dominated spectrum, whereas a smaller SSR reflects relatively stronger broadband side-emission.

To ensure that SSR is reproducible across devices and drive conditions, we apply a fixed short-wavelength shoulder window common to all samples, [1.14-1.17] µm, and compute the ratio on peak-normalised spectra using Eqs. 7.1 and 7.2.

$$SSR(x) = \frac{I_{cavity,peak}}{I_{sideband}} \quad \text{and} \tag{7.1}$$

$$I_{sideband} = \int_{1.14\mu m}^{1.17\mu m} I_{norm}(\lambda) d\lambda\,, \tag{7.2}$$

where x denotes the swept variable (current I in this section, temperature T in Sec. 7.3.3) and where $I_{cavity,peak}$ is the peak intensity of the cavity line and the denominator is the integrated, peak-normalised intensity over the fixed short-wavelength shoulder (definition highlighted in Fig. 7.8). Using peak-normalised traces removes absolute-power effects; applying the same window and baseline to every condition ensures a fair comparison. The red marker indicates the centre $\lambda_{sb}\approx 1.155$ µm; the analysis uses the mean intensity within the fixed window [1.14,1.17] µm for all devices and currents when computing SSR(I).

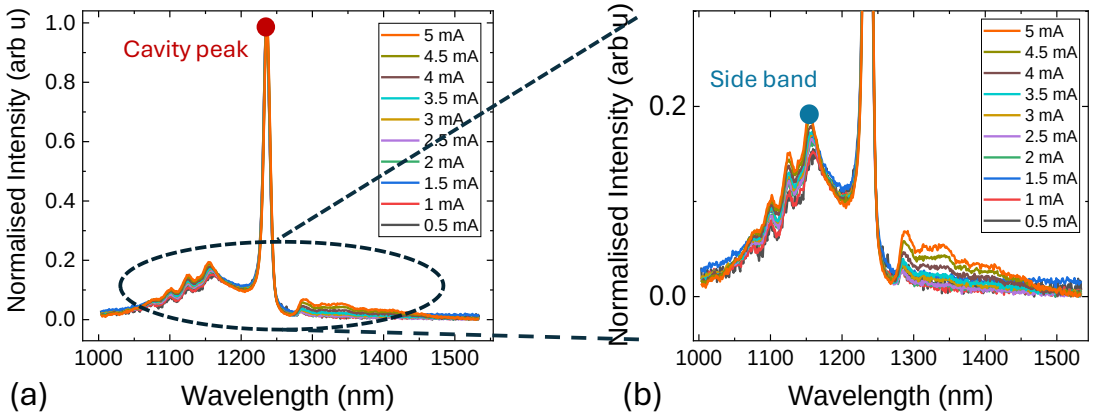

Fig. 7.8: Definition of the cavity peak and sideband used in the ratio R. (a) Peak-normalised room-temperature EL spectra of the 100-µm device for 0.5-5 mA. The dashed ellipse marks the short-wavelength sideband region of the QR ensemble; the red dot highlights the cavity peak. (b) Zoom-in of the sideband shoulder.

This convention underlies the SSR-current plots in Fig. 7.9 and ensures a geometry-independent and internally consistent comparison across mesa sizes. Using an integral instead of a mean over the same window would differ only by a constant multiplicative factor and therefore does not affect any physical trends. Since each SSR point was obtained from a single spectrum at each bias, the curves in Fig. 7.9 are used to assess overall trends rather than statistical reproducibility.

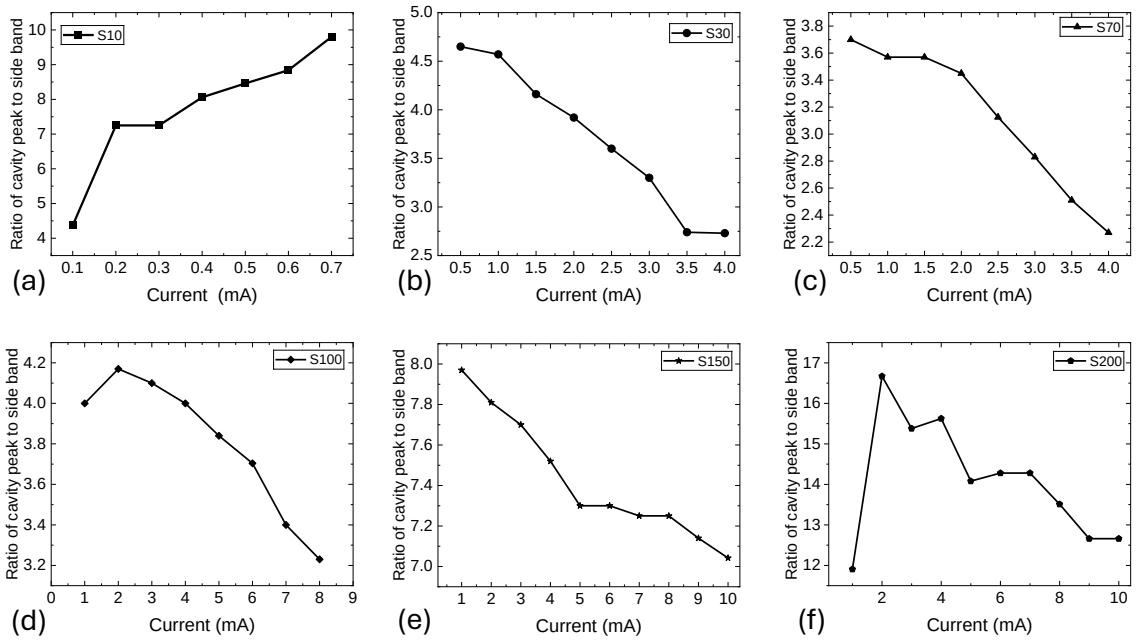

Fig. 7.9: Ratio of cavity-to-sideband vs current for (a) S10, (b) S30, (c) S70, (d) S100, (e) S150 and (f) S200 mesas, showing improved spectral cleanliness at reduced current (S30-S200) and in S10 a low-current signal-to-noise ratio (SNR) rise. Error bars are not shown because each point was extracted from a single spectrum at each bias and repeated acquisitions were not performed.

When we look at the sideband behaviour, a larger ratio implies higher spectral purity, i.e., a stronger cavity enhancement relative to the off-resonant ensemble.

- For S10 (10 μm), SSR increases across the sub-milliamp window (≈ 4 to 10 for 0.1-0.7 mA). However, in this smallest mesa the total emitted power is very low, and at the lowest currents the sideband region lies close to the noise floor. The apparent increase in SSR with drive is therefore likely dominated by improved signal-to-noise ratio rather than a genuine change in cavity filtering.
- For S30 (30 μm) and S70 (70 μm), SSR decreases monotonically with current (≈ 4.6 to 2.7 for 0.5-4 mA in S30; ≈ 3.7 to 2.2 for 0.5-4 mA in S70) indicating that the short-wavelength sideband strengthens faster than the cavity peak.
- S100 (100 μm) shows a shallow maximum at low current followed by a steady decline (≈ 4.1 to 3.2 for 1-8 mA).

- S150 (150 μm) maintains high and relatively flat contrast with a gentle drop. (≈ 7.9 to 7.0 for 1-10 mA).
- S200 (200 μm) shows a very low SSR at 1 mA, which is inconsistent with neighbouring points and is likely dominated by scatter or low-SNR variability. Excluding this outlier, S200 shows the strongest overall decline in SSR with current, consistent with increased self-heating and reduced cavity contrast in the widest aperture

Across the six devices, SSR(I) decreases with increasing drive in all mesas except S10. For S30, S70 and S150 the trend is smooth and monotonic. S100 shows an initial increase in SSR before thermal roll-off above ≈2 mA. In S200, the first datapoint at 1 mA is anomalously low and likely dominated by scatter or low-SNR variability; excluding this outlier, S200 exhibits the strongest overall decline, consistent with the weakest cavity filtering in the widest aperture. The rise observed in S10 is also not attributed to cavity physics but to low-SNR artefacts at the lowest currents.

Several mechanisms may contribute to the reduction in SSR at higher currents. Most significantly, cavity-selected emission can saturate earlier than the broadband QR background, reducing the spectral contrast even in the absence of secondary effects. In larger mesas, lateral voltage drops and current crowding near the contact can make injection increasingly non-uniform, which may enhance the relative contribution of off-resonant background emission and further lower SSR. We therefore interpret the observed trends primarily as a saturation effect modulated by device geometry. Notably, the spectral quality improves at higher temperatures (detailed below), indicating that thermal effects are unlikely to be the dominant driver of the SSR roll-off. At reduced current, the cavity remains optimally matched to the gain spectrum, yielding spectrally clean emission, an advantageous operating point for low-power quantum-photonic applications and particularly promising for SPLEDs, where extremely low operating currents are required.

When we look at the linewidth, Fig. 7.10 summarises the extracted FWHM for all diameters. Although device-to-device values cluster within nearly 10-12 nm, there are weak, diameter-dependent drifts with current:

- S10: essentially constant around 11.0-11.3 nm over 0.1-0.7 mA.
- S30: slightly non-monotonic, peaking near ~10.6-10.7 nm at ~2-2.5 mA and decreasing to ≈ 10.0 nm by ~3.5-4 mA.
- S70: a clear decrease from ≈ 12.1 nm (0.5 mA) to ≈ 10.0 nm (4 mA).
- S100: a gradual decrease from ≈ 12.1 nm (1 mA) to ≈ 10.6 nm (8 mA).
- S150: nearly flat, ~11.3 ± 0.1 nm across 1-10 mA.
- S200: decreasing from ≈ 12.7 nm (1 mA) to ≈ 11.0 nm (10 mA).

Given the instrumental resolution (~0.3 nm), the observed diameter-dependent drifts are small on the scale of the overall linewidth (≈10-12 nm) and do not change the conclusion

that the cavity emission is spectrally stable across this current range. The dominant current-dependent effect is the modulation of sideband intensity relative to the cavity peak, rather than substantial broadening of the peak itself.

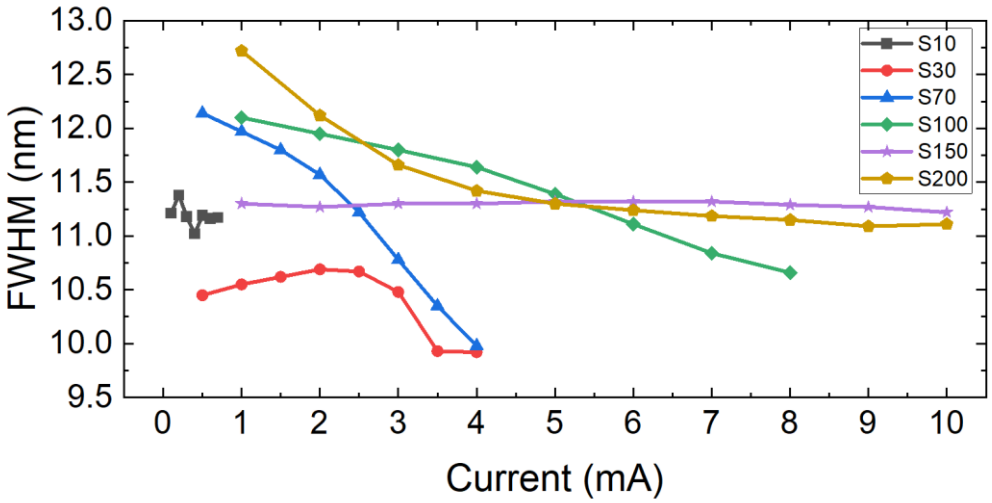

Fig. 7.10: FWHM versus current for S10, S30, S70, S100, S150 and S200 mesa, all devices (10-12 nm band with weak trends).

Across all diameters, the DBR cavity reliably selects a single narrow O-band line from the QR ensemble. The peak wavelength remains constant with current within the spectrometer resolution (≈0.3 nm), and the linewidth sits in the 10-12 nm range with only weak, device-dependent drifts. When the spectra are normalised, the cavity-to-sideband ratio is largest at reduced current for the S30-S200 devices, indicating cleaner, more cavity-dominated emission at modest drive. Only the smallest mesa (S10) shows an initial increase in this ratio within the sub-milliamp window, reflecting the rapid improvement in signal-to-background in that regime.

The linewidth evolution is summarised in Fig. 7.11, now plotted against current density to enable a fair cross-device comparison. All mesas show only weak FWHM variation with current density, and the linewidths remain clustered in the 10-12 nm range, with changes comparable to the spectrometer resolution (≈0.3 nm). Devices S70, S100 and S200 show a mild narrowing with increasing current density, whereas S10 and S150 remain essentially constant. These trends confirm that the dominant current-dependent spectral change is the sideband content, not the cavity linewidth itself.

In practical terms, spectral purity is therefore maximised at low to moderate currents, whereas higher currents trade cleanliness for absolute brightness, an observation that guides the choice of operating points in the temperature-dependent measurements in the next section.

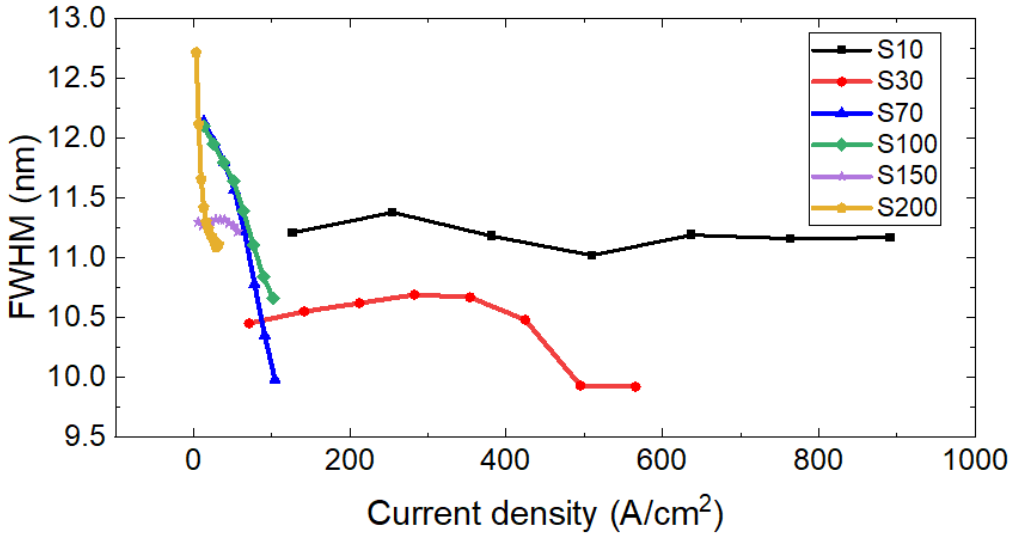

Fig. 7.11: FWHM versus current density for all mesa diameters, showing only weak linewidth variations (≈10-12 nm) across the full drive range.

7. 3.3. Temperature-Dependent Electroluminescence Measurement at Fixed Current

To assess performance above room temperature, relevant for cooler-free operation, we recorded EL from six circular mesas (10-200 µm) while stepping the temperature from 20 °C to 80 °C at a fixed drive current for each device (S10: 0.7 mA; S30: 2 mA; S70: 2 mA; S100: 7 mA; S150: 10 mA; S200: 10 mA; see legends in Fig. 7.12). These set-points sit in the mid-bias regime identified in sec.7.3.2 where (i) series-resistance heating is modest, (ii) signal-to-noise is high, and (iii) the cavity line is well defined. Using constant current mirrors practical operation conditions and avoids artefacts from re-optimising both current and temperature simultaneously. Unless stated otherwise, "intensity" refers to the cavity-selected line at 1.24-1.25 µm and "background" denotes off-resonant QR-ensemble emission. Figure 7.13 shows zoomed spectra of the cavity line for each mesa diameter, highlighting the thermo-optic red-shift from 20 °C to 80 °C at the fixed drive currents indicated in the legend of Fig. 7.14.

Across all diameters the spectra retain the room-temperature fingerprint: a spectrally narrow cavity line sitting atop a broad type-II background. Two robust temperature trends emerge. First, the cavity mode red-shifts approximately linearly with temperature (Fig. 7.13). Using Varshni parameters for GaSb ($\alpha \approx 4.2\times10^{-4}$ eV/K, $\beta \approx 140$ K), a 60 K increase from 20 °C to 80 °C would be expected to shrink the band gap by ≈25 meV, corresponding to a wavelength shift of ≈13-15 nm at 1.24 µm. In contrast, the measured cavity red-shift over the same range is only ≈6-8 nm, consistent with thermo-optic tuning of the DBR Fabry-Pérot cavity (increased effective refractive index and optical thickness) rather than a band-gap shift in the active region. Second, the off-resonant background is progressively suppressed relative to the cavity line under constant drive with increasing temperature, most clearly seen in peak-normalised spectra (Fig. 7.15). We quantify spectral contrast using the

same sideband-suppression ratio defined in Eq. (7.1) and Eq. (7.2), where $I_{cavity,peak}$ is taken at the cavity-line maximum and $I_{sideband}$ is the integrated intensity within the fixed short-wavelength window.

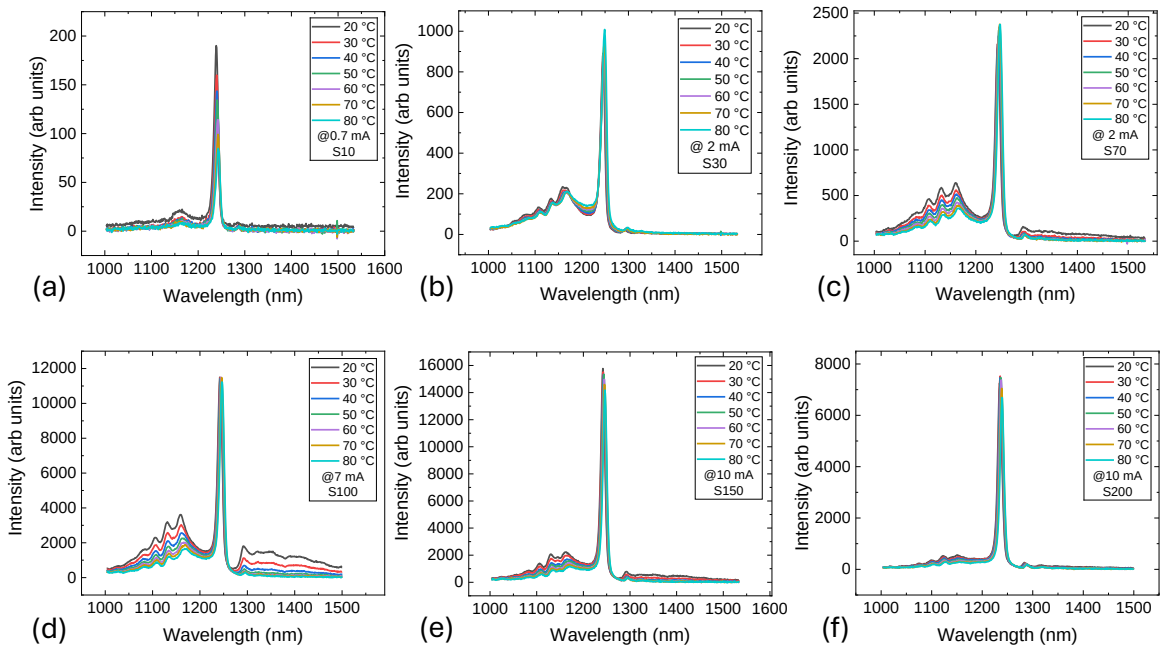

Fig. 7.12: Temperature-dependent EL spectra at fixed current. (a) S10 (0.7 mA), (b) S30 (2 mA), (c) S70 (2 mA), (d) S100 (7 mA), (e) S150 (10 mA), (f) S200 (10 mA) as temperature is stepped from 20 °C to 80 °C.

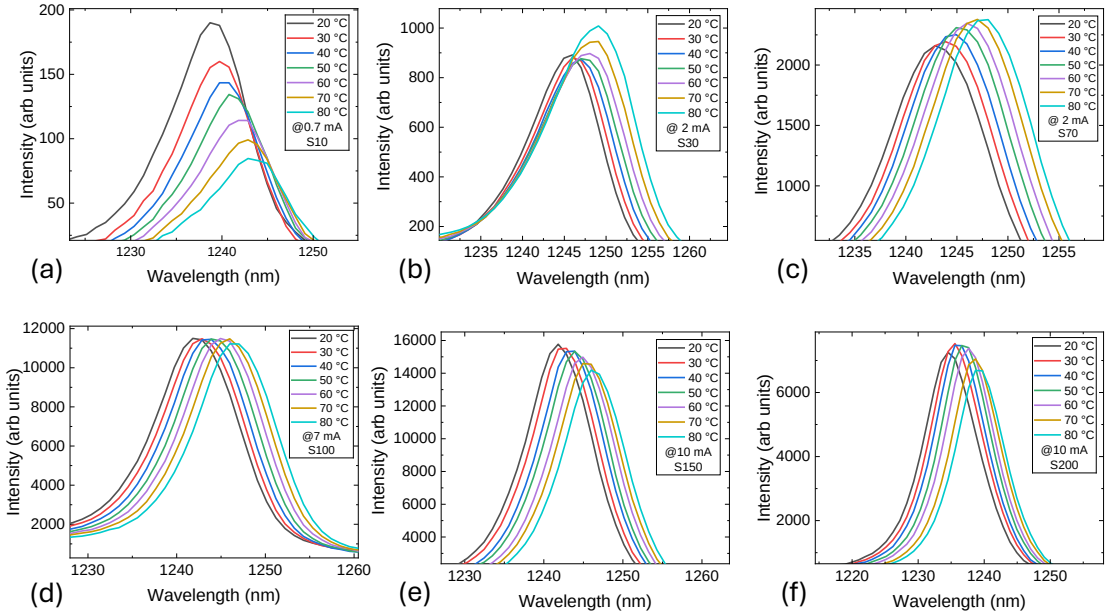

Fig. 7.13: Zoom of the cavity line: thermo-optic red-shift (20-80 °C). (a) S10 (0.7 mA), (b) S30 (2 mA), (c) S70 (2 mA), (d) S100 (7 mA), (e) S150 (10 mA), (f) S200 (10 mA).

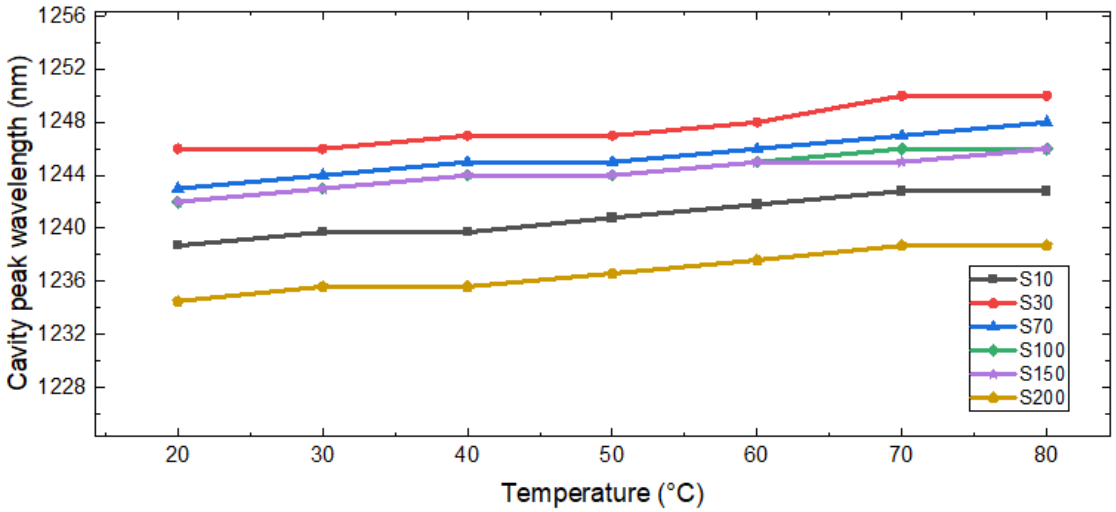

Fig. 7.14: Cavity peak wavelength as a function of temperature for SPLED devices with different mesa diameters. All devices exhibit a near-linear red-shift with increasing temperature, with comparable slopes across diameters, consistent with thermo-optic tuning of the cavity.

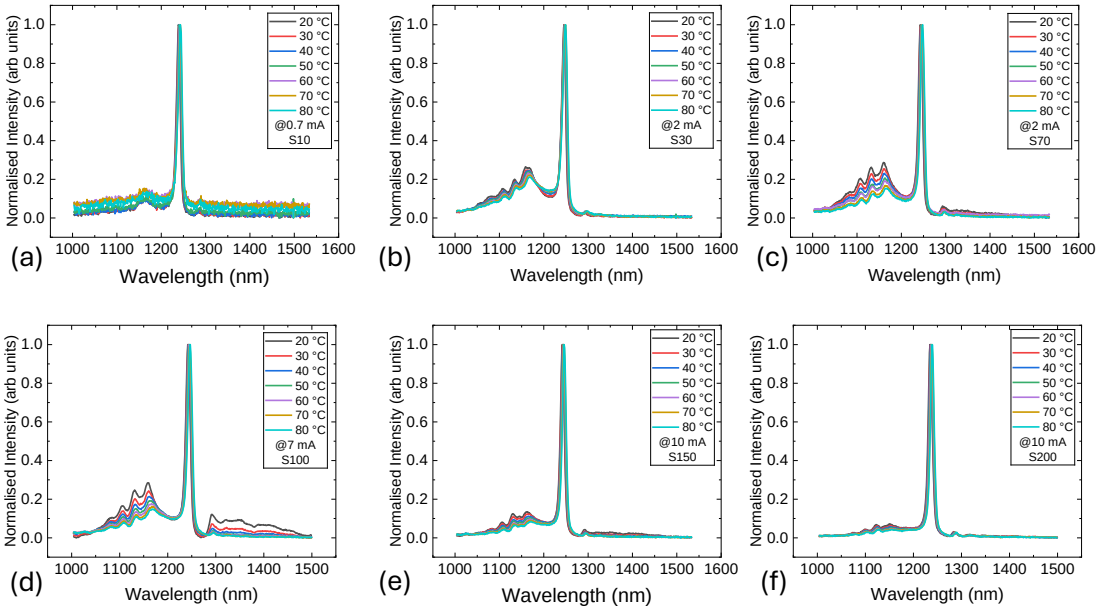

Fig. 7.15: Normalised EL spectra revealing side-band suppression with temperature. (a) S10 (0.7 mA), (b) S30 (2 mA), (c) S70 (2 mA), (d) S100 (7 mA), (e) S150 (10 mA), (f) S200 (10 mA).

A simple physical picture captures both trends. With increasing temperature, non-radiative recombination channels in the QR ensemble become more active, introducing stronger competition between radiative and non-radiative pathways. Off-resonant spontaneous emission, which is weakly coupled to the cavity and proceeds with a comparatively slower radiative rate, is therefore preferentially quenched as non-radiative recombination increases. In contrast, the cavity-selected transition benefits from a much higher effective radiative recombination rate due to strong coupling to the cavity mode, as discussed previously for

cavity-based systems [137], making it more resilient to thermally activated non-radiative loss. As a result, the off-resonant background is suppressed more strongly than the cavity line, leading to an overall improvement in spectral contrast even though the total collected emission typically decreases with temperature.

The cavity linewidth itself remains essentially stable across the 20-80 °C range. Figure 7.16 shows the extracted FWHM of the cavity-selected emission peak as a function of temperature for all mesa diameters, measured at the fixed drive currents used in the temperature-dependent EL experiments. Across all devices, the linewidth remains confined to the ~10-12 nm range and exhibits only small, device-specific variations without any systematic thermal broadening. This behaviour contrasts with the LRED structures discussed earlier, where a progressive linewidth increase with temperature was observed, as expected for emission dominated by the active medium rather than cavity filtering.

Given that the spectrometer resolution is ≈0.3 nm, far smaller than the measured cavity linewidth, the observed FWHM is not instrument-limited. Instead, it is set by the cavity properties, principally DBR reflectivity and optical losses, rather than by homogeneous broadening in the active region.

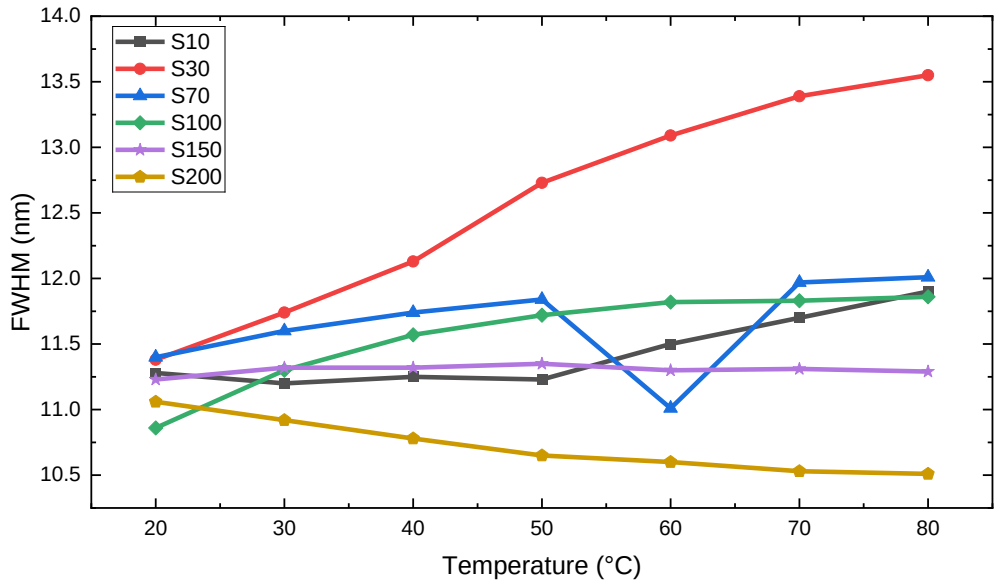

Fig. 7.16: Temperature dependence of the cavity linewidth for all mesa diameters (10-200 µm), measured at fixed drive currents. The FWHM remains within ~10-12 nm across 20-80 °C, with only weak, device-specific drifts and no significant thermal broadening.

For S30-S200, SSR(T) increases monotonically (Fig. 7.17), indicating progressively cleaner, cavity-dominated emission at elevated temperature. In contrast, the 10-µm device (S10) exhibits a weakly non-monotonic dependence, with a shallow minimum near 60-70 °C and partial recovery at 80 °C. This behaviour likely reflects the combination of very low absolute cavity intensity in S10 and its increased sensitivity to small temperature-induced detuning between the cavity resonance and the emission spectrum, which can disproportionately affect the measured SSR at low signal levels. We note, however, that this effect is not

systematic across all devices and may partly reflect device-specific variations rather than a universal temperature response.

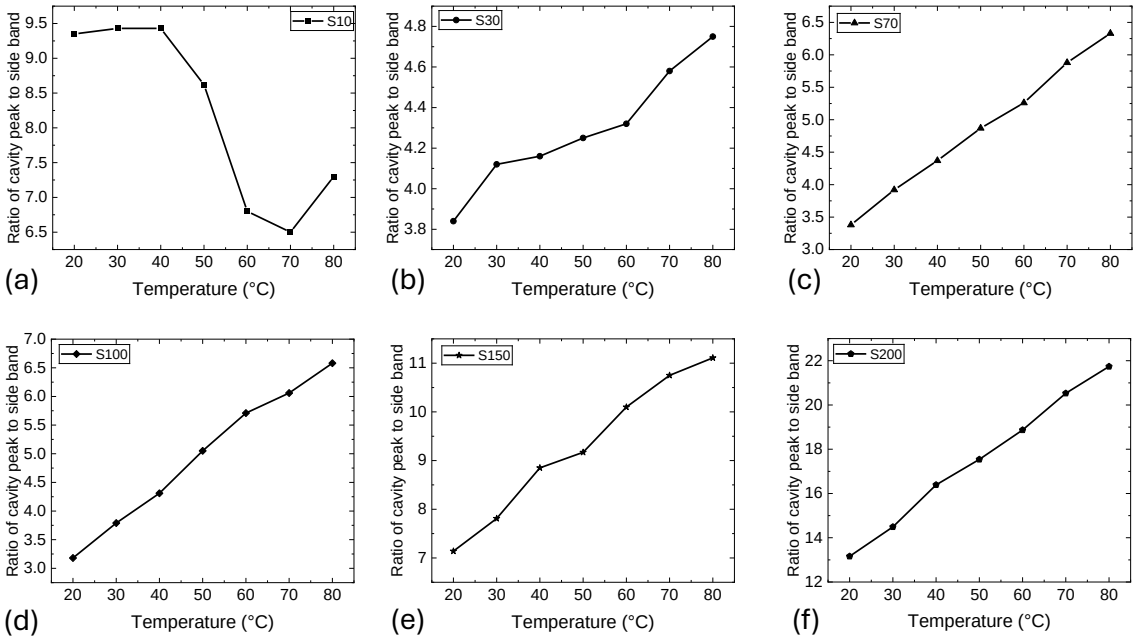

Fig. 7.17: Cavity-to-sideband ratio vs temperature at fixed current. (a) S10, (b) S30, (c) S70, (d) S100, (e) S150, (f) S200.

Integrated cavity-line intensity at fixed current evolves with temperature in a device-specific manner (Fig. 7.18). For S10, S70, S100, S150 and S200 it decreases monotonically, consistent with increasing non-radiative recombination and a possible secondary contribution from temperature-induced cavity-emitter detuning. Unlike the other mesas, S30 exhibits a slight non-monotonic trend. The slightly different behaviour may also reflect device-specific fabrication or material-quality variations rather than a distinct underlying physical mechanism

We tentatively attribute this to a more favourable evolution of cavity-gain alignment in that particular die, most likely arising from lateral wafer non-uniformity (e.g. local thickness/composition variations), rather than any systematic bias or geometry effect.

To enable direct comparison of thermal quenching across devices with different absolute brightness, Fig. 7.19 shows the integrated cavity-line intensity normalised to its 20 °C value for each device. While the cavity-line intensity generally decreases with increasing temperature, the quenching is moderate and strongly device-dependent, supporting the robustness of cavity-selected emission under elevated-temperature operation.

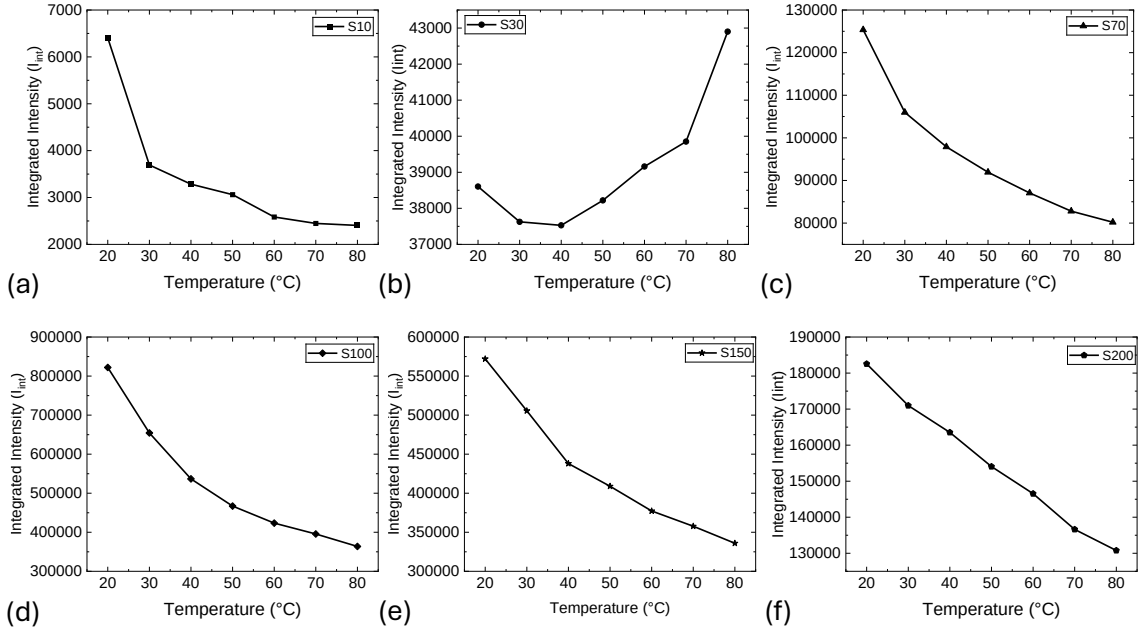

Fig. 7.18: Integrated cavity-line intensity versus temperature. I_{int} for the same bias points. S10, S70, S100, S150, S200 quench monotonically; S30 increases at high T, consistent with improved cavity-gain alignment.

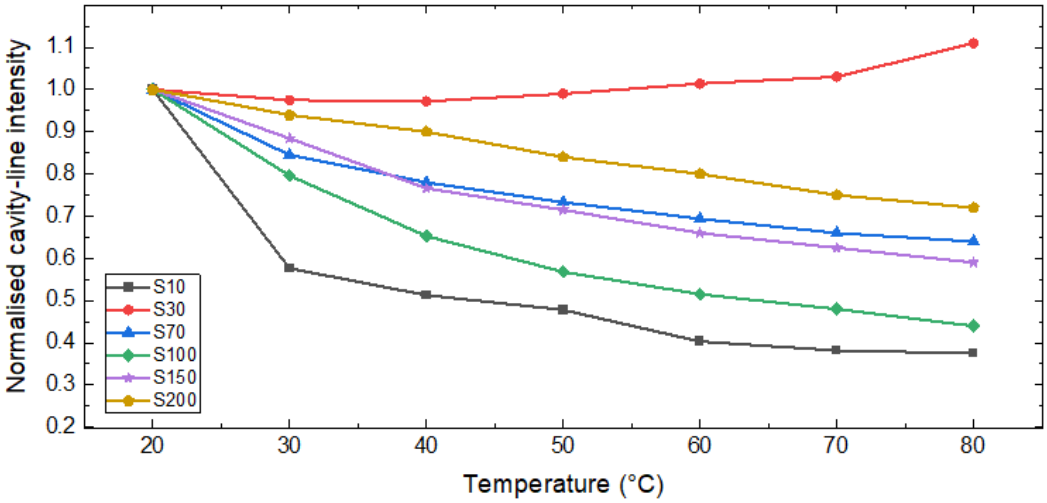

Fig. 7.19: Normalised integrated cavity-line intensity as a function of temperature for SPLED devices with different mesa diameters, recorded at fixed drive current. The intensity is scaled to the 20 °C value for each device to highlight device-dependent thermal quenching behaviour.

Where intensity quenches monotonically, we apply a one-channel Arrhenius linearisation is applied by plotting $ln\left(\frac{I_0}{I}-1\right)$ against $1/T$ which yields sensible activation energies with good linearity (device-wise fits in Fig. 7.20). Here I_0 is obtained from the fit as the high-temperature asymptote of the chosen model. Fits are performed over the strictly monotonic quenching range. The extracted activation energies for the devices that show

intensity decay with temperature are summarised in table 7.3. A clear monotonic increase with device diameter is observed. A plausible explanation is that larger mesas probe a broader lateral ensemble of QR states, sampling regions with deeper confinement and thicker effective barriers, which require higher thermal activation to quench.

Unlike the other devices, the integrated cavity intensity for S30 increases with temperature at fixed current: ≈+11% from 20 to 80 °C, corresponding to a linear slope of (1.73×10^{-3}) $°C^{-1}$ ($R^2 = 0.62$). Because *I(T)* does not decrease with *T* in this device, an Arrhenius analysis is not applicable. We therefore refrain from quoting an activation energy for S30 and instead report the empirical slope together with the temperature-induced improvement in spectral cleanliness (Fig. 7.19(b)).

From an applications standpoint the picture is encouraging: the cavity line remains narrow and thermally stable and spectral cleanliness generally improves with temperature. Practically, low-to-moderate drive currents (limiting series-resistance heating) together with device operation in the 40-80 °C window yield the most cavity-dominated spectra across the diameter series, useful guidance when selecting operating points for subsequent $g^{(2)}(0)$ measurements.

Table 7.3. Activation energies extracted from Arrhenius fits for devices showing monotonic thermal quenching

Device	**Diameter (µm)**	**Activation Energy *Ea* (eV)**
S10	10 µm	0.16 ± 0.02
S70	70 µm	0.20 ± 0.01
S100	100 µm	0.28 ± 0.04
S150	150 µm	0.29 ± 0.05
S200	200 µm	0.33 ± 0.02

Given that fixed-current EL conflates internal efficiency, cavity-gain overlap and extraction, we regard E*a* in this analysis as an effective, device-level figure of merit rather than a fundamental material constant.

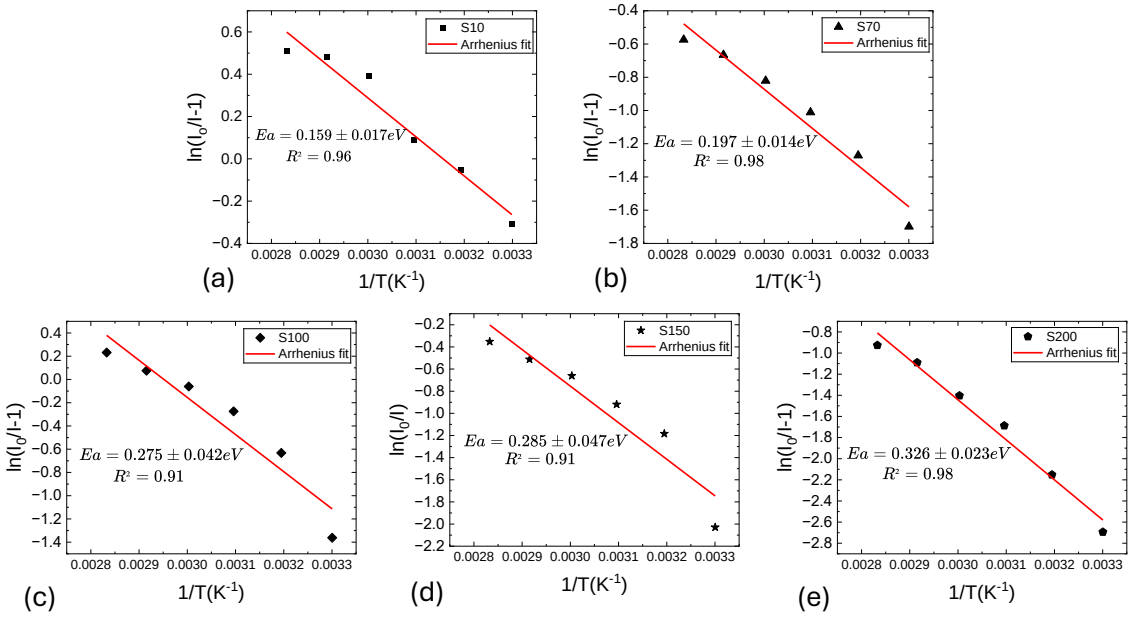

Fig. 7.20: Arrhenius linearisation of devices with monotonic quenching. (a) S10, (b) S70, (c) S100, (d) S150, (e) S200. Fit windows and R^2 values are indicated in-panel; S30 is omitted (non-quenching at the chosen drive).

Taken together, the temperature-dependent EL measurements at fixed current demonstrate that the cavity-selected emission in GaSb/GaAs QR-SPLEDs is remarkably robust against thermal effects up to 80 °C. While the absolute cavity-line intensity generally softens with increasing temperature due to thermally activated non-radiative recombination, the suppression of the broadband background is stronger, leading to improved spectral cleanliness. The cavity resonance exhibits a stable linewidth and a predictable thermo-optic red-shift, confirming that cavity filtering remains effective over the full temperature range studied. Device-to-device variations in the degree of thermal quenching are observed, with one die (S30) showing enhanced cavity-gain alignment at elevated temperature, highlighting the role of wafer-level non-uniformity rather than systematic geometry effects. Overall, these results identify low-to-moderate drive currents and operation in the 40-80 °C window as favourable conditions for cavity-dominated emission, providing a robust operating regime for subsequent single-photon characterisation.

7. 4. Conclusions and Outlook

We have established a clear, reproducible picture of the EL from GaSb QR-SPLEDs across device diameter and operating conditions. At room temperature, all mesas exhibit a single, cavity-selected O-band line centred near 1.24-1.25 µm whose wavelength is essentially invariant with current within the spectrometer resolution (Figs. 7.5-7.6). The linewidth remains confined to ~10-12 nm with only weak, device-specific drifts (Fig. 7.8), indicating that the measured width is cavity-limited rather than governed by homogeneous broadening in the active medium. Using a single, device-independent metric for spectral cleanliness (SSR; Eq. 7.1), we find that at room temperature the spectral contrast is maximised at low-to-moderate drive for S30-S200. For S10, SSR increases more gradually across its sub-mA

window, which we attribute mainly to an improving signal-to-noise ratio in this small-area device as the cavity peak rises further above the background.

Under fixed-current operation, increasing temperature from 20 °C to 80 °C produces a near-linear thermo-optic red-shift of the cavity mode (Fig. 7.15) and a systematic suppression of the off-resonant background, with SSR(T) rising monotonically for S30-S200 (Fig. 7.17). S10 shows a shallow minimum near 60-70 °C followed by a small recovery. The cavity linewidth remains stable across this range, confirming that the cavity resonance is spectrally robust against thermal perturbation.

The integrated cavity intensity decreases with temperature for S10, S70, S100, S150 and S200, whereas S30 exhibits a mild increase, consistent with improved cavity-gain matching at that bias/diameter (Fig. 7.13). For the devices showing monotonic quenching, Arrhenius linearisation (Eq. 7.3) allows extraction of an effective activation energy; the corresponding fits are shown in Fig. 7.20. The extracted energy values should be interpreted as comparative metrics rather than material constants because the fixed-current EL signal reflects a convolution of internal efficiency, cavity-gain overlap and extraction. As S30 does not exhibit quenching over 20-80 °C, an activation energy is not assigned for this device.

Practically, these results identify an operating window, low-to-moderate currents and device temperatures in the 40-80 °C range, that yields the cleanest, most cavity-dominated spectra across the diameter series. This is a very encouraging regime for follow-on quantum-optical characterisation, including $g^{(2)}(0)$ measurements, and it notably implies that spectral contrast can improve above room temperature, a very unusual and useful attribute for cooler-free deployment.

Chapter 8 Conclusion and Future Work

8. 1. Summary of Key Findings

This thesis has developed and experimentally validated a series of type-II GaSb/GaAs quantum-ring (QR) light-emitting architectures aimed at enabling future single-photon operation at telecom wavelengths. The work spans materials growth, device fabrication, optical engineering and cavity-integrated LED design, and shows that type-II GaSb/GaAs quantum rings form a robust, near-room-temperature platform for O-band emission compatible with established III-V processing methods. Broadband QR-LEDs fabricated from a single MBE-grown wafer exhibited the canonical signatures of type-II recombination,1.18-1.28 μm emission, current-induced blue-shifts, temperature-induced red-shifts and activation energies of 110-125 meV, confirming strong hole confinement and low non-radiative loss in well-passivated geometries.

To address the intrinsic extraction bottleneck of III-V LEDs, a monolithic DBT was designed through transfer-matrix optimisation and grown with high fidelity. The DBT provided substantial enhancement of collected emission by optimising optical extraction rather than altering carrier dynamics, establishing it as a practical, fabrication-compatible approach to improving fibre-compatible photon escape. Building on this foundation, a cavity-integrated architecture incorporating GaSb/GaAs quantum rings, a GaAs quantum-dot single-electron filter, and a DBR cavity produced a narrow, cavity-selected emission line around 1.24-1.25 μm with a stable linewidth (~10-12 nm) and improved spectral contrast at elevated temperatures. Across 20-80 °C, the resonance followed predictable thermo-optic tuning while the off-resonant background was systematically suppressed, indicating that the combined electronic and photonic design satisfies several key pre-conditions for future single-photon operation. Collectively, these results establish a coherent technological progression, from broadband LEDs, to extraction-enhanced emitters, to cavity-stabilised structures, demonstrating that type-II GaSb/GaAs quantum rings provide a promising basis for scalable, electrically injected telecom-band quantum-light devices.

8. 2. Scientific Significance

The results show that type-II GaSb/GaAs quantum-ring structures, when integrated with engineered optical stacks and controlled carrier-injection schemes, provide stable and efficient electrically driven emission at telecom wavelengths under near-room-temperature conditions. The work contributes:

• Comprehensive optoelectronic characterisation of type-II GaSb/GaAs quantum rings**,** establishing their suitability as broadband O-band emitters and clarifying relationships between geometry, thermal environment and spectral response.

• A monolithic extraction-engineering approach**,** where the DBT increases photon escape without imposing electrical or kinetic penalties.

• Experimental validation of a cavity-integrated architecture**,** indicating the feasibility of constructing a future single-photon-oriented device within a single epitaxial and fabrication flow.

• Identification of practical operating windows, particularly the improvement of spectral contrast at elevated temperatures, relevant for cooler-free quantum-communication hardware.

• Methodological contributions**,** providing a framework for systematic study of type-II heterostructure optoelectronics and cavity-integrated quantum-light devices.

8. 3. Commercial and Technological Impact

Beyond its scientific contributions, this research has supported the formation of Photarix Ltd, a Lancaster University spin-out established to develop and ultimately commercialise GaSb/GaAs quantum-ring-based quantum-light technologies for quantum-secure communication. The fabrication flows, optical-engineering concepts and device-level insights developed in this thesis constitute part of Photarix's early technical foundation and outline a clear path from fundamental research to application-driven quantum hardware.

The underlying device concepts benefit from compatibility with mature III-V manufacturing workflows, particularly those used for VCSEL production. This alignment provides a realistic and cost-effective route toward large-scale fabrication, reducing the barriers typically associated with quantum-light-source development.

8. 4. Outstanding Challenges and Future Work

Despite the advances presented in this thesis, important challenges remain before QR-SPLEDs can be fully deployed in practical quantum communication systems.

1) Single-Photon Characterisation:

The immediate next step is experimental verification of single-photon emission through second-order correlation measurements $g^2(0)$ and time-resolved photon statistics. While the cavity-enhanced device architecture and thermal stability demonstrated in Chapter 7 lay promising groundwork, direct measurement of photon purity remain essential. This requires implementation of autocorrelation and cross-correlation measurements using superconducting single-photon detectors or other high-efficiency photodiodes; quantification of Hanbury-Brown-Twiss $g^2(0)$ at the device operating point (low-to-moderate bias, 40-80 °C); and systematic study of how cavity detuning, temperature, and injection current affect photon statistics. Such measurements will clarify whether the combination of single-electron injection and cavity enhancement is sufficient to suppress multi-photon emission, or whether additional filtering or feedback mechanisms are required.

2) Room-Temperature QKD Demonstration:

A key target is the demonstration of a complete QKD protocol (e.g., BB84 or decoy-state variants) using QR-SPLED sources operating at or near room temperature. This requires integration of the QR-SPLED with standard single-photon detectors, filters, and classical feedback electronics; measurement of key generation rates under realistic fibre-transmission conditions; comparison of system performance and cost-per-distributed-key metrics with competing SPS platforms (InAs QDs, defect centres, spontaneous parametric down-

conversion); and assessment of long-term stability under continuous operation, including monitoring for spectral drift, intensity fluctuations and blinking. Successfully completing such a demonstration would validate QR-SPLEDs as practical alternatives for quantum networks and accelerate commercial interest.

3) Statistical Characterisation and Scalability:

The current thesis examined single devices or small device sets, acquiring data in separate fabrication sessions. Future work must address reproducibility and scaling through systematic fabrication of multiple devices per nominal geometry under identical conditions, enabling robust statistical analysis of size-dependent confinement, thermal resistance and spectral properties; standardised optical coupling and characterisation to eliminate session-to-session variations; wafer-scale uniformity mapping via spectrophotometry and electroluminescence to identify composition/thickness gradients and optimise growth parameters; and extension to larger device arrays, transitioning from proof-of-concept to manufacturing-relevant volume. Such characterisation will clarify whether the trends observed in Chapter 5 reflect fundamental physics or statistical artefact, and will guide design choices for commercial prototypes.

4) Entanglement Generation

While single-photon sources are essential for QKD, many advanced quantum networks also benefit from entangled photon pairs. Future research could explore two-photon generation via cascade processes by investigating whether carefully engineered band structures enable cascade emission with sufficient correlation; parametric down-conversion through integration of nonlinear $\chi^{(2)}$ materials (e.g. $Al_xGa_{(1-x)}As$ waveguides) with QR-SPLED sources to generate photon pairs; and cavity-mediated processes that exploit high-finesse cavities to enhance weak nonlinear interactions or facilitate exotic many-body processes. Success in any of these directions would substantially expand the utility of QR-SPLED technology beyond single-photon QKD to entanglement-based protocols and distributed quantum computing.

5) Extended Wavelength Coverage

While this thesis focused on the O-band (1260-1360 nm), quantum communication infrastructure increasingly demands sources across the full telecom range, including the C-band (1530-1565 nm) and L-band (1565-1625 nm). Notably, previous work has demonstrated cavity resonances at wavelengths up to 1482 nm in related GaSb-based structures, indicating that extension towards longer telecom wavelengths may be achievable through cavity re-optimisation alone, without requiring fundamental changes to the active material system.

Future work should therefore explore longer-wavelength QR-SPLED variants through optical and epitaxial design strategies that preserve room-temperature operation and scalability, enabling compatibility with wavelength-division-multiplexed quantum communication architectures. Extended wavelength coverage would increase the addressable market and facilitate integration with existing telecom infrastructure.

6) Cavity-QED and Purcell Enhancement

The DBR cavities employed in this work primarily act as spectral filters and are not optimised to exploit Purcell enhancement. Future work could explore higher-quality-factor cavity designs to enhance light-matter interaction strength, potentially increasing radiative recombination rates and improving spectral purity. Incorporating controlled cavity tunability may further enable dynamic compensation of spectral drift and stabilisation of the emission wavelength. More generally, cavity-QED-inspired approaches offer a promising route to improving the performance of QR-SPLEDs beyond purely spectral filtering, while remaining compatible with scalable semiconductor device architectures.

7) Integration with Quantum Photonic Platforms

Beyond stand-alone operation, QR-SPLEDs should be integrated into larger quantum photonic systems through chip-scale integration, monolithic co-integration of QR-SPLEDs with on-chip waveguides, filters, modulators, and detectors on a single III-V platform; hybrid integration through heterogeneous bonding of QR-SPLED chiplets with silicon-on-insulator circuits for low-loss routing and active control; and network integration demonstrating QR-SPLED operation within multi-node quantum network testbeds, assessing compatibility with classical network infrastructure and real-world propagation challenges. Such integration would accelerate the transition from isolated device demonstrations to deployed quantum communication systems.

8. 5. Commercialisation Pathway

The most significant barriers to QR-SPLED commercialisation are the robust demonstration of reliable single-photon emission and the transition to large-scale manufacturing. This thesis advances the commercialisation pathway by refining the proof-of-concept device through optimisation of fabrication procedures, identification of high-yield process windows, and validation of performance across device ensembles; demonstrating cost-effective manufacturability by leveraging existing VCSEL and DBR-mirror infrastructure, eliminating the need for novel capital equipment and reducing per-unit production costs; establishing quantitative performance benchmarks providing experimentally validated metrics (spectral linewidth, thermal stability, extraction efficiency) against which commercial prototypes can be measured; and identifying application niches clarifying where QR-SPLEDs offer distinctive advantages relative to competing platforms. Strong relationships with Lancaster University and industrial partners provide a cost-effective pathway for technology de-risking and scaling, avoiding the large capital outlays traditionally required for quantum-photonics start-ups. This positions Photarix to bring practical, affordable quantum-secure communication systems to market within a realistic commercial timeline.

8. 6. Concluding Remarks

This thesis establishes type-II GaSb/GaAs quantum-ring structures as a viable, scalable and economically attractive platform for telecom-wavelength single-photon light sources. By integrating materials engineering, device physics and experimental nanophotonics, the work demonstrates that careful design of band structure, carrier injection and photonic environment can deliver the stability, efficiency, and operational simplicity required for practical quantum communication systems.

The results do not constitute a complete, fully characterised single-photon source, that achievement awaits rigorous $g^2(0)$ measurements. Rather, the thesis provides the experimental foundations, design principles, and methodologies upon which such characterisation can be reliably built. The convergence of strong carrier confinement, stable cavity-enhanced emission, systematic thermal robustness, and compatibility with high-volume manufacturing suggests that the underlying approach is fundamentally sound.

Looking forward, the priority is experimental verification of single-photon statistics, followed by QKD protocol demonstrations and statistical characterisation of device reproducibility. Success in these areas would establish QR-SPLEDs as a distinct, commercially viable category within the broader landscape of quantum-light sources, enabling a new generation of scalable, affordable, room-temperature quantum communication networks.

The journey from fundamental semiconductor physics to practical quantum technology is long and uncertain, but the trajectory is clear. The insights and methodologies developed in this thesis, grounded in rigorous materials characterisation, device engineering and experimental innovation, provide a solid foundation for the next chapter of this research programme.

References

[1] W. Shi, C. Zou, Y. Cao, and J. Liu, “The progress and trend of heterogeneous integration silicon/III-V semiconductor optical amplifiers,” in *Photonics*, MDPI, 2023, p. 161.

[2] M. Fukuda, *Optical semiconductor devices*. John Wiley & Sons, 1998.

[3] H. Lei, “GaAs-based distributed feedback lasers based on GaAs-InGaP regrowth technology,” 2017, *University of Sheffield*.

[4] M. Hayne *et al.*, “Electron localization by self-assembled GaSb/GaAs quantum dots,” *Appl. Phys. Lett.*, vol. 82, no. 24, pp. 4355–4357, 2003.

[5] N. Gregersen, D. P. S. McCutcheon, and J. Mørk, “Single-photon sources,” *Handb. Optoelectron. Device Model. Simul.*, pp. 585–608, 2017.

[6] X. Ding *et al.*, “On-demand single photons with high extraction efficiency and near-unity indistinguishability from a resonantly driven quantum dot in a micropillar,” *Phys. Rev. Lett.*, vol. 116, no. 2, p. 20401, 2016.

[7] S. Harrison, *Exploring and exploiting charge-carrier confinement in semiconductor nanostructures: heterodimensionality in sub-monolayer InAs in GaAs and photoelectrolysis using type-II heterojunctions*. Lancaster University (United Kingdom), 2016.

[8] Brunschwig B., “User Guide for Cary 5000 spectrometer with external DRA 1800 attachment,” pp. 1–17, 2021.

[9] M. Levinshtein, *Handbook series on semiconductor parameters*, vol. 1. World scientific, 1997.

[10] M. S. Shur, *Handbook series on semiconductor parameters*, vol. 1. World Scientific, 1996.

[11] “GaSb- Gallium Antimonide.” [Online]. Available: https://www.ioffe.ru/SVA/NSM/Semicond/GaSb/

[12] “GaAs- Gallium Arsenide”, [Online]. Available: https://www.ioffe.ru/SVA/NSM/Semicond/GaAs/

[13] Y. Zhang *et al.*, “The magic of III-Vs,” in *Earth and Space: From Infrared to Terahertz (ESIT 2022)*, SPIE, 2023, pp. 155–171.

[14] S. Mokkapati and C. Jagadish, “III-V Compound Semiconductor Optoelectronic Devices,” *Wiley Encycl. Electr. Electron. Eng.*, pp. 1–26, 1999.

[15] S. J. Sweeney and J. Mukherjee, “Optoelectronic devices and materials,” *Springer Handb. Electron. photonic Mater.*, p. 1, 2017.

[16] X.-L. Wang, “III-V group compound semiconductor light-emitting diode,” Jul. 19, 2011, *Google Patents*.

[17] J. S. Major, D. F. Welch, and D. R. Scifres, “III-V aresenide-nitride semiconductor materials and devices,” Nov. 18, 1997, *Google Patents*.

[18] T. Eales, “Influence of electronic band structure on the efficiency of mid-infrared

photonic devices.," 2020, *University of Surrey*.

[19] G. Shukla, K. Gupta, R. Singh, A. Devgan, A. Yash, and L. Singh, "Understanding the Mechanism of Some Important Heterostructures for Optoelectronic Application," in *2022 International Conference on Computational Intelligence and Sustainable Engineering Solutions (CISES)*, IEEE, 2022, pp. 314–318.

[20] H. Kalt and H. Kalt, "Introduction to Semiconductor Band Structures," *Opt. Prop. III–V Semicond. Influ. Multi-Valley Band Struct.*, pp. 1–16, 1996.

[21] C. HILSUM and A. C. ROSE-INNES, "Chapter 3 - BAND STRUCTURE," in *Semiconducting III–V Compounds*, C. HILSUM and A. C. ROSE-INNES, Eds., Pergamon, 1961, pp. 27–67. doi: https://doi.org/10.1016/B978-0-08-009499-1.50008-0.

[22] L.-D. Yuan, H.-X. Deng, S.-S. Li, S.-H. Wei, and J.-W. Luo, "Unified theory of direct or indirect band-gap nature of conventional semiconductors," *Phys. Rev. B*, vol. 98, no. 24, p. 245203, 2018.

[23] I. Vurgaftman, J. Á. R. Meyer, and L. R. Ram-Mohan, "Band parameters for III–V compound semiconductors and their alloys," *J. Appl. Phys.*, vol. 89, no. 11, pp. 5815–5875, 2001.

[24] H. K. Zimmermann and H. Zimmermann, "Silicon Light Emitters," *Integr. Silicon Optoelectron.*, pp. 237–256, 2010.

[25] D. J. Lockwood, "Progress in light emission from silicon and germanium nanostructures," *ECS Trans.*, vol. 85, no. 3, p. 23, 2018.

[26] E. F. Schubert, *Light-emitting diodes*. Cambridge university press, 2006.

[27] W. Joyce, "Expression for the Fermi energy in narrow-bandgap semiconductors," *IEEE J. Quantum Electron.*, vol. 19, no. 11, pp. 1625–1627, 1983.

[28] J. Lazzari *et al.*, "Carrier concentration control of GaSb/GaInAsSb system," in *AIP Conference Proceedings*, American Institute of Physics, 2007, pp. 115–126.

[29] J. Buckeridge, T. D. Veal, C. R. A. Catlow, and D. O. Scanlon, "Intrinsic point defects and the n-and p-type dopability of the narrow gap semiconductors GaSb and InSb," *Phys. Rev. B*, vol. 100, no. 3, p. 35207, 2019.

[30] M. P. Mikhailova, K. D. Moiseev, and Y. P. Yakovlev, "Discovery of III–V semiconductors: physical properties and application," *Semiconductors*, vol. 53, pp. 273–290, 2019.

[31] S. M. Sze, Y. Li, and K. K. Ng, *Physics of semiconductor devices*. John wiley & sons, 2021.

[32] L. A. Coldren, S. W. Corzine, and M. L. Mashanovitch, *Diode lasers and photonic integrated circuits*. John Wiley & Sons, 2012.

[33] "GaSb- Gallium Antimonide Band structure and carrier concentration." [Online]. Available: https://www.ioffe.ru/SVA/NSM/Semicond/GaSb/bandstr.html

[34] J. H. Davies, *The physics of low-dimensional semiconductors: an introduction*. Cambridge university press, 1998.

[35] P. D. Hodgson, M. Hayne, M. Ahmad Kamarudin, Q. D. Zhuang, S. Birindelli, and M. Capizzi, “Hydrogenation of GaSb/GaAs quantum rings,” *Appl. Phys. Lett.*, vol. 105, no. 8, 2014.

[36] R. J. Young, E. P. Smakman, A. M. Sánchez, P. Hodgson, P. M. Koenraad, and M. Hayne, “Optical observation of single-carrier charging in type-II quantum ring ensembles,” *Appl. Phys. Lett.*, vol. 100, no. 8, 2012.

[37] N. N. Ledentsov *et al.*, “Radiative states in type-II GaSb/GaAs quantum wells,” *Phys. Rev. B*, vol. 52, no. 19, p. 14058, 1995.

[38] K. F. Brennan, *The physics of semiconductors: with applications to optoelectronic devices*. Cambridge university press, 1999.

[39] G. Stollwerck, O. V Sulima, and A. W. Bett, “Characterization and simulation of GaSb device-related properties,” *IEEE Trans. Electron Devices*, vol. 47, no. 2, pp. 448–457, 2000.

[40] “Energy band gap Eg of AlxGa1-xAs alloys.” [Online]. Available: https://www.batop.de/information/Eg_AlGaAs.html

[41] J.-B. Wang *et al.*, “Band edge alignment of pseudomorphic GaAs 1− y Sb y on GaAs,” *Phys. Rev. B—Condensed Matter Mater. Phys.*, vol. 70, no. 19, p. 195339, 2004.

[42] Y. Wang, F. Zahid, Y. Zhu, L. Liu, J. Wang, and H. Guo, “Band offset of GaAs/AlxGa1− xAs heterojunctions from atomistic first principles,” *Appl. Phys. Lett.*, vol. 102, no. 13, 2013.

[43] P. J. Carrington, A. S. Mahajumi, M. C. Wagener, J. R. Botha, Q. Zhuang, and A. Krier, “Type II GaSb/GaAs quantum dot/ring stacks with extended photoresponse for efficient solar cells,” *Phys. B Condens. Matter*, vol. 407, no. 10, pp. 1493–1496, 2012.

[44] S.-C. Hsu *et al.*, “Positioning effect of type-II GaSb/GaAs quantum ring layer on solar cell performances,” in *2015 IEEE 42nd Photovoltaic Specialist Conference (PVSC)*, IEEE, 2015, pp. 1–3.

[45] R. L. Anderson, “Experiments on ge-gaas heterojunctions,” *Solid. State. Electron.*, vol. 5, no. 5, pp. 341–351, 1962.

[46] G. Acar, L. Leguay, S. Jones, P. Hodgson, A. Schliwa, and M. Hayne, “Towards GaSb/GaAs quantum-ring single-photon LEDs: Recent progress and prospects,” *Light. Devices, Mater. Appl. XXVIII*, vol. 12906, pp. 41–47, 2024.

[47] P. D. Hodgson, “The Optical Properties of Self-Assembled Quantum Dots, Rings and Posts,” 2014, *Lancaster University (United Kingdom)*.

[48] P. D. Hodgson, R. J. Young, M. A. Kamarudin, Q. D. Zhuang, and M. Hayne, “Hole migration and optically induced charge depletion in GaSb/GaAs wetting layers and quantum rings,” *Phys. Rev. B—Condensed Matter Mater. Phys.*, vol. 88, no. 15, p. 155322, 2013.

[49] I. Filikhin, S. G. Matinyan, and B. Vlahovic, “Quantum mechanics of semiconductor quantum dots and rings,” *Fingerprints Opt. Transp. Prop. Quantum Dots*, vol. 333, 2012.

[50] H. Kroemer, “The 6.1 A family (InAs, GaSb, AlSb) and its heterostructures: a selective review,” *Phys. E Low-dimensional Syst. Nanostructures*, vol. 20, no. 3–4, pp. 196–203, 2004.

[51] A. Rogalski, *Infrared detectors*. CRC press, 2000.

[52] A. Rogalski, P. Martyniuk, and M. Kopytko, “InAs/GaSb type-II superlattice infrared detectors: Future prospect,” *Appl. Phys. Rev.*, vol. 4, no. 3, 2017.

[53] Y. U. Peter and M. Cardona, *Fundamentals of semiconductors: physics and materials properties*. Springer Science & Business Media, 2010.

[54] P. Bhattacharya, *Semiconductor optoelectronic devices*. Prentice-Hall, Inc., 1997.

[55] “AlxGa1-xAs.” [Online]. Available: https://www.ioffe.ru/SVA/NSM/Semicond/AlGaAs/

[56] D. Lane, P. D. Hodgson, R. J. Potter, R. Beanland, and M. Hayne, “ULTRARAM: toward the development of a III–V semiconductor, nonvolatile, random access memory,” *IEEE Trans. Electron Devices*, vol. 68, no. 5, pp. 2271–2274, 2021.

[57] P. D. Hodgson, D. Lane, P. J. Carrington, E. Delli, R. Beanland, and M. Hayne, “ULTRARAM: A Low-Energy, High-Endurance, Compound-Semiconductor Memory on Silicon,” *Adv. Electron. Mater.*, vol. 8, no. 4, p. 2101103, 2022.

[58] P. J. Carrington *et al.*, “Type II GaSb/GaAs quantum rings with extended photoresponse for efficient solar cells,” in *Next Generation Technologies for Solar Energy Conversion VII*, SPIE, 2016, pp. 29–35.

[59] M. Grundmann, *The physics of semiconductors*, vol. 13. Springer, 2006.

[60] D. M. Cárdenes, *Type-II GaSb/GaAs Quantum Ring Intermediate Band Solar Cell*. Lancaster University (United Kingdom), 2019.

[61] U. Keller and A. C. Tropper, “Passively modelocked surface-emitting semiconductor lasers,” *Phys. Rep.*, vol. 429, no. 2, pp. 67–120, 2006.

[62] M. S. Liang, T. J. Bullough, and T. B. Joyce, “Thermal stability of C-doped GaAs/AlAs DBR structures,” *Solid. State. Electron.*, vol. 52, no. 8, pp. 1256–1259, 2008.

[63] B. Zhang *et al.*, “Fabrication of InAs quantum dots in AlAs⁄ GaAs DBR pillar microcavities for single photon sources,” *J. Appl. Phys.*, vol. 97, no. 7, 2005.

[64] H. Gebretsadik, K. Kamath, K. K. Linder, P. Bhattacharya, C. Caneau, and R. Bhat, “Growth and characterization of defect-free GaAs/AlAs distributed Bragg reflector mirrors on patterned InP-based heterostructures,” *J. Vac. Sci. Technol. B Microelectron. Nanom. Struct. Process. Meas. Phenom.*, vol. 16, no. 3, pp. 1417–1421, 1998.

[65] A. Perona *et al.*, “AlAsSb/GaSb doped distributed Bragg reflectors for electrically pumped VCSELs emitting around 2.3 μm,” *Semicond. Sci. Technol.*, vol. 22, no. 10, p. 1140, 2007.

[66] L. Cerutti, A. Garnache, A. Ouvrard, and F. Genty, “High temperature continuous wave operation of Sb-based vertical external cavity surface emitting laser near 2.3 μm,” *J. Cryst. Growth*, vol. 268, no. 1–2, pp. 128–134, 2004.

[67] Z. I. ALFERov, “CONCEPT AND ITS APPLICATIONS IN PHYSICS”.

[68] Q. Lv *et al.*, “Realization of highly efficient InGaN green LEDs with sandwich-like multiple quantum well structure: role of enhanced interwell carrier transport,” *Acs Photonics*, vol. 6, no. 1, pp. 130–138, 2018.

[69] N. Holonyak, R. Kolbas, R. Dupuis, and P. Dapkus, “Quantum-well heterostructure lasers,” *IEEE J. Quantum Electron.*, vol. 16, no. 2, pp. 170–186, 1980.

[70] M. Dyksik *et al.*, “Carrier transfer between confined and localized states in type II InAs/GaAsSb quantum wells,” *Opt. Quantum Electron.*, vol. 49, pp. 1–8, 2017.

[71] E. A. de A. e Silva, “Optical transition energies for lead-salt semiconductor quantum wells,” *Phys. Rev. B*, vol. 60, no. 12, p. 8859, 1999.

[72] D. A. B. Miller, “Optoelectronic applications of quantum wells,” *Opt. Photon. News*, vol. 1, no. 1, pp. 7–15, 1990.

[73] L. Cerutti *et al.*, “GaSb-based composite quantum wells for laser diodes operating in the telecom wavelength range near 1.55-μm,” *Appl. Phys. Lett.*, vol. 106, no. 10, 2015.

[74] R. A. Stradling, “The electronic properties and applications of quantum wells and superlattices of III-V narrow gap semiconductors,” *Brazilian J. Phys.*, vol. 26, pp. 7–20, 1996.

[75] C. Fuchs *et al.*, “Temperature-dependent spectral properties of (GaIn) As/Ga (AsSb)/(GaIn) As W-quantum well heterostructure lasers,” *arXiv Prepr. arXiv2012.01522*, 2020.

[76] I. Mal, A. Hazra, D. P. Samajdar, and T. D. Das, “Investigation of Electronic and Optical Properties of GaSbBi/GaAs Type-II Quantum Wells Using 14-Band k· p Hamiltonian,” in *International Workshop on the Physics of Semiconductor and Devices*, Springer, 2017, pp. 1013–1020.

[77] L. C. Andreani, G. Panzarini, A. V Kavokin, and M. R. Vladimirova, “Effect of inhomogeneous broadening on optical properties of excitons in quantum wells,” *Phys. Rev. B*, vol. 57, no. 8, p. 4670, 1998.

[78] D. Ding *et al.*, “Study on the Quantum Confinement of Photo-Generated Carriers in Quantum Wells,” *IEEE Photonics J.*, vol. 15, no. 3, pp. 1–4, 2023.

[79] K. Kash, “Optical properties of III–V semiconductor quantum wires and dots,” *J. Lumin.*, vol. 46, no. 2, pp. 69–82, 1990.

[80] E. Kapon, S. Simhony, R. Bhat, and D. M. Hwang, “Single quantum wire semiconductor lasers,” *Appl. Phys. Lett.*, vol. 55, no. 26, pp. 2715–2717, 1989.

[81] J. M. Rorison, “Theoretical model of excitons for type-II quantum-wire systems,” *Phys. Rev. B*, vol. 50, no. 11, p. 8008, 1994.

[82] X.-L. Wang and V. Voliotis, “Epitaxial growth and optical properties of semiconductor quantum wires,” *J. Appl. Phys.*, vol. 99, no. 12, 2006.

[83] M. A. Kastner, “Artificial atoms,” *Phys. Today*, vol. 46, no. 1, pp. 24–31, 1993.

[84] T. Takagahara, “Excitonic Structures and Optical Properties of Quantum Dots,”

Semicond. Quantum Dots Physics, Spectrosc. Appl., pp. 59–114, 2002.

[85] T. P. Smith III, K. Y. Lee, C. M. Knoedler, J. M. Hong, and D. P. Kern, "Electronic spectroscopy of zero-dimensional systems," *Phys. Rev. B*, vol. 38, no. 3, p. 2172, 1988.

[86] D. Loss and D. P. DiVincenzo, "Quantum computation with quantum dots," *Phys. Rev. A*, vol. 57, no. 1, p. 120, 1998.

[87] F. Hatami *et al.*, "Radiative recombination in type-II GaSb/GaAs quantum dots," *Appl. Phys. Lett.*, vol. 67, no. 5, pp. 656–658, 1995.

[88] M. Geller, C. Kapteyn, L. Müller-Kirsch, R. Heitz, and D. Bimberg, "450 meV hole localization in GaSb/GaAs quantum dots," *Appl. Phys. Lett.*, vol. 82, no. 16, pp. 2706–2708, 2003.

[89] M. A. Kamarudin *et al.*, "GaSb quantum dot morphology for different growth temperatures and the dissolution effect of the GaAs capping layer," *J. Phys. D. Appl. Phys.*, vol. 43, no. 6, p. 65402, 2010.

[90] M. Ahmad Kamarudin, M. Hayne, R. J. Young, Q. D. Zhuang, T. Ben, and S. I. Molina, "Tuning the properties of exciton complexes in self-assembled GaSb/GaAs quantum rings," *Phys. Rev. B—Condensed Matter Mater. Phys.*, vol. 83, no. 11, p. 115311, 2011.

[91] M. Hayne *et al.*, "The structural, electronic and optical properties of GaSb/GaAs nanostructures for charge-based memory," *J. Phys. D. Appl. Phys.*, vol. 46, no. 26, p. 264001, 2013.

[92] T. Fukui, H. Saito, M. Kasu, and S. Ando, "MOCVD methods for fabricating GaAs quantum wires and quantum dots," *J. Cryst. Growth*, vol. 124, no. 1–4, pp. 493–496, 1992.

[93] P. M. Petroff and S. P. DenBaars, "MBE and MOCVD growth and properties of self-assembling quantum dot arrays in III-V semiconductor structures," *Superlattices Microstruct.*, vol. 15, no. 1, p. 15, 1994.

[94] F. Luckert, K. Poetschke, T. Warming, and D. Bimberg, "Growth of sub-monolayer quantum dots by MOCVD," 2008.

[95] A. J. Martin *et al.*, "Analysis of defect-free GaSb/GaAs (001) quantum dots grown on the Sb-terminated (2× 8) surface," *J. Vac. Sci. Technol. B*, vol. 30, no. 2, 2012.

[96] T.-C. Lin, L.-C. Li, S.-D. Lin, Y.-W. Suen, and C.-P. Lee, "Anomalous optical magnetic shift of self-assembled GaSb/GaAs quantum dots," *J. Appl. Phys.*, vol. 110, no. 1, 2011.

[97] G. G. Zegrya and A. D. Andreev, "Mechanism of suppression of Auger recombination processes in type-II heterostructures," *Appl. Phys. Lett.*, vol. 67, no. 18, pp. 2681–2683, 1995.

[98] J. P. Philbin and E. Rabani, "Auger recombination lifetime scaling for type I and quasi-type II core/shell quantum dots," *J. Phys. Chem. Lett.*, vol. 11, no. 13, pp. 5132–5138, 2020.

[99] A. Nirschl *et al.*, "Towards quantification of the crucial impact of auger

recombination for the efficiency droop in (AlInGa) N quantum well structures," *Opt. Express*, vol. 24, no. 3, pp. 2971–2980, 2016.

[100] Y.-S. Park, W. K. Bae, T. Baker, J. Lim, and V. I. Klimov, "Effect of Auger recombination on lasing in heterostructured quantum dots with engineered core/shell interfaces," *Nano Lett.*, vol. 15, no. 11, pp. 7319–7328, 2015.

[101] M. E. Rubin, H. R. Blank, M. A. Chin, H. Kroemer, and V. Narayanamurti, "Local conduction band offset of GaSb self-assembled quantum dots on GaAs," *Appl. Phys. Lett.*, vol. 70, no. 12, pp. 1590–1592, 1997.

[102] J. M. Garcıa *et al.*, "Intermixing and shape changes during the formation of InAs self-assembled quantum dots," *Appl. Phys. Lett.*, vol. 71, no. 14, pp. 2014–2016, 1997.

[103] R. Timm *et al.*, "Self-organized formation of GaSb/GaAs quantum rings," *Phys. Rev. Lett.*, vol. 101, no. 25, p. 256101, 2008.

[104] P. Offermans *et al.*, "Atomic-scale structure of self-assembled In (Ga) As quantum rings in GaAs," *Appl. Phys. Lett.*, vol. 87, no. 13, 2005.

[105] P. D. Hodgson, M. Hayne, A. J. Robson, Q. D. Zhuang, and L. Danos, "GaSb quantum rings in GaAs/AlxGa1− xAs quantum wells," *J. Appl. Phys.*, vol. 119, no. 4, 2016.

[106] S. Kobayashi, C. Jiang, T. Kawazu, and H. Sakaki, "Self-assembled growth of GaSb type II quantum ring structures," *Jpn. J. Appl. Phys.*, vol. 43, no. 5B, p. L662, 2004.

[107] E. P. Smakman, J. K. Garleff, R. J. Young, M. Hayne, P. Rambabu, and P. M. Koenraad, "GaSb/GaAs quantum dot formation and demolition studied with cross-sectional scanning tunneling microscopy," *Appl. Phys. Lett.*, vol. 100, no. 14, 2012.

[108] J. M. Ulloa *et al.*, "Suppression of InAs⁄ GaAs quantum dot decomposition by the incorporation of a GaAsSb capping layer," *Appl. Phys. Lett.*, vol. 90, no. 21, 2007.

[109] T. Nowozin *et al.*, "800 meV localization energy in GaSb/GaAs/Al0. 3Ga0. 7As quantum dots," *Appl. Phys. Lett.*, vol. 102, no. 5, 2013.

[110] P. D. Hodgson *et al.*, "Blueshifts of the emission energy in type-II quantum dot and quantum ring nanostructures," *J. Appl. Phys.*, vol. 114, no. 7, 2013.

[111] S. O. Jones, P. D. Hodgson, and M. Hayne, "GaSb quantum-rings for vertical-cavity surface-emitting lasers emitting at telecommunications and mobile sensing wavelengths," in *Vertical-Cavity Surface-Emitting Lasers XXVIII*, SPIE, 2024, pp. 146–155.

[112] G. P. Agrawal, N. K. Dutta, G. P. Agrawal, and N. K. Dutta, "Recombination mechanisms in semiconductors," *Semicond. Lasers*, pp. 74–146, 1993.

[113] W. Shockley and W. T. Read Jr, "Statistics of the recombinations of holes and electrons," *Phys. Rev.*, vol. 87, no. 5, p. 835, 1952.

[114] H.-Y. Ryu, J.-K. Hwang, D.-S. Song, I.-Y. Han, Y.-H. Lee, and D.-H. Jang, "Effect of nonradiative recombination on the light-emitting property of two-dimensional photonic crystals," in *Technical Digest. Summaries of papers presented at the Conference on Lasers and Electro-Optics. Postconference Technical Digest (IEEE Cat. No. 01CH37170)*, IEEE, 2001, pp. 292–293.

[115] P. T. Landsberg, *Recombination in semiconductors*. Cambridge University Press, 2003.

[116] D. Bimberg, M. Grundmann, and N. N. Ledentsov, *Quantum dot heterostructures*. John Wiley & Sons, 1999.

[117] M. Deppner, F. Römer, and B. Witzigmann, "Auger recombination and carrier transport effects in III-nitride quantum well light emitting diodes," in *Physics and Simulation of Optoelectronic Devices XXI*, SPIE, 2013, pp. 332–341.

[118] Y. P. Yakovlev *et al.*, "Suppression of Auger recombination in the diode lasers based on type II InAsSb/InAsSbP and InAs/GaInAsSb heterostructures," in *In-Plane Semiconductor Lasers: from Ultraviolet to Midinfrared*, SPIE, 1997, pp. 356–363.

[119] G. G. Zegrya and A. D. A. AF, "Theory of the recombination of nonequilibrium carriers in type-ll heterostructures," *semiconductors*, vol. 2, p. 3, 1996.

[120] W. W. Bewley *et al.*, "Lifetimes and Auger coefficients in type-II W interband cascade lasers," *Appl. Phys. Lett.*, vol. 93, no. 4, 2008.

[121] R. Q. Yang, C. J. Hill, and Y. Qiu, "Mid-IR interband cascade lasers," *MRS Online Proc. Libr.*, vol. 891, pp. 0891-EE01, 2005.

[122] C. A. Hurni *et al.*, "Bulk GaN flip-chip violet light-emitting diodes with optimized efficiency for high-power operation," *Appl. Phys. Lett.*, vol. 106, no. 3, 2015.

[123] B. R. Bennett, R. A. Soref, and J. A. Del Alamo, "Carrier-induced change in refractive index of InP, GaAs and InGaAsP," *IEEE J. Quantum Electron.*, vol. 26, no. 1, pp. 113–122, 1990.

[124] J. Piprek, "Efficiency droop in nitride-based light-emitting diodes," *Phys. status solidi*, vol. 207, no. 10, pp. 2217–2225, 2010.

[125] P. Martyniuk and A. Rogalski, "HOT infrared photodetectors," *Opto-Electronics Rev.*, vol. 21, no. 2, pp. 239–257, 2013.

[126] J. Piprek, *Optoelectronic devices*. Springer, 2005.

[127] Y. Arakawa and M. J. Holmes, "Progress in quantum-dot single photon sources for quantum information technologies: A broad spectrum overview," *Appl. Phys. Rev.*, vol. 7, no. 2, 2020.

[128] S. M. Sze and K. K. Ng, "LEDs and lasers," *Phys. Semicond. devices*, vol. 3, pp. 601–657, 2006.

[129] M. Felle *et al.*, "Interference with a quantum dot single-photon source and a laser at telecom wavelength," *Appl. Phys. Lett.*, vol. 107, no. 13, 2015.

[130] X. Cao, M. Zopf, and F. Ding, "Telecom wavelength single photon sources," *J. Semicond.*, vol. 40, no. 7, p. 71901, 2019.

[131] S. Adachi, *GaAs and related materials: bulk semiconducting and superlattice properties*. World Scientific, 1994.

[132] S. Noda, M. Fujita, and T. Asano, "Spontaneous-emission control by photonic crystals and nanocavities," *Nat. Photonics*, vol. 1, no. 8, pp. 449–458, 2007.

[133] T. Nowozin *et al.*, "Linking structural and electronic properties of high-purity self-

assembled GaSb/GaAs quantum dots," *Phys. Rev. B—Condensed Matter Mater. Phys.*, vol. 86, no. 3, p. 35305, 2012.

[134] R. Q. Yang, C. J. Hill, L. E. Christensen, and C. R. Webster, "Mid-IR type-II interband cascade lasers and their applications," in *Semiconductor and Organic Optoelectronic Materials and Devices*, SPIE, 2005, pp. 413–422.

[135] K. J. Vahala, "Optical microcavities," *Nature*, vol. 424, no. 6950, pp. 839–846, 2003.

[136] R. K. Chang and A. J. Campillo, *Optical processes in microcavities*, vol. 3. World scientific, 1996.

[137] S. O. Jones, "A Study of GaSb Quantum Ring Vertical-Cavity Surface-Emitting Devices at Telecommunications Wavelengths," 2024, *Lancaster University (United Kingdom)*.

[138] S. Gandan *et al.*, "Photoluminescence Properties of Type-II GaSb/GaAs Quantum Rings," *Adv. Photonics Res.*, p. 2500125, 2025.

[139] S. Niu *et al.*, "Brief review of epitaxy and emission properties of GaSb and related semiconductors," *Crystals*, vol. 7, no. 11, p. 337, 2017.

[140] S. L. Chuang, *Physics of photonic devices*. John Wiley & Sons, 2012.

[141] P. K. Basu, B. Mukhopadhyay, and R. Basu, *Semiconductor nanophotonics*, vol. 26. Oxford University Press, 2022.

[142] W.-C. Miao *et al.*, "Modified distributed Bragg reflectors for color stability in InGaN red micro-LEDs," *Nanomaterials*, vol. 13, no. 4, p. 661, 2023.

[143] B.-L. Dai *et al.*, "Investigation and comparison of the influence of modified DBR and yellow color filters for quantum dot color conversion-based micro LED applications," *Heliyon*, vol. 10, no. 16, 2024.

[144] Y. Weng *et al.*, "Fabrication and color conversion of patterned InP/ZnS quantum dots photoresist film via a laser-assisted route," *Opt. Laser Technol.*, vol. 140, p. 107026, 2021.

[145] Y. Sun, L. Shi, P. Du, X. Zhao, and S. Zhou, "Rational Distributed Bragg Reflector Design for Improving Performance of Flip-Chip Micro-LEDs," *Electronics*, vol. 11, no. 19, p. 3030, 2022.

[146] H.-J. Lee, J.-Y. Park, L.-K. Kwac, and J. Lee, "Improvement of Near-Infrared Light-Emitting Diodes' Optical Efficiency Using a Broadband Distributed Bragg Reflector with an AlAs Buffer," *Nanomaterials*, vol. 14, no. 4, p. 349, 2024.

[147] F. Jiang, Z. Xiao, M. Dong, J. Song, and Y. Wang, "Effect of distributed Bragg reflectors on photoluminescence properties of CH3NH3PbI3 film," *Sci. Rep.*, vol. 12, no. 1, p. 10934, 2022.

[148] K. Tai, L. Yang, Y. H. Wang, J. D. Wynn, and A. Y. Cho, "Drastic reduction of series resistance in doped semiconductor distributed Bragg reflectors for surface-emitting lasers," *Appl. Phys. Lett.*, vol. 56, no. 25, pp. 2496–2498, 1990.

[149] U. Sinha, S. N. Sahoo, A. Singh, K. Joarder, R. Chatterjee, and S. Chakraborti, "Single-photon sources," *Opt. Photonics News*, vol. 30, no. 9, pp. 32–39, 2019.

[150] Y. Lin, Y. Ye, and W. Fang, “Electrically driven single-photon sources,” *J. Semicond.*, vol. 40, no. 7, p. 71904, 2019.

[151] S. Pirandola *et al.*, “Advances in quantum cryptography,” *Adv. Opt. photonics*, vol. 12, no. 4, pp. 1012–1236, 2020.

[152] C. C. Gerry and P. L. Knight, *Introductory quantum optics*. Cambridge university press, 2023.

[153] B. Lounis and M. Orrit, “Single-photon sources,” *Reports Prog. Phys.*, vol. 68, no. 5, p. 1129, 2005.

[154] N. Gregersen, P. Kaer, and J. Mørk, “Modeling and design of high-efficiency single-photon sources,” *IEEE J. Sel. Top. Quantum Electron.*, vol. 19, no. 5, pp. 1–16, 2013.

[155] J. Brendel, N. Gisin, W. Tittel, and H. Zbinden, “Pulsed energy-time entangled twin-photon source for quantum communication,” *Phys. Rev. Lett.*, vol. 82, no. 12, p. 2594, 1999.

[156] H.-K. Lo, X. Ma, and K. Chen, “Decoy state quantum key distribution,” *Phys. Rev. Lett.*, vol. 94, no. 23, p. 230504, 2005.

[157] D. Rosenberg *et al.*, “Long-distance decoy-state quantum key distribution in optical fiber,” *Phys. Rev. Lett.*, vol. 98, no. 1, p. 10503, 2007.

[158] V. Scarani, H. Bechmann-Pasquinucci, N. J. Cerf, M. Dušek, N. Lütkenhaus, and M. Peev, “The security of practical quantum key distribution,” *Rev. Mod. Phys.*, vol. 81, no. 3, pp. 1301–1350, 2009.

[159] M. Esmann, S. C. Wein, and C. Antón-Solanas, “Solid-state single-photon sources: recent advances for novel quantum materials,” *Adv. Funct. Mater.*, vol. 34, no. 30, p. 2315936, 2024.

[160] A. J. Shields, “Semiconductor quantum light sources,” *Nat. Photonics*, vol. 1, no. 4, pp. 215–223, 2007.

[161] P. Michler *et al.*, “A quantum dot single photon source,” *Adv. Solid State Phys.*, pp. 3–14, 2001.

[162] P. Michler, “Quantum dot single-photon sources,” in *Single semiconductor quantum dots*, Springer, 2009, pp. 185–225.

[163] M. Paul *et al.*, “Single-photon emission at 1.55 μm from MOVPE-grown InAs quantum dots on InGaAs/GaAs metamorphic buffers,” *Appl. Phys. Lett.*, vol. 111, no. 3, 2017.

[164] G. E. Digeronimo *et al.*, “Integration of single-photon sources and detectors on GaAs,” in *Photonics*, MDPI, 2016, p. 55.

[165] E. Stock *et al.*, “Single-photon emission from InGaAs quantum dots grown on (111) GaAs,” *Appl. Phys. Lett.*, vol. 96, no. 9, 2010.

[166] P. Holewa *et al.*, “Optical and electronic properties of low-density InAs/InP quantum-dot-like structures designed for single-photon emitters at telecom wavelengths,” *Phys. Rev. B*, vol. 101, no. 19, p. 195304, 2020.

[167] T. Miyazawa *et al.*, “Single-photon generation in the 1.55-μm optical-fiber band from

an InAs/InP quantum dot," *Jpn. J. Appl. Phys.*, vol. 44, no. 5L, p. L620, 2005.

[168] A. Jaffal *et al.*, "InAs quantum dot in a needlelike tapered InP nanowire: a telecom band single photon source monolithically grown on silicon," *Nanoscale*, vol. 11, no. 45, pp. 21847–21855, 2019.

[169] M. Benyoucef, M. Yacob, J. P. Reithmaier, J. Kettler, and P. Michler, "Telecom-wavelength (1.5 μm) single-photon emission from InP-based quantum dots," *Appl. Phys. Lett.*, vol. 103, no. 16, 2013.

[170] G. V Astakhov *et al.*, "Spin centres in SiC for quantum technologies," *Appl. Magn. Reson.*, vol. 47, no. 7, pp. 793–812, 2016.

[171] S. Majety, V. A. Norman, P. Saha, A. H. Rubin, S. Dhuey, and M. Radulaski, "Wafer-scale integration of freestanding photonic devices with color centers in silicon carbide," *npj Nanophotonics*, vol. 2, no. 1, p. 3, 2025.

[172] N. Mendelson *et al.*, "Identifying carbon as the source of visible single-photon emission from hexagonal boron nitride," *Nat. Mater.*, vol. 20, no. 3, pp. 321–328, 2021.

[173] A. B. D. Shaik and P. Palla, "Optical quantum technologies with hexagonal boron nitride single photon sources," *Sci. Rep.*, vol. 11, no. 1, p. 12285, 2021.

[174] G. Grosso *et al.*, "Tunable and high-purity room temperature single-photon emission from atomic defects in hexagonal boron nitride," *Nat. Commun.*, vol. 8, no. 1, pp. 1–8, 2017.

[175] M. T. Uysal *et al.*, "Spin-photon entanglement of a single Er 3+ ion in the telecom band," *Phys. Rev. X*, vol. 15, no. 1, p. 11071, 2025.

[176] J.-Y. Huang *et al.*, "Stark tuning of telecom single-photon emitters based on a single Er3+," *Chinese Phys. Lett.*, vol. 40, no. 7, p. 70301, 2023.

[177] S. Ren, Q. Tan, and J. Zhang, "Review on the quantum emitters in two-dimensional materials," *J. Semicond.*, vol. 40, no. 7, p. 71903, 2019.

[178] T. Gao, M. von Helversen, C. Antón-Solanas, C. Schneider, and T. Heindel, "Atomically-thin single-photon sources for quantum communication," *npj 2D Mater. Appl.*, vol. 7, no. 1, p. 4, 2023.

[179] P. J. Carrington, R. J. Young, P. D. Hodgson, A. M. Sanchez, M. Hayne, and A. Krier, "Long-wavelength photoluminescence from stacked layers of high-quality type-II GaSb/GaAs quantum rings," *Cryst. Growth Des.*, vol. 13, no. 3, pp. 1226–1230, 2013.

[180] V. Zapatero *et al.*, "Advances in device-independent quantum key distribution," *npj quantum Inf.*, vol. 9, no. 1, p. 10, 2023.

[181] H. Qin, "QKD and high-speed classical data hybrid metropolitan network," 2020.

[182] A. Broadbent and C. Schaffner, "Quantum cryptography beyond quantum key distribution," *Des. Codes Cryptogr.*, vol. 78, no. 1, pp. 351–382, 2016.

[183] M. Zahidy *et al.*, "Quantum key distribution using deterministic single-photon sources over a field-installed fibre link," *npj Quantum Inf.*, vol. 10, no. 1, p. 2, 2024.

[184] C. H. Bennett and G. Brassard, "Quantum cryptography: Public key distribution and

coin tossing," *Theor. Comput. Sci.*, vol. 560, pp. 7–11, 2014.

[185] C. C. W. Lim, C. Portmann, M. Tomamichel, R. Renner, and N. Gisin, "Device-independent quantum key distribution with local Bell test," *Phys. Rev. X*, vol. 3, no. 3, p. 31006, 2013.

[186] H.-K. Lo, M. Curty, and B. Qi, "Measurement-device-independent quantum key distribution," *Phys. Rev. Lett.*, vol. 108, no. 13, p. 130503, 2012.

[187] B. Da Lio *et al.*, "A pure and indistinguishable single-photon source at telecommunication wavelength," *Adv. Quantum Technol.*, vol. 5, no. 5, p. 2200006, 2022.

[188] M. B. Ward *et al.*, "Electrically driven telecommunication wavelength single-photon source," *Appl. Phys. Lett.*, vol. 90, no. 6, 2007.

[189] T. Gao *et al.*, "A quantum key distribution testbed using a plug&play telecom-wavelength single-photon source," *Appl. Phys. Rev.*, vol. 9, no. 1, 2022.

[190] P. Holewa, A. Reiserer, T. Heindel, S. Sanguinetti, A. Huck, and E. Semenova, "Solid-state single-photon sources operating in the telecom wavelength range," *Nanophotonics*, vol. 14, no. 11, pp. 1729–1774, 2025.

[191] I. Aharonovich, D. Englund, and M. Toth, "Solid-state single-photon emitters," *Nat. Photonics*, vol. 10, no. 10, pp. 631–641, 2016.

[192] C. J. Chunnilall, I. Pietro Degiovanni, S. Kück, I. Müller, and A. G. Sinclair, "Metrology of single-photon sources and detectors: a review," *Opt. Eng.*, vol. 53, no. 8, p. 81910, 2014.

[193] D. K. Thapa and S. Biswas, "Single photon generation from quantum dots: recent advances, challenges and future directions," *Nanoscale*, vol. 17, no. 13, pp. 7651–7672, 2025.

[194] S. Kück, "Single photon sources for absolute radiometry–a review about the current state of the art," *Meas. Sensors*, vol. 18, p. 100219, 2021.

[195] P. Laferriére, S. Haffouz, D. B. Northeast, P. J. Poole, R. L. Williams, and D. Dalacu, "Position-controlled telecom single photon emitters operating at elevated temperatures," *Nano Lett.*, vol. 23, no. 3, pp. 962–968, 2023.

[196] A. Schlehahn *et al.*, "A stand-alone fiber-coupled single-photon source," *Sci. Rep.*, vol. 8, no. 1, p. 1340, 2018.

[197] F. Bouchard *et al.*, "Two-photon interference: the Hong–Ou–Mandel effect," *Reports Prog. Phys.*, vol. 84, no. 1, p. 12402, 2020.

[198] D. A. Vajner, *From Quantum Dots to Quantum Communication Advances in Quantum Light Generation from Semiconductor Quantum Dots*. Technische Universitaet Berlin (Germany), 2025.

[199] C. L. Phillips *et al.*, "Purcell-enhanced single photons at telecom wavelengths from a quantum dot in a photonic crystal cavity," *Sci. Rep.*, vol. 14, no. 1, p. 4450, 2024.

[200] M. D. Birowosuto *et al.*, "Fast Purcell-enhanced single photon source in 1,550-nm telecom band from a resonant quantum dot-cavity coupling," *Sci. Rep.*, vol. 2, no. 1, p. 321, 2012.

[201] Y. Chen, M. Zopf, R. Keil, F. Ding, and O. G. Schmidt, “Highly-efficient extraction of entangled photons from quantum dots using a broadband optical antenna,” *Nat. Commun.*, vol. 9, no. 1, p. 2994, 2018.

[202] K. G. Lee *et al.*, “A planar dielectric antenna for directional single-photon emission and near-unity collection efficiency,” *Nat. Photonics*, vol. 5, no. 3, pp. 166–169, 2011.

[203] G. C. K. S. Mathur, *Fiber Optics Fundamentals and Advances in Optical Communications*. Blue Rose Publishers, 2021.

[204] T. Müller *et al.*, “A quantum light-emitting diode for the standard telecom window around 1,550 nm,” *Nat. Commun.*, vol. 9, no. 1, p. 862, 2018.

[205] N. Ajnef, M. M. Habchi, and A. Rebey, “GaAs-based strain-balanced GaNxAs1-x-yBiy type-I and-II multi-quantum wells for near-infrared photodetection range,” *Thin Solid Films*, vol. 726, p. 138655, 2021.

[206] J. Wu, Z. Xu, J. Chen, and L. He, “Temperature-dependent photoluminescence of the InAs-based and GaSb-based type-II superlattices,” *Infrared Phys. Technol.*, vol. 92, pp. 18–23, 2018.

[207] A.-S. Mahajumi *et al.*, “Rapid thermal annealing and photoluminescence of type-II GaSb single monolayer quantum dot stacks,” *J. Phys. D. Appl. Phys.*, vol. 46, no. 30, p. 305104, 2013.

[208] M. P. Young *et al.*, “Photoluminescence studies of individual and few GaSb/GaAs quantum rings,” *Aip Adv.*, vol. 4, no. 11, 2014.

[209] J. Michl *et al.*, “Strain-free GaSb quantum dots as single-photon sources in the telecom S-band,” *Adv. Quantum Technol.*, vol. 6, no. 12, p. 2300180, 2023.

[210] S. Scheel, “Single-photon sources–an introduction,” *J. Mod. Opt.*, vol. 56, no. 2–3, pp. 141–160, 2009.

[211] E. Hulicius, A. Hospodková, and M. Zíková, “Quantum Dots,” *Met. Vap. Phase Ep. Growth, Mater. Prop. Appl.*, pp. 175–215, 2019.

[212] J. Richter *et al.*, “GaSb quantum dots on GaAs with high localization energy of 710 meV and an emission wavelength of 1.3 μm,” *J. Cryst. Growth*, vol. 404, pp. 48–53, 2014.

[213] R. Heitz *et al.*, “Excited states and energy relaxation in stacked InAs/GaAs quantum dots,” *Phys. Rev. B*, vol. 57, no. 15, p. 9050, 1998.

[214] X. Wang *et al.*, “III–V compounds as single photon emitters,” *J. Semicond.*, vol. 40, no. 7, p. 71906, 2019.

[215] A. H. Proppe *et al.*, “Highly stable and pure single-photon emission with 250 ps optical coherence times in InP colloidal quantum dots,” *Nat. Nanotechnol.*, vol. 18, no. 9, pp. 993–999, 2023.

[216] M. Gong, K. Duan, C.-F. Li, R. Magri, G. A. Narvaez, and L. He, “Electronic structure of self-assembled In As⁄ In P quantum dots: Comparison with self-assembled In As⁄ Ga As quantum dots,” *Phys. Rev. B—Condensed Matter Mater. Phys.*, vol. 77, no. 4, p. 45326, 2008.

[217] S. Kako, C. Santori, K. Hoshino, S. Götzinger, Y. Yamamoto, and Y. Arakawa, “A gallium nitride single-photon source operating at 200 K,” *Nat. Mater.*, vol. 5, no. 11, pp. 887–892, 2006.

[218] A. F. Jarjour, R. A. Oliver, and R. A. Taylor, “Nitride-based quantum dots for single photon source applications,” *Phys. status solidi*, vol. 206, no. 11, pp. 2510–2523, 2009.

[219] C. Couteau *et al.*, “Correlated photon emission from a single II–VI quantum dot,” *Appl. Phys. Lett.*, vol. 85, no. 25, pp. 6251–6253, 2004.

[220] K. Sebald, P. Michler, T. Passow, D. Hommel, G. Bacher, and A. Forchel, “Single-photon emission of CdSe quantum dots at temperatures up to 200 K,” *Appl. Phys. Lett.*, vol. 81, no. 16, pp. 2920–2922, 2002.

[221] Y. Kutovyi *et al.*, “Efficient single-photon sources based on chlorine-doped ZnSe nanopillars with growth controlled emission energy,” *ACS Nano*, vol. 16, no. 9, pp. 14582–14589, 2022.

[222] N. Somaschi *et al.*, “Near-optimal single-photon sources in the solid state,” *Nat. Photonics*, vol. 10, no. 5, pp. 340–345, 2016.

[223] P. Senellart, G. Solomon, and A. White, “High-performance semiconductor quantum-dot single-photon sources,” *Nat. Nanotechnol.*, vol. 12, no. 11, pp. 1026–1039, 2017.

[224] S. L. Portalupi, M. Jetter, and P. Michler, “InAs quantum dots grown on metamorphic buffers as non-classical light sources at telecom C-band: a review,” *Semicond. Sci. Technol.*, vol. 34, no. 5, p. 53001, 2019.

[225] Y. Yu *et al.*, “Telecom-band quantum dot technologies for long-distance quantum networks,” *Nat. Nanotechnol.*, vol. 18, no. 12, pp. 1389–1400, 2023.

[226] M. Benyoucef and A. Musiał, “Telecom Wavelengths InP-Based Quantum Dots for Quantum Communication,” *Photonic Quantum Technol. Sci. Appl.*, vol. 2, pp. 463–507, 2023.

[227] R. Sittig *et al.*, “Thin-film InGaAs metamorphic buffer for telecom C-band InAs quantum dots and optical resonators on GaAs platform,” *Nanophotonics*, vol. 11, no. 6, pp. 1109–1116, 2022.

[228] L. Seravalli, G. Trevisi, and P. Frigeri, “Design and growth of metamorphic InAs/InGaAs quantum dots for single photon emission in the telecom window,” *CrystEngComm*, vol. 14, no. 20, pp. 6833–6838, 2012.

[229] T. Heindel *et al.*, “Quantum key distribution using quantum dot single-photon emitting diodes in the red and near infrared spectral range,” *New J. Phys.*, vol. 14, no. 8, p. 83001, 2012.

[230] X. You *et al.*, “Quantum interference with independent single-photon sources over 300 km fiber,” *Adv. Photonics*, vol. 4, no. 6, p. 66003, 2022.

[231] J. Yang *et al.*, “High-rate intercity quantum key distribution with a semiconductor single-photon source,” *Light Sci. Appl.*, vol. 13, no. 1, p. 150, 2024.

[232] W.-H. Lin, K.-W. Wang, Y.-A. Liao, C.-W. Pao, and S.-Y. Lin, “The formation mechanisms and optical characteristics of GaSb quantum rings,” *J. Appl. Phys.*, vol.

114, no. 5, 2013.

[233] R. Timm *et al.*, “Confined states of individual type-II GaSb/GaAs quantum rings studied by cross-sectional scanning tunneling spectroscopy,” *Nano Lett.*, vol. 10, no. 10, pp. 3972–3977, 2010.

[234] H.-T. Lin *et al.*, “Photonic crystal circular nanobeam cavity laser with type-II GaSb/GaAs quantum rings as gain material,” *Sci. Rep.*, vol. 10, no. 1, p. 4757, 2020.

[235] Y. Chu and M. D. Lukin, “Quantum optics with nitrogen-vacancy centers in diamond,” *Quantum Opt. Nanophotonics*, pp. 229–270, 2015.

[236] F. Jelezko and J. Wrachtrup, “Single defect centres in diamond: A review,” *Phys. status solidi*, vol. 203, no. 13, pp. 3207–3225, 2006.

[237] F. Dolde, “The nitrogen vacancy center in internal and external fields,” 2014, *Universitätsbibliothek der Universität Stuttgart*.

[238] P. P. Filippatos, A. Chroneos, and C. A. Londos, “Re-examination of important defect complexes in silicon: From microelectronics to quantum computing,” *J. Appl. Phys.*, vol. 137, no. 23, 2025.

[239] M. Nahra, “Color Centers in Nanodiamonds for Quantum Optics Applications,” 2021, *Troyes*.

[240] C. Chen, B. Jiang, and X. Hu, “Research progress on silicon vacancy color centers in diamond,” *Funct. Diam.*, vol. 4, no. 1, p. 2332346, 2024.

[241] S. Häußler *et al.*, “Photoluminescence excitation spectroscopy of SiV− and GeV− color center in diamond,” *New J. Phys.*, vol. 19, no. 6, p. 63036, 2017.

[242] C.-M. Lee *et al.*, “High-efficiency single photon emission from a silicon T-center in a nanobeam,” *ACS Photonics*, vol. 10, no. 11, pp. 3844–3849, 2023.

[243] Z. Sharifi *et al.*, “Isolating and enhancing single-photon emitters for 1550 nm quantum light sources using double nanohole optical tweezers,” *J. Chem. Phys.*, vol. 154, no. 18, 2021.

[244] I. R. Berkman *et al.*, “Long optical and electron spin coherence times for erbium ions in silicon,” *npj Quantum Inf.*, vol. 11, no. 1, p. 66, 2025.

[245] L. J. Martınez *et al.*, “Efficient single photon emission from a high-purity hexagonal boron nitride crystal,” *Phys. Rev. B*, vol. 94, no. 12, p. 121405, 2016.

[246] L. Zeng *et al.*, “Single-photon emission from point defects in hexagonal boron nitride induced by plasma treatment,” *ACS Appl. Mater. Interfaces*, vol. 16, no. 19, pp. 24899–24907, 2024.

[247] S. Hou *et al.*, “Engineering Quantum Emitters in 2D Materials,” *Adv. Opt. Mater.*, p. 2500693.

[248] J. Vuckovic, T. Heinz, and F. Jornada, “Programmable quantum emitter arrays,” Stanford Univ., CA (United States), 2024.

[249] X. Sun *et al.*, “Twisted van der Waals quantum materials: fundamentals, tunability, and applications,” *Chem. Rev.*, vol. 124, no. 4, pp. 1992–2079, 2024.

[250] Q. Fu, Z. Hu, M. Zhou, J. Lu, and Z. Ni, “Excitonic emission in atomically thin

electroluminescent devices," *Laser Photon. Rev.*, vol. 15, no. 6, p. 2000587, 2021.

[251] U. Paudel, "Mode Engineering of Single Photons from Cavity Spontaneous Parametric Down-Conversion Source and Quantum Dots," 2017.

[252] D. Kang, "On-chip generation of quantum states of photons," 2015.

[253] T. J. Steiner, "Integrated Quantum Photonics with III-V Semiconductors," 2024, *University of California, Santa Barbara*.

[254] K. A. Meier, "Comparison, optimization, and application of various spontaneous parametric downconversion sources of polarization-entangled photon pairs," 2021, *University of Illinois at Urbana-Champaign*.

[255] M. Borghi, A. Trenti, and L. Pavesi, "Four wave mixing control in a photonic molecule made by silicon microring resonators," *Sci. Rep.*, vol. 9, no. 1, p. 408, 2019.

[256] P. Kultavewuti, E. Y. Zhu, L. Qian, V. Pusino, M. Sorel, and J. Stewart Aitchison, "Correlated photon pair generation in AlGaAs nanowaveguides via spontaneous four-wave mixing," *Opt. Express*, vol. 24, no. 4, pp. 3365–3376, 2016.

[257] M. B. Ward *et al.*, "On-demand single-photon source for 1.3 μm telecom fiber," *Appl. Phys. Lett.*, vol. 86, no. 20, 2005.

[258] T. Miyazawa *et al.*, "Development of electrically driven single-quantum-dot device at optical fiber bands," *Jpn. J. Appl. Phys.*, vol. 45, no. 4S, p. 3621, 2006.

[259] C. Zinoni *et al.*, "Time-resolved and antibunching experiments on single quantum dots at 1300nm," *Appl. Phys. Lett.*, vol. 88, no. 13, 2006.

[260] Y. Xue *et al.*, "1.3 μm single-photon emission from strain-coupled bilayer of InAs/GaAs quantum dots at the temperature up to 120 K," *Appl. Phys. Lett.*, vol. 111, no. 18, 2017.

[261] Z.-S. Chen, B. Ma, X.-J. Shang, H.-Q. Ni, J.-L. Wang, and Z.-C. Niu, "Bright single-photon source at 1.3 μm based on InAs bilayer quantum dot in micropillar," *Nanoscale Res. Lett.*, vol. 12, no. 1, p. 378, 2017.

[262] C. Carmesin *et al.*, "Structural and optical properties of InAs/(In) GaAs/GaAs quantum dots with single-photon emission in the telecom C-band up to 77 K," *Phys. Rev. B*, vol. 98, no. 12, p. 125407, 2018.

[263] N. Srocka *et al.*, "Deterministically fabricated quantum dot single-photon source emitting indistinguishable photons in the telecom O-band," *Appl. Phys. Lett.*, vol. 116, no. 23, 2020.

[264] P. Holewa *et al.*, "Thermal stability of emission from single InGaAs/GaAs quantum dots at the telecom O-band," *Sci. Rep.*, vol. 10, no. 1, p. 21816, 2020.

[265] C. Nawrath *et al.*, "Resonance fluorescence of single In (Ga) As quantum dots emitting in the telecom C-band," *Appl. Phys. Lett.*, vol. 118, no. 24, 2021.

[266] S. Kolatschek *et al.*, "Bright Purcell enhanced single-photon source in the telecom O-band based on a quantum dot in a circular Bragg grating," *Nano Lett.*, vol. 21, no. 18, pp. 7740–7745, 2021.

[267] K. Takemoto *et al.*, "An optical horn structure for single-photon source using

quantum dots at telecommunication wavelength," *J. Appl. Phys.*, vol. 101, no. 8, 2007.

[268] T. Miyazawa *et al.*, "Single-photon emission at 1.5 μm from an InAs/InP quantum dot with highly suppressed multi-photon emission probabilities," *Appl. Phys. Lett.*, vol. 109, no. 13, 2016.

[269] Ł. Dusanowski *et al.*, "Single-photon emission of InAs/InP quantum dashes at 1.55 μm and temperatures up to 80 K," *Appl. Phys. Lett.*, vol. 108, no. 16, 2016.

[270] C.-M. Lee, M. A. Buyukkaya, S. Aghaeimeibodi, A. Karasahin, C. J. K. Richardson, and E. Waks, "A fiber-integrated nanobeam single photon source emitting at telecom wavelengths," *Appl. Phys. Lett.*, vol. 114, no. 17, 2019.

[271] A. Musiał *et al.*, "InP-based single-photon sources operating at telecom C-band with increased extraction efficiency," *Appl. Phys. Lett.*, vol. 118, no. 22, 2021.

[272] A. N. Wakileh *et al.*, "Single photon emission in the telecom C-band from nanowire-based quantum dots," *Appl. Phys. Lett.*, vol. 124, no. 4, 2024.

[273] J.-H. Kim, T. Cai, C. J. K. Richardson, R. P. Leavitt, and E. Waks, "Two-photon interference from a bright single-photon source at telecom wavelengths," *Optica*, vol. 3, no. 6, pp. 577–584, 2016.

[274] Z. Yuan *et al.*, "Electrically driven single-photon source," *Science (80-.).*, vol. 295, no. 5552, pp. 102–105, 2002.

[275] S. Zaske *et al.*, "Visible-to-telecom quantum frequency conversion of light from a single quantum emitter," *Phys. Rev. Lett.*, vol. 109, no. 14, p. 147404, 2012.

[276] A. Dréau, A. Tchebotareva, A. El Mahdaoui, C. Bonato, and R. Hanson, "Quantum frequency conversion of single photons from a nitrogen-vacancy center in diamond to telecommunication wavelengths," *Phys. Rev. Appl.*, vol. 9, no. 6, p. 64031, 2018.

[277] T. FUYUKI, T. GO, H. YOSHINAGA, and S. YOSHIMOTO, "1.3 μm-Wavelength Laser with Type-II Active Layer on GaAs Substrate".

[278] F. Qiu *et al.*, "An investigation of exciton behavior in type-II self-assembled GaSb/GaAs quantum dots," *Nanotechnology*, vol. 27, no. 6, p. 65602, 2015.

[279] M. W. Wang, D. A. Collins, T. C. McGill, R. W. Grant, and R. M. Feenstra, "Effect of interface composition and growth order on the mixed anion InAs/GaSb valence band offset," *Appl. Phys. Lett.*, vol. 66, no. 22, pp. 2981–2983, 1995.

[280] S. Wu *et al.*, "In-plane optical anisotropy of InAs/GaSb superlattices with alternate interfaces," *Nanoscale Res. Lett.*, vol. 8, no. 1, p. 298, 2013.

[281] C. Fuchs *et al.*, "Electrical injection type-II (GaIn) As/Ga (AsSb)/(GaIn) As single 'W'-quantum well laser at 1.2 μm," *Electron. Lett.*, vol. 52, no. 22, pp. 1875–1877, 2016.

[282] S. Sprengel *et al.*, "InP-based type-II quantum-well lasers and LEDs," *IEEE J. Sel. Top. Quantum Electron.*, vol. 19, no. 4, p. 1900909, 2013.

[283] S. K. Jangir, H. K. Malik, S. Kumari, G. Upadhayaya, R. Raman, and P. Mishra, "Influence of MBE growth parameters on GaSb/GaAs quantum dot morphology," *Phys. E Low-dimensional Syst. Nanostructures*, vol. 118, p. 113911, 2020.

[284] K. Suzuki, R. A. Hogg, and Y. Arakawa, “Structural and optical properties of type II GaSb/GaAs self-assembled quantum dots grown by molecular beam epitaxy,” *J. Appl. Phys.*, vol. 85, no. 12, pp. 8349–8352, 1999.

[285] P. D. Hodgson *et al.*, “Optical and structural properties of InGaSb/GaAs quantum dots grown by molecular beam epitaxy,” *Semicond. Sci. Technol.*, vol. 33, no. 12, p. 125021, 2018.

[286] W.-H. Lin, K.-W. Wang, S.-Y. Lin, and M.-C. Wu, “Long-wavelength electroluminescence of InGaAs-capped type-II GaSb/GaAs quantum-rings at room temperature,” *J. Cryst. Growth*, vol. 378, pp. 571–575, 2013.

[287] W.-H. Lin, K.-W. Wang, S.-W. Chang, M.-H. Shih, and S.-Y. Lin, “Type-II GaSb/GaAs coupled quantum rings: Room-temperature luminescence enhancement and recombination lifetime elongation for device applications,” *Appl. Phys. Lett.*, vol. 101, no. 3, 2012.

[288] J. F. Klem, O. Blum, S. R. Kurtz, I. J. Fritz, and K. D. Choquette, “GaAsSb/InGaAs type-II quantum wells for long-wavelength lasers on GaAs substrates,” *J. Vac. Sci. Technol. B Microelectron. Nanom. Struct. Process. Meas. Phenom.*, vol. 18, no. 3, pp. 1605–1608, 2000.

[289] A. Barbiero *et al.*, “Polarization-selective enhancement of telecom wavelength quantum dot transitions in an elliptical bullseye resonator,” *Nano Lett.*, vol. 24, no. 9, pp. 2839–2845, 2024.

[290] A. Jain, P. V Sakhiya, and R. K. Bahl, “Design and development of weak coherent pulse source for quantum key distribution system,” in *2020 IEEE International Conference on Electronics, Computing and Communication Technologies (CONECCT)*, IEEE, 2020, pp. 1–5.

[291] M. Boyer, D. Kenigsberg, and T. Mor, “Quantum key distribution with classical Bob,” in *2007 First International Conference on Quantum, Nano, and Micro Technologies (ICQNM’07)*, IEEE, 2007, p. 10.

[292] H. Lu and Q.-Y. Cai, “Quantum key distribution with classical Alice,” *Int. J. Quantum Inf.*, vol. 6, no. 06, pp. 1195–1202, 2008.

[293] D. Rusca and N. Gisin, “Quantum cryptography: An overview of quantum key distribution,” *arXiv Prepr. arXiv2411.04044*, 2024.

[294] R. M. Boiselle, “Secure by Nature: The BB84 Protocol from Quantum Theory to Practical Demonstration,” 2025.

[295] Y. Liu *et al.*, “Experimental measurement-device-independent quantum key distribution,” *Phys. Rev. Lett.*, vol. 111, no. 13, p. 130502, 2013.

[296] A. Orieux, M. A. M. Versteegh, K. D. Jöns, and S. Ducci, “Semiconductor devices for entangled photon pair generation: a review,” *Reports Prog. Phys.*, vol. 80, no. 7, p. 76001, 2017.

[297] C. Schimpf, M. Reindl, F. Basso Basset, K. D. Jöns, R. Trotta, and A. Rastelli, “Quantum dots as potential sources of strongly entangled photons: Perspectives and challenges for applications in quantum networks,” *Appl. Phys. Lett.*, vol. 118, no. 10, 2021.

[298] F. Basso Basset *et al.*, “Quantum key distribution with entangled photons generated on demand by a quantum dot,” *Sci. Adv.*, vol. 7, no. 12, p. eabe6379, 2021.

[299] E. Cervero-Martín and M. Tomamichel, “Device independent security of quantum key distribution from monogamy-of-entanglement games,” *Quantum*, vol. 9, p. 1652, 2025.

[300] I. W. Primaatmaja, K. T. Goh, E. Y.-Z. Tan, J. T.-F. Khoo, S. Ghorai, and C. C.-W. Lim, “Security of device-independent quantum key distribution protocols: a review,” *arXiv Prepr. arXiv2206.04960*, 2022.

[301] H.-L. Yin *et al.*, “Measurement-device-independent quantum key distribution over a 404 km optical fiber,” *Phys. Rev. Lett.*, vol. 117, no. 19, p. 190501, 2016.

[302] Y. Li *et al.*, “High-speed robust polarization modulation for quantum key distribution,” *Opt. Lett.*, vol. 44, no. 21, pp. 5262–5265, 2019.

[303] Y.-L. Tang *et al.*, “Measurement-device-independent quantum key distribution over untrustful metropolitan network,” *Phys. Rev. X*, vol. 6, no. 1, p. 11024, 2016.

[304] A. Tomita *et al.*, “High speed quantum key distribution system,” *Opt. Fiber Technol.*, vol. 16, no. 1, pp. 55–62, 2010.

[305] K. Inoue, E. Waks, and Y. Yamamoto, “Differential phase shift quantum key distribution,” *Phys. Rev. Lett.*, vol. 89, no. 3, p. 37902, 2002.

[306] F. Marsili *et al.*, “Detecting single infrared photons with 93% system efficiency,” *Nat. Photonics*, vol. 7, no. 3, pp. 210–214, 2013.

[307] L. You, “Superconducting nanowire single-photon detectors for quantum information,” *Nanophotonics*, vol. 9, no. 9, pp. 2673–2692, 2020.

[308] M. Sasaki *et al.*, “Field test of quantum key distribution in the Tokyo QKD Network,” *Opt. Express*, vol. 19, no. 11, pp. 10387–10409, 2011.

[309] B. Korzh *et al.*, “Provably secure and practical quantum key distribution over 307 km of optical fibre,” *Nat. Photonics*, vol. 9, no. 3, pp. 163–168, 2015.

[310] P. Eraerds, N. Walenta, M. Legré, N. Gisin, and H. Zbinden, “Quantum key distribution and 1 Gbps data encryption over a single fibre,” *New J. Phys.*, vol. 12, no. 6, p. 63027, 2010.

[311] F. Flamini, N. Spagnolo, and F. Sciarrino, “Photonic quantum information processing: a review,” *Reports Prog. Phys.*, vol. 82, no. 1, p. 16001, 2018.

[312] R. G. Pousa, D. K. L. Oi, and J. Jeffers, “Comparison of non-decoy single-photon source and decoy weak coherent pulse in quantum key distribution,” *arXiv Prepr. arXiv2405.19963*, 2024.

[313] C. L. Morrison *et al.*, “Single-emitter quantum key distribution over 175 km of fibre with optimised finite key rates,” *Nat. Commun.*, vol. 14, no. 1, p. 3573, 2023.

[314] K. Takemoto *et al.*, “Quantum key distribution over 120 km using ultrahigh purity single-photon source and superconducting single-photon detectors,” *Sci. Rep.*, vol. 5, no. 1, p. 14383, 2015.

[315] X. Liu, D. Luo, Z. Luo, S. Li, Z. Zhang, and K. Wei, “Reference-frame-independent

quantum key distribution over 250 km of optical fiber," *Phys. Rev. Appl.*, vol. 22, no. 6, p. 64018, 2024.

[316] S. Wang *et al.*, "Twin-field quantum key distribution over 830-km fibre," *Nat. Photonics*, vol. 16, no. 2, pp. 154–161, 2022.

[317] J.-P. Chen *et al.*, "Twin-field quantum key distribution over a 511 km optical fibre linking two distant metropolitan areas," *Nat. Photonics*, vol. 15, no. 8, pp. 570–575, 2021.

[318] J.-P. Chen *et al.*, "Sending-or-not-sending with independent lasers: Secure twin-field quantum key distribution over 509 km," *Phys. Rev. Lett.*, vol. 124, no. 7, p. 70501, 2020.

[319] D. Cozzolino, B. Da Lio, D. Bacco, and L. K. Oxenløwe, "High-dimensional quantum communication: benefits, progress, and future challenges," *Adv. Quantum Technol.*, vol. 2, no. 12, p. 1900038, 2019.

[320] T. Le Roy-Deloison, E. P. Lobo, J. Pauwels, and S. Pironio, "Device-independent quantum key distribution based on routed Bell tests," *PRX Quantum*, vol. 6, no. 2, p. 20311, 2025.

[321] F. Grünenfelder *et al.*, "Fast single-photon detectors and real-time key distillation enable high secret-key-rate quantum key distribution systems," *Nat. Photonics*, vol. 17, no. 5, pp. 422–426, 2023.

[322] F. Picciariello *et al.*, "Intermodal quantum key distribution field trial with active switching between fiber and free-space channels," *EPJ Quantum Technol.*, vol. 12, no. 1, p. 6, 2025.

[323] Z. Yuan *et al.*, "10-Mb/s quantum key distribution," *J. Light. Technol.*, vol. 36, no. 16, pp. 3427–3433, 2018.

[324] M. Pittaluga *et al.*, "600-km repeater-like quantum communications with dual-band stabilization," *Nat. Photonics*, vol. 15, no. 7, pp. 530–535, 2021.

[325] M. Lucamarini, Z. L. Yuan, J. F. Dynes, and A. J. Shields, "Overcoming the rate–distance limit of quantum key distribution without quantum repeaters," *Nature*, vol. 557, no. 7705, pp. 400–403, 2018.

[326] J. R. Arthur, "Molecular beam epitaxy," *Surf. Sci.*, vol. 500, no. 1–3, pp. 189–217, 2002.

[327] R. F. C. Farrow, *Molecular beam epitaxy: applications to key materials*. Elsevier, 1995.

[328] K. W. Böer, "Survey of semiconductor physics," *(No Title)*, 1992.

[329] J. H. Neave, B. A. Joyce, and P. J. Dobson, "Dynamic RHEED observations of the MBE growth of GaAs: Substrate temperature and beam azimuth effects," *Appl. Phys. A*, vol. 34, no. 3, pp. 179–184, 1984.

[330] W. Braun, *Applied RHEED: reflection high-energy electron diffraction during crystal growth*, vol. 154. Springer Science & Business Media, 1999.

[331] A. Ichimiya and P. I. Cohen, *Reflection high-energy electron diffraction*. Cambridge University Press, 2004.

[332] A. Robinson and R. Lawson, *Materials and processes for next generation lithography*, vol. 11. Elsevier, 2016.

[333] M. J. Madou, *Manufacturing techniques for microfabrication and nanotechnology*. CRC press, 2011.

[334] B. Thedjoisworo, D. Cheung, and V. Crist, "Comparison of the effects of downstream H2-and O2-based plasmas on the removal of photoresist, silicon, and silicon nitride," *J. Vac. Sci. Technol. B*, vol. 31, no. 2, 2013.

[335] D. Li, *Encyclopedia of microfluidics and nanofluidics*. Springer Science & Business Media, 2008.

[336] D. M. Mattox, *Handbook of physical vapor deposition (PVD) processing*. William Andrew, 2010.

[337] D. Lane, *Ultraram^{TM}: Design, Modelling, Fabrication and Testing of Ultra-Low-Power III-V Memory Devices and Arrays*. Lancaster University (United Kingdom), 2021.

[338] M. JE, *MSE-474 Physical vapor deposition of thin films*. John Wiley & Sons, 2000.

[339] R. F. Bunshah, *Handbook of deposition technologies for films and coatings: science, applications and technology*. William Andrew, 1994.

[340] J. Handley, "Product review: quartz crystal microbalances," 2001, *ACS Publications*.

[341] S. E. Alexandrov and M. L. Hitchman, "Plasma enhanced chemical vapour deposition processes," 2008.

[342] L. Martinu, O. Zabeida, and J. E. Klemberg-Sapieha, "Plasma-enhanced chemical vapor deposition of functional coatings," *Handb. Depos. Technol. Film. coatings*, pp. 392–465, 2010.

[343] T. Aoki, "Photoluminescence spectroscopy," *Charact. Mater.*, pp. 1–12, 2002.

[344] W. W. Piper and F. E. Williams, "Electroluminescence," in *Solid State Physics*, vol. 6, Elsevier, 1958, pp. 95–173.

[345] T. J. Wilson, P. D. Hodgson, A. J. Robson, C. Jackson, B. Grew, and M. Hayne, "A detailed comparison of measured and simulated optical properties of a short-period GaAs/AlxGa1− xAs distributed Bragg reflector," *Semicond. Sci. Technol.*, vol. 35, no. 5, p. 55003, 2020.

[346] A. Rothen, "The ellipsometer, an apparatus to measure thicknesses of thin surface films," *Rev. Sci. Instrum.*, vol. 16, no. 2, pp. 26–30, 1945.

[347] D. Gonçalves and E. A. Irene, "Fundamentals and applications of spectroscopic ellipsometry," *Quim. Nova*, vol. 25, pp. 794–800, 2002.

[348] D. Shindo and H. Kenji, *High-resolution electron microscopy for materials science*. Springer Science & Business Media, 2012.

[349] W.-H. Lin, M.-Y. Lin, S.-Y. Wu, and S.-Y. Lin, "Room-temperature electro-luminescence of type-II GaSb/GaAs quantum rings," *IEEE Photonics Technol. Lett.*, vol. 24, no. 14, pp. 1203–1205, 2012.

[350] L. Meriggi *et al.*, "Enhanced emission from mid-infrared AlInSb light-emitting

diodes with p-type contact grid geometry," *J. Appl. Phys.*, vol. 117, no. 6, 2015.

[351] M. Hong, D. Vakhshoori, J. P. Mannaerts, and J. Kwo, "Low-Resistivity Non-Alloyed Ohmic Contacts to p-and n-Gaas Using In-Situ Integrated Process," *MRS Online Proc. Libr.*, vol. 337, no. 1, pp. 287–293, 1994.

[352] T. Lin, J. Xie, S. Ning, Q. Li, and B. Li, "Study on the p-type ohmic contact in GaAs-based laser diode," *Mater. Sci. Semicond. Process.*, vol. 124, p. 105622, 2021.

[353] S. Mokkapati and C. Jagadish, "III-V compound SC for optoelectronic devices," *Mater. today*, vol. 12, no. 4, pp. 22–32, 2009.

[354] S.-Y. Tan, T. Zhai, R.-K. Zhang, D. Lu, W. Wang, and C. Ji, "Graded doping low internal loss 1060-nm InGaAs/AlGaAs quantum well semiconductor lasers," *Chinese Phys. B*, vol. 24, no. 6, p. 64211, 2015.

[355] J. R. Shealy, "Optimizing the performance of AlGaAs graded index separate confining heterostructure quantum well lasers," *Appl. Phys. Lett.*, vol. 50, no. 23, pp. 1634–1636, 1987.

[356] M. Kamp, G. Mörsch, J. Gräber, and H. Lüth, "Te doping of GaAs using diethyl-tellurium," *J. Appl. Phys.*, vol. 76, no. 3, pp. 1974–1976, 1994.

[357] W. Jiang, N. X. Nguyen, R. D. Underwood, U. K. Mishra, and R. G. Wilson, "Tellurium-doped Al0. 43Ga0. 57As/(In0. 2) GaAs modulation doped heterostructures by molecular-beam-epitaxy," *Appl. Phys. Lett.*, vol. 66, no. 7, pp. 845–847, 1995.

[358] S. O. Jones, E. Bancroft, S. P. Jarvis, and M. Hayne, "Au/Ni/Au as a contact for p-type GaAs," *Semicond. Sci. Technol.*, vol. 39, no. 12, p. 125011, 2024.

[359] C.-Y. Lu and J.-W. Pan, "Quantum-dot single-photon sources for the quantum internet," *Nat. Nanotechnol.*, vol. 16, no. 12, pp. 1294–1296, 2021.

[360] T. Smołka *et al.*, "Optical quality of InAs/InP quantum dots on distributed Bragg reflector emitting at 3rd telecom window grown by molecular beam epitaxy," *Materials (Basel).*, vol. 14, no. 21, p. 6270, 2021.

[361] J. Kaupp *et al.*, "Purcell-Enhanced Single-Photon Emission in the Telecom C-Band," *Adv. Quantum Technol.*, vol. 6, no. 12, p. 2300242, 2023.

[362] P. E. Vullum *et al.*, "Quantitative strain analysis of InAs/GaAs quantum dot materials," *Sci. Rep.*, vol. 7, no. 1, p. 45376, 2017.

[363] S. Sabri, R. Malek, and K. Kassmi, "A theoretical study of InAs/InP and InAs/GaAs QDs systems: Formation mechanisms and photoluminescence characterization," *Mater. Today Proc.*, vol. 72, pp. 3495–3501, 2023.

[364] K. Gradkowski *et al.*, "Complex emission dynamics of type-II GaSb/GaAs quantum dots," *Appl. Phys. Lett.*, vol. 95, no. 6, 2009.

[365] K. Gradkowski *et al.*, "Coulomb-induced emission dynamics and self-consistent calculations of type-II Sb-containing quantum dot systems," *Phys. Rev. B—Condensed Matter Mater. Phys.*, vol. 85, no. 3, p. 35432, 2012.

[366] Y. P. Varshni, "Temperature dependence of the energy gap in semiconductors," *physica*, vol. 34, no. 1, pp. 149–154, 1967.

[367] M. Hayne *et al.*, “Optically induced charging effects in self-assembled Ga Sb⁄ Ga As quantum dots,” *Phys. Rev. B—Condensed Matter Mater. Phys.*, vol. 70, no. 8, p. 81302, 2004.

[368] M. Hayne, “WO2018162894A1_SPLED patent.pdf” [Online]. Available: https://patents.google.com/patent/WO2018162894A1

[369] L. Turyanska, A. Baumgartner, A. Chaggar, A. Patanè, L. Eaves, and M. Henini, “Sharp-line electroluminescence from individual quantum dots by resonant tunneling injection of carriers,” *Appl. Phys. Lett.*, vol. 89, no. 9, 2006.

[370] M. J. Conterio, N. Sköld, D. J. P. Ellis, I. Farrer, D. A. Ritchie, and A. J. Shields, “A quantum dot single photon source driven by resonant electrical injection,” *Appl. Phys. Lett.*, vol. 103, no. 16, 2013.

[371] J. S. J. Asirvatham, *Characterization of Type-II GaSb Quantum Rings in GaAs Solar Cells*. Lancaster University (United Kingdom), 2015.

[372] S. K. Cheung and N. W. Cheung, “Extraction of Schottky diode parameters from forward current-voltage characteristics,” *Appl. Phys. Lett.*, vol. 49, no. 2, pp. 85–87, 1986.

[373] W. N. Cheung, P. J. Edwards, and G. N. French, “Determination of LED equivalent circuits using network analyser measurements,” in *1998 Conference on Optoelectronic and Microelectronic Materials and Devices. Proceedings (Cat. No. 98EX140)*, IEEE, 1998, pp. 232–235.

[374] K. Takemoto *et al.*, “Transmission experiment of quantum keys over 50 km using high-performance quantum-dot single-photon source at 1.5 μm wavelength,” *Appl. Phys. Express*, vol. 3, no. 9, p. 92802, 2010.

[375] N. Mizuochi *et al.*, “Electrically driven single-photon source at room temperature in diamond,” *Nat. Photonics*, vol. 6, no. 5, pp. 299–303, 2012.

[376] T. T. Tran *et al.*, “Robust multicolor single photon emission from point defects in hexagonal boron nitride,” *ACS Nano*, vol. 10, no. 8, pp. 7331–7338, 2016.

[377] L. Yang, S. Wang, M. Shen, J. Xie, and H. X. Tang, “Controlling single rare earth ion emission in an electro-optical nanocavity,” *Nat. Commun.*, vol. 14, no. 1, p. 1718, 2023.

[378] M. Almendros *et al.*, “Bandwidth-tunable single-photon source in an ion-trap quantum network,” *Phys. Rev. Lett.*, vol. 103, no. 21, p. 213601, 2009.

[379] Y. Zhang *et al.*, “Experimental Single-Photon Quantum Key Distribution Surpassing the Fundamental Weak Coherent-State Rate Limit,” *Phys. Rev. Lett.*, vol. 134, no. 21, p. 210801, 2025.